Numerical modeling of turbulence by Richardson number-based and VMS models

Modelado numérico de la turbulencia mediante
modelos de Richardson y de Multiescala Variacional

Memoria escrita por

Samuele Rubino

Para optar al grado de doctor del
Programa Oficial de Doctorado Matemáticas
Universidad de Sevilla

V^o B^o Los Directores del Trabajo

Tomás Chacón Rebollo, Macarena Gómez Mármol

Dpto. Ecuaciones Diferenciales y Análisis Numérico
Facultad de Matemáticas
Universidad de Sevilla

2 de abril de 2014

To my wife, Alice, for her unconditional support.
In memory of my grandfathers.

"Observe the motion of the surface of the water, which resembles that of hair, which has two motions, of which one is caused by the weight of the hair, the other by the direction of the curls; thus the water has eddying motions, one part of which is due to the principal current, the other to the random and reverse motion."
- Leonardo Da Vinci (1452-1519) [Trans. Ugo Piomelli] -

Abstract

The present thesis addresses the numerical modeling of turbulence by Richardson number-based and Variational Multi-Scale (VMS) models.

In the first part, we focus on Richardson number-based models, frequently used in oceanography. The ocean is a fundamentally turbulent system. Indeed, when we observe animations of the ocean's sea level changes, what is most striking is that the ocean is full of small-scale eddies and meanders, at all latitude bands. Thus, it is crucial to model the oceanic turbulence, in order to improve the understanding of its effects. Here, algebraic closure models based on the gradient Richardson number are theoretically and numerically studied. These are Unsteady Reynolds Averaged Navier-Stokes (URANS) turbulence models, largely used by physical oceanographers to parameterize the mixing layer in the context of Oceanic General Circulation Models (OGCM), in order to better take into account the influence of the atmosphere-ocean surface interactions. We perform a non-linear stability analysis of algebraic turbulence models for oceanic mixing layers, supported by realistic numerical experiments. This establishes a more general criterion for the analysis of mixing-layer models with respect to the existing references.

In the second part, VMS models for the simulation of laminar and turbulent incompressible flows are studied. These are an emerging class of Large Eddy Simulation (LES) turbulence models, that are increasingly used as a valid alternative to LES as they provide a similar accuracy, and avoid some drawbacks. The simulation of wall-bounded flows with VMS models, however, may become very expensive in terms of computational resources due to the computation of boundary layers, that requires very fine meshes in the normal direction to the walls. An alternative to overcome this difficulty is given by the use of wall laws. Wall laws are widely used in engineering simulation of turbulence, usually in RANS models. Here, we focus on the use of VMS-LES models with mixed boundary conditions including wall laws. We propose to work with a projection-based VMS-LES model, that provides a three-scale separation. In view of proposing a viable numerical method for the approximation of both laminar and turbulent flows, we also consider the combination with stabilized *ad-hoc* discretizations, that perfectly fit into the VMS framework. The numerical analysis and the validation through the simulation of 3D relevant flows on coarse grids justify the interest of our approach. The proposed method performs similarly to more complex state-of-the-art VMS models, and offers a good balance between accuracy and computational complexity.

Resumen

La presente tesis aborda el modelado numérico de la turbulencia mediante modelos de Richardson y de Multiescala Variacional (VMS).

En la primera parte, nos centramos en los modelos basados en el número de Richardson, que se utilizan con frecuencia en Oceanogrfía. El océano es un sistema básicamente turbulento. Por lo tanto, es crucial modelar la turbulencia océanica, con el fin de mejorar la comprensión de sus efectos. En este trabajo, los modelos algebraicos basados en el número gradiente de Richardson son teórica y numéricamente estudiados. Estos modelos pertenecen a la clase de modelos de turbulencia URANS (Unsteady Reynolds Averaged Navier-Stokes), y son en gran medida utilizados por los físicos oceanógrafos para parametrizar la capa de mezcla en el contexto de los Modelos de Circulación Oceánica General (OGCM), con el fin de tener mejor en cuenta la influencia de interacciones entre la atmósfera y la superficie del océano. Llevamos a cabo un análisis de estabilidad no-lineal de modelos algebraicos de turbulencia para capas de mezcla oceánicas, apoyado por experimentos numéricos. Este estudio establece un criterio más general para el análisis de modelos de capa de mezcla con respecto a las referencias existentes.

En la segunda parte, se estudian los modelos VMS para la simulación de flujos incompresibles en régimen laminar y turbulento. Estos modelos se utilizan cada vez más como una válida alternativa a modelos de tipo LES (Large Eddy Simulation), ya que proporcionan una precisión similar, y evitan algunas desventajas. La simulación de flujos limitados por paredes sólidas a través de modelos VMS, sin embargo, puede llegar a ser muy costosa en términos de recursos computacionales debido al cálculo de las capas límite, que requiere un mallado muy fino en la dirección normal a las paredes. Una alternativa para superar esta dificultad viene dada por el uso de leyes de pared. Las leyes de pared son ampliamente utilizadas en la simulación de la turbulencia en Ingeniería, usualmente en modelos de tipo RANS. En este trabajo, nos centramos en el uso de modelos VMS-LES con condiciones de contorno mixtas, que incluyen leyes de pared. Proponemos trabajar con un modelo de proyección VMS-LES, que proporciona una separación del flujo en tres escalas. Para proponer un método numérico viable para la aproximación de flujos laminares y turbulentos, también consideramos la combinación con métodos estabilizados, que encajan perfectamente en el marco VMS. El análisis numérico y la validación a través de la simulación de flujos relevantes en 3D justifican el interés de nuestro enfoque. El método propuesto proporciona resultados similares a los de otros modelos VMS más complejos existentes en la literatura, y ofrece un buen balance entre precisión y complejidad computacional.

Acknowledgements

I am sincerely grateful to my advisors, Tomás Chácon Rebollo and Macarena Gómez Mármol, for everything they have done for me during my Ph.D. experience. Thank you for all the knowledge that, with dedication and passion, you have transmitted to me, and all the valuable and essential advices that have contributed to enrich my scientific background. You deserve a special thanks also for all the help you gave me whenever I needed it. It has been really a pleasure to work with you during these years, and to share good times together.

I also wish to thank all the people of "Climate Dynamics Section" of the "Alfred Wegener Institute" in Bremerhaven, for their hospitality and help during my stay. A special thanks goes to Sergey Danilov, Martin Losch, and Jens Schröter, who have largely contributed with fruitful discussions and continuous support to enrich this thesis.

Moreover, I would like to thank the "Departamento de Ecuaciones Diferenciales y Análisis Numérico" of the University of Seville, and the research group M2S2M. You have been like a big family for me during these years.

To conclude, a huge thanks goes to my wife, Alice. Your constant and unconditional support has been essential to complete this work. Grazie di esistere!

Contents

List of Figures

List of Tables

Introduction

One of the most challenging scientific problem of our days is the understanding of turbulence. Turbulent phenomena are present in the everyday-life, so that its understanding is of primary importance, but there is no a rigorous definition of it, and many physical mechanisms governing turbulent motions remain unknown. Only to give an example on how turbulence strongly influences our daily life, we can mention that without the mixing it provides, we could get no fresh air to breath and everything in the modern world would overheat or freeze. Although the problem of understanding turbulence is still far from being solved, some facts can be deduced from observations and experiments. Nevertheless, large numerical simulations by means of turbulence models on huge computers seem to be increasingly the key for understanding and predicting the turbulent motion of fluids.

In this work, we will focus our attention on incompressible flows. The incompressible flows are specified mathematically by the incompressible version of the set of Navier-Stokes equations, as well established by the classical theory of fluid mechanics. This is theoretically valid at the same time for two crucial regimes of the flow, laminar and turbulent, although they are very different to each other from the physical point of view. The occurrence of one or the other state strongly depends on the so-called *Reynolds number* associated to the flow. This was observed by Osborne Reynolds (1842-1912) in the later half of the 19th century. In typical industrial, environmental, and other applications of practical interest, turbulent flows (occurring at high Reynolds numbers) are surely prevalent due to its positive features like a more effective transport and mixing ability with respect to a comparable laminar flow, that is why they have raised a very high interest among the scientific community.

The major problem in treating turbulent flows is due to the wide range of scales involved. For laminar flows already, a substantial range of scales may be encountered. Dealing with turbulent flows, however, it means to deal with even broader ranges of scales in comparison to laminar flows, that are also in non-linear interaction with each other. This makes an analytical analysis extremely complex. Thus, a high hope is put on a numerical way of solving this challenging problem. The straightforward approach, i.e. solving directly the Navier-Stokes equations with appropriate boundary conditions in a numerical manner discover its limitation very soon. Indeed, this procedure, called Direct Numerical Simulation (DNS), demands for a enormously high computational effort (beyond the limits of the currently available computer power in most cases) to accurately solve with extremely fine grids the broad range of scales involved. Turbulence models are then introduced, in order to reduce this computational complexity.

One of the approaches to turbulence modeling that substantially lower the demand of resolution is given by simulations based on the Reynolds Averaged Navier-Stokes (RANS) equations. This approach guarantees the lowest computing cost among the turbulence models, but this fact is counter-balanced by a full degree of modeling. Indeed, this procedure relies on the so-called *Reynolds decomposition*, which consists in decomposing all the variables that determine the flow motion into a mean value, aimed at describing its behavior at large scales, and a fluctuating part, aimed at describing its behavior at small scales. According to this, the complete Reynolds stress tensor has to be modeled. Turbulence models have to be used for this purpose which are, however, lacking generality, since they have to model an extremely wide range of scales. A large number of related turbulence modeling approaches (see Wilcox [88]) have been developed ranging from simple algebraic models to a full Reynolds stress closure. To the category of URANS (Unsteady RANS) models belong the algebraic models based on the so-called *Richardson number*, frequently used in oceanography, that parameterize the turbulence by means of algebraic expressions in terms of the gradient Richardson number, representing the balance between stabilizing buoyancy forces and destabilizing shearing forces.

An improvement to RANS is given by the so-called Large Eddy Simulation (LES) models, for which there exists a really extensive literature. It is an intermediate approach in its requirement of computational effort and degree of modeling between DNS and the simulation utilizing the RANS equations. The strategy of LES consists of resolving the larger flow structures and modeling the effect of the smaller flow structures on the larger structures. The traditional LES relies on a filter to separate resolved and un-resolved scales. On the one hand, a coarser discretization, which is substantially coarser than a comparable DNS discretization, is sufficient for resolving the larger scales and, on the other hand, the universal character of the statistical behavior for the smaller scales justifies the modeling process (see Kolmogorov [64]). The principal advantage with respect to RANS models is that only the action of the smaller scales, with their more universal character, on the resolved flow (larger scales) have to be parameterized through a subgrid-scale model, aspect that is lost within the RANS technique. Historically, the Smagorinsky (*cf.* [56]) model was the first subgrid-scale model introduced, and is still a commonly used one in the framework of LES due to its attractive simplicity. Since it was introduced in 1963 in the context of atmospheric weather prediction, a number of shortcomings of the standard Smagorinsky model based on a constant coefficient have been detected in the meantime, giving rise to more complex and advanced LES models.

Currently, we have distinguished three basic conceptual alternatives for the numerical simulation of turbulence: DNS, LES, and simulations based on the RANS equations. Within this classification, the three concepts for the numerical simulation of turbulent flows struggle with different problems in terms of computational accuracy and efficiency. Note that an important feature of a turbulence model should be to replicate laminar flow regimes too.

In view of this situation, the Variational Multi-Scale (VMS) method appears to be a valuable framework for developing improved numerical models in fluid mechanics. The VMS procedure was introduced in 1998 by Hughes et al. in [51] for multi-scale modeling in computational mechanics problems, and subsequently applied to turbulence modeling in computational fluid dynamics in order to generate a new approach to LES (*cf.* [53], [54], [55]). Nowadays, the VMS models constitute a particular class of LES models, and are increasingly used as a valid alternative to LES for the approximation of the incompressible Navier-Stokes equations, as they provide a similar accuracy and avoid some drawbacks. The basic concept consists in differentiating scale groups. In contrast to the use of a filter in the aforementioned traditional LES, a variational projection between function spaces separates scale ranges within the VMS method. In its original version, it is assumed a separation of two scale groups, with coupling terms. Usually, in analogy to the terminology of LES methods, it may be referred to them as resolved scales and un-resolved scales. The "closure" problem in this case is to provide an approximate solution to the un-resolved small scale flow in terms of the resolved flow. Nevertheless, the framework allows various other arrangements, going beyond this two-scale decomposition, so that several classes of VMS methods have been distinguished in the meantime. In Collis [33] and Gravemeier [43], for instance, the VMS method for LES, which may be abbreviated as VMS-LES, was broadened by raising the number of separated scale groups beyond the original two-scale separation to three scale groups. As in the two-scale separation, a completely different numerical treatment for any of these groups is enabled. The three-scale separation accounts specifically for "large resolved scales", "small resolved scales", and "small un-resolved scales".

In this framework, the direct influence of the subgrid-scale model, usually of (Smagorinsky) eddy viscosity-type in the applications to date, is confined to the small resolved scales. As a result, the large resolved scales are solved as a DNS in the three-scale VMS methods, i.e. without any direct influence of the modeling term. Of course, the large resolved scales are still influenced indirectly by the subgrid-scale model due to the inherent coupling of all scales. The restriction of the direct influence of the subgrid-scale model to the smaller resolved scales also approaches an established principle in turbulence theory, namely *Richardson's energy cascade* (*cf.* [75]). At the beginning of Richardson's energy cascade, the kinetic energy is brought into the turbulent flow by productive mechanisms at the largest scales. Following the picture of a cascade, the energy is then transmitted to smaller and smaller scales by processes not depending on the kinematic viscosity. The viscosity merely acts at the end of the cascade, which is constituted by the smallest scales, by enforcing dissipation of the energy. Thus, the energy cascade proceeds due to a breaking-up of larger eddies which transfers the energy formerly attributed to them to smaller eddies. This goes on until a finally stable eddy motion is reached, and the dissipation of kinetic energy can then take place. Within this cascade, most of the energy that is exchanged across a certain scale-size level comes from the previous larger scale-size level and goes to the next smaller scale-size level. Kolmogorov quantified Richardson's picture of an energy cascade through the well-known *Kolmogorov's energy spectrum* (*cf.* [64]), that has been established and confirmed as a typical energy spectrum of turbulence at sufficiently high Reynolds number in the meantime. In the context of the three-scale separation of

the VMS-LES, the energy cascade principle implies that it is reasonable to assume the mutual influence of the large resolved scales (i.e., the largest scales of the problem) and the un-resolved scales (i.e., the smallest scales of the problem) to be of minor relevance. This feature is in contrast to the Smagorinsky model, where the effect of the un-resolved scales is typically taken into account equally for all resolved scales. As a consequence, the large resolved scales are usually over-damped, and this yields results with low accuracy, un-useful for most flows of practical interest. Such difficulty is solved by more advanced LES models, where the eddy viscosity affects only a short range of resolved small scales (see, for instance, the Taylor and Rational LES models [28], [39], [56]), similarly to VMS methods. However, there is another important aspect of turbulence modeling that seems could be overcome by VMS, but not by LES models. Indeed, no commutation error between the variational projection and differential operators occurs, that arises for LES models because the averaged/filtered equations do not satisfy the boundary conditions (*cf.* [58]). On the contrary, VMS are intrinsically discrete models, and not approximations of an intermediate averaged model. Several works (*cf.* [44], [59]) show the commutation between the projection operator defining the large scales in certain VMS methods and differential operators.

In this work, we take into account several alternatives for the numerical simulation of turbulence already presented, with a special mathematical insight on the numerical modeling of turbulence by Richardson number-based and VMS models. The emphasis is on the numerical analysis of these models in the context of the Finite Element Method (FEM), without disregarding however theoretical aspects of a more general mathematical analysis, that has allowed to shed some new light on various aspects of turbulence modeling for practical fields of interest, especially in oceanography and engineering. I am pretty convinced that the mathematical rigor can continue to offer a significant contribution to understand turbulence, that despite the promising recent advances is still a problem presenting lots of obscure aspects and open questions to work on. In this direction goes the spirit of this work, where we have gathered different issues of modeling, mathematical and numerical analysis, with the aim of trying to take another step forward towards a better modeling of turbulence.

This work is structured in two parts. The first part concerns the study of Richardson number-based models for the simulation of oceanic turbulent mixing layers, while the second part is focused on projection-based VMS turbulence models improved with wall laws for the simulation of laminar and turbulent incompressible flows. We are going to describe more in detail the overview of each part, stating the difficulties and the state of the art of the problems dealt with, as well as the strategies used to address and solve them in this work.

Part I:

Richardson number-based Mixing Layer Turbulence Models.

The mixing layer is located immediately below the ocean surface, and its formation is due to atmospheric-oceanic factors of exchange driven by the wind-stress, that generates a strong turbulent mixing dominated by vertical fluxes. The dynamics of mixing layers play an important role in the global oceanic circulation and global climate changes. Indeed, due to the larger specific heat of seawater with respect to air, the top 2.5 m deep oceanic layer holds as much heat as the full atmosphere over it. The depth of the mixed layer, which is the upper homogeneous part of the mixing layer with almost constant density, is thus of high interest for determining the Sea Surface Temperature (SST) range in oceanic and coastal areas. In addition, the heat stored within the oceanic mixed layer provides a source for heat that drives global variability such as El Niño. The mixed layer has also a deep impact in the evolution of polar ices [25], and it is closely related to different aspects of the oceanic bio-systems too. In global oceanic circulation, it determines how momentum, heat and eventually freshwater are entering or leaving the ocean [3], and for large time scales it is a central component of the global meridional overturning circulation [52], that determines the ventilation of deep ocean.

The bottom of the mixed layer corresponds to the top of the pycnocline, a thin layer with a large gradient of density (see [16], [34] for a physical description of the structure of mixing layers). For instance, in tropical seas, where the density is just a function of the temperature through a state law, a sharp thermocline (zone of high gradients of temperature) is formed. A similar structure of the mixing layer takes place when haline stratification is observed (*cf.* [62]).

The Oceanic General Circulation Models (OGCM) include mixing-layer parameterizations in order to better take into account the influence of the atmosphere-ocean surface interactions (*cf.* [8], [63]). Indeed, they incorporate specific turbulence models for mixing layers, and within these the algebraic ones, that parameterize the turbulent viscosity and diffusion by means of algebraic expressions in terms of the gradient Richardson number. The Richardson number represents the balance between stabilizing buoyancy forces and destabilizing shearing forces. These kinds of first-order closure models were introduced in the 80's by Pacanowski and Philander [49], and they apply to stratified shear flows, that are assumed to have reached a vertical equilibrium, after the vertical mixing generated by the wind-stress has been re-stabilized by buoyancy forces. The model proposed by Pacanowski and Philander (1981) was modified in several ways, in order to obtain a better fitting with experimental data (see the model of Gent (1991) [22]). The cited models are referred as local models, since they only describe local phenomena such as turbulence induced by wind-stress. Another kind of improvement was based upon the parameterization of the vertical profile of turbulent kinetic energy (KPP model of Large et al. (1994) [32]). This model is called mixed model, as it combines a local and non-local approach, that allows to take into account also non-local phenomena such as convection.

The estimation of parameters characterizing local and non-local phenomena is based on the well-known Monin-Obukhov similarity theory (*cf.* [46]). Note that in all models introduced, only vertical eddy viscosity and diffusion effects are included. More complex and sophisticated parameterizations of the vertical turbulent mixing of $k - \varepsilon$ kind have also been developed (e.g., second-order closure models of Mellor and Yamada (1982) [44], and Gaspar et al. (1990) [21]), and widely used in physical oceanographic applications in the context of OGCM.

In the recent years, the mathematical community has shown an increasing interest in the theoretical and numerical analysis of geophysical flow problems. This interest has been mainly addressed to models for large scale oceanic flows, frequently using shallow water approaches in simulating coastal and tidal dynamics. The parameterization of turbulence in the mixing layer must take into account the two forces that act in the momentum and mass exchange produced by mixing effects: buoyancy and shear. However, rather minor attention has been paid to buoyant turbulence effects. Despite that, the behavior of SST strongly depends on a correct description of the turbulent mass and momentum mixing in the upper oceanic layer, where buoyancy plays a key role. This introduces additional complexities with respect to the usual modeling of turbulent flows with constant density, from both the physical and mathematical standpoint. There are several relevant questions concerning mixing-layer models (MLM in the following) that may be analyzed in mathematical terms, but that nowadays have received few attention from the mathematical community. The main one is to determine whether they provide accurate numerical predictions of the oceanic flow in the surface layer, as this is the goal of these models. This requires to determine whether these models are mathematically well posed problems (in the sense of Hadamard), and whether their numerical approximations are stable and provide discrete solutions close to the theoretical ones. Another relevant issue is to analyze the mathematical stability of physically stable configurations. These configurations correspond to decreasing (from ocean surface to the bottom) density profiles, associated to well-mixed turbulent layers, i.e. to stable distribution of mass and momentum, and are typical in tropical oceans. A right numerical simulation of such configurations only will be possible if they are mathematically stable. A third mathematical issue of interest is the analysis of existence and asymptotic stability of continuous and discrete equilibria related to MLM, and their relationship with the above-referenced well-mixed layer configurations. This requires to determine whether well-mixed layers could act as a kind of "absorbing configurations" in finite-time, that asymptotically evolve to steady states.

In general, the mathematical and numerical analysis of MLM technically faces hard difficulties, and up to my knowledge, there are just a few references addressing this analysis on the last cited more complex and sophisticated second-order closure models at the present date. These studies has been mainly conducted in the geophysical community by Burchard and Deleersnijder (*cf.* [17], [7]), and they address a linear stability analysis on strongly simplified versions of second-order closure schemes. Hereafter, we focus our attention on the classical first-order algebraic closure models of Pacanowski-Philander [49] and Gent [22], and on a more recent algebraic turbulent MLM, proposed by Bennis et al. in [2]. Despite their apparent simplicity, the mathematical analysis of these models is

quite involved. This mainly occurs because the turbulent viscosities and diffusions depend on the gradients of the unknowns. In general, energy methods fail to obtain estimates in norms strong enough (these should be of $W^{2,p}$ kind) to handle uniformly bounded gradients from below and from above. In [2], we find an attempt to give a mathematical and numerical insight to the study of algebraic closure models, by a linear analysis of asymptotic stability for continuous and discrete equilibria. From the theoretical point of view, the purpose of this first part of the thesis is mainly to improve and extend this study to the actual non-linear case, performing a non-linear stability analysis of algebraic turbulence models for oceanic mixing layers. The importance of such a study lies on the fact that a linear analysis is simply justified as long as the perturbation from a smooth solution (and its gradient in this case) is small, but only a non-linear analysis can precisely delineate the effective boundaries of the stability region. This establishes a more general criterion for the analysis of mixing-layer models with respect to the existing references.

The structure of **Part I** is as follows:

- In **Chapter 1**, we perform a mathematical analysis of unsteady algebraic closure MLM, focused on the existence and non-linear stability of solutions close to steady states, via the inverse function theorem in Banach spaces.

- In **Chapter 2**, we study the numerical stability of algebraic oceanic turbulent MLM, discretized by the standard FEM. This analysis deals with existence and uniqueness of discrete steady states, convergence of discrete equilibria to the continuous ones, and non-linear asymptotic convergence of discrete time iterates to the continuous equilibria. We will also introduce a Primitive Equations LES model for mixing layers, that we will use as a benchmark for a numerical investigation of the finite-time stability of MLM with respect to multidimensional perturbations.

- Finally, in **Chapter 3**, we investigate the finite-time (characteristic times of formation of well-developed mixing layers) and asymptotic behavior of algebraic turbulent MLM by numerical simulations, using data corresponding to tropical seas as well as to polar regions. The main purpose is to test on one hand the theoretical predictions of the performed analysis, and on another hand the practical performances of the studied models in realistic situations, in comparison with more complex models.

The main results of **Part I** are the product of the papers [10], [11], [12], [54] (see **Bibliography Part I**), written in close collaboration with the advisors of this thesis, Drs. Tomás Chacón-Rebollo and Macarena Gómez-Mármol, and of the stay at the Alfred Wegener Institute (AWI, Bremerhaven, Germany), where I have worked in close collaboration with Drs. Sergey Danilov, Martin Losch, and Jens Schröter of Climate Dynamics Section.

Part II:

Finite Element Projection-based VMS Turbulence Models.

We focus here on the projection-based VMS-LES turbulence models (*cf.* [51], [53], [54], [55]). These are three-level models with "large resolved scales", "small resolved scales" (or sub-filter scales), and "small un-resolved scales". The multi-scale setting clarifies the use of sub-grid eddy viscosity to model the interaction between sub-filter scales and the small un-resolved scales. In particular, we will address a multi-scale Smagorinsky modeling of the eddy viscosity, which contains the restriction to the sub-filter scales through a projection/interpolation operator, thus the adjective "projection-based". A variant of such methods consists in filtering the small scales of the deformation tensor to construct the eddy diffusion term. This method has been studied by John and co-workers (*cf.* [58], [59], [60], [62]). A more complex alternative approach to projection-based VMS methods is the "residual-based" VMS turbulence modeling (*cf.* [2]). The basic procedure is to keep all terms in the residual-driven structure of the resolved flow equations, and to compute an approximated analytical element-wise solution of the small-scale flow. Thus, this procedure does not make use of the statistical theory of equilibrium turbulence, and no eddy viscosity modeling is required by the residual-based VMS models.

The simulation of wall-bounded flows with VMS models, however, may become very expensive in terms of computational resources due to the computation of boundary layers with complex structures, as this requires very fine meshes in the normal direction to the wall (see, for instance, John and Kindl [62], Bazilevs et al. [2]). A way to overcome this difficulty, recently applied to VMS models, is to weakly impose no-slip (or Dirichlet homogeneous) boundary conditions (*cf.* [3], [4]), i.e. to replace them by non-linear Neumann-like boundary conditions. This is an alternative to the use of wall laws, which in their turn replace the usual no-slip boundary conditions by modeled conditions that set the stress of the flow at some distance from the wall. Wall laws are widely used in engineering simulation of turbulence, usually in RANS models. In this work, we focus on the combined use of VMS-LES models with general non-linear wall-law boundary conditions, in the context of FEM.

The most common wall law is the logarithmic law, introduced by Prandtl in 1925 (*cf.* [73]), and derived by similarity laws by Von Karmán in 1930 (*cf.* [87]). The mathematical and numerical analysis of wall laws, as boundary conditions for the Smagorkinsky LES turbulence model, was introduced by Parés (*cf.* [71]). A serious difficulty linked to the approximation of wall laws is the discretization of slip boundary conditions. A strong imposition of these laws only applies to polyhedric domains. The more general treatment, introduced by Verfürth (*cf.* [85], [86]), is by duality. This kind of discretization is quite involved, as it requires a specific boundary finite element space for the multipliers. In [72], Parés introduces a weak formulation of the slip condition. However, the analysis of these techniques has not been extended to mixed boundary conditions, in which other kinds of boundary conditions are imposed, in combination with wall laws, in different parts of the

boundary. This is due to a lack of density results by smooth functions for the functional spaces involved. Here, we will analyze the case of mixed boundary conditions including wall laws, replacing the lacking density result by smooth functions by a similar one with finite element functions, for polyhedric domains.

Our main goal is to propose a viable numerical method for the approximation of laminar and turbulent flows, so that we also consider the combination with stabilized discretizations. We will use high-order term-by-term stabilization to stabilize each single term that could lead to unstable discretizations (e.g., convection, pressure gradient), with high accuracy (*cf.* [19], [20], [22]). This allows in particular to use polynomials of the same degree to interpolate velocity and pressure. We will see as this stabilization procedure perfectly fits into the framework of the VMS method. This further improvement too has contributed to build a quite robust method for the simulation of laminar and turbulent incompressible flows, that provides a good compromise between accuracy and computational complexity.

The structure of **Part II** is as follows:

- In **Chapter 4**, we derive the mathematical formulation of a projection-based VMS model that approximate a mixed boundary value problem for the steady incompressible Navier-Stokes equations, including Dirichlet and wall-law boundary conditions to take into account inflow and solid wall boundaries at the same time. The proposed model only needs a (fine) grid and interpolation operators on a (virtual) coarser grid. The large scales are represented in the (virtual) coarse grid, while the sub-filter scales are their complement into the fine grid.

- In **Chapter 5**, we perform the numerical analysis of the finite element approximation of steady laminar and turbulent flows by the proposed VMS model. We prove stability in natural norms and perform a convergence analysis to the Navier-Stokes equations with rather realistic boundary conditions, that include wall laws and inflow boundary conditions, in steady regime. Moreover, we perform an error analysis, which strengthen the fact that the proposed model is suitable both for laminar and turbulent flows. In particular, for diffusion-dominated flows we recover optimal convergence rates. The error analysis permits to prove the strong convergence of the stabilized VMS method for slightly smooth flows, and a consequent asymptotic energy balance of the system, in which the deformation and the friction boundary energy are asymptotically conserved, and the dissipated eddy energy so as the sub-grid energy due to stabilizing terms tend to zero. Note that the analysis of more complex VMS methods, in particular of residual-based methods, requires further adaptations of the analysis that we present here. Indeed, the sub-grid terms have a very complex structure that includes convective interactions between large and small scales, thus setting serious technical problems just to prove stability.

- Finally, in **Chapter 6**, we analyze the numerical performances of the proposed projection-based VMS model applied to the computation of relevant 3D laminar and turbulent flows, with and without wall-law boundary conditions. The numerical

results are compared with experimental and DNS data, and other results related to more complex VMS methods.

The main results of **Part II** are the product of the papers [21], [22], [23] (see **Bibliography Part II**), written in close collaboration with the advisors of this thesis, Drs. Tomás Chacón-Rebollo and Macarena Gómez-Mármol, and other co-authors.

Part I: Richardson number-based Mixing Layer Turbulence Models

Chapter 1

Algebraic Oceanic Turbulent Mixing-Layer Models (MLM)

1.1 Introduction

In this chapter, we first introduce the governing equations of the ocean. Afterwards, we derive the mathematical formulation of vertical (1D) algebraic closure mixing-layer models (MLM) from a statistical Reynolds averaging of the Boussinesq equations of the ocean. We then perform a mathematical analysis of unsteady algebraic closure MLM, focused on the existence and non-linear stability of solutions close to steady states, via the inverse function theorem in Banach spaces.

The chapter is structured as follows: In Section 1.2, we introduce the Boussinesq Equations of the ocean. In Section 1.3, we derive the mathematical formulation of vertical (1D) algebraic closure MLM from a statistical Reynolds averaging of the Boussinesq Equations. Finally, in Section 1.4, we determine the steady states of perturbed algebraic closure MLM (Subsection 1.4.1), we prove existence and uniqueness of unsteady solutions close to a given equilibrium state (Subsection 1.4.2), and we use the result of existence to prove the non-linear asymptotic stability of equilibrium solutions, for small enough data of the problem (Subsection 1.4.3).

The main results presented in this chapter can be found in [11].

1.2 Basic equations of the ocean

We introduce the governing equations of the ocean. Following Kowalik and Murty [30], the effects of the Earth's curvature on the motion of a fluid at relatively small horizontal distances of the order of 1000 km may be neglected. To describe this motion, a rectangular system of coordinates will be employed, thus making the equations and discussion much simpler. Let us introduce a right-handed rectangular coordinate system in the tangent plane to the origin (located at the undisturbed level of the free sea surface). The coordinate system is such that the i axis points towards east, the j axis points towards

north, and the k axis points upwards, towards zenith (see Figure 1.1). Anyway, let us re-

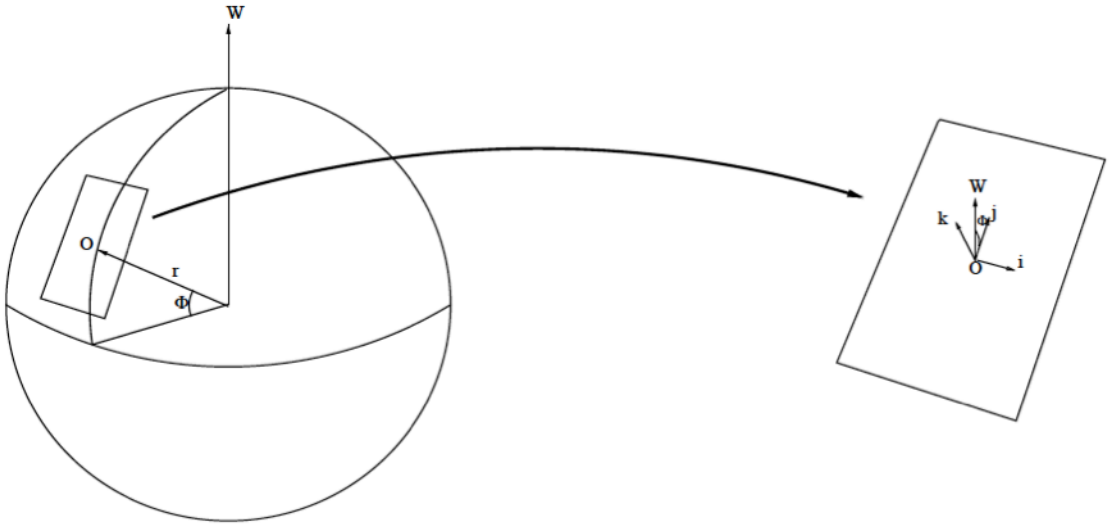

Figure 1.1:
Rectangular coordinate system.

mark that in OGCM, spherical coordinates (see, for instance, the OPA-Ocean PArallelise model [38], developed by the LODYC-Laboratoire d'Océanographie Dynamique et de Climatologie, France, or the FESOM-Finite Element Sea-ice Ocean Model [63], developed by the AWI-Alfred Wegener Institute, Germany) are often used.

Let us consider a connected domain $\omega \in \mathbb{R}^2$. We shall assume that the fluid fills the domain:

$$\Omega = \{(\mathbf{x}, z) \in \mathbb{R}^3; \mathbf{x} = (x, y) \in \omega, -D(\mathbf{x}) < z < \eta(\mathbf{x}; t)\}, \tag{1.1}$$

where $D : \overline{\omega} \to \mathbb{R}_+$ denotes the ocean bottom and $\eta : \overline{\omega} \times [0, \mathcal{T}]$ is the free sea surface, being t the time variable, and $\mathcal{T}$ a fixed time. The physical variables describing the state of the ocean are:

- the velocity $\mathbf{U}$:
$$\mathbf{U} = \mathbf{u} + w\mathbf{k} = u\mathbf{i} + v\mathbf{j} + w\mathbf{k},$$
where $\mathbf{u}$ and w denotes the horizontal and vertical components;
- the pressure p;
- the potential temperature Θ and the salinity S;
- the density ρ.

Due to Earth's rotation, oceanic flows are affected by Coriolis force. Therefore, the governing equations of the ocean are the following (*cf.* [23], [50]):

- **Momentum conservation equations**:

$$\rho\partial_t\mathbf{U} + \rho\nabla\cdot(\mathbf{U}\otimes\mathbf{U}) + 2\rho\mathbf{W}\times\mathbf{U} + \rho\mathbf{W}\times(\mathbf{W}\times\mathbf{r}) - \nabla\cdot\sigma = -\rho\mathbf{g}, \tag{1.2}$$

where σ is the stress tensor, $\mathbf{W} = \theta(0, \cos\Phi, \sin\Phi)$ is the Earth's rotation vector, θ the angular rotation rate of the Earth and Φ the latitude. The vectorial product $\mathbf{W}\times\mathbf{U}$ represents the Coriolis acceleration, $\mathbf{r}$ the position vector of an arbitrary fluid element, $\mathbf{W}\times(\mathbf{W}\times\mathbf{r})$ the centripetal acceleration, and $\mathbf{g} = (0, 0, g)$ the gravity acceleration. Both Coriolis and centripetal accelerations are a consequence of expressing the equations in a rotating coordinate frame.

- **Mass conservation equation**:

$$D_t\rho + \rho\nabla\cdot\mathbf{U} = 0, \tag{1.3}$$

where $D_t = \partial_t + \mathbf{U}\cdot\nabla$ denotes the total derivative.

- **Internal energy conservation equation**:

$$\rho c_p D_t\Theta + \Theta(\partial_\Theta\rho/\rho)(D_t p) = K_c^t\Delta\Theta, \tag{1.4}$$

where c_p denotes the specific heat of the fluid at constant pressure, and K_c^t its thermal conductivity. In (1.4), the first summand represents convection by the velocity field $\mathbf{U}$, the second energy variations due to pressure fluctuations, and the r.h.s. represents energy dissipation due to molecular diffusion.

- **Salinity conservation equation**:

$$D_t(\rho S) = K_c^s\Delta S, \tag{1.5}$$

where K_c^s is the coefficient of salt diffusion.

- **Equation of state**:

$$\rho = \rho(\Theta, S, p). \tag{1.6}$$

In the ocean, complications arise because the density of seawater can depend in subtle ways on potential temperature Θ, salinity S, and pressure p (*cf.* [61]). Actually, equation (1.6) is a non-linear equation of Θ, S and p, and different accurate formulations can be derived for it (e.g., Jackett and McDougall [28], McDougall et al. [41], implemented in MITgcm [45]). However, often in theoretical studies a simplified equation of state is adopted of the form:

$$\rho = \rho_r(1 - \alpha_\Theta(\Theta - \Theta_r) + \beta_S(S - S_r)), \tag{1.7}$$

where the subscript r denotes a reference value, and α_Θ, β_S are respectively the thermal expansion and haline contraction (positive) coefficients of seawater.

In the Coriolis acceleration term in (1.2), since vertical velocities are of the order of thousandths of the horizontal ones, the contribution provided by the vertical velocity is usually neglected. We may rewrite:

$$2\mathbf{W}\times\mathbf{U}\approx(-fv,fu,-2u\theta\cos\Phi)=\mathbf{C},$$

where $f=2\theta\sin\Phi$, and denote this term by $\mathbf{C}$. About the centripetal acceleration term in (1.2), we may use a potential Φ_c to write (*cf.* [50]):

$$\mathbf{W}\times(\mathbf{W}\times\mathbf{r})=-\nabla\Phi_c,\quad \Phi_c=\frac{\|\mathbf{W}\times\mathbf{r}\|^2}{2}.$$

One of the mean features of the ocean is that the only term where density variations are important is the buoyancy (or gravity) term in the vertical component of the momentum equations (1.2). This approach is called *Boussinesq approximation*, and it leads to the so-called *Boussinesq Equations*:

$$\begin{cases}
(a)\quad \partial_t\mathbf{U}+(\mathbf{U}\cdot\nabla)\mathbf{U}-\nu\Delta\mathbf{U}+\mathbf{C}+\dfrac{\nabla p}{\rho_r}=-\dfrac{\rho}{\rho_r}\mathbf{g} & \text{in}\quad \Omega\times(0,\mathcal{T})\\
(b)\quad \nabla\cdot\mathbf{U}=0 & \text{in}\quad \Omega\times(0,\mathcal{T})\\
(c)\quad \partial_t\Theta+\mathbf{U}\cdot\nabla\Theta-K_\Theta\Delta\Theta=0 & \text{in}\quad \Omega\times(0,\mathcal{T})\\
(d)\quad \partial_t S+\mathbf{U}\cdot\nabla S-K_S\Delta S=0 & \text{in}\quad \Omega\times(0,\mathcal{T})\\
(e)\quad \rho=\rho(\Theta,S,p) & \text{in}\quad \Omega\times(0,\mathcal{T})
\end{cases}\tag{1.8}$$

In (1.8), we have approximated seawater by a Newtonian viscous incompressible fluid, so that the stress tensor takes the form:

$$\sigma_{i,j}=-p\delta_{i,j}+\tau_{i,j},$$

where $\delta_{i,j}$ is the Kronecker delta, and:

$$\tau_{i,j}=\mu\left(\frac{\partial u_i}{\partial x_j}+\frac{\partial u_j}{\partial x_i}\right),$$

is the viscous stress, with μ the dynamic (or molecular) viscosity. Moreover, we have considered the density variable as a deviation from a reference seawater density ρ_r, and we have called the kinematic viscosity $\nu=(\mu/\rho_r)$, the temperature diffusion $K_\Theta=(K_c^t/\rho_r c_p)$ and the salinity diffusion $K_S=(K_c^s/\rho_r)$.

1.3 Setting of algebraic closure models

We derive the mathematical formulation of vertical (1D) algebraic closure MLM from a statistical Reynolds averaging of the Boussinesq Equations (1.8). The ocean flow is fundamentally turbulent, and it is necessary to model the oceanic turbulence in order to give a better understanding of its effects. In this work, we choose to use the URANS (Unsteady Reynolds Averaged Navier-Stokes) approach (*cf.* [34]), and we briefly describe

it. The first step consists in decomposing all the variables that determine the flow motion into a mean value ($^-$), which describes its behavior at large scales, and a fluctuating part ($'$), which describes its behavior at small scales. This is the so-called *Reynolds decomposition*, and for an arbitrary scalar variable ϕ of the flow, it reads as $\phi = \overline{\phi} + \phi'$. If we call ϕ and ψ two generic scalar field variables, we have that the averaging operator ($^-$) must satisfy the following rules, called *Reynolds axioms*:

- Linearity:
$$\overline{\phi + \psi} = \overline{\phi} + \overline{\psi} \text{ and } \overline{a\phi} = a\overline{\phi},\ a \in \mathbb{R}.$$
- Commutativity with temporal or spatial differentiation:
$$\overline{\partial_s \phi} = \partial_s \overline{\phi},\ s = t \text{ or } s = x, y, z.$$
- Generalized idempotence:
$$\overline{\overline{\phi}\psi} = \overline{\phi}\,\overline{\psi}.$$

There exist different ways of averaging, being ensemble, time and space averaging the main ones. Here, we choose to work with ensemble (or statistical) averaging, that is the most general, and of course satisfies the Reynolds axioms. It consists in taking into account the measurements from N identical experiments or numerical simulations. If we denote by ϕ^n the $n-th$ result for an arbitrary scalar variable ϕ of the flow, the ensemble averaging is obtained as:

$$\overline{\phi}(\mathbf{x}; t) = \lim_{N \to \infty} \frac{1}{N} \sum_{i=1}^{N} \phi^n(\mathbf{x}; t). \tag{1.9}$$

By applying the Reynolds decomposition to system (1.8), and averaging by the ensemble operator (1.9), we obtain the statistical averaged Boussinesq Equations for the mean flow:

$$\begin{cases} (a) & \partial_t \overline{\mathbf{U}} + (\overline{\mathbf{U}} \cdot \nabla)\overline{\mathbf{U}} + \nabla \cdot \mathcal{R} - \nu \Delta \overline{\mathbf{U}} + \mathbf{C} + \dfrac{\nabla \overline{p}}{\rho_r} = -\dfrac{\overline{\rho}}{\rho_r}\mathbf{g} & \text{in} & \Omega \times (0, \mathcal{T}) \\ (b) & \nabla \cdot \overline{\mathbf{U}} = 0 & \text{in} & \Omega \times (0, \mathcal{T}) \\ (c) & \partial_t \overline{\Theta} + \overline{\mathbf{U}} \cdot \nabla \overline{\Theta} + \nabla \cdot T_\Theta - K_\Theta \Delta \overline{\Theta} = 0 & \text{in} & \Omega \times (0, \mathcal{T}) \\ (d) & \partial_t \overline{S} + \overline{\mathbf{U}} \cdot \nabla \overline{S} + \nabla \cdot T_S - K_S \Delta \overline{S} = 0 & \text{in} & \Omega \times (0, \mathcal{T}) \\ (e) & \overline{\rho} = \overline{\rho}(\overline{\Theta}, \overline{S}, \overline{p}) & \text{in} & \Omega \times (0, \mathcal{T}) \end{cases} \tag{1.10}$$

where $\mathcal{R}$ is the Reynolds stress tensor, given by:

$$\mathcal{R} = \overline{\mathbf{U}' \otimes \mathbf{U}'}, \tag{1.11}$$

and:

$$T_\Theta = \overline{\Theta' \mathbf{U}'}, \quad T_S = \overline{S' \mathbf{U}'}. \tag{1.12}$$

From the statistical averaging of the Boussinesq Equations (1.10), we derive the mathematical formulation of vertical (1D) algebraic closure MLM. Note that the classical algebraic MLM of Pacanowski-Philander [49] and Gent [22] have been introduced to parameterize the vertical mixing in tropical oceans. In this situation, several physical approximations could be applied to system (1.10):

- **Hypothesis of horizontal homogeneity**: The mixing layer is assumed to be strongly dominated by vertical fluxes in the region considered, so that velocity $\mathbf{U}$, pressure p, potential temperature Θ, salinity S and, as consequence, density ρ of the fluid are assumed to be horizontally homogeneous. Thus, only vertical viscosity and diffusion effects are included.

- **Hydrostatic hypothesis**: The flow is assumed to be turbulent and well-mixed, so that the statistical mean vertical velocity $\overline{w}$ is assumed to vanish. Physically, this means that the cited models apply to stratified shear flows, that are assumed to have reached a vertical equilibrium, after the vertical mixing generated by the wind-stress has been re-stabilized by buoyancy forcing.

- **Hypothesis of incompressibility**: In tropical seas, the mixing layer normally reaches depths of the order of 100 m, so that the density can be considered as independent of pressure, since the effects of compression are only relevant at greater depths (*cf.* [23]). In this way, the density is just a function of temperature and salinity through a state law, so it can be considered as a thermodynamic variable, which is intended to represent temperature and salinity variations.

- **Hypothesis of null rotation**: The Coriolis term $\mathbf{C}$ can be neglected, which is a valid approximation since the influence of the Coriolis force is very small in Equatorial regions (*cf.* [50]).

All the previous assumptions lead to a simplified vertical (1D) system, where the convection terms disappear, and the continuity (or mass conservation) equation is automatically verified. To describe it, let $z \in [-h, 0]$ be the vertical spatial variable, where $h > 0$ denotes the thickness of the analyzed layer, that must contain the mixing layer, and $t \in [0, \mathcal{T}]$ be the time variable. The system affects the statistical mean horizontal velocity $(\overline{u}, \overline{v})$, the statistical mean pressure $\overline{p}$ and the statistical mean density $\overline{\rho}$ as functions of the variables z and t. The equations governing the mixing layer becomes:

$$\begin{cases} (a) \quad \partial_t \overline{u} - \nu_L \partial^2_{zz} \overline{u} = -\partial_z(\,\overline{u'w'}\,) & \text{in} \quad (-h,0)\times(0,\mathcal{T}) \\ (b) \quad \partial_t \overline{v} - \nu_L \partial^2_{zz} \overline{v} = -\partial_z(\,\overline{v'w'}\,) & \text{in} \quad (-h,0)\times(0,\mathcal{T}) \\ (c) \quad \dfrac{\partial_z \overline{p}}{\rho_r} = -\dfrac{\overline{\rho}}{\rho_r} g - \partial_z(\,\overline{w'w'}\,) & \text{in} \quad (-h,0)\times(0,\mathcal{T}) \\ (d) \quad \partial_t \overline{\rho} - K_L \partial^2_{zz} \overline{\rho} = -\partial_z(\,\overline{\rho'w'}\,) & \text{in} \quad (-h,0)\times(0,\mathcal{T}) \end{cases} \tag{1.13}$$

where ν_L and K_L denotes respectively the laminar viscosity and (density) diffusion coefficients, and we recall that $(u',\, v',\, w')$ and ρ' are the fluctuations of the velocity and density of the fluid, respectively. Equations in (1.13) are the classical equations corresponding to the modeling of a water column. Note that equations in (1.13) are not closed, as mean variables appear coupled with their corresponding fluctuating part. To overcome the *closure problem*, typical in turbulence modeling, the vertical fluxes appearing in the r.h.s. of (1.13) need to be modeled.

The algebraic closure MLM use the concept of eddy viscosity and diffusion in order to represent turbulent fluxes. In particular, we set:

$$-\overline{u'w'} = \nu_T \partial_z \overline{u}, \quad -\overline{v'w'} = \nu_T \partial_z \overline{v}, \quad -\overline{\rho'w'} = K_T \partial_z \overline{\rho},$$

where ν_T and K_T are the vertical eddy viscosity and diffusivity coefficients. Note that, by hydrostatic hypothesis, equation (c) in (1.13) is reduced to the so-called *hydrostatic equation*:

$$\partial_z \overline{p} = -\overline{\rho} g, \tag{1.14}$$

that we can skip in the following analysis as it is decoupled from the remaining equations. The eddy coefficients ν_T and K_T are expressed as functions of the gradient Richardson number R, defined as:

$$R = -\frac{g}{\rho_r} \frac{\partial_z \overline{\rho}}{(\partial_z \overline{u})^2 + (\partial_z \overline{v})^2}, \tag{1.15}$$

where we recall that g is the gravity acceleration, and ρ_r a reference density for seawater ($\rho_r \approx 10^3$ kg m^{-3}). When $R >> 1$, a strongly stratified layer takes place. This corresponds to a stable configuration. When $0 < R << 1$, a slightly stratified layer takes place. This corresponds to a configuration with low stability. The case $R < 0$ corresponds to a configuration statically unstable, for which $\partial_z \overline{\rho} > 0$.

Without risk of confusion, we can omit hereafter the symbol ($^-$) to denote statistical mean values, and system (1.13) now reads as:

$$\begin{cases} (a) \quad \partial_t u - \partial_z(\nu \partial_z u) = 0 \quad \text{in} \quad (-h, 0) \times (0, \mathcal{T}) \\ (b) \quad \partial_t v - \partial_z(\nu \partial_z v) = 0 \quad \text{in} \quad (-h, 0) \times (0, \mathcal{T}) \\ (c) \quad \partial_t \rho - \partial_z(K \partial_z \rho) = 0 \quad \text{in} \quad (-h, 0) \times (0, \mathcal{T}) \end{cases} \tag{1.16}$$

where $\nu = \nu_L + \nu_T$, $K = K_L + K_T$ respectively are the total viscosity and diffusion. We describe hereafter the modeling of the eddy coefficients ν_T and K_T made by the standard Pacanowski-Philander [49] and Gent [22] models, and a more recent model proposed by Bennis et al. [2]. The eddy coefficients corresponding to the Pacanowski-Philander (PP) model are given by:

$$\nu = f_1(R), \quad K = f_2(R),$$

where:

$$f_1(R) = a_1 + \frac{b_1}{(1 + 5R)^2}, \quad f_2(R) = a_2 + \frac{f_1(R)}{1 + 5R}, \tag{1.17}$$

with $a_1 = 10^{-4}$, $b_1 = 10^{-2}$, $a_2 = 10^{-5}$ (units: m^{2}s^{-1}). The Gent model is a variant of the PP model, designed to better fit experimental data, given by:

$$f_1(R) = a_1 + \frac{b_1}{(1 + 10R)^2}, \quad f_2(R) = a_2 + \frac{b_1}{(1 + 10R)^3}, \tag{1.18}$$

with $a_1 = 10^{-4}$, $b_1 = 10^{-1}$, $a_2 = 10^{-5}$ (units: m^{2}s^{-1}). The main physical reason for the structure of f_1 in (1.17) and (1.18) is that buoyancy stratification inhibits mixing effects,

so that the inhibition increases as R increases, and mixing effects should tend to disappear as R tends to infinity. This suggests a structure for the turbulent viscosity as:

$$\nu_T = \frac{\nu_0}{(1+\sigma R)^n},$$

for some positive adjustable parameters ν_0, σ and n, chosen respecting the best agreement of numerical results with observations done in different tropical areas. The expression for f_2 in (1.17) and (1.18) is largely dictated by measurements: K_T/ν_T has to decrease to zero as R increases. This suggests a similar modeling, although this is less clear than the one of ν_T, so that there exist different possibilities, as shown by the different parameterization of PP and Gent models. The experimental origins of this kind of modeling may be found in Robinson [53] and Jones [29].

The PP and Gent models apply to vertical stable configurations, and so to well-mixed layer, for which $\partial_z \rho \leq 0$, and thus $R \geq 0$. It means that although turbulence may be generated by wind shear stress and buoyancy, these models describes the state of the flow once the vertical configuration has been stabilized by buoyancy forces. However, we shall need a more global parameterization of vertical mixing to perform numerical experiments, in order to take into account realistic initial conditions with unstable configurations, corresponding to the case $R < 0$. Indeed, note that in their original form PP and Gent models are no longer physically valid respectively for $R \in (-3.13, -0.2)$ and $R \in (-2.25, -0.1)$, since the diffusion coefficient f_2 becomes negative. Moreover, in [1] it is proved by a linear stability analysis that both formulations present a numerical instability zone for a certain range of negative R (respectively, $R \in [-0.2, -0.1]$ and $R \in [-0.1, -0.0524]$). So that these models result useless in their original form for a large range of negative R (respectively, $R \in (-3.13, -0.1]$ and $R \in (-2.25, -0.0524]$). In practice, ocean modelers bypass this problem by limiting the eddy viscosities and diffusivities to values below a certain positive constant. In Bennis et al. [2], a modeling of the eddy diffusion that remains useful for a larger range of negative values of R was introduced:

$$f_1(R) = a_1 + \frac{b_1}{(1+5R)^2}, \quad f_2(R) = a_2 + \frac{f_1(R)}{(1+5R)^2}, \tag{1.19}$$

with the same constants of the PP model. This model always provide positive diffusion for negative values of R, so that it does not present a zone of physically unreasonable solutions. Actually, it only presents a numerical instability zone ($R \in [-0.37, -0.2]$, *cf.* [1]) where the model can not be used in its original form, and the eddy coefficients need to be smoothly extended to positive constant values, in order to model a forced return to a vertical stable configuration. However, this model seems to be more natural and smoother in handling static instabilities with respect to the artificial imposition of limited viscosities and diffusivities in PP and Gent models for negative R, as usual.

In formulas (1.17) to (1.19), the eddy coefficients ν_T and K_T are defined as functions of the gradient Richardson number R through the terms $(1+\gamma R)^n$ appearing at the denominator. Hereafter, these three formulations could also be denoted respectively by $R213$, $R23$ and $R224$, where the integer values are the exponents of $(1+\gamma R)$ in the definitions

of ν_T and K_T. The results on the linear stability analysis for the different models are summarized in Figure 1.2. Here, the blue line represents a zone where the solution is physically not valid, and this is the case for the $R23$ and $R213$ formulations, while the red zone is a numerical instability region, common to all formulations. Nevertheless, one observes that for each model mathematical stability (green zone) holds for non-negative R.

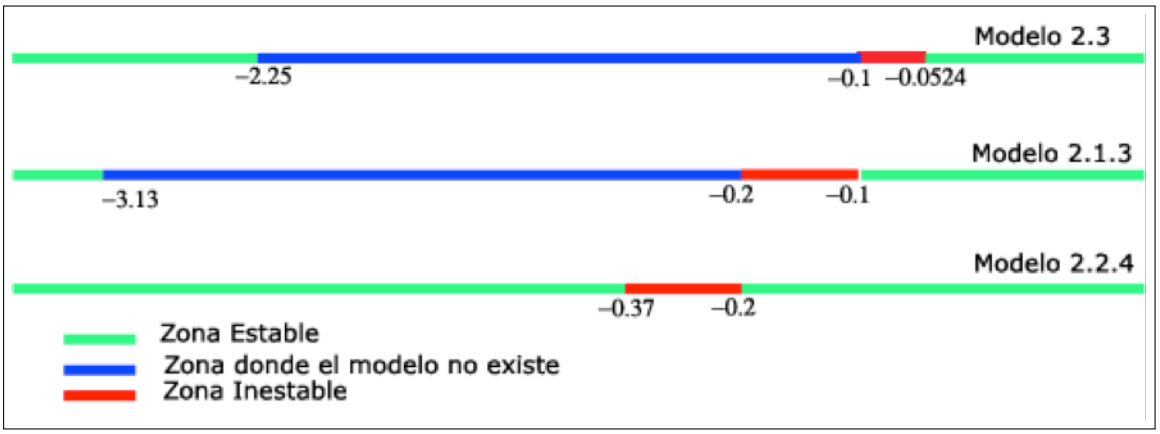

Figure 1.2:
Linear stability analysis for models $R224$, $R213$ and $R23$.

More in detail, the eddy coefficients defined by models $R213$, $R23$ and $R224$ all present a singularity for a negative value of the gradient Richardson number R. In Figure 1.3, we have plotted the curves $\nu = f_1(R)$ and $K = f_2(R)$, obtained with the different formulations, where we graphically see that for $R213$ (in green) and $R23$ (in blue) models, the diffusivity coefficient K becomes negative for a certain range of negative values of R.

For a deeper analysis of the aforementioned models, we shall consider the following initial and boundary conditions associated to problem (1.16):

$$\begin{cases} (d) \quad \nu\partial_z u = Q_u(t),\ \nu\partial_z v = Q_v(t),\ K\partial_z \rho = Q_\rho(t) & \text{at} \quad z = 0 \\ (e) \quad u = u_b(t),\ v = v_b(t),\ \rho = \rho_b(t) & \text{at} \quad z = -h \\ (f) \quad u = u_0(z),\ v = v_0(z),\ \rho = \rho_0(z) & \text{at} \quad t = 0 \end{cases} \tag{1.20}$$

The Neumann boundary conditions at $z = 0$ represent the fluxes at the sea-surface that model the forcing by the atmosphere. In particular Q_u, Q_v are the surface momentum fluxes, and Q_ρ represents thermodynamic fluxes: warming or cooling, precipitations or evaporation. The momentum fluxes are given by:

$$Q_u(t) = \frac{\rho_a}{\rho_r} V_u(t), \quad Q_v(t) = \frac{\rho_a}{\rho_r} V_v(t),$$

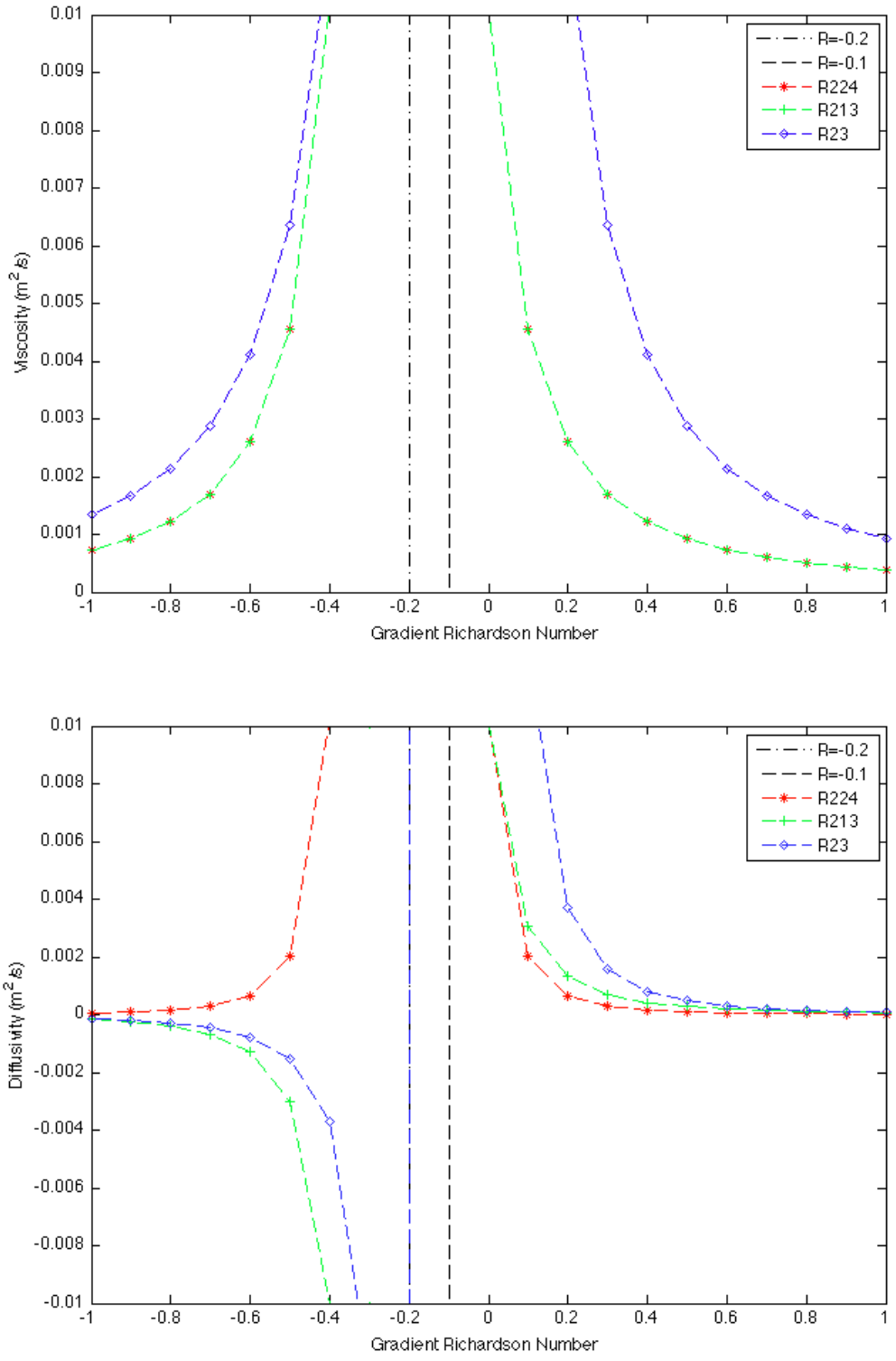

Figure 1.3:
Viscosity and diffusivity for models $R224$, $R213$ and $R23$.

where ρ_a is the air density ($\rho_a \approx 1$ kg m^{-3}), and V_u, V_v respectively are the stresses exerted by the zonal and the meridional winds:

$$(V_u(t), V_v(t)) = C_D |\mathbf{U}_a(t)| \mathbf{U}_a(t),$$

with $\mathbf{U}_a(t) = (u_a(t), v_a(t))$ the air velocity at the atmospheric boundary layer, and C_D ($= 1.2 \times 10^{-3}$) a friction coefficient (*cf.* [30]). The circulation for $z < -h$, under the mixing layer, is supposed to be known, either by observations or a deep circulation numerical model. This justifies the choice of Dirichlet boundary conditions at $z = -h$.

Note that model (1.16)-(1.20) is not expected to describe all the interaction phenomena occurring in the mixing layer. Its purpose is mainly to give a better understanding of algebraic closure models for oceanic turbulent mixing layers, and it is also used as a pretext for the study of such kind of complex systems in a rather abstract framework. Therefore, we shall use simplified equations governing the variables u (zonal velocity), v (meridional velocity) and ρ (density). In practice, mixing-layer models are coupled with 3D models of global oceanic circulation, that yield the boundary values for velocity and density at the bottom of the layer. The coupling of 1D mixing-layer models to 3D OGCM for the inner oceanic flows causes that the 1D model may be affected by multidimensional perturbations.

1.4 Analysis of continuous solutions

In this section, we determine the steady states of perturbed algebraic closure MLM (Subsection 1.4.1), we prove existence and uniqueness of unsteady solutions close to a given equilibrium state (Subsection 1.4.2), and we use the result of existence to prove the non-linear asymptotic stability of equilibrium solutions, for small enough data of the problem (Subsection 1.4.3).

1.4.1 Existence and uniqueness of continuous equilibria

We prove in this subsection that there exist smooth steady solutions of model (1.16)-(1.20) for slightly perturbed data. These perturbations may correspond to errors in the experimental measurements, roundoff computational errors, errors in the boundary data coming from the approximate solution of the 3D global model, etc. The steady solutions correspond to an equilibrium between destabilizing wind shear effects and stabilizing thermodynamic fluxes. The result of existence of smooth equilibria permits to have effectively a real smooth solution for the studied problem, to be used in the sequel for the proof of the non-linear asymptotic stability.

Let us consider the perturbed model:

$$\begin{cases} (a) \quad \partial_t u - \partial_z(\nu \partial_z u) = D_u \quad \text{in} \quad (-h, 0) \times (0, \mathcal{T}) \\ (b) \quad \partial_t v - \partial_z(\nu \partial_z v) = D_v \quad \text{in} \quad (-h, 0) \times (0, \mathcal{T}) \\ (c) \quad \partial_t \rho - \partial_z(K \partial_z \rho) = D_\rho \quad \text{in} \quad (-h, 0) \times (0, \mathcal{T}) \end{cases} \tag{1.21}$$

with the perturbed initial and boundary conditions:

$$\begin{cases} (d) & \nu\partial_z u = \widetilde{Q}_u(t),\ \nu\partial_z v = \widetilde{Q}_v(t),\ K\partial_z \rho = \widetilde{Q}_\rho(t) & \text{at} \quad z = 0 \\ (e) & u = \widetilde{u}_b(t),\ v = \widetilde{v}_b(t),\ \rho = \widetilde{\rho}_b(t) & \text{at} \quad z = -h \\ (f) & u = \widetilde{u}_0(z),\ v = \widetilde{v}_0(z),\ \rho = \widetilde{\rho}_0(z) & \text{at} \quad t = 0 \end{cases} \tag{1.22}$$

where D_u, D_v, D_ρ are smooth functions of z and t. Since we are searching for equilibria, we remove the dependence on time from system (1.21)-(1.22), and we mark by the apex ^{e} the corresponding equilibrium quantities. Let us denote the space interval $I = (-h, 0)$, and define the functions:

$$d_u(z) = \int_z^0 D_u^e(s)\, ds, \quad d_v(z) = \int_z^0 D_v^e(s)\, ds, \quad d_\rho(z) = \int_z^0 D_\rho^e(s)\, ds.$$

The existence and uniqueness of equilibria for problem (1.21)-(1.22) are given by the following:

Theorem 1.1. *Assume that for any $z \in I$ the implicit algebraic equation:*

$$R = G(z)\frac{[f_1(R)]^2}{f_2(R)}, \tag{1.23}$$

where $G(z)$ is the function defined by:

$$G(z) = -\frac{g}{\rho_r}\ \frac{d_\rho(z) + \widetilde{Q}_\rho^e}{\left(d_u(z) + \widetilde{Q}_u^e\right)^2 + \left(d_v(z) + \widetilde{Q}_v^e\right)^2}, \tag{1.24}$$

admits at least a solution R^e. Then, to each solution R^e there exists a unique associated equilibrium solution of problem (1.21)-(1.22), given by:

$$\begin{cases} u^e(z) = \widetilde{u}_b^e + \Psi_u(z), \quad \Psi_u(z) = \displaystyle\int_{-h}^z \frac{d_u(s) + \widetilde{Q}_u^e}{f_1(R^e(s))} ds; \\ \\ v^e(z) = \widetilde{v}_b^e + \Psi_v(z), \quad \Psi_v(z) = \displaystyle\int_{-h}^z \frac{d_v(s) + \widetilde{Q}_v^e}{f_1(R^e(s))} ds; \\ \\ \rho^e(z) = \widetilde{\rho}_b^e + \Psi_\rho(z), \quad \Psi_\rho(z) = \displaystyle\int_{-h}^z \frac{d_\rho(s) + \widetilde{Q}_\rho^e}{f_2(R^e(s))} ds. \end{cases} \tag{1.25}$$

Proof. The equilibrium states of (1.21), if these exist, are solutions of the system:

$$\begin{cases} -\partial_z(f_1(R)\partial_z u) &= D_u^e, \\ \\ -\partial_z(f_1(R)\partial_z v) &= D_v^e, \\ \\ -\partial_z(f_2(R)\partial_z \rho) &= D_\rho^e. \end{cases} \tag{1.26}$$

Integrating the three equations in (1.26) with respect to z, we obtain:

$$\begin{cases} \partial_z u &= (d_u(z) + \widetilde{Q}_u^e)/f_1(R), \\ \partial_z v &= (d_v(z) + \widetilde{Q}_v^e)/f_1(R), \\ \partial_z \rho &= (d_\rho(z) + \widetilde{Q}_\rho^e)/f_2(R). \end{cases} \tag{1.27}$$

From (1.15), we deduce that the equilibrium profiles R^e satisfy the implicit algebraic equation (1.23), and then are functions of z. By integrating with respect to z the three equations in (1.27), we deduce that the equilibrium solutions of problem (1.21)-(1.22) are given by (1.25). ■

The existence of solutions of the algebraic equation (1.23) is ensured under the following:

Hypothesis 1.2. *The fluxes satisfy $Q_u^e > 0$, $Q_v^e > 0$, $Q_\rho^e < 0$ and for some $\lambda \in (0,1)$ it holds:*

$$|\widetilde{Q}_u^e - Q_u^e| < (1-\lambda)Q_u^e, \quad |\widetilde{Q}_v^e - Q_v^e| < (1-\lambda)Q_v^e, \quad |\widetilde{Q}_\rho^e - Q_\rho^e| < (1-\lambda)|Q_\rho^e|; \tag{1.28}$$

$$\|D_u^e\|_{L^1(I)} < \frac{\lambda}{2}\, Q_u^e, \quad \|D_v^e\|_{L^1(I)} < \frac{\lambda}{2}\, Q_v^e, \quad \|D_\rho^e\|_{L^1(I)} < \frac{\lambda}{2}\, |Q_\rho^e|. \tag{1.29}$$

The assumption $Q_u^e > 0$, $Q_v^e > 0$ means that the wind velocity acts as a destabilizing agent for the mixing layer flow, while $Q_\rho^e < 0$ means that the thermodynamic flux plays a stabilizing role. The conditions (1.28) and (1.29) mean that we are considering small perturbations of the boundary data and also of the r.h.s. of equations (1.16). We conclude that for all considered models, there exist smooth steady solutions of problem (1.16)-(1.20) for perturbed data given by (1.25):

Corollary 1.3. *Assume that Hypothesis 1.2 holds. Then, the algebraic equation (1.23) admits at least a solution for the PP (1.17), Gent (1.18) and Bennis et al. (1.19) models. As a consequence, to each solution of equation (1.23) there corresponds a unique smooth equilibrium solution of (1.21)-(1.22) given by (1.25).*

Proof. The solutions of the implicit algebraic equation (1.23) may be interpreted as the intersection of the curves:

$$h_z(R) = \frac{1}{G(z)} R, \quad k(R) = \frac{[f_1(R)]^2}{f_2(R)}.$$

For the Bennis et al. model $R224$, there exists a unique gradient Richardson number R^e whenever $G(z) > 0$, as this implies that the slope of the straight line h_z is positive (See Figure 1.4). For the PP $R213$ and Gent $R23$ models, if $G(z) > 0$ there exist two solutions of equation (1.23) (See Figures 1.5, 1.6). Hypothesis 1.2 implies that $G(z) > 0$ for all $z \in [-h, 0]$. By the expressions given by (1.25), we obtain that the equilibrium solutions have regularity $C^\infty[(\overline{I})]^3$. ■

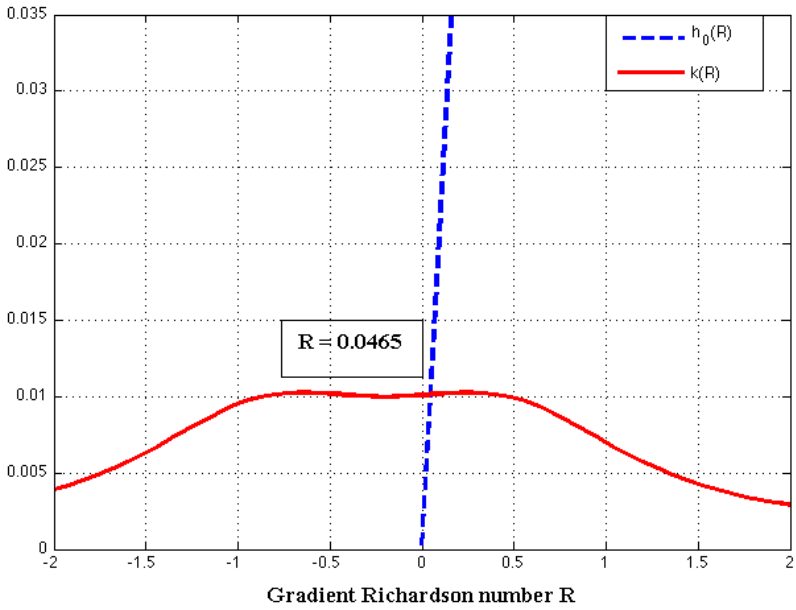

Figure 1.4:
Solution of the equation for equilibrium gradient Richardson number with model $R224$.

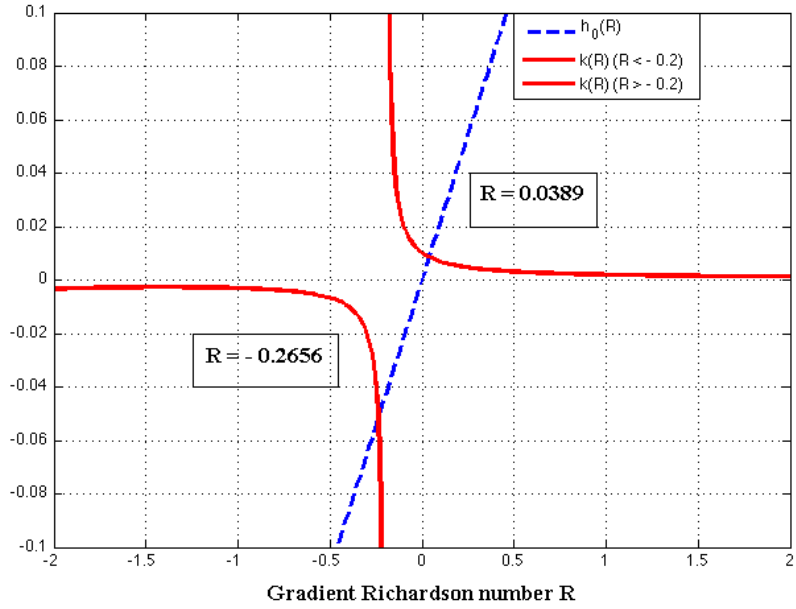

Figure 1.5:
Solution of the equation for equilibrium gradient Richardson number with model $R213$.

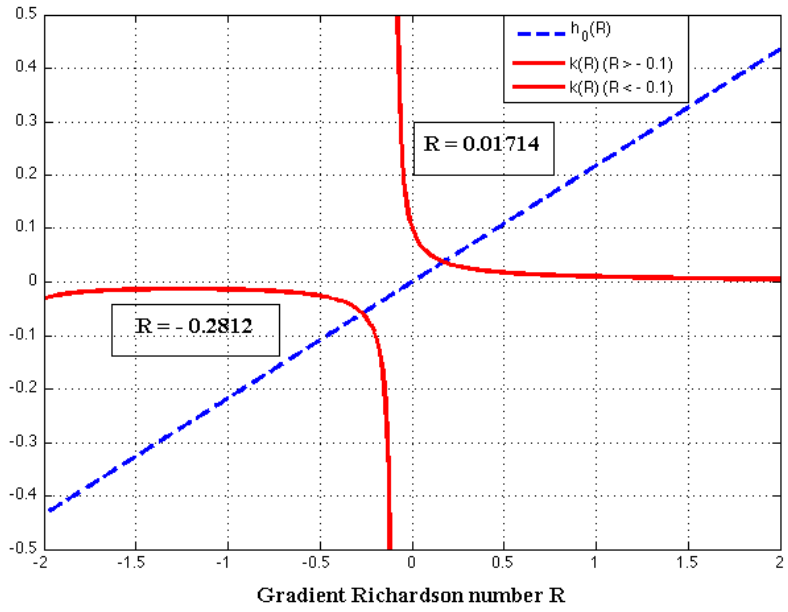

Figure 1.6:
Solution of the equation for equilibrium gradient Richardson number with model $R23$.

Remark 1.4. *The equilibria of the un-perturbed model (1.16) is studied in [2]. In that case, R^e does not depend on z, and, as consequence, the equilibrium profiles for velocity and density are linear. The equilibria for the perturbed model (1.21)-(1.22) provided by Theorem 1.1 converge to those of the un-perturbed model as the perturbations in the data vanish. This readily follows from identities (1.23) to (1.25).*

1.4.2 Existence and uniqueness of continuous unsteady solutions

In this subection, we prove the existence and uniqueness of solutions for the initial-boundary value problem (1.21)-(1.22), close to a given equilibrium state, by using the inverse function theorem in Banach spaces (*cf.* [14]), and a classical result of Ladyženskaya et al. [31] on the solvability of initial-boundary value problems for generic linear parabolic systems. Hereafter, we will use the following convention on the notation: we denote with the dot $(\cdot)$ the usual product between a matrix and a vector, to distinguish it from the component to component product between two vectors, for which we do not use any symbol. Moreover, for brevity of notation, we shall denote by $L^p(\mathbf{L}^q)$ the space $L^p(0,\mathcal{T};[L^q(I)]^3)$, and similarly the spaces $L^q(\mathbf{H}^k)$. The result of Ladyženskaya et al. [31] adapted to our situation reads as:

Theorem 1.5. *Consider an initial-boundary value problem for a linear parabolic system of the form:*

$$\begin{cases} \partial_t \mathbf{W} - \partial_z \left(M \cdot \partial_z \mathbf{W} \right) = \mathbf{\Psi} & \text{in} \quad I = (-h, 0) \times (0, \mathcal{T}), \\ M \cdot \partial_z \mathbf{W} = \mathbf{\Gamma}(t) & \text{at} \quad z = 0, \\ \mathbf{W} = \mathbf{W}_b(t) & \text{at} \quad z = -h, \\ \mathbf{W} = \mathbf{W}_0(z) & \text{at} \quad t = 0, \end{cases} \tag{1.30}$$

where $\mathbf{W} = (w_1, w_2, w_3)^T$*, and* M *is a* 3×3 *matrix with time-independent coefficients belonging to* $H^1(I)$*, such that all its eigenvalues have positive real part, for any* $z \in I$*. Assume that* $\mathbf{\Psi} \in L^2(\mathbf{L}^2)$*,* $\mathbf{\Gamma}(t) \in [L^2(0, \mathcal{T})]^3$*,* $\mathbf{W}_b(t) \in [C^0(0, \mathcal{T})]^3$*, and* $\mathbf{W}_0(z) \in [H^1(I)]^3$*. Then, problem (1.30) has a unique solution* $\mathbf{W} \in L^2(\mathbf{H}^2)$*, with* $\partial_t \mathbf{W} \in L^2(\mathbf{L}^2)$*, and the following estimate holds:*

$$\|\mathbf{W}\|_{L^2(\mathbf{H}^2)} + \|\partial_t \mathbf{W}\|_{L^2(\mathbf{L}^2)} \leq C \left(\|\mathbf{\Psi}\|_{L^2(\mathbf{L}^2)} + \|\mathbf{\Gamma}\|_{L^2(0,\mathcal{T})} + \|\mathbf{W}_b\|_{L^\infty(0,\mathcal{T})} + \|\mathbf{W}_0\|_{H^1(I)} \right),$$

where C *is a positive constant depending only on* I*,* $\mathcal{T}$ *and the coefficients of* M*.*

Actually, we will prove our existence theorem in a rather abstract framework, where all the MLM considered fit as particular cases. To do that, we consider an initial-boundary value problem for the unknown vector $\mathbf{U} = (u_1, u_2, u_3)^T$ of the form:

$$\begin{cases} \partial_t \mathbf{U} - \partial_z \left(\boldsymbol{\nu}(\partial_z \mathbf{U}) \partial_z \mathbf{U} \right) + \mathbf{D}(\mathbf{U}) = \mathbf{0} & \text{in} \quad I = (-h, 0) \times (0, \mathcal{T}), \\ \boldsymbol{\nu}(\partial_z \mathbf{U}) \partial_z \mathbf{U} = \mathbf{C}(t) & \text{at} \quad z = 0, \\ \mathbf{U} = \mathbf{U}_b(t) & \text{at} \quad z = -h, \\ \mathbf{U} = \mathbf{U}_0(z) & \text{at} \quad t = 0, \end{cases} \tag{1.31}$$

where $\boldsymbol{\nu} = (\nu_1, \nu_2, \nu_3)^T$, $\mathbf{D} = (D_1, D_2, D_3)^T$ (supposed to be a smooth function of z, t) and we assume the following:

Hypothesis 1.6. *The vector function* $\boldsymbol{\nu} \in [W^{3,\infty}_{loc}(\mathbb{R}^3)]^3$*, and there exists a constant* $\gamma > 0$ *such that its components are greater than* γ *on* $\mathbb{R}^3$*.*

Hypothesis 1.7. *Problem (1.31) admits an equilibrium solution:*

$$\mathbf{U}^e(z) = (u_1^e(z), u_2^e(z), u_3^e(z)),$$

with at least $[H^2(I)]^3$*-regularity, and the linearization of problem (1.31) around the equilibrium is a parabolic system of the form (1.30), where* $M = M(\mathbf{U}^e(z))$ *is such that all its eigenvalues have positive real part, for any* $z \in I$*.*

Problem (1.21)-(1.22) in vector form is a particular case of problem (1.31) by considering:

- $\mathbf{U} = (u, v, \rho)^T$, $\boldsymbol{\nu} = (\nu, \nu, K)^T$, $\mathbf{D}(\mathbf{U}) = -(D_u, D_v, D_\rho)^T$;
- $\mathbf{C}(t) = (\widetilde{Q}_u(t), \widetilde{Q}_v(t), \widetilde{Q}_\rho(t))^T$;
- $\mathbf{U}_b(t) = (\widetilde{u}_b(t), \widetilde{v}_b(t), \widetilde{\rho}_b(t))^T$;
- $\mathbf{U}_0(z) = (\widetilde{u}_0(z), \widetilde{v}_0(z), \widetilde{\rho}_0(z))^T$.

Note that the eddy viscosities and diffusivities given by MLM (1.17) to (1.19) are not defined for $R = -1/\sigma$ for some $\sigma > 0$ ($\sigma = 5$ for PP and Bennis et al. models, $\sigma = 10$ for Gent model), and also for $(\partial_z u, \partial_z v, \partial_z \rho) = (0, 0, 0)$. Moreover, they generate physical invalid values (except for the Bennis et al. model) and numerical instabilities in a neighborhood of $R = -1/\sigma$ (see Section 1.3). This situation is solved in practice by ocean modelers extending the eddy viscosities and diffusivities to these regions with positive constant values (*cf.* [22], [58], [45]). Here, we adapt this technique to verify Hypothesis 1.6. Indeed, let us introduce the new variables:

$$\alpha = \partial_z u, \quad \beta = \partial_z v, \quad \theta = \partial_z \rho,$$

and denote $\mathbf{Z} = (\alpha, \beta, \theta)$. The gradient Richardson number, in terms of these variables, is given by:

$$R = R(\mathbf{Z}) = -\frac{g}{\rho_r} \frac{\theta}{(\alpha^2 + \beta^2)},$$

and, as consequence, the turbulent viscosity and diffusion previously described by MLM (1.17) to (1.19) are functions of $\mathbf{Z}$. For instance, Bennis et al. model (1.19) reads as:

$$f_1(\mathbf{Z}) = a_1 + \frac{b_1(\alpha^2 + \beta^2)^2}{(\alpha^2 + \beta^2 - \sigma(g/\rho_r)\theta)^2}, \quad \sigma = 5,$$

$$f_2(\mathbf{Z}) = a_2 + \frac{f_1(\mathbf{Z})(\alpha^2 + \beta^2)^2}{(\alpha^2 + \beta^2 - \sigma(g/\rho_r)\theta)^2}, \quad \sigma = 5,$$

and similarly for PP model (1.17) and Gent model (1.18).

We split the $\mathbf{Z}$ space into three regions:

- A region containing the positive equilibrium gradient Richardson numbers, whose boundary is formed by the union of the surfaces $R(\mathbf{Z}) = -1/\sigma + \tau$ and $\alpha^2 + \beta^2 + \theta^2 = r^2$ for positive r, τ small enough (Region 1 in Figure 1.7, where for simplicity of presentation we have assumed $\beta = 0$).
- A region containing the physically invalid and numerical unstable gradient Richardson numbers, whose boundary is formed by the union of the surfaces $R(\mathbf{Z}) = -1/\sigma$ and $\alpha^2 + \beta^2 + \theta^2 = (r/2)^2$ (Region 3 in Figure 1.7).

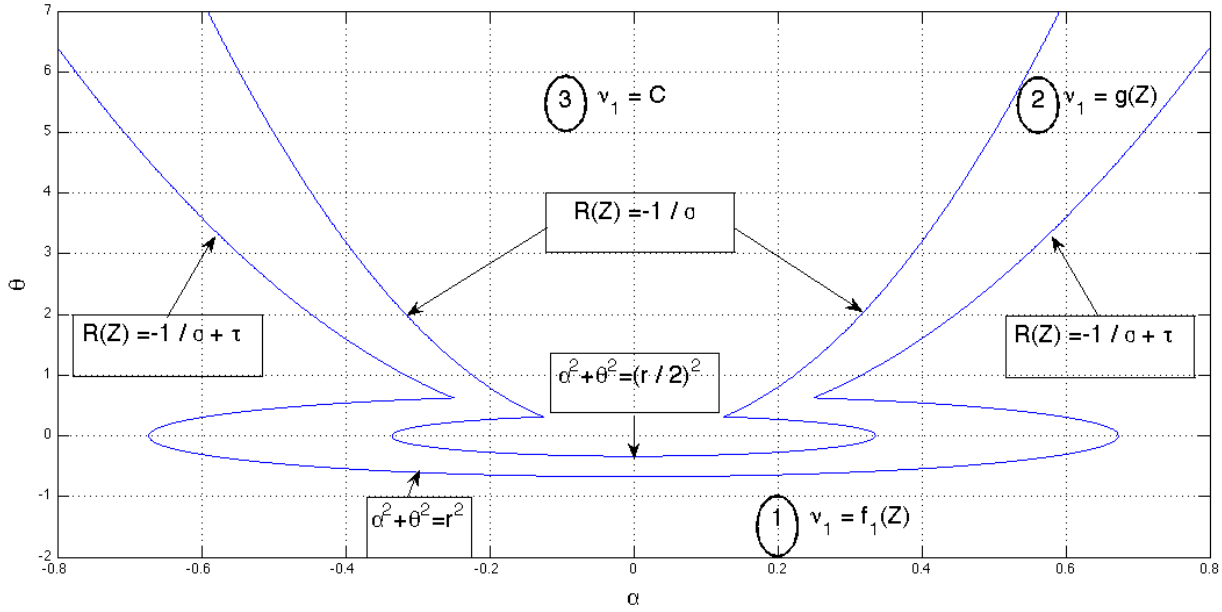

Figure 1.7:
Example of a smooth extension of ν in the plane (α, θ) (similarly for K).

- A buffer region whose boundary is the union of the boundaries of Regions 1 and 3 (Region 2 in Figure 1.7).

We then consider an extension of the total viscosity and diffusion ν, K such that:

(a) In Region 1: If $\mathbf{Z}$ is in Region 1, then:

$$\nu = f_1(\mathbf{Z}), \quad K = f_2(\mathbf{Z}).$$

(b) In Region 3: The functions ν, K take positive constant values, set by physical criteria.

(c) In Region 2: The functions ν, K in Region 2 are smooth extensions of their values in Regions 1 and 3, such that that $\nu, K \in W^{3,\infty}_{loc}(\mathbb{R}^3)$ and there exist two positive constants γ_1, γ_2 verifying $0 < \gamma_1 \leq \nu(\mathbf{Z}), K(\mathbf{Z}) \leq \gamma_2$ for all $\mathbf{Z}$ in Region 2.

Observe that it is possible to obtain $\nu, K \in W^{3,\infty}_{loc}(\mathbb{R}^3)$, because ν, K have C^∞-regularity in Regions 1 and 2. Also, typically ν, K are set to rather large values in Region 2, forcing the flow to become suddenly stable. Usually, Region 2 does not explicitly appear in the computations, simply Region 1 is changed into Region 3 from a grid line to the next. By construction, problem (1.21)-(1.22) with smoothly extended ν, K verifies Hypothesis 1.6. In addition, it verifies Hypothesis 1.7. This proof is rather lengthy and we report it to Corollary 1.10.

To prove the existence theorem for problem (1.31), let us define the Banach space:

$$\mathbf{X} = \left\{ L^2(\mathbf{H}^2) \text{ such that } \partial_t \in L^2(\mathbf{L}^2) \right\},$$

and let us consider the set $\boldsymbol{\mathcal{U}} = \boldsymbol{\mathcal{B}}(\mathbf{U}^e, \varepsilon) = \{\mathbf{U} \in \mathbf{X} : \|\mathbf{U} - \mathbf{U}^e\|_{\mathbf{X}} < \varepsilon\}$, with ε small enough. We will also use the following result of Verfürth on a posteriori error estimates for non-linear problems (*cf.* [60]):

Lemma 1.8. *Let X, Y be two Banach spaces. Let $F : X \to Y$ be a continuously Fréchet differentiable function. Let $u^* \in X$ be a regular solution of $F(u) = 0$, i.e. $DF(u^*)$ is a Banach space isomorphism from X onto Y, where DF denotes the Fréchet derivative of F. Assume in addition that DF is Lipschitz continuous at u^*, i.e. there exists an $R^* > 0$ such that:*

$$\gamma := \sup_{u \in \mathcal{B}(u^*, R^*)} \frac{\|DF(u) - DF(u^*)\|_{\mathcal{L}(X,Y)}}{\|u - u^*\|_X} < \infty,$$

where $\mathcal{L}(X, Y)$ is the space of bounded linear maps from X to Y. Set:

$$R = \min\{R^*, \gamma^{-1}\|u^*\|_X^{-1}, 2\gamma^{-1}\|DF(u^*)\|_{\mathcal{L}(X,Y)}\}.$$

Then, the following error estimate holds for all $u \in \mathcal{B}(u^*, R)$:

$$\|u - u^*\|_X \leq 2\|u_0\|_X \|F(u)\|_Y.$$

The existence and uniqueness of solutions for problem (1.31) close to the equilibrium state is given by the following:

Theorem 1.9. *Assume that Hypotheses 1.6 and 1.7 hold. Then, if $\mathbf{C}(t) \in [L^2(0, \mathcal{T})]^3$, $\mathbf{U}_b(t) \in [C^0(0, \mathcal{T})]^3$, $\mathbf{U}_0(z) \in [H^1(I)]^3$, and these quantities are close enough to the corresponding quantities at the equilibrium (respectively $\mathbf{C}^e$, $\mathbf{U}_b^e$ and $\mathbf{U}^e$), problem (1.31) admits a unique solution in an open neighborhood $\widehat{\boldsymbol{\mathcal{U}}} \subset \boldsymbol{\mathcal{U}}$, satisfying the estimate:*

$$\|\mathbf{U} - \mathbf{U}^e\|_{\mathbf{X}} \leq C \left(\|\mathbf{C}(t) - \mathbf{C}^e\|_{L^2(0,\mathcal{T})} + \|\mathbf{U}_b(t) - \mathbf{U}_b^e\|_{L^\infty(0,\mathcal{T})} + \|\mathbf{U}_0 - \mathbf{U}^e\|_{H^1(I)} \right), \quad (1.32)$$

where C is a positive constant independent of $\mathbf{U}$.

Proof. Let $\mathbf{Y}$ be the Banach space:

$$\mathbf{Y} = L^2(\mathbf{L}^2) \times [L^2(0, \mathcal{T})]^3 \times [C^0(0, \mathcal{T})]^3 \times [H^1(I)]^3,$$

and let us define the mapping:

$$\boldsymbol{\Phi} : \boldsymbol{\mathcal{U}} \longrightarrow \mathbf{Y},$$

$$\begin{aligned} \boldsymbol{\Phi}(\mathbf{U}) \;=\; & \{(\partial_t \mathbf{U} - \partial_z(\boldsymbol{\nu}(\partial_z \mathbf{U})\partial_z \mathbf{U}) + \mathbf{D}(\mathbf{U})), \left(\boldsymbol{\nu}\partial_z \mathbf{U}_{|_{z=0}} - \mathbf{C}^e\right), \\ & \left(\mathbf{U}_{|_{z=-h}} - \mathbf{U}_b^e\right), \left(\mathbf{U}_{|_{t=0}} - \mathbf{U}^e\right)\}. \end{aligned}$$

As the vector $\mathbf{D}$ stands for smooth known perturbations, we may assume it as a linear map from $\mathbb{R}^3$ to $\mathbb{R}^3$. Observe that $\boldsymbol{\Phi}(\mathbf{U}^e) = \mathbf{0}$. If the hypotheses of the inverse function theorem are satisfied, we can conclude that there exists an open neighborhood $\widehat{\boldsymbol{\mathcal{U}}}$ of $\mathbf{U}^e$ in $\mathbf{X}$, $\widehat{\boldsymbol{\mathcal{U}}} \subset \boldsymbol{\mathcal{U}}$, and an open neighborhood $\boldsymbol{\mathcal{V}}$ of $\boldsymbol{\Phi}(\mathbf{U}^e)$ in $\mathbf{Y}$ such that $\boldsymbol{\Phi} : \widehat{\boldsymbol{\mathcal{U}}} \longrightarrow \boldsymbol{\mathcal{V}}$ is invertible, with continuously differentiable inverse. So, if $\mathbf{C}(t) \in [L^2(0, \mathcal{T})]^3$, $\mathbf{U}_b(t) \in [C^0(0, \mathcal{T})]^3$, $\mathbf{U}_0(z) \in [H^1(I)]^3$, and these quantities are close enough to the corresponding quantities

at the steady state in an obvious sense, then there exists a unique solution of problem (1.31) in $\widehat{\boldsymbol{\mathcal{U}}}$. In addition, the inequality (1.32) follows by applying Lemma 1.8, because $D\boldsymbol{\Phi}$ (i.e., the Fréchet derivative of $\boldsymbol{\Phi}$) is locally Lipschitz continuous (we prove it below, in **Step 1**). We next prove that effectively the hypotheses of the inverse function theorem are satisfied.

Step 1. $\boldsymbol{\Phi}$ is continuously Fréchet differentiable.
By definition of Fréchet derivative (*cf.* [14]), we have to prove that:

$$\lim_{\|\mathbf{W}\|_{\mathbf{X}}\to 0} \frac{\|\boldsymbol{\Phi}(\mathbf{U}+\mathbf{W}) - \boldsymbol{\Phi}(\mathbf{U}) - \langle D\boldsymbol{\Phi}(\mathbf{U}), \mathbf{W}\rangle\|_{\mathbf{Y}}}{\|\mathbf{W}\|_{\mathbf{X}}} = 0, \quad \forall \mathbf{U} \in \boldsymbol{\mathcal{U}}, \tag{1.33}$$

where $\langle D\boldsymbol{\Phi}(\mathbf{U}), \mathbf{W}\rangle$ denotes the Gâteaux derivative of $\boldsymbol{\Phi}$ at $\mathbf{U}$. We have:

$$\begin{aligned} & \langle D\boldsymbol{\Phi}(\mathbf{U}), \mathbf{W}\rangle = \frac{\mathrm{d}}{\mathrm{ds}}\boldsymbol{\Phi}(\mathbf{U}+\mathrm{s}\mathbf{W})_{|_{\mathrm{s}=0}} \\ = \; & \{(\partial_t \mathbf{W} - \partial_z(\boldsymbol{\nu}(\partial_z\mathbf{U})\partial_z\mathbf{W} + \langle D\boldsymbol{\nu}(\partial_z\mathbf{U}), \mathbf{W}\rangle\partial_z\mathbf{U}) + \mathbf{D}(\mathbf{W})), \\ & (\boldsymbol{\nu}\partial_z\mathbf{W} + \langle D\boldsymbol{\nu}(\partial_z\mathbf{U}), \mathbf{W}\rangle\partial_z\mathbf{U})_{|_{z=0}}, (\mathbf{W})_{|_{z=-h}}, (\mathbf{W})_{|_{t=0}}\}, \end{aligned}$$

where:

$$\langle D\boldsymbol{\nu}(\partial_z\mathbf{U}), \mathbf{W}\rangle = \frac{\mathrm{d}}{\mathrm{ds}}\boldsymbol{\nu}(\partial_z\mathbf{U} + \mathrm{s}\,\partial_z\mathbf{W})_{|_{\mathrm{s}=0}} = \nabla\boldsymbol{\nu}(\partial_z\mathbf{U})\cdot\partial_z\mathbf{W}.$$

Let us set $\mathbf{f}(\mathrm{t}) = \boldsymbol{\Phi}(\mathbf{U}+\mathrm{t}\mathbf{W})$. Observe that $\mathbf{f}(\mathrm{t})$ belongs to $[W^{2,\infty}_{loc}(\mathbb{R})]^3$ as $\boldsymbol{\nu}$ belongs to $[W^{3,\infty}_{loc}(\mathbb{R}^3)]^3$ from Hypothesis 1.6. So, the numerator appearing in expression (1.33) can be rewritten as:

$$\|\mathbf{f}(1) - \mathbf{f}(0) - \mathbf{f}'(0)\|_{\mathbf{Y}} = \|\mathbf{R}_1(1)\|_{\mathbf{Y}},$$

where $\mathbf{R}_1(\mathrm{t}) = \displaystyle\int_0^{\mathrm{t}} \mathbf{f}''(\mathrm{s})(\mathrm{t}-\mathrm{s})\,d\mathrm{s}$ is the integral form of the reminder in the Taylor's expansion formula up to the first order. We have:

$$\mathbf{f}''(\mathrm{t}) = \left\langle D^2\boldsymbol{\Phi}(\mathbf{U}+\mathrm{t}\mathbf{W}), (\mathbf{W},\mathbf{W})\right\rangle = \{\mathbf{A}(\mathrm{t}), \mathbf{B}(\mathrm{t}), \mathbf{0}, \mathbf{0}\},$$

where:

$$\mathbf{A}(\mathrm{t}) = -\partial_z[2(\nabla\boldsymbol{\nu}(\partial_z\widetilde{\mathbf{U}})\cdot\partial_z\mathbf{W})\partial_z\mathbf{W} + \langle D^2\boldsymbol{\nu}(\partial_z\widetilde{\mathbf{U}}), (\mathbf{W},\mathbf{W})\rangle\partial_z\widetilde{\mathbf{U}}],$$

$$\mathbf{B}(\mathrm{t}) = [2(\nabla\boldsymbol{\nu}(\partial_z\widetilde{\mathbf{U}})\cdot\partial_z\mathbf{W})\partial_z\mathbf{W} + \langle D^2\boldsymbol{\nu}(\partial_z\widetilde{\mathbf{U}}), (\mathbf{W},\mathbf{W})\rangle\partial_z\widetilde{\mathbf{U}}]_{|_{z=0}},$$

with $\widetilde{\mathbf{U}} = \widetilde{\mathbf{U}}(\mathrm{t}) = \mathbf{U} + \mathrm{t}\mathbf{W}$, and:

$$\begin{aligned} \langle D^2\boldsymbol{\nu}(\partial_z\widetilde{\mathbf{U}}), (\mathbf{W},\mathbf{W})\rangle &= \frac{\mathrm{d}}{\mathrm{ds}}\nabla\boldsymbol{\nu}(\partial_z(\widetilde{\mathbf{U}}+\mathrm{s}\mathbf{W}))_{|_{\mathrm{s}=0}}\cdot\partial_z\mathbf{W} \\ &= \begin{pmatrix} (H\nu_1(\partial_z\widetilde{\mathbf{U}})\cdot\partial_z\mathbf{W})^T \\ (H\nu_2(\partial_z\widetilde{\mathbf{U}})\cdot\partial_z\mathbf{W})^T \\ (H\nu_3(\partial_z\widetilde{\mathbf{U}})\cdot\partial_z\mathbf{W})^T \end{pmatrix}\cdot\partial_z\mathbf{W}, \end{aligned}$$

H denoting the Hessian matrix. We have to verify that:

$$\lim_{\|\mathbf{W}\|_{\mathbf{X}}\to 0} \frac{\left\| \int_0^1 \mathbf{A}(\mathrm{s})(1-\mathrm{s})\, d\mathrm{s} \right\|_{L^2(\mathbf{L}^2)}}{\|\mathbf{W}\|_{\mathbf{X}}} = 0, \tag{1.34}$$

$$\lim_{\|\mathbf{W}\|_{\mathbf{X}}\to 0} \frac{\left\| \int_0^1 \mathbf{B}(\mathrm{s})(1-\mathrm{s})\, d\mathrm{s} \right\|_{[L^2(0,\mathcal{T})]^3}}{\|\mathbf{W}\|_{\mathbf{X}}} = 0. \tag{1.35}$$

From Hypothesis 1.6, the components of $\nabla\boldsymbol{\nu}$ and $H\boldsymbol{\nu}$ belong to $W^{1,\infty}_{loc}(\mathbb{R}^3)$. Then, the following estimates hold:

$$\begin{aligned}
\left\| \int_0^1 \mathbf{A}(\mathrm{s})(1-\mathrm{s})\, d\mathrm{s} \right\|_{L^2(\mathbf{L}^2)} &\leq C\left(||\mathbf{W}||^2_{L^2(\mathbf{H}^2)} + ||\mathbf{W}||^3_{L^2(\mathbf{H}^2)} \right), \\
\left\| \int_0^1 \mathbf{B}(\mathrm{s})(1-\mathrm{s})\, d\mathrm{s} \right\|_{[L^2(0,\mathcal{T})]^3} &\leq C\left(||\mathbf{W}||^2_{L^2(\mathbf{H}^2)} + ||\mathbf{W}||^3_{L^2(\mathbf{H}^2)} \right),
\end{aligned}$$

with C a positive constant. We conclude that (1.34) and (1.35) hold, and thus $\boldsymbol{\Phi}$ is Fréchet differentiable.

Next, we have to prove that the Fréchet derivative $D\boldsymbol{\Phi}$ is continuous, i.e. we have to show, for any $\mathbf{U} \in \boldsymbol{\mathcal{U}}$, that:

$$\lim_{\|\mathbf{U}-\mathbf{V}\|_{\mathbf{X}}\to 0} \|D\boldsymbol{\Phi}(\mathbf{U}) - D\boldsymbol{\Phi}(\mathbf{V})\|_{\mathcal{L}(\mathbf{X},\mathbf{Y})} = 0,$$

where $\boldsymbol{\mathcal{L}}(\mathbf{X},\mathbf{Y})$ is the space of bounded linear maps from $\mathbf{X}$ to $\mathbf{Y}$. It is easy to check that this is reduced to prove that:

$$\begin{aligned}
\lim_{\|\mathbf{U}-\mathbf{V}\|_{\mathbf{X}}\to 0} \left(\sup_{\mathbf{W}\in\mathbf{X},\mathbf{W}\neq\mathbf{0}} \frac{\|-\partial_z[\mathbf{E}(\partial_z\mathbf{U}) - \mathbf{E}(\partial_z\mathbf{V})]\|_{L^2(\mathbf{L}^2)}}{\|\mathbf{W}\|_{\mathbf{X}}} \right) &= 0, \\
\lim_{\|\mathbf{U}-\mathbf{V}\|_{\mathbf{X}}\to 0} \left(\sup_{\mathbf{W}\in\mathbf{X},\mathbf{W}\neq\mathbf{0}} \frac{\|[\mathbf{E}(\partial_z\mathbf{U}) - \mathbf{E}(\partial_z\mathbf{V})]_{|z=0}\|_{[L^2(0,\mathcal{T})]^3}}{\|\mathbf{W}\|_{\mathbf{X}}} \right) &= 0,
\end{aligned}$$

where:

$$\begin{aligned}
\mathbf{E}(\partial_z\mathbf{U}) &= \boldsymbol{\nu}(\partial_z\mathbf{U})\partial_z\mathbf{W} + \langle D\boldsymbol{\nu}(\partial_z\mathbf{U}), \mathbf{W}\rangle \partial_z\mathbf{U} \\
&= \boldsymbol{\nu}(\partial_z\mathbf{U})\partial_z\mathbf{W} + (\nabla\boldsymbol{\nu}(\partial_z\mathbf{U})\cdot\partial_z\mathbf{W})\partial_z\mathbf{U}. \quad \text{(Similarly for } \mathbf{E}(\partial_z\mathbf{V})\text{)}.
\end{aligned}$$

By adding and subtracting the quantity $(\nabla\boldsymbol{\nu}(\partial_z\mathbf{U})\cdot\partial_z\mathbf{W})\partial_z\mathbf{V}$ to $\mathbf{E}(\partial_z\mathbf{U}) - \mathbf{E}(\partial_z\mathbf{V})$, we obtain:

$$\begin{aligned}
\mathbf{E}(\partial_z\mathbf{U}) - \mathbf{E}(\partial_z\mathbf{V}) = [\boldsymbol{\nu}(\partial_z\mathbf{U}) - \boldsymbol{\nu}(\partial_z\mathbf{V})]\partial_z\mathbf{W} + [\nabla\boldsymbol{\nu}(\partial_z\mathbf{U})\cdot\partial_z\mathbf{W}]\partial_z(\mathbf{U}-\mathbf{V}) \\
+\{[\nabla\boldsymbol{\nu}(\partial_z\mathbf{U}) - \nabla\boldsymbol{\nu}(\partial_z\mathbf{V})]\cdot\partial_z\mathbf{W}\}\partial_z\mathbf{V}.
\end{aligned}$$

We define:

$$\mathbf{g}(\mathrm{t}) = \boldsymbol{\nu}(\partial_z(\mathbf{V} + \mathrm{t}(\mathbf{U} - \mathbf{V}))), \quad \mathbf{H}(\mathrm{t}) = \nabla\boldsymbol{\nu}(\partial_z(\mathbf{V} + \mathrm{t}(\mathbf{U} - \mathbf{V}))).$$

Then:

$$\mathbf{E}(\partial_z\mathbf{U}) - \mathbf{E}(\partial_z\mathbf{V}) = \left(\int_0^1 \mathbf{g}'(\mathrm{s})\, d\mathrm{s}\right)\partial_z\mathbf{W} + [\nabla\boldsymbol{\nu}(\partial_z\mathbf{U})\cdot\partial_z\mathbf{W}]\partial_z(\mathbf{U}-\mathbf{V}) + \left(\left(\int_0^1 \mathbf{H}'(\mathrm{s})\, d\mathrm{s}\right)\cdot\partial_z\mathbf{W}\right)\partial_z\mathbf{V},$$

where:

$$\mathbf{g}'(\mathrm{t}) = \nabla\boldsymbol{\nu}(\partial_z\widetilde{\mathbf{U}})\cdot\partial_z(\mathbf{U}-\mathbf{V}), \quad \mathbf{H}'(\mathrm{t}) = \begin{pmatrix} \left[H\nu_1(\partial_z\widetilde{\mathbf{U}})\cdot\partial_z(\mathbf{U}-\mathbf{V})\right]^T \\ \left[H\nu_2(\partial_z\widetilde{\mathbf{U}})\cdot\partial_z(\mathbf{U}-\mathbf{V})\right]^T \\ \left[H\nu_3(\partial_z\widetilde{\mathbf{U}})\cdot\partial_z(\mathbf{U}-\mathbf{V})\right]^T \end{pmatrix},$$

with $\widetilde{\mathbf{U}} = \widetilde{\mathbf{U}}(\mathrm{t}) = \mathbf{V} + \mathrm{t}(\mathbf{U}-\mathbf{V})$, and H denoting the Hessian matrix. As before, from Hypothesis 1.6, we deduce the following estimates:

$$\|-\partial_z[\mathbf{E}(\partial_z\mathbf{U}) - \mathbf{E}(\partial_z\mathbf{V})]\|_{L^2(\mathbf{L}^2)} \leq C\left(\|\mathbf{U}-\mathbf{V}\|_{L^2(\mathbf{H}^2)}\|\mathbf{W}\|_{L^2(\mathbf{H}^2)}\right),$$

$$\|[\mathbf{E}(\partial_z\mathbf{U}) - \mathbf{E}(\partial_z\mathbf{V})]_{|_{z=0}}\|_{[L^2(0,\mathcal{T})]^3} \leq C\left(\|\mathbf{U}-\mathbf{V}\|_{L^2(\mathbf{H}^2)}\|\mathbf{W}\|_{L^2(\mathbf{H}^2)}\right),$$

with C a positive constant. We conclude that $D\boldsymbol{\Phi}$ is continuous (really, $D\boldsymbol{\Phi}$ is locally Lipschitz continuous). Thus, we have proved that $\boldsymbol{\Phi}$ is continuously Fréchet differentiable.

Step 2. The mapping $D\boldsymbol{\Phi}(\mathbf{U}^e)$ is a Banach space isomorphism from X onto Y. We need to prove the well-posedness (in the sense of Hadamard) of the linear problem:

$$\begin{cases} \partial_t\mathbf{W} - \partial_z\left[\boldsymbol{\nu}(\partial_z\mathbf{U}^e)\partial_z\mathbf{W} + \partial_z\mathbf{U}^e\left(\nabla\boldsymbol{\nu}(\partial_z\mathbf{U}^e)\cdot\partial_z\mathbf{W}\right)\right] = \boldsymbol{\Psi} & \text{in} \quad I = (-h,0)\times(0,\mathcal{T}), \\ \boldsymbol{\nu}(\partial_z\mathbf{U}^e)\partial_z\mathbf{W} + \partial_z\mathbf{U}^e\left(\nabla\boldsymbol{\nu}(\partial_z\mathbf{U}^e)\cdot\partial_z\mathbf{W}\right) = \boldsymbol{\Gamma}(t) & \text{at} \quad z = 0, \\ \mathbf{W} = \mathbf{W}_b(t) & \text{at} \quad z = -h, \\ \mathbf{W} = \mathbf{W}_0(z) & \text{at} \quad t = 0, \end{cases} \tag{1.36}$$

with data $\mathbf{G} = (\boldsymbol{\Psi}, \boldsymbol{\Gamma}, \mathbf{W}_b, \mathbf{W}_0) \in \mathbf{Y}$, where $\mathbf{D}(\mathbf{W})$ is embedded in $\boldsymbol{\Psi}$. Thus, we have to prove, for any $\mathbf{G}\in\mathbf{Y}$, that this problem admits a unique solution $\mathbf{W}$ that continuously depends on $\mathbf{G}$. Note that problem (1.36) can be rewritten as:

$$\begin{cases} \partial_t\mathbf{W} - \partial_z\left(M^e\cdot\partial_z\mathbf{W}\right) = \boldsymbol{\Psi} & \text{in} \quad I = (-h,0)\times(0,\mathcal{T}), \\ M^e\cdot\partial_z\mathbf{W} = \boldsymbol{\Gamma}(t) & \text{at} \quad z = 0, \\ \mathbf{W} = \mathbf{W}_b(t) & \text{at} \quad z = -h, \\ \mathbf{W} = \mathbf{W}_0(z) & \text{at} \quad t = 0, \end{cases} \tag{1.37}$$

where $M^e = M(\mathbf{U}^e(z))$. By Hypotheses 1.6 and 1.7, problem (1.36) is a well-posed coupled linear parabolic problem with $H^1(I)$ time-independent coefficients. So that, from Theorem 1.5, as $\mathbf{G} = (\mathbf{\Psi}, \mathbf{\Gamma}, \mathbf{W}_b, \mathbf{W}_0) \in \mathbf{Y}$, then there exists a unique $\mathbf{W} \in \mathbf{X}$, solution of problem (1.36), that continuously depends on the data, with the estimate $||\mathbf{W}||_{\mathbf{X}} \leq C\,||\mathbf{G}||_{\mathbf{Y}}$. ■

Corollary 1.10. *Assume that* $(\widetilde{Q}_u(t), \widetilde{Q}_v(t), \widetilde{Q}_\rho(t))^T \in [L^2(0,\mathcal{T})]^3$, $(\widetilde{u}_b(t), \widetilde{v}_b(t), \widetilde{\rho}_b(t))^T \in [C^0(0,\mathcal{T})]^3$, $(\widetilde{u}_0(z), \widetilde{v}_0(z), \widetilde{\rho}_0(z))^T \in [H^1(I)]^3$, *and these quantities are close enough to the corresponding quantities at an equilibrium corresponding to a positive gradient Richardson number; then, problem (1.21)-(1.22) with smoothly extended viscosity* ν *and diffusivity* K *admits a unique solution in an open neighborhood* $\widehat{\boldsymbol{\mathcal{U}}} \subset \boldsymbol{\mathcal{U}}$, *satisfying the estimate (1.32).*

Proof. We have to prove that problem (1.21)-(1.22) with the above extension of the viscosity ν and diffusivity K satisfies Hypotheses 1.6 and 1.7. Then, the thesis will follow by Theorem 1.9, since problem (1.21)-(1.22) will be a particular case of problem (1.31). Problem (1.21)-(1.22) with smoothly extended ν, K verifies Hypothesis 1.6 by construction. Moreover, it admits equilibrium solutions (1.25) with $C^\infty(\overline{I})$-regularity, as shown in Theorem 1.1, corresponding to a positive gradient Richardson number. The linearization of problem (1.21)-(1.22) around them is given by a system of the form (1.37), where M^e is the matrix:

$$M^e = \begin{pmatrix} \nu^e + \alpha^e \left(\dfrac{\partial \nu}{\partial \alpha}\right)^e & \alpha^e \left(\dfrac{\partial \nu}{\partial \beta}\right)^e & \alpha^e \left(\dfrac{\partial \nu}{\partial \theta}\right)^e \\ \beta^e \left(\dfrac{\partial \nu}{\partial \alpha}\right)^e & \nu^e + \beta^e \left(\dfrac{\partial \nu}{\partial \beta}\right)^e & \beta^e \left(\dfrac{\partial \nu}{\partial \theta}\right)^e \\ \theta^e \left(\dfrac{\partial K}{\partial \alpha}\right)^e & \theta^e \left(\dfrac{\partial K}{\partial \beta}\right)^e & K^e + \theta^e \left(\dfrac{\partial K}{\partial \theta}\right)^e \end{pmatrix}, \tag{1.38}$$

with:

$$\nu^e = \nu(\partial_z \mathbf{U}^e) = \nu(\alpha^e, \beta^e, \theta^e),$$

$$\left(\frac{\partial \nu}{\partial \alpha}\right)^e = \left(\frac{\partial \nu}{\partial \alpha}\right)_{|\mathbf{Z}=\partial_z \mathbf{U}^e}, \left(\frac{\partial \nu}{\partial \beta}\right)^e = \left(\frac{\partial \nu}{\partial \beta}\right)_{|\mathbf{Z}=\partial_z \mathbf{U}^e}, \left(\frac{\partial \nu}{\partial \theta}\right)^e = \left(\frac{\partial \nu}{\partial \theta}\right)_{|\mathbf{Z}=\partial_z \mathbf{U}^e},$$

and similarly for K. We have to prove that all the eigenvalues of M^e have positive real part, for any $z \in I$. To ensure that, it is enough that three independent invariants of matrix M^e are positive, for any $z \in I$. By means of a Computer Algebra System (CAS) it is verified that, since $R^e = R(\partial_z \mathbf{U}^e) > 0$, then there exist some positive constants δ_1, δ_2, δ_3 independent of z such that:

$$\text{Trace}(M^e) = 2f_1(R^e) + f_2(R^e) + R^e(f_2'(R^e) - 2f_1'(R^e)) > \delta_1,$$

$$\text{Det}(M^e) = f_1(R^e)(f_1(R^e)f_2(R^e) + R^e f_1(R^e) f_2'(R^e) - 2R^e f_2(R^e) f_1'(R^e)) > \delta_2,$$

$$\begin{aligned} \text{Trace}(\text{Adj}M^e) &= 2f_1(R^e)f_2(R^e) + 2f_1(R^e)R^e[f_2'(R^e) - f_1'(R^e)] \\ &- 2f_2(R^e)R^e f_1'(R^e) + f_1(R^e)^2 > \delta_3. \end{aligned}$$

So, problem (1.21)-(1.22) with smoothly extended viscosity ν and diffusivity K verifies Hypothesis 1.7. ■

This result proves that $\|\partial_z \mathbf{U} - \partial_z \mathbf{U}^e\|_{L^2(\mathbf{L}^\infty)}$ can be made arbitrarily small by choosing the data for problem (1.21)-(1.22) close enough to those corresponding to the equilibrium solution $\mathbf{U}^e$ related to a positive gradient Richardson number. If instead we had a similar estimate in $L^\infty(\mathbf{L}^\infty)$, then Theorem 1.9 and Corollary 1.10 would apply to the original model with eddy viscosity and diffusivity given by either (1.17), (1.18) or (1.19). Indeed, such an estimate would imply that, for data close enough to those corresponding to the equilibrium solution, $\partial_z \mathbf{U}(z,t)$ remains in the Region 1, for all $z \in I$ and for all $t \in [0, \mathcal{T}]$, as $\partial_z \mathbf{U}^e(z)$ lies in the interior of Region 1, for all $z \in I$. Then, $\nu(\partial_z \mathbf{U}) = f_1(\partial_z \mathbf{U})$ and $K(\partial_z \mathbf{U}) = f_2(\partial_z \mathbf{U})$ in $I \times (0, \mathcal{T})$.

Unfortunately, the existence result of Theorem (1.5) does not apply to L^∞-regularity in time (*cf.* [31]). Thus, we only may conclude a weaker result, as follows:

Theorem 1.11. *The solution of problem (1.21)-(1.22) with smoothly extended viscosity ν and diffusivity K provided by Corollary 1.10 is also a solution of the same problem with the eddy viscosity and diffusivity given by either (1.17), (1.18) or (1.19) in a set $I \times ((0, \mathcal{T}) \setminus \mathcal{A})$, where $\mathcal{A}$ is a set whose Lebesgue measure tends to zero as the distance between the data:*

$$\|\mathbf{C}(t) - \mathbf{C}^e\|_{L^2(0,\mathcal{T})} + \|\mathbf{U}_b(t) - \mathbf{U}_b^e\|_{L^\infty(0,\mathcal{T})} + \|\mathbf{U}_0 - \mathbf{U}^e\|_{H^1(I)},$$

tends to zero.

Proof. As $\partial_z \mathbf{U}^e(z)$ lies in Region 1 for all $z \in I$, there exists a $\delta > 0$ such that if $|\partial_z \mathbf{U}(z,t) - \partial_z \mathbf{U}^e(z)| \leq \delta$, then $\partial_z \mathbf{U}(z,t)$ lies in Region 1. Define the set:

$$\mathcal{A} = \{t \in [0, \mathcal{T}] : |\partial_z \mathbf{U}(z,t) - \partial_z \mathbf{U}^e(z)| > \delta, \text{ for some } z \in I\}.$$

Then:

$$\|\partial_z \mathbf{U} - \partial_z \mathbf{U}^e\|_{L^2(\mathbf{L}^\infty)} > \delta\, |\mathcal{A}|^{1/2}.$$

As $\|\partial_z \mathbf{U} - \partial_z \mathbf{U}^e\|_{L^2(\mathbf{L}^\infty)}$ can be arbitrarily small by making small the distance between the data, then $|\mathcal{A}|$ should tend to zero as this distance tends to zero. ■

Note that this result applies to all formulas for the eddy viscosity and diffusion given by either (1.17), (1.18) or (1.19), the only need is that the coefficients a_1, b_1 and a_2 are positive. The actual values of these coefficients will affect the Lebesgue measure of the set $\mathcal{A}$, but in all cases this measure will tend to zero as the distance between the data tends to zero.

1.4.3 Non-linear stability of continuous equilibria

In this subsection, we prove the non-linear exponential asymptotic stability of the equilibrium states, for small data of the problem (1.21)-(1.22). To do that in a more general

context, we assume that Hypotheses 1.6 and 1.7 previously defined in Subsection 1.4.2 hold.

Let us consider an initial perturbation of a given equilibrium solution of the form:

$$\mathbf{U}_0 = \mathbf{U}^e + \mathbf{U}'_0 \in [H^1(I)]^3.$$

We consider problem (1.31) with the same boundary data as $\mathbf{U}^e$ and initial condition $\mathbf{U}_0$. We assume that the initial perturbation $\mathbf{U}'_0$ is small enough in $[H^1(I)]^3$-norm, in order to guarantee that the initial condition $\mathbf{U}_0$ belongs to the neighborhood of the equilibrium that ensures the existence of $\mathbf{U}$, solution of problem (1.31), stated in Theorem 1.9.

Theorem 1.12. *Assume that Hypotheses 1.6 and 1.7 hold. Then, for small enough data* $\mathbf{C}^e$ *and* $\mathbf{D}$*, the equilibrium solution of problem (1.31) is non-linearly exponentially asymptotically stable, in the sense that:*

$$\|\mathbf{U}'(t)\|_{L^2(I)} \leq \mathrm{e}^{-\lambda t}\|\mathbf{U}'_0\|_{L^2(I)},$$

for some $\lambda > 0$*, where* $\mathbf{U}' = \mathbf{U} - \mathbf{U}^e$*.*

Proof. In weak form, as the perturbation $\mathbf{U}'$ satisfies homogeneous boundary conditions, we have:

$$\int_{-h}^{0} (\partial_t \mathbf{U}) \cdot \mathbf{W} + \int_{-h}^{0} [\boldsymbol{\nu}(\partial_z \mathbf{U})\partial_z \mathbf{U}] \cdot \partial_z \mathbf{W} = L(\mathbf{U}, \mathbf{W}), \tag{1.39}$$

$$\int_{-h}^{0} (\partial_t \mathbf{U}^e) \cdot \mathbf{W} + \int_{-h}^{0} [\boldsymbol{\nu}(\partial_z \mathbf{U}^e)\partial_z \mathbf{U}^e] \cdot \partial_z \mathbf{W} = L(\mathbf{U}^e, \mathbf{W}), \tag{1.40}$$

for all $\mathbf{W} \in [H^1(I)]^3$ such that $\mathbf{W}(-h; t) = \mathbf{0}$, where:

$$L(\mathbf{U}, \mathbf{W}) = \mathbf{C}^e \cdot \mathbf{W}(0; t) - \int_{-h}^{0} \mathbf{D}(\mathbf{U}) \cdot \mathbf{W},$$

$$L(\mathbf{U}^e, \mathbf{W}) = \mathbf{C}^e \cdot \mathbf{W}(0; t) - \int_{-h}^{0} \mathbf{D}(\mathbf{U}^e) \cdot \mathbf{W},$$

and the dot $(\cdot)$ denotes the Euclidean scalar product in $\mathbb{R}^3$. We take the difference between (1.39) and (1.40), and we add and subtract the quantity:

$$\int_{-h}^{0} [\boldsymbol{\nu}(\partial_z \mathbf{U})\partial_z \mathbf{U}^e] \cdot \partial_z \mathbf{W}.$$

We obtain:

$$\begin{aligned} &\int_{-h}^{0} (\partial_t \mathbf{U}') \cdot \mathbf{W} + \int_{-h}^{0} [\boldsymbol{\nu}(\partial_z \mathbf{U})\partial_z \mathbf{U}'] \cdot \partial_z \mathbf{W} \\ = &\int_{-h}^{0} \{[\boldsymbol{\nu}(\partial_z(\mathbf{U}^e)) - \boldsymbol{\nu}(\partial_z \mathbf{U})]\, \partial_z \mathbf{U}^e\} \cdot \partial_z \mathbf{W} - \int_{-h}^{0} \mathbf{D}(\mathbf{U}') \cdot \mathbf{W}. \end{aligned} \tag{1.41}$$

Applying the same technique used in the proof of Theorem 1.9 on the right-hand side of equation (1.41), we have:

$$\begin{aligned}
&\int_{-h}^{0}(\partial_t \mathbf{U}')\cdot\mathbf{W}+\int_{-h}^{0}[\boldsymbol{\nu}(\partial_z\mathbf{U})\partial_z\mathbf{U}']\cdot\partial_z\mathbf{W}\\
=\;&-\int_{-h}^{0}\left[\left(\int_0^1 \mathbf{g}'(\mathrm{s})\,d\mathrm{s}\right)\partial_z\mathbf{U}^e\right]\cdot\partial_z\mathbf{W}-\int_{-h}^{0}\mathbf{D}(\mathbf{U}')\cdot\mathbf{W},
\end{aligned}\tag{1.42}$$

where $\mathbf{g}(\mathrm{t})=\boldsymbol{\nu}(\partial_z(\mathbf{U}^e+\mathrm{t}\mathbf{U}'))$. Let us take $\mathbf{W}=\mathbf{U}'$. From (1.42), we deduce:

$$\begin{aligned}
&\frac{1}{2}\frac{d}{dt}||\mathbf{U}'||^2_{L^2(I)}+\int_{-h}^{0}[\boldsymbol{\nu}(\partial_z\mathbf{U})\,\partial_z\mathbf{U}']\cdot\partial_z\mathbf{U}'\\
=\;&-\int_{-h}^{0}\left\{\left[\int_0^1\left(\nabla\boldsymbol{\nu}(\partial_z\widetilde{\mathbf{U}})\,\partial_z\mathbf{U}'\right)\,d\mathrm{s}\right]\partial_z\mathbf{U}^e\right\}\cdot\partial_z\mathbf{U}'-\int_{-h}^{0}\mathbf{D}(\mathbf{U}')\cdot\mathbf{U}',
\end{aligned}$$

with $\widetilde{\mathbf{U}}=\widetilde{\mathbf{U}}(\mathrm{s})=\mathbf{U}^e+\mathrm{s}\mathbf{U}'$. From Hypothesis 1.6, we have:

$$\begin{aligned}
&\frac{d}{dt}\|\mathbf{U}'\|^2_{L^2(I)}+2\gamma\|\partial_z\mathbf{U}'\|^2_{L^2(I)}\\
\leq\;&-2\int_{-h}^{0}\left\{\left[\int_0^1\left(\nabla\boldsymbol{\nu}(\partial_z\widetilde{\mathbf{U}})\,\partial_z\mathbf{U}'\right)\,d\mathrm{s}\right]\partial_z\mathbf{U}^e\right\}\cdot\partial_z\mathbf{U}'\\
\leq\;&\frac{1}{\gamma}\left\|\left[\int_0^1\left(\nabla\boldsymbol{\nu}(\partial_z\widetilde{\mathbf{U}})\,\partial_z\mathbf{U}'\right)\,d\mathrm{s}\right]\partial_z\mathbf{U}^e\right\|^2_{L^2(I)}+\gamma\|\partial_z\mathbf{U}'\|^2_{L^2(I)}+\|\mathbf{D}(\mathbf{U}')\cdot\mathbf{U}'\|_{L^1(I)},
\end{aligned}$$

where we have used Young's inequality. By Hölder's inequality, we obtain:

$$\begin{aligned}
&\frac{d}{dt}\|\mathbf{U}'\|^2_{L^2(I)}+\gamma\|\partial_z\mathbf{U}'\|^2_{L^2(I)}\\
\leq\frac{1}{\gamma}&\left\|\sup_{s\in[0,1],\,i,j=1,2,3}\left|\left[\nabla\boldsymbol{\nu}(\partial_z\widetilde{\mathbf{U}})\right]_{ij}\right|\right\|^2_{L^\infty(I)}\|\partial_z\mathbf{U}'\|^2_{L^2(I)}\|\partial_z\mathbf{U}^e\|^2_{L^\infty(I)}+\|\mathbf{D}(\mathbf{U}')\|_{L^2(I)}\|\mathbf{U}'\|_{L^2(I)}.
\end{aligned}$$

From Hypothesis 1.6, it follows that $\|\partial_z\mathbf{U}^e\|_{L^\infty(I)}\leq C/\gamma$, where C is a positive constant depending on the data, i.e. $C=C\left(\max_{i=1,2,3}\|D_i(\mathbf{U}^e)\|_{L^\infty(I)}+\|\mathbf{C}^e\|_\infty\right)$. Moreover, we have that:

$$\left\|\sup_{s\in[0,1],\,i,j=1,2,3}\left|\left[\nabla\boldsymbol{\nu}(\partial_z\widetilde{\mathbf{U}})\right]_{ij}\right|\right\|_{L^\infty(I)}\leq\overline{C}.$$

So that, using Poincaré inequality, we deduce:

$$\frac{d}{dt}||\mathbf{U}'||^2_{L^2(I)}+\gamma||\partial_z\mathbf{U}'||^2_{L^2(I)}\leq\Lambda||\partial_z\mathbf{U}'||^2_{L^2(I)},$$

where Λ is a positive constant depending on the data. Reiterating the use of Poincaré inequality, we have:

$$\frac{d}{dt}\|\mathbf{U}'\|^2_{L^2(I)}+\lambda\|\mathbf{U}'\|^2_{L^2(I)}\leq 0,$$

where λ is a positive constant for small enough data. Finally, by Grönwall's lemma, we conclude:

$$\|\mathbf{U}'(t)\|^2_{L^2(I)} \leq \mathrm{e}^{-\lambda t}\,\|\mathbf{U}'_0\|^2_{L^2(I)} \overset{t\to+\infty}{\longrightarrow} 0.$$

■

Corollary 1.13. *Under the hypotheses of Corollary 1.10, the equilibrium solutions of problem (1.21)-(1.22) with smoothly extended viscosity ν and diffusivity K are non-linearly exponentially asymptotically stable for small data.*

Remark 1.14. *This analysis implies a weak result on the asymptotic stability of the original problem (1.21)-(1.22) with the eddy viscosities and diffusivities given by either (1.17), (1.18) or (1.19). Indeed, from Theorem 1.11 we know that for each time interval $[0,\mathcal{T}]$ and for each $\varepsilon > 0$ there exists a subset $\mathcal{A}_{\varepsilon,\mathcal{T}} \subset [0,\mathcal{T}]$ such that $\lim_{\varepsilon\to 0} |\mathcal{A}_{\varepsilon,\mathcal{T}}| = 0$, and if $\|\mathbf{U}'_0\|_{H^1(I)} < \varepsilon$, then $\mathbf{U}(z;t)$ is the solution of this original problem in $I \times ((0,\mathcal{T}) \setminus \mathcal{A}_{\varepsilon,\mathcal{T}})$. From Theorem 1.12, this imples that, for small data:*

$$\|\mathbf{U}'(t)\|^2_{L^2(I)} \leq \mathrm{e}^{-\lambda t}\,\|\mathbf{U}'_0\|^2_{L^2(I)},\ \textit{if } t \notin \mathcal{A}_{\varepsilon,\mathcal{T}}.$$

Resuming, we have analyzed the existence of regular solutions around equilibria for oceanic turbulent MLM based on the gradient Richardson number, and we have studied the non-linear asymptotic stability of the equilibrium states. In general, it is not possible to ensure the existence of solutions for Richardson-number based turbulence models, due to the singularity presented by all the eddy coefficients defined by relations (1.17) to (1.19). Here, we have obtained the proof about the existence and uniqueness of unsteady solutions for the regularized version of these models around equilibria, based upon their smoothness. As consequence, it follows the asymptotic exponential stability of the equilibrium solutions, thanks to the dissipative nature of the equations of the problem. These results imply the existence of solutions of the original non-regularized models out from a small time set, as well as a weak asymptotic stability result.

Chapter 2

Numerical Analysis of Algebraic Oceanic MLM

2.1 Introduction

In this chapter, we study the numerical stability of algebraic oceanic turbulent MLM, discretized by the standard Finite Element Method (FEM). Actually, this discretization is used to perform the numerical analysis. To run the numerical tests, a conservative finite difference (FD) discretization is used in practice by physical oceanographers (*cf.* [8], [45]), derived by applying mass-lumping and quadrature formulas to approximate the integrals appearing in the FEM formulation.

Following this strategy, we initially discretize the initial-boundary value problem (1.21)-(1.22) by piecewise affine finite elements, and we next present how to obtain the standard conservative implicit and semi-implicit FD schemes, that we will use in Chapter 3 to run numerical simulations. Coming back to the FEM formulation, we perform the numerical stability analysis of the discretized models. We prove that, under certain hypotheses on the turbulent viscosities and diffusions, the discretization introduced is well suited, in the sense that is stable (in low-order parabolic norms), and verify a maximum principle. However, this preliminary analysis, introduced in [2] for the un-perturbed model (1.16)-(1.20), presents some limitations. On one hand, the low-order parabolic norm of the stability result are not strong enough to deduce the existence of solutions for the continuous problem (see Chapter 1). To do that, we should prove stability in $W^{2,p}$-norm, which would allow to bound the gradients of the discrete solutions, and then to prove the convergence of the scheme, but it still remains an open problem. On another hand, the hypotheses required on the turbulent viscosities and diffusions result to be somewhat unrealistic. So that, we will develop in the sequel a specific analysis for the actual turbulent viscosities and diffusivities corresponding to PP [49], Gent [22], and Bennis et al. [2] models, with much less restrictive conditions. This analysis deals with existence and uniqueness of discrete steady states, convergence of discrete equilibria to the continuous ones, and non-linear asymptotic convergence of discrete time iterates to the continuous equilibria. Note that, as proved in [2], in the case of the un-perturbed model the equilibria of the discrete problem coincide with those of the continuous problem, so

that the existence of discrete steady states as well as the convergence to the continuous ones are trivially proved. This is not the case for the perturbed model (1.21)-(1.22) under consideration, for which we have to use not-straightforward techniques. Moreover, we will extend to the non-linear case the linear stability analysis of discrete equilibria carried out in [2]. Numerical tests in Chapter 3 will be performed to analyze the theoretical predictions on the non-linear asymptotic stability of MLM. Finally, we will introduce a Primitive Equations Large-Eddy Simulation (LES) model for mixing layers, that we will use as a benchmark in Chapter 3 for a numerical investigation of the finite-time stability of MLM with respect to multidimensional perturbations.

The chapter is structured as follows: In Section 2.2, we introduce the numerical discretization of algebraic oceanic MLM, which is analyzed in Section 2.3. This analysis concerns the existence and uniqueness of discrete steady states (Subsection 2.3.1), convergence of discrete equilibria to the continuous ones (Subsection 2.3.2), and the non-linear stability of the discrete equilibria (Subsection 2.3.3). Finally, in Section 2.4, we present a LES approach, where a hydrostatic ocean model is introduced in order to perform in Chapter 3 a numerical investigation of the finite-time stability of algebraic MLM with respect to multidimensional perturbations.

The main results presented in this chapter can be found in [12].

2.2 Discretization of vertical Richardson number - based schemes

We initially discretize the initial-boundary value problem (1.21)-(1.22) by linear piecewise finite elements. To describe this approximation, assume that the interval $\overline{I} = [-h, 0]$ is divided into N subintervals of length $\Delta z = h/N$, with nodes $z_i = -h + i\,\Delta z,\ i = 0, \ldots, N$, and construct the finite element space:

$$V_\Delta = \{ w_\Delta \in C^0(\overline{I}) \,|\, w_{\Delta|_{(z_{i-1}, z_i)}} \text{ is affine}, i = 1, \ldots, N;\ w_\Delta(-h) = 0 \}. \tag{2.1}$$

To discretize the equation for u, for instance, we consider on one hand the semi-implicit method:

$$\text{Obtain} \quad u_\Delta \in \widetilde{u}_b + V_\Delta \quad \text{such that}$$

$$(P_\Delta) \quad \int_{-h}^{0} \frac{u_\Delta^{n+1} - u_\Delta^n}{\Delta t}\, w_\Delta + \int_{-h}^{0} f_1(R_\Delta^n)\, \partial_z u_\Delta^{n+1} \partial_z w_\Delta = L_u^{n+1}(w_\Delta), \quad \forall w_\Delta \in V_\Delta, \tag{2.2}$$

where:

$$L_u^{n+1}(w_\Delta) = \widetilde{Q}_u^{n+1}\, w_\Delta(0) + \int_{-h}^{0} D_u^{n+1}\, w_\Delta. \tag{2.3}$$

On another hand, we also consider the implicit method:

$$\text{Obtain} \quad u_\Delta \in \widetilde{u}_b + V_\Delta \quad \text{such that}$$

$$(Q_\Delta) \quad \int_{-h}^{0} \frac{u_\Delta^{n+1} - u_\Delta^n}{\Delta t}\, w_\Delta + \int_{-h}^{0} f_1(R_\Delta^{n+1})\, \partial_z u_\Delta^{n+1} \partial_z w_\Delta = L_u^{n+1}(w_\Delta), \quad \forall w_\Delta \in V_\Delta, \tag{2.4}$$

which will be used hereafter to prove the non-linear stability of discrete equilibrium solutions (Section 2.3.3). We consider similar discretizations for v and ρ. These discretizations were introduced in [2] for the un-perturbed model (1.16)-(1.20). Following the guidelines given in [2], we preliminarily prove that both discretizations proposed, under certain hypotheses, are stable and verify a maximum principle. Denote by $\mathbf{U}_\Delta$ the continuous piecewise affine function from $[0,T]$ onto $[V_\Delta]^3$ whose value in t_n is $\mathbf{U}_\Delta^n = (u_\Delta^n,\, v_\Delta^n,\, \rho_\Delta^n)$, and by $\mathbf{L}_\Delta$ the piecewise constant in time function whose value in (t_n, t_{n+1}) is $\mathbf{L}^{n+1} = (L_u^{n+1},\, L_v^{n+1},\, L_\rho^{n+1})$. This function is defined *a.e.* in $[0, \mathcal{T}]$. We have the following:

Lemma 2.1. *Assume that the turbulent viscosities f_1, f_2 are uniformly bounded and positive:*

$$\exists \quad m, M \in \mathbb{R}_+ \text{ such that } m \leq f_1(R), f_2(R) \leq M, \quad \forall R \in \mathbb{R}. \tag{2.5}$$

Then, the discrete unsteady solution $\mathbf{U}_\Delta$ (in its semi-implicit and implicit version) satisfies:

$$\|\mathbf{U}_\Delta\|_{L^\infty(\mathbf{L}^2)} + \|\mathbf{U}_\Delta\|_{L^2(\mathbf{H}^1)} + \|\partial_t \mathbf{U}_\Delta\|_{L^2(\mathbf{H}^{-1})} \leq \|\widetilde{\mathbf{U}}_0\|_{L^2(I)} + C\|\mathbf{L}_\Delta\|_{L^2(\mathbf{H}^{-1})}, \tag{2.6}$$

where C is a positive constant that only depends on the data (and not on Δz and Δt), and $\widetilde{\mathbf{U}}_0 = (\widetilde{u}_0, \widetilde{v}_0, \widetilde{\rho}_0)$.

Proof. We assume, without loss of generality, that $\widetilde{\mathbf{U}}_b = (\widetilde{u}_b, \widetilde{v}_b, \widetilde{\rho}_b) = \mathbf{0}$. The estimates for $\mathbf{U}_\Delta$ in $L^\infty(\mathbf{L}^2)$ and $L^2(\mathbf{H}^1)$ are standard, by taking $\mathbf{W}_\Delta = \mathbf{U}_\Delta^{n+1}$ and using the identity:

$$(a-b)a = \frac{1}{2}\left(|a|^2 - |b|^2 + |a-b|^2\right), \quad \forall a, b \in \mathbb{R}.$$

The estimate for $\partial_t \mathbf{U}_\Delta$ is more involved, because as f_1 and f_2 are not constant, the usual techniques to obtain estimates in $L^2(\mathbf{L^2})$ fail. However, we may obtain estimates in $L^2(\mathbf{H^{-1}})$ as follows: Let Π_Δ denote the orthogonal projection from $L^2(I)$ onto V_Δ. As V_Δ is a 1D finite element space of continuous piecewise linear functions with fixed element size, Π_Δ is also stable in $H^1(I)$ (*cf.* [5], Section 6), i.e. there exists a constant C_1 such that:

$$\|\Pi_\Delta w\|_{H^1(I)} \leq C_1 \|w\|_{H^1(I)}, \quad \forall w \in H^1(I). \tag{2.7}$$

Let us consider method (P_Δ) for the unknown u_Δ. For any $w \in H^1(I)$, and $t \in (t_n, t_{n+1})$, by Hypothesis (2.5) and (2.7) we have:

$$\begin{aligned}
\int_{-h}^0 \partial_t u_\Delta \, w \;&=\; \int_{-h}^0 \frac{u_\Delta^{n+1} - u_\Delta^n}{\Delta t}\, \Pi_\Delta w = -\int_{-h}^0 f_1(R_\Delta^n)\partial_z u_\Delta^{n+1} \partial_z \Pi_\Delta w + L_u^{n+1}(\Pi_\Delta w) \\
&\leq\; \left(\|L_u^{n+1}\|_{H^{-1}(I)} + M\|u_\Delta^{n+1}\|_{H^1(I)}\right) \|\Pi_\Delta w\|_{H^1(I)} \\
&\leq\; C_1 \left(\|L_u^{n+1}\|_{H^{-1}(I)} + M\|u_\Delta^{n+1}\|_{H^1(I)}\right) \|w\|_{H^1(I)}.
\end{aligned} \tag{2.8}$$

The same estimate applies to the implicit method (Q_Δ). From (2.8), we deduce:

$$\|\partial_t u_\Delta\|_{H^{-1}(I)} \leq C_1 \left(\|L_u^{n+1}\|_{H^{-1}(I)} + M\|u_\Delta^{n+1}\|_{H^1(I)}\right).$$

As a similar estimate also holds for v_Δ and ρ_Δ, we conclude:

$$\|\partial_t \mathbf{U}_\Delta\|_{L^2(\mathbf{H}^{-1})} \leq C_2 \left(\|\mathbf{U}_\Delta\|_{L^2(\mathbf{H}^1)} + \|\mathbf{L}_\Delta\|_{L^2(\mathbf{H}^{-1})} \right),$$

and the thesis follows. ■

Note that $\|\mathbf{L}_\Delta\|_{L^2(\mathbf{H}^{-1})} \leq C \sum_{n=1}^{N_t} \Delta t \left(||\widetilde{\mathbf{Q}}^n||_2^2 + ||\mathbf{D}^n||_{L^2(I)}^2 \right)$, where $\widetilde{\mathbf{Q}}^n = (\widetilde{Q}_u^n, \widetilde{Q}_v^n, \widetilde{Q}_\rho^n)$ and $\mathbf{D}^n = (D_u^n, D_v^n, D_\rho^n)$.

Remark 2.2. *Lemma 2.1 proves the stability of the discrete solutions in (quasi-)standard norms for parabolic problems. The issue of existence of solutions for the implicit method (Q_Δ) is solved with the help of the stability result (2.6). Indeed, it allows to apply a standard finite-dimensional fixed-point argument based upon linearization of the equations of the method.*

The FEM discretizations proposed are replaced in practice by centered conservative FD schemes obtained by numerical integration. In particular, we use the canonical piecewise affine basis functions of V_Δ as test functions, we approximate the integrals containing the viscous and diffusive terms by the mid-point rule, and we apply mass-lumping to the mass and forcing integral. Concerning for instance the semi-implicit method (P_Δ), used in the numerical experiments, the following FD scheme is proposed for u:

$$\frac{u_i^{n+1} - u_i^n}{\Delta t} - \frac{f_1(R_{i-1/2}^n) u_{i-1}^{n+1} - \left[f_1(R_{i-1/2}^n) + f_1(R_{i+1/2}^n) \right] u_i^{n+1} + f_1(R_{i+1/2}^n) u_{i+1}^{n+1}}{(\Delta z)^2} = D_{u,i}^{n+1}, \tag{2.9}$$

for $i = 1, \ldots, N-1$. For $i = N$, the Neumann condition at the sea-surface is discretized by:

$$f_1(R_{N-1/2}^n) \frac{u_N^{n+1} - u_{N-1}^{n+1}}{\Delta z} = \widetilde{Q}_u^{n+1}. \tag{2.10}$$

In matrix form, this discretization reads as:

$$A^{n+1} \mathbf{U}^{n+1} = \mathbf{B}^{n+1},$$

where $\mathbf{U}^{n+1}$ is the vector of the unknowns:

$$\mathbf{U}^{n+1} = (u_1^{n+1}, \ldots, u_{N-1}^{n+1})^T,$$

while A^{n+1} and $\mathbf{B}^{n+1}$ are respectively the tridiagonal matrix and the vector of known terms defined as:

$$\begin{cases} & A_{1,1}^{n+1} = 1 + \alpha_{1/2}^n + \alpha_{3/2}^n, & A_{1,2}^{n+1} = -\alpha_{3/2}^n, \\ A_{i,i-1}^{n+1} = -\alpha_{i-1/2}^n, & A_{i,i}^{n+1} = 1 + \alpha_{i-1/2}^n + \alpha_{i+1/2}^n, & A_{i,i+1}^{n+1} = -\alpha_{i+1/2}^n, \quad i = 2 : N-2 \\ A_{N-1,N-2}^{n+1} = -\alpha_{N-3/2}^n, & A_{N-1,N-1}^{n+1} = 1 + \alpha_{N-3/2}^n, & \end{cases}$$

$$\mathbf{B}^{n+1} = (u_1^n + \alpha_{1/2}^n \tilde{u}_b^{n+1} + \Delta t D_{u,1}^{n+1}, \ldots, u_i^n + \Delta t D_{u,i}^{n+1}, \ldots, u_{N-1}^n + \frac{\Delta t}{\Delta z} \widetilde{Q}_u^{n+1} + \Delta t D_{u,N-1}^{n+1})^T,$$

with:

$$\alpha^n_{i-1/2} = \frac{\Delta t}{(\Delta z)^2}\, f_1(R^n_{i-1/2}), \quad \alpha^n_{i+1/2} = \frac{\Delta t}{(\Delta z)^2}\, f_1(R^n_{i+1/2}).$$

By using an analogous notation, also the implicit method (Q_Δ) may be written in matrix form as:

$$A^{n+1}(\mathbf{U}^{n+1})\,\mathbf{U}^{n+1} = \mathbf{B}^{n+1}.$$

We consider similar discretizations for v and ρ.

We now prove that this approximation (in its semi-implicit and implicit version) verifies a maximum principle:

Lemma 2.3. *Assume $f_1 > 0$. If the initial datum $\widetilde{u}_0$, the Dirichlet boundary condition $\widetilde{u}_b$ and the zonal wind-stress $\widetilde{Q}_u$ are positive, and the forcing term D_u is non-negative, then u_Δ is positive in $[-h, 0] \times [0, +\infty)$.*

Proof. Let us prove this result for the semi-implicit version of the approximation. We proceed by induction on n: we suppose $u^n_i > 0$, $i = 0, \dots, N$. We prove $u^{n+1}_i > 0$, $i = 0, \dots, N$. Let $m^{n+1} = \min\limits_{i=0,\dots,N} u^{n+1}_i$. Let $k \in \{0, \dots, N\}$ such that $u^{n+1}_k = m^{n+1}$. If $k = 0$, for $i = 0, \dots, N$ we have $u^{n+1}_i \geq m^{n+1} = \tilde{u}^{n+1}_b > 0$. If $k = N$, from the discretized Neumann boundary condition (2.10), we have:

$$\begin{aligned} m^{n+1} = u^{n+1}_N = \left[\left(\Delta z \widetilde{Q}^{n+1}_u\right)/f_1(R^n_{N-1/2})\right] + u^{n+1}_{N-1} &\geq \left[\left(\Delta z \widetilde{Q}^{n+1}_u\right)/f_1(R^n_{N-1/2})\right] + m^{n+1} \\ \Longrightarrow \left[\left(\Delta z \widetilde{Q}^{n+1}_u\right)/f_1(R^n_{N-1/2})\right] &\leq 0, \end{aligned}$$

that is impossible for the assumptions of the Lemma. As consequence, $k \in \{0, \dots, N-1\}$, and $u^{n+1}_N \geq u^{n+1}_i$, $i = 0, \dots, N-1$. If $k \in \{1, \dots, N-1\}$, from the FD scheme (2.9), we have:

$$\begin{aligned} (1 + \alpha^n_{k-1/2} + \alpha^n_{k+1/2}) m^{n+1} &= (1 + \alpha^n_{k-1/2} + \alpha^n_{k+1/2}) u^{n+1}_k \\ = u^n_k + \alpha^n_{k-1/2} u^{n+1}_{k-1} + \alpha^n_{k+1/2} u^{n+1}_{k+1} + \Delta t D^{n+1}_{u,k} &\geq (\alpha^n_{k-1/2} + \alpha^n_{k+1/2}) m^{n+1} + m^n + \Delta t D^{n+1}_{u,k} \\ \Longrightarrow m^{n+1} \geq m^n + \Delta t D^{n+1}_{u,k} &\geq m^0 + \Delta t \sum_{r=1}^{n+1} D^r_{u,k}, \end{aligned} \tag{2.11}$$

where $m^0 \geq \min\limits_{z\in[-h,0]} \widetilde{u}_0(z)$. Since by hypothesis $D_u \geq 0$, we conclude $m^{n+1} > 0$. Similarly, it is possible to deduce this result for v_Δ. The same proof applies to the implicit version of the approximation. ■

Remark 2.4. *If the time components of $D_{u,k}$, $k \in \{1, \dots, N-1\}$, are negative, from (2.11) the same argument proves that u_Δ is positive in a time interval $[0, \mathcal{T}]$ such that $\sum\limits_{r=1}^{n+1} D^r_{u,k} > -\left(\min\limits_{z\in[-h,0]} \widetilde{u}_0(z)\right)\frac{1}{\mathcal{T}}$, $\mathcal{T} = (n+1)\Delta t$, for all k. This is reasonable from a physical point of view, as in this case the forcing term is adverse and will revert the direction of the velocity if it is applied for a long enough time.*

2.3 Analysis of discrete equilibrium states

As we already mention in Section 2.1, the preliminary numerical analysis of Section 2.2 presents some limitations. On one hand, the low-order parabolic norm of Lemma 2.1 are not strong enough to deduce the existence of solutions for the continuous problem (see Chapter 1). On another hand, the assumption that the turbulent viscosities and diffusions are uniformly bounded is somewhat unrealistic, as in practice f_1 and f_2 are unbounded for some negative gradient Richardson numbers.

In this section, we develop a specific analysis for the actual turbulent viscosities and diffusivities corresponding to PP [49], Gent [22] and Bennis et al. [2] models, with much less restrictive conditions. In particular, we prove existence and uniqueness of discrete equilibrium (Subsection 2.3.1), and its convergence to the continuous one as $\Delta z \to 0$ (Subsection 2.3.2). We also prove a result of practical interest: the continuous equilibria are asymptotically reached by the solutions of the implicit scheme (2.4) as $n \to +\infty$ and $\Delta z \to 0$ (Subsection 2.3.3). We assume the following:

Hypothesis 2.5. *The turbulent viscosities and diffusions $f_1, f_2 \in C^1([0,+\infty))$, and are uniformly bounded and positive for $R \geq 0$, that is:*

$$\exists \quad m, M \in \mathbb{R}_+ \text{ such that } m \leq f_1(R), f_2(R) \leq M, \quad \forall R \geq 0. \tag{2.12}$$

The turbulent viscosities and diffusions of PP (1.17), Gent (1.18) and Bennis et al. (1.19) models satisfy Hyptohesis 2.5. Indeed, for PP and Bennis et al. models:

$$a_1 \leq f_1(R) \leq a_1 + b_1, \quad a_2 \leq f_2(R) \leq a_2 + a_1 + b_1, \quad \forall R \geq 0,$$

while for Gent model:

$$a_1 \leq f_1(R) \leq a_1 + b_1, \quad a_2 \leq f_2(R) \leq a_2 + b_1, \quad \forall R \geq 0.$$

2.3.1 Existence and uniqueness of discrete equilibria

We prove existence and uniqueness of discrete equilibrium solutions. The main problem that we face is that for zero gradient velocities, the gradient Richardson number is not defined. We prove that under Hypothesis 2.5, there exists an equilibrium with bounded (from below and from above) velocity gradient.

We reformulate the discrete steady problem as a system of algebraic equations for the unknowns:

$$\alpha_\Delta = \partial_z u_\Delta, \quad \beta_\Delta = \partial_z v_\Delta, \quad \theta_\Delta = \partial_z \rho_\Delta.$$

To do that, we define the piecewise constant finite element space:

$$G_\Delta = \left\{ \varphi_\Delta \in L^2(I) \text{ such that } \varphi_{\Delta|_{(z_{i-1},z_i)}} \text{ is constant, } i = 1, \dots, N \right\}.$$

The equilibria of the discrete problem, if these exist, are solutions:

$$(u^e_\Delta, v^e_\Delta, \rho^e_\Delta) \in (\widetilde{u}_b, \widetilde{v}_b, \widetilde{\rho}_b) + [V_\Delta]^3,$$

of the non-linear system of equations:

$$\begin{cases} \displaystyle\int_{-h}^{0} f_1(R_\Delta)\,\partial_z u_\Delta \partial_z w_{1\Delta} = L_u^e(w_{1\Delta}), & \forall w_{1\Delta} \in V_\Delta, \\ \displaystyle\int_{-h}^{0} f_1(R_\Delta)\,\partial_z v_\Delta \partial_z w_{2\Delta} = L_v^e(w_{2\Delta}), & \forall w_{2\Delta} \in V_\Delta, \\ \displaystyle\int_{-h}^{0} f_2(R_\Delta)\,\partial_z \rho_\Delta \partial_z w_{3\Delta} = L_\rho^e(w_{3\Delta}), & \forall w_{3\Delta} \in V_\Delta, \end{cases} \tag{2.13}$$

where:

$$R_\Delta = -\frac{g}{\rho_r}\,\frac{\partial_z \rho_\Delta}{(\partial_z u_\Delta)^2 + (\partial_z v_\Delta)^2},$$

$$L_u^e(w_{1\Delta}) = \widetilde{Q}_u^e\, w_{1\Delta}(0) + \int_{-h}^{0} D_u^e\, w_{1\Delta}, \quad L_v^e(w_{2\Delta}) = \widetilde{Q}_v^e\, w_{2\Delta}(0) + \int_{-h}^{0} D_v^e\, w_{2\Delta},$$

$$L_\rho^e(w_{3\Delta}) = \widetilde{Q}_\rho^e\, w_{3\Delta}(0) + \int_{-h}^{0} D_\rho^e\, w_{3\Delta}.$$

We prove that problem (2.13) is equivalent to:

$$(\alpha_\Delta, \beta_\Delta, \theta_\Delta) \in [G_\Delta]^3 \text{ s.t. } \begin{cases} \displaystyle\int_{-h}^{0} f_1(\widetilde{R}_\Delta)\,\alpha_\Delta \varphi_{1\Delta} = L_u^e(w(\varphi_{1\Delta})), & \forall \varphi_{1\Delta} \in G_\Delta, \\ \displaystyle\int_{-h}^{0} f_1(\widetilde{R}_\Delta)\,\beta_\Delta \varphi_{2\Delta} = L_v^e(w(\varphi_{2\Delta})), & \forall \varphi_{2\Delta} \in G_\Delta, \\ \displaystyle\int_{-h}^{0} f_2(\widetilde{R}_\Delta)\,\theta_\Delta \varphi_{3\Delta} = L_\rho^e(w(\varphi_{3\Delta})), & \forall \varphi_{3\Delta} \in G_\Delta, \end{cases} \tag{2.14}$$

where:

$$\widetilde{R}_\Delta = \widetilde{R}_\Delta(\alpha_\Delta, \beta_\Delta, \theta_\Delta) = -\frac{g}{\rho_r}\,\frac{\theta_\Delta}{(\alpha_\Delta)^2 + (\beta_\Delta)^2},$$

$$(w(\varphi_\Delta))(z) = \int_{-h}^{z} \varphi_\Delta(s)\,ds \text{ (see Figure 2.1).}$$

Lemma 2.6. *Problem (2.13) is equivalent to problem (2.14), in the sense that* $(\alpha_\Delta, \beta_\Delta, \theta_\Delta)$ *is a solution of (2.14) if and only if the triplet:*

$$u_\Delta(z) = \widetilde{u}_b + \int_{-h}^{z} \alpha_\Delta(s)\,ds, \quad v_\Delta(z) = \widetilde{v}_b + \int_{-h}^{z} \beta_\Delta(s)\,ds, \quad \rho_\Delta(z) = \widetilde{\rho}_b + \int_{-h}^{z} \theta_\Delta(s)\,ds,$$

is a solution of (2.13).

Proof. On one hand, as $G_\Delta = \{\partial_z w_\Delta : w_\Delta \in V_\Delta\}$, if $(u_\Delta, v_\Delta, \rho_\Delta) \in (\widetilde{u}_b, \widetilde{v}_b, \widetilde{\rho}_b) + [V_\Delta]^3$ is solution of problem (2.13), then $(\alpha_\Delta, \beta_\Delta, \theta_\Delta) \in [G_\Delta]^3$ is solution of problem (2.14). On another hand, if $(\alpha_\Delta, \beta_\Delta, \theta_\Delta) \in [G_\Delta]^3$ is solution of problem (2.14), as:

$$\begin{cases} \partial_z u_\Delta = \alpha_\Delta, & \partial_z v_\Delta = \beta_\Delta, & \partial_z \rho_\Delta = \theta_\Delta, \\ u_\Delta(-h) = \widetilde{u}_b, & v_\Delta(-h) = \widetilde{v}_b, & \rho_\Delta(-h) = \widetilde{\rho}_b, \end{cases} \tag{2.15}$$

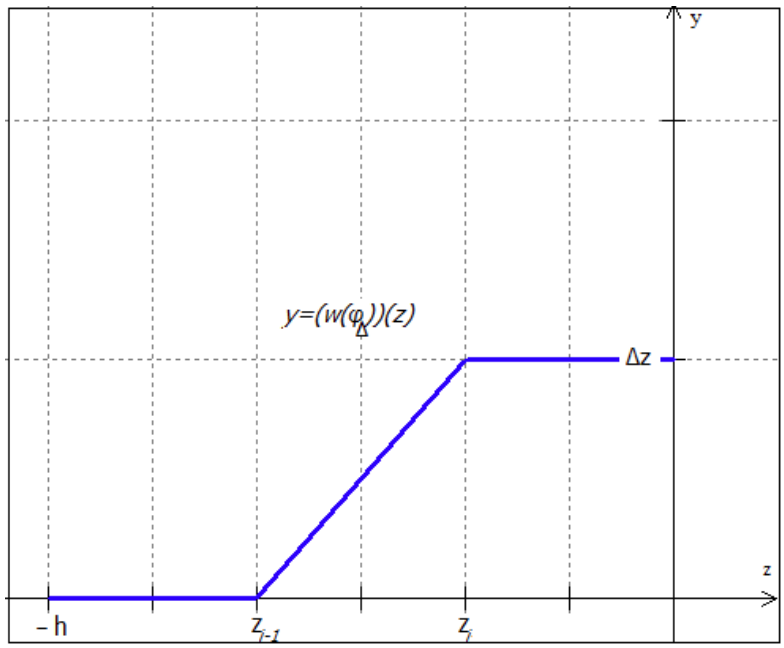

Figure 2.1:
Graphic of the function $y = (w(\varphi_\Delta))(z)$.

then $(u_\Delta, v_\Delta, \rho_\Delta) \in (\widetilde{u}_b, \widetilde{v}_b, \widetilde{\rho}_b) + [V_\Delta]^3$ is solution of problem (2.13). ■

To prove existence of discrete equilibria, we may refer to problem (2.14):

Theorem 2.7. *Under Hypotheses 1.2 and 2.5, problem (2.14) admits at least a solution that verifies:*

$$\alpha_\Delta > 0, \quad \beta_\Delta > 0, \quad \theta_\Delta < 0, \quad \textit{and} \quad C_1 \leq |\alpha_\Delta|, |\beta_\Delta|, |\theta_\Delta| \leq C_2, \tag{2.16}$$

where:

$$C_1 = \frac{\lambda}{2M} \min\left\{Q_u^e,\, Q_v^e,\, |Q_\rho^e|\right\}, \quad C_2 = 3\,\frac{\lambda}{2m} \max\left\{Q_u^e,\, Q_v^e,\, |Q_\rho^e|\right\}. \tag{2.17}$$

Proof. We initially focus on the first component of the velocity. Let α_Δ, β_Δ, $\theta_\Delta \in G_\Delta$. Assume that $\widetilde{R}_\Delta = \widetilde{R}_\Delta(\alpha_\Delta, \beta_\Delta, \theta_\Delta) > 0$. Consider the following linearization of the first equation of system (2.14):

$$\widehat{\alpha}_\Delta \in G_\Delta \text{ such that } \int_{-h}^{0} f_1(\widetilde{R}_\Delta)\, \widehat{\alpha}_\Delta \varphi_{1\Delta} = L_u^e(w(\varphi_{1\Delta})), \quad \forall \varphi_{1\Delta} \in G_\Delta. \tag{2.18}$$

Problem (2.14) is exactly solved as follows:

Set $\widehat{\alpha}_\Delta = \sum_{i=1}^{N} \widehat{\alpha}_i \varphi_{1\Delta}$, where $\varphi_{1\Delta} = \mathbf{1}_{(z_{i-1}, z_i)} = \varphi_{1i} \in G_\Delta$, and $\mathbf{1}_{(z_{i-1}, z_i)}$ is the indicator function of the subinterval (z_{i-1}, z_i). Then, (2.18) becomes:

$$\widehat{\alpha}_i \int_{z_{i-1}}^{z_i} f_1(\widetilde{R}_\Delta) = L_u^e(w(\varphi_{1i})), \text{ for } i = 1, \ldots, N.$$

It implies that:

$$\widehat{\alpha}_i = L_u^e(w(\varphi_{1i}))\left(\int_{z_{i-1}}^{z_i} f_1(\widetilde{R}_\Delta)\right)^{-1}.$$

Observe that:

$$L_u^e(w(\varphi_{1i})) = \widetilde{Q}_u^e\,(w(\varphi_{1i}))(0) + \int_{-h}^{0} D_u^e\, w(\varphi_{1i}),$$

$$(w(\varphi_{1i}))(z) = \int_{-h}^{z} \varphi_{1i}(s)\,ds = \begin{cases} 0, & \text{if } z < z_{i-1}; \\ z - z_{i-1}, & \text{if } z_{i-1} < z < z_i; \\ z_i - z_{i-1} = \Delta z, & \text{if } z > z_i. \end{cases}$$

Then, we obtain:

$$(w(\varphi_{1i}))(0) = \Delta z,$$

$$\int_{-h}^{0} D_u^e(z)\,(w(\varphi_{1i}))(z)dz = \int_{z_{i-1}}^{z_i} D_u^e(z)\,(z - z_{i-1})\,dz + \Delta z \int_{z_i}^{0} D_u^e(z)\,dz.$$

Moreover, we can write:

$$\int_{z_{i-1}}^{z_i} f_1(\widetilde{R}_\Delta) = \Delta z f_1(R_i), \text{ with } R_i = \widetilde{R}(\alpha_i, \beta_i, \theta_i).$$

Thus, we have:

$$\widehat{\alpha}_i = \left(\widetilde{Q}_u^e + \int_{z_{i-1}}^{z_i} D_u^e(z)\,(z - z_{i-1})/\Delta z\,dz + \int_{z_i}^{0} D_u^e(z)\,dz\right)(f_1(R_i))^{-1}. \tag{2.19}$$

As:

$$\left|\int_{z_{i-1}}^{z_i} D_u^e(z)\,(z - z_{i-1})/\Delta z\,dz + \int_{z_i}^{0} D_u^e(z)\,dz\right| \leq \|D_u^e\|_{L^1(I)},$$

using Hypothesis 1.2, we obtain:

$$\frac{\lambda}{2}\,Q_u^e \leq \widetilde{Q}_u^e + \int_{z_{i-1}}^{z_i} D_u^e(z)\,(z - z_{i-1})/\Delta z\,dz + \int_{z_i}^{0} D_u^e(z)\,dz \leq 3\,\frac{\lambda}{2}\,Q_u^e.$$

Using Hypothesis 2.5, this implies that:

$$0 < \frac{\lambda}{2}\,\frac{Q_u^e}{M} \leq \widehat{\alpha}_\Delta \leq 3\,\frac{\lambda}{2}\,\frac{Q_u^e}{m}. \tag{2.20}$$

Similarly:

$$0 < \frac{\lambda}{2}\,\frac{Q_v^e}{M} \leq \widehat{\beta}_\Delta \leq 3\,\frac{\lambda}{2}\,\frac{Q_v^e}{m} \quad \text{and} \quad 3\,\frac{\lambda}{2}\,\frac{Q_\rho^e}{m} \leq \widehat{\theta}_\Delta \leq \frac{\lambda}{2}\,\frac{Q_\rho^e}{M} < 0. \tag{2.21}$$

Let us define the set:

$$K_\Delta(C_1, C_2) = \left\{(w_{1\Delta}, w_{2\Delta}, w_{3\Delta}) \in [G_\Delta]^3 \text{ such that } C_1 \leq |w_{i\Delta}| \leq C_2, i = 1, 2, 3\right\}, \tag{2.22}$$

where C_1 and C_2 are given by (2.17). The set $K_\Delta(C_1, C_2)$ is a non-empty convex compact subset of the finite-dimensional vector space $[G_\Delta]^3$. Let $\tau : K_\Delta(C_1, C_2) \longrightarrow K_\Delta(C_1, C_2)$ be the map defined by:

$$\tau(\alpha_\Delta, \beta_\Delta, \theta_\Delta) = (\widehat{\alpha}_\Delta, \widehat{\beta}_\Delta, \widehat{\theta}_\Delta).$$

By (2.19), it is clear that τ is continuous. By applying Brouwer's fixed point theorem (*cf.* [6]), it follows the existence of at least a solution of the discrete steady problem (2.14). ■

We next step to the analysis of uniqueness of solution of problem (2.14). We state at first a technical result. We denote by $|\cdot|$ the Euclidean norm on $\mathbb{R}^n$, and without risk of confusion, hereafter we omit the apex ^{e} to denote equilibrium fluxes.

Lemma 2.8. *Let the set:*

$$S = \left[\frac{\lambda}{2M}\,Q_u, \frac{3\lambda}{2m}\,Q_u\right] \times \left[\frac{\lambda}{2M}\,Q_v, \frac{3\lambda}{2m}\,Q_v\right] \times \left[\frac{3\lambda}{2m}\,Q_\rho, \frac{\lambda}{2M}\,Q_\rho\right]. \tag{2.23}$$

Then, for any $\mathcal{A}_1 = (\alpha_1, \beta_1, \theta_1)$, $\mathcal{A}_2 = (\alpha_2, \beta_2, \theta_2) \in S$, the following estimates hold:

$$|f_1(R(\mathcal{A}_1)) - f_1(R(\mathcal{A}_2))| \leq K_1\,|\mathcal{A}_1 - \mathcal{A}_2|, \tag{2.24}$$

$$|f_2(R(\mathcal{A}_1)) - f_2(R(\mathcal{A}_2))| \leq K_2\,|\mathcal{A}_1 - \mathcal{A}_2|, \tag{2.25}$$

where:

$$R(\mathcal{A}_i) = -\frac{g}{\rho_r}\,\frac{\theta_i}{\alpha_i^2 + \beta_i^2}, \quad i = 1,\, 2, \tag{2.26}$$

and:

$$K_1 = \frac{C}{(1+\overline{R})^3}\left(\frac{M^2}{m\lambda}\right)^2\left[\frac{(Q_u + Q_v)\overline{R} + 1}{Q_u^2 + Q_v^2}\right], \tag{2.27}$$

$$K_2 = \frac{C}{(1+\overline{R})^n}\left(\frac{M^2}{m\lambda}\right)^2\left[\frac{(Q_u + Q_v)\overline{R} + 1}{Q_u^2 + Q_v^2}\right], \tag{2.28}$$

with:

$$\overline{R} = \frac{|Q_\rho|}{Q_u^2 + Q_v^2}, \quad n = \begin{cases} 4 & \text{if } f_1,\, f_2 \text{ are defined by PP (1.17), Gent (1.18),} \\ 5 & \text{if } f_1,\, f_2 \text{ are defined by Bennis et al. (1.19),} \end{cases}$$

and C a numerical constant.

Proof. Observe that, if $\mathcal{A} = (\alpha, \beta, \theta) \in S$, then the associated gradient Richardson number $R = -\dfrac{g}{\rho_r}\,\dfrac{\theta}{\alpha^2 + \beta^2}$ is positive. So, $f_1(R(\cdot))$ and $f_2(R(\cdot))$ are smooth functions on S. By the mean value theorem:

$$\begin{aligned} |f_i(R(\mathcal{A}_1)) - f_i(R(\mathcal{A}_2))| &\leq \|f_i'\|_{L^\infty(J)}|R(\mathcal{A}_1) - R(\mathcal{A}_2)| \\ &\leq \|f_i'\|_{L^\infty(J)}|\nabla R(\mathcal{B})|\,|\mathcal{A}_1 - \mathcal{A}_2|, \quad i = 1, 2, \end{aligned} \tag{2.29}$$

for some $\mathcal{B}$ in the open segment of extremities $\mathcal{A}_1$ and $\mathcal{A}_2$, and J denoting the set:

$$J = \left[\frac{g}{\rho_r} \frac{2m}{3\lambda} \overline{R}, \frac{g}{\rho_r} \frac{2M}{\lambda} \overline{R} \right].$$

Assume, for instance, that f_1 and f_2 are given by Gent model (1.18). Then:

$$\begin{aligned} f_1'(R) &= -20b_1(1+10R)^{-3}, \quad f_2'(R) = -30b_1(1+10R)^{-4}; \\ \nabla R(\alpha,\beta,\theta) &= \frac{g}{\rho_r} \left(2\alpha\theta(\alpha^2+\beta^2)^{-2},\ 2\beta\theta(\alpha^2+\beta^2)^{-2},\ -(\alpha^2+\beta^2)^{-1}\right). \end{aligned}$$

By estimates (2.16)-(2.17), we deduce:

$$\begin{aligned} \|f_1'\|_{L^\infty(J)} &\leq \frac{C_1}{(1+\overline{R})^3}, \quad \|f_2'\|_{L^\infty(J)} \leq \frac{C_2}{(1+\overline{R})^4}, \\ \|\nabla R\|_{L^\infty(S)} &\leq C_3 \left(\frac{M^2}{m\lambda}\right)^2 \left[\frac{(Q_u+Q_v)\overline{R}+1}{Q_u^2+Q_v^2}\right], \end{aligned}$$

where:

$$C_1 = 20\, b_1 \max\left\{ \left(\frac{M}{m}\right)^2, \frac{9\,\lambda}{20} \frac{M}{m^2} \frac{\rho_r}{g} \right\}^3, \quad C_2 = 30\, b_1 \max\left\{ \left(\frac{M}{m}\right)^2, \frac{9\,\lambda}{20} \frac{M}{m^2} \frac{\rho_r}{g} \right\}^4,$$

$$C_3 = 72\, \frac{g}{\rho_r}.$$

Combining with (2.29), estimates (2.24) and (2.25) follow.

When f_1 and f_2 are given by PP (1.17) and Bennis et al. (1.19) models, estimates (2.24) and (2.25) follow in the same manner, as in these cases:

$$\|f_1'\|_{L^\infty(J)} \leq \frac{C_1}{(1+\overline{R})^3}, \quad \|f_2'\|_{L^\infty(J)} \leq \frac{C_2}{(1+\overline{R})^n},$$

for some numerical constants C_1, $C_2 > 0$, and $n = 4, 5$ respectively for PP (1.17) and Bennis et al. (1.19) models. These exponents indicate the leading terms in the computation of f_2', and are justified by the fact that the present analysis holds for tropical seas, where usually $\overline{R} \sim 10^2$ (See Section 3.2), and so $R \in J \sim \left[\frac{2\cdot 10^{-5}\lambda}{3}, \frac{2\cdot 10^{-2}}{\lambda}\right]$, since $\frac{g}{\rho_r} \sim 10^{-2}$, and $m = 10^{-5}$, $M \sim 10^{-2}$ for PP (1.17) and Bennis et al. (1.19) models. It implies that, at least for $\lambda \geq 10^{-1}$, $R \leq 0.2$, and the aforementioned exponents are recovered in the leading terms of f_2'. ■

We can now state the result of uniqueness of solution for problem (2.14):

Theorem 2.9. *Under Hypotheses 1.2 and 2.5, for large enough (negative) surface thermodynamic fluxes Q_ρ, problem (2.14) admits a unique solution.*

Proof. Assume that α_Δ and α^1_Δ are both solutions of the first equation of system (2.14). Let us set $\delta\alpha_\Delta = \alpha_\Delta - \alpha^1_\Delta$. As $\displaystyle\int_{-h}^{0} f_1(\widetilde{R}_\Delta)\alpha_\Delta\varphi_{1\Delta} = \int_{-h}^{0} f_1(\widetilde{R}^1_\Delta)\alpha^1_\Delta\varphi_{1\Delta}$, with obvious notation, we have:

$$\int_{-h}^{0} f_1(\widetilde{R}_\Delta)\,\delta\alpha_\Delta\varphi_{1\Delta} = \int_{-h}^{0} [f_1(\widetilde{R}^1_\Delta) - f_1(\widetilde{R}_\Delta)]\,\alpha^1_\Delta\varphi_{1\Delta}, \quad \forall\varphi_{1\Delta} \in G_\Delta. \tag{2.30}$$

Using Lemma 2.8:

$$\int_{-h}^{0} f_1(\widetilde{R}_\Delta)\,\delta\alpha_\Delta\varphi_{1\Delta} \le K_1 \int_{-h}^{0} |\delta\mathcal{A}_\Delta|\,|\alpha^1_\Delta|\,|\varphi_{1\Delta}|, \tag{2.31}$$

where $\delta\mathcal{A}_\Delta = (\alpha^1_\Delta - \alpha_\Delta, \beta^1_\Delta - \beta_\Delta, \theta^1_\Delta - \theta_\Delta)$.

Let $\varphi_{1\Delta} = \delta\alpha_\Delta$, so that, as $f_1 \ge a_1$, we obtain:

$$a_1\,\|\delta\alpha_\Delta\|_{L^2(I)} \le K_1\,\|\delta\mathcal{A}_\Delta\|_{L^2(I)}\,\|\alpha^1_\Delta\|_{L^\infty(I)} \le N_u\,\|\delta\mathcal{A}_\Delta\|_{L^2(I)}, \tag{2.32}$$

where $N_u = \dfrac{3\lambda}{2m}\,K_1\,Q_u$. Similarly:

$$a_1\,\|\delta\beta_\Delta\|_{L^2(I)} \le N_v\,\|\delta\mathcal{A}_\Delta\|_{L^2(I)}, \tag{2.33}$$

where $N_v = \dfrac{3\lambda}{2m}\,K_1\,Q_v$, and:

$$a_2\,\|\delta\theta_\Delta\|_{L^2(I)} \le N_\rho\,\|\delta\mathcal{A}_\Delta\|_{L^2(I)}, \tag{2.34}$$

where $N_\rho = \dfrac{3\lambda}{2m}\,K_2\,|Q_\rho|$. Then, we can write:

$$\widehat{C}\|\delta\mathcal{A}_\Delta\|_{L^2(I)} \le 0,$$

where:

$$\widehat{C} = m(1-N), \quad m = \min\{a_1, a_2\},$$

and:

$$N = \frac{C}{(1+\overline{R})^3}\left(\frac{M}{m}\right)^4\left[\frac{(Q_u+Q_v)\overline{R}+1}{Q_u^2+Q_v^2}\right](Q_u+Q_v+|Q_\rho|), \tag{2.35}$$

for some numerical constant $C > 0$. Assuming $\sigma \le Q_u, Q_v \le \tau$ for some $0 < \sigma < \tau$, then the bound:

$$N \le \frac{C}{(1+\overline{R})^3}\left(\frac{M}{m}\right)^4\left[3\,\overline{R} + \tau/\sigma^2 + 2\,\tau\,\overline{R}^2\right],$$

holds. It implies that $N < 1$ if $|Q_\rho|$ is large enough, and consequently, the solution of the discrete problem (2.14) is unique. ■

Remark 2.10. *We have proved the uniqueness of solutions of the discrete model (2.14) for flows dominated by negative (warming) surface thermodynamic fluxes. This is coherent from a physical point of view, as the warming of the surface has a stabilizing effect on the mixing layer. The flow in the tropical seas fits into this case, as Q_ρ is typically negative. However, for all models, if we consider realistic values of the momentum and heat surface fluxes in tropical seas (See Section 3.2), the constant N defined by (2.35) is typically greater than one. Nevertheless, if we move in a small neighborhood of a fixed discrete equilibrium, i.e. we restrict considerably the set S, the estimate for the constant N given by (2.35) can be directly replaced by an expression in terms of the fixed discrete equilibrium solution, and thus can be reduced enough, resulting to be effectively smaller than one for all models.*

2.3.2 Convergence of discrete equilibria to the continuous ones

We next prove that the discrete equilibria converge to the continuous ones, for large enough (negative) surface thermodynamic fluxes. This analysis implies the existence of equilibria of problem (1.21)-(1.22) as weak solutions of the steady version of this problem, so as its stability with respect to numerical discretizations.

Theorem 2.11. *Assume that Hypotheses 1.2 and 2.5 hold, and that D_u, D_v, $D_\rho \in L^\infty(I)$. Then, for large enough (negative) surface thermodynamic fluxes Q_ρ, the sequence $\{(u_\Delta, v_\Delta, \rho_\Delta)\}_{\Delta z>0}$ is strongly convergent in $[H^1(I)]^3$ to a weak solution (u, v, ρ) of the steady version of problem (1.21)-(1.22).*

Proof. We prove that $\alpha_\Delta, \beta_\Delta, \theta_\Delta$ are BV (bounded variation) functions on $I = (-h, 0)$. Indeed, let us consider the total variation of α_Δ on I, that is defined as:

$$TV_{(I)}(\alpha_\Delta) = \sum_{i=1}^{N-1} |\alpha_{i+1} - \alpha_i|.$$

By identity (2.19) and Hypotheses 1.2 and 2.5, we have:

$$|\alpha_{i+1} - \alpha_i| = \left| \frac{\widetilde{Q}_u + \dfrac{1}{\Delta z}\displaystyle\int_{-h}^{0} D_u\, w(\varphi_{1,i+1})\, dz}{f_1(R_{i+1})} - \frac{\widetilde{Q}_u + \dfrac{1}{\Delta z}\displaystyle\int_{-h}^{0} D_u\, w(\varphi_{1,i})\, dz}{f_1(R_i)} \right|$$

$$\leq \left|\widetilde{Q}_u\right| \left| \frac{f_1(R_{i+1}) - f_1(R_i)}{f_1(R_{i+1}) f_1(R_i)} \right| + \frac{1}{\Delta z} \left| \frac{\displaystyle\int_{-h}^{0} D_u\, \left[w(\varphi_{1,i+1}) f_1(R_i) - w(\varphi_{1,i}) f_1(R_{i+1}) \right] dz}{f_1(R_{i+1}) f_1(R_i)} \right|$$

$$\leq (2-\lambda)\, \frac{Q_u}{m^2}\, |f_1(R_{i+1}) - f_1(R_i)| + \frac{f_1(R_i)}{\Delta z\, m^2} \left| \int_{-h}^{0} D_u\, \left[w(\varphi_{1,i+1}) - w(\varphi_{1,i}) \right] dz \right|$$

$$+ \frac{1}{\Delta z\, m^2} \left| \int_{-h}^{0} D_u\, w(\varphi_{1,i})\, \left[f_1(R_i) - f_1(R_{i+1}) \right] dz \right|$$

$$\leq \frac{1}{m^2} \left[(2-\lambda) Q_u + \|D_u\|_{L^1(I)} \right] |f_1(R_{i+1}) - f_1(R_i)| + 2\, \frac{M}{m^2}\, \|D_u\|_{L^\infty(I)}\, \Delta z, \qquad (2.36)$$

where the last inequality follows from $|w(\varphi_{1,i})| \leq \Delta z$ and from the estimate:

$$\begin{aligned}
& \left| \int_{-h}^{0} D_u \left[w(\varphi_{1,i+1}) - w(\varphi_{1,i}) \right] dz \right| \\
\leq & \left| \int_{z_i}^{z_{i+1}} D_u(z) \, (z - z_i) \, dz - \int_{z_{i-1}}^{z_i} D_u(z) \, (z - z_{i-1}) \, dz \right| \\
+ & \left| \int_{z_{i+1}}^{0} D_u(z) \, \Delta z \, dz - \int_{z_i}^{0} D_u(z) \, \Delta z \, dz \right| \\
\leq & \| D_u \|_{L^\infty(I)} \Delta z^2 + \Delta z \int_{z_i}^{z_{i+1}} |D_u(z)| \, dz \leq 2 \, \| D_u \|_{L^\infty(I)} \Delta z^2.
\end{aligned}$$

Recall that, by Theorem 1.9, for all $\Delta z > 0$ the triplet $(\alpha_\Delta, \beta_\Delta, \theta_\Delta)$ lies in the set S defined by (2.23). By Lemma 2.8:

$$|f_1(R_{i+1}) - f_1(R_i)| \leq K_1 \left[|\alpha_{i+1} - \alpha_i| + |\beta_{i+1} - \beta_i| + |\theta_{i+1} - \theta_i| \right],$$

where K_1 is given by (2.27). Combining this estimate with (2.36), we obtain:

$$|\alpha_{i+1} - \alpha_i| \leq L_1 [|\alpha_{i+1} - \alpha_i| + |\beta_{i+1} - \beta_i| + |\theta_{i+1} - \theta_i|] + 2 \, \frac{M}{m^2} \, \| D_u \|_{L^\infty(I)} \, \Delta z,$$

where $L_1 = \dfrac{C_1}{(1 + \overline{R})^3} \left(\dfrac{M^2}{m^2 \lambda} \right)^2 \left[\dfrac{(Q_u + Q_v)\overline{R} + 1}{Q_u^2 + Q_v^2} \right] Q_u$. Similar estimates hold for $|\beta_{i+1} - \beta_i|$ and $|\theta_{i+1} - \theta_i|$, so we can write:

$$(1 - L_2) \sum_{i=1}^{N-1} \left(|\alpha_{i+1} - \alpha_i| + |\beta_{i+1} - \beta_i| + |\theta_{i+1} - \theta_i| \right) \leq L_3 \sum_{i=1}^{N-1} \Delta z \leq L_3 h,$$

where:

$$L_2 = \frac{C_2}{(1 + \overline{R})^3} \left(\frac{M^2}{m^2 \lambda} \right)^2 \left[\frac{(Q_u + Q_v)\overline{R} + 1}{Q_u^2 + Q_v^2} \right] (Q_u + Q_v + |Q_\rho|),$$

for some numerical constant $C_2 > 0$, and:

$$L_3 = 2 \, \frac{M}{m^2} \, \left(\| D_u \|_{L^\infty(I)} + \| D_v \|_{L^\infty(I)} + \| D_\rho \|_{L^\infty(I)} \right).$$

Arguing as in the proof of Theorem 2.9, the constant L_2 is smaller than one if $|Q_\rho|$ is large enough, then:

$$\sum_{i=1}^{N-1} (|\alpha_{i+1} - \alpha_i| + |\beta_{i+1} - \beta_i| + |\theta_{i+1} - \theta_i|) \leq \frac{L_3}{1 - L_2} h.$$

It implies that α_Δ, β_Δ, θ_Δ are uniformly bounded in $BV(I)$. As $BV(I)$ is compactly embedded in $L^1(I)$ (*cf.* [24]), there exists a sub-sequence $\{(\alpha_{\Delta'}, \beta_{\Delta'}, \theta_{\Delta'})\}$ of $\{(\alpha_\Delta, \beta_\Delta, \theta_\Delta)\}$ strongly convergent in $[L^1(I)]^3$ to (α, β, θ). We deduce that there exists a sub-sequence of $\{(\alpha_{\Delta'}, \beta_{\Delta'}, \theta_{\Delta'})\}$, that we may denote in the same way, such that $(\alpha_{\Delta'}, \beta_{\Delta'}, \theta_{\Delta'}) \to (\alpha, \beta, \theta)$

a.e. in I. It follows that $f_1(\widetilde{R}_{\Delta'}) \to f_1(\widetilde{R})$ a.e. in I. At the same time, $\{f_1(\widetilde{R}_{\Delta'})\}$ is bounded in $L^2(I)$, so that, up to a sub-sequence, $f_1(\widetilde{R}_{\Delta'})$ weakly converges to a function g in $L^2(I)$. Let $\varphi \in L^2(I)$. For a positive constant C, we have:

$$|f_1(\widetilde{R}_{\Delta'})||\varphi| \leq C|\varphi|, \quad f_1(\widetilde{R}_{\Delta'})\varphi \to f_1(\widetilde{R})\varphi \text{ a.e. in } I.$$

By the dominated convergence theorem (*cf.* [20]):

$$\int_{-h}^{0} f_1(\widetilde{R}_{\Delta'})\varphi \to \int_{-h}^{0} f_1(\widetilde{R})\varphi.$$

As $f_1(\widetilde{R}_{\Delta'}) \rightharpoonup g$ in $L^2(I)$, we obtain:

$$\int_{-h}^{0} (f_1(\widetilde{R}) - g)\varphi = 0, \quad \forall \varphi \in L^2(I) \Rightarrow f_1(\widetilde{R}) = g.$$

So that, $f_1(\widetilde{R}_{\Delta'}) \rightharpoonup f_1(\widetilde{R})$ in $L^2(I)$. Moreover, for a positive constant C:

$$|f_1(\widetilde{R}_{\Delta'})|^2 \leq C, \quad |f_1(\widetilde{R}_{\Delta'})|^2 \to |f_1(\widetilde{R})|^2 \text{ a.e. in } I.$$

By the dominated convergence theorem:

$$||f_1(\widetilde{R}_{\Delta'})||_{L^2(I)} \to ||f_1(\widetilde{R})||_{L^2(I)}.$$

It follows that $\{f_1(\widetilde{R}_{\Delta'})\}$ strongly converges to $f_1(\widetilde{R})$ in $L^2(I)$. Let us consider $\varphi \in C^0(\overline{I})$. There exists a sequence $\{\varphi_{\Delta'}\}$ with $\varphi_{\Delta'} \in G_\Delta$ such that $\varphi_{\Delta'} \to \varphi$ in $L^\infty(I)$. Then:

$$f_1(\widetilde{R}_{\Delta'})\varphi_{\Delta'} \to f_1(\widetilde{R})\varphi \text{ in } L^2(I).$$

Finally, as $\alpha_{\Delta'} \rightharpoonup \alpha$ in $L^2(I)$, we can conclude:

$$\int_{-h}^{0} f_1(\widetilde{R}_{\Delta'})\alpha_{\Delta'}\varphi_{\Delta'} \to \int_{-h}^{0} f_1(\widetilde{R})\alpha\varphi.$$

Then, $\{(u_{\Delta'}, v_{\Delta'}, \rho_{\Delta'})\}$ strongly converges in $[H^1(I)]^3$ to a weak solution (u, v, ρ) of the steady version of problem (1.21)-(1.22). Since we proved in Theorem 1.1 that (u, v, ρ) is unique, then the whole sequence $\{(u_\Delta, v_\Delta, \rho_\Delta)\}$ converges to it. ■

Remark 2.12. *It holds an analogous of Remark 2.10, i.e. the result of convergence holds for mixing layer flows dominated by negative (warming) surface thermodynamic fluxes.*

2.3.3 Non-linear stability of discrete equilibria

We analyze in this section the asymptotic stability of the discrete equilibria. The objective is to prove that the continuous equilibria are well approximated by the solution of the evolutive (implicit and semi-implicit) discrete problems (2.2) and (2.4), which are computable in practice. We give a positive answer when the time iterates have bounded derivatives. Actually, we prove the asymptotic stability of the implicit discrete model (Q_Δ) given by (2.4). We assume the following:

Hypothesis 2.13. *The sequence* $\{\partial_z \mathbf{U}_\Delta^n\}_{n\in\mathbb{N}}$ *remains in the set* S *given by (2.23), for all* $n \in \mathbb{N}$.

The proof of this hypothesis is still an open problem. Under this hypothesis, we prove the asymptotic stability of the implicit discrete model (Q_Δ). Let us denote by Π_Δ the standard nodal interpolation operator from continuous functions onto the space V_Δ.

Theorem 2.14. *Assume that Hypotheses 1.2, 2.5 and 2.13 hold, and that* D_u, D_v, D_ρ *are smooth functions of* z *(and* t*). Then, for large enough (negative) surface thermodynamic fluxes* Q_ρ*, the implicit discrete method* (Q_Δ) *is asymptotically stable, in the sense that:*

$$\limsup_{n\to+\infty} \|\mathbf{U}_\Delta^n - \Pi_\Delta \mathbf{U}^e\|_{L^2(I)} \leq C\Delta z, \tag{2.37}$$

where $\mathbf{U}_\Delta^n = (u_\Delta^n,\, v_\Delta^n,\, \theta_\Delta^n)$, $\mathbf{U}^e = (u^e,\, v^e,\, \theta^e)$ *and* C *is a positive constant.*

Proof. Let us look for u_Δ^n as $u_\Delta^n = \Pi_\Delta u^e + \hat{u}_\Delta^n$, where $\hat{u}_\Delta^n$ is a perturbation with homogeneous boundary conditions. As $\Pi_\Delta u^e \in \widetilde{u}_b + V_\Delta$, then $\hat{u}_\Delta^n \in V_\Delta$. If we set $\Pi_\Delta^* u^e = \Pi_\Delta u^e - u^e$, for all $w_\Delta \in V_\Delta$, we have that:

$$\int_{-h}^0 \frac{u_\Delta^{n+1} - u_\Delta^n}{\Delta t} w_\Delta + \int_{-h}^0 f_1(R_\Delta^{n+1}) \partial_z u_\Delta^{n+1} \partial_z w_\Delta = L_u^{n+1}(w_\Delta), \tag{2.38}$$

$$\int_{-h}^0 \frac{\Pi_\Delta u^e - \Pi_\Delta u^e}{\Delta t} w_\Delta + \int_{-h}^0 f_1(R^e) \partial_z \Pi_\Delta u^e \partial_z w_\Delta = L_{u^e}(w_\Delta) + \int_{-h}^0 f_1(R^e) \partial_z \Pi_\Delta^* u^e \partial_z w_\Delta. \tag{2.39}$$

We take the difference between (2.38) and (2.39), and we add and subtract the quantity:

$$\int_{-h}^0 f_1(R_\Delta^{n+1}) \partial_z \Pi_\Delta u^e \partial_z w_\Delta.$$

We obtain:

$$\begin{aligned} & \int_{-h}^0 (\hat{u}_\Delta^{n+1} - \hat{u}_\Delta^n) w_\Delta + \Delta t \int_{-h}^0 f_1(R_\Delta^{n+1}) \partial_z \hat{u}_\Delta^{n+1} \partial_z w_\Delta \\ = \;& \Delta t \int_{-h}^0 [f_1(R^e) - f_1(R_\Delta^{n+1})] \partial_z \Pi_\Delta u^e \partial_z w_\Delta - \Delta t \int_{-h}^0 f_1(R^e) \partial_z \Pi_\Delta^* u^e \partial_z w_\Delta \\ - \;& \int_{-h}^0 D(u_\Delta^{n+1} - u^e) w_\Delta. \end{aligned} \tag{2.40}$$

Let us take $w_\Delta = \hat{u}_\Delta^{n+1}$. Using the identity $(a-b)a = \frac{1}{2}\left(|a|^2 - |b|^2 + |a-b|^2\right)$, we deduce:

$$\begin{aligned} & \|\hat{u}_\Delta^{n+1}\|_{L^2(I)}^2 + \|\hat{u}_\Delta^{n+1} - \hat{u}_\Delta^n\|_{L^2(I)}^2 + 2m\,\Delta t \|\partial_z \hat{u}_\Delta^{n+1}\|_{L^2(I)}^2 \\ \leq \;& \|\hat{u}_\Delta^n\|_{L^2(I)}^2 + 2\Delta t \int_{-h}^0 [f_1(R^e) - f_1(R_\Delta^{n+1})] \partial_z \Pi_\Delta u^e \partial_z \hat{u}_\Delta^{n+1} \\ - \;& 2\Delta t \int_{-h}^0 f_1(R^e) \partial_z \Pi_\Delta^* u^e \partial_z \hat{u}_\Delta^{n+1} - \int_{-h}^0 D(u_\Delta^{n+1} - u^e) \hat{u}_\Delta^{n+1}, \end{aligned}$$

where we have used $f_1(R_\Delta^{n+1}) \geq m > 0$ from Hypotheses 2.5 and 2.13. By Lemma 2.8, we have:

$$\begin{aligned}
&\int_{-h}^{0} [f_1(R^e) - f_1(R_\Delta^{n+1})] \partial_z \Pi_\Delta u^e \partial_z \hat{u}_\Delta^{n+1} \\
\leq\ & K_1 \, \|\partial_z (\mathbf{U}^e - \mathbf{U}_\Delta^{n+1})\|_{L^2(I)} \, \|\partial_z \Pi_\Delta u^e\|_{L^\infty(I)} \, \|\partial_z \hat{u}_\Delta^{n+1}\|_{L^2(I)},
\end{aligned}$$

where K_1 is defined by (2.27). From (1.27) and Hypothesis 1.2, it follows:

$$||\partial_z \Pi_\Delta u^e\|_{L^\infty(I)} \leq ||\partial_z u^e\|_{L^\infty(I)} \leq 2 \, \frac{Q_u}{m},$$

so that:

$$\begin{aligned}
&\int_{-h}^{0} [f_1(R^e) - f_1(R_\Delta^{n+1})] \partial_z \Pi_\Delta u^e \partial_z \hat{u}_\Delta^{n+1} \\
\leq\ & K_u \, \|\partial_z (\mathbf{U}^e - \mathbf{U}_\Delta^{n+1})\|_{L^2(I)} \, \|\partial_z \hat{u}_\Delta^{n+1}\|_{L^2(I)} \\
\leq\ & K_u \left(\|\partial_z \Pi_\Delta^* \mathbf{U}^e\|_{L^2(I)} + \|\partial_z \widehat{\mathbf{U}}_\Delta^{n+1}\|_{L^2(I)} \right) \|\partial_z \hat{u}_\Delta^{n+1}\|_{L^2(I)},
\end{aligned}$$

where we denote $K_u = 2 \, K_1 \, \dfrac{Q_u}{m}$. Then:

$$\begin{aligned}
&\|\hat{u}_\Delta^{n+1}\|_{L^2(I)}^2 + 2m \, \Delta t \|\partial_z \hat{u}_\Delta^{n+1}\|_{L^2(I)}^2 \\
\leq\ & \|\hat{u}_\Delta^{n}\|_{L^2(I)}^2 + 2\Delta t \, K_u \, \|\partial_z \widehat{\mathbf{U}}_\Delta^{n+1}\|_{L^2(I)} \, \|\partial_z \hat{u}_\Delta^{n+1}\|_{L^2(I)} \\
+\ & 2\Delta t \, \left(K_u \, \|\partial_z \Pi_\Delta^* \mathbf{U}^e\|_{L^2(I)} + M \, \|\partial_z \Pi_\Delta^* u^e\|_{L^2(I)} + C \right) \|\partial_z \hat{u}_\Delta^{n+1}\|_{L^2(I)},
\end{aligned}$$

as $f_1(R^e) \leq M$ from Hypothesis 2.5. Similar estimates apply to the perturbations:

$$\hat{v}_\Delta^{n+1} = v_\Delta^n - \Pi_\Delta v^e, \quad \hat{\theta}_\Delta^{n+1} = \theta_\Delta^n - \Pi_\Delta \theta^e.$$

Summing these up, we deduce:

$$\begin{aligned}
&\|\widehat{\mathbf{U}}_\Delta^{n+1}\|_{L^2(I)}^2 + 2m \, \Delta t \|\partial_z \widehat{\mathbf{U}}_\Delta^{n+1}\|_{L^2(I)}^2 \\
\leq\ & \|\widehat{\mathbf{U}}_\Delta^{n}\|_{L^2(I)}^2 + 2\Delta t \, K \, \|\partial_z \widehat{\mathbf{U}}_\Delta^{n+1}\|_{L^2(I)}^2 \\
+\ & 2\Delta t \, (K + M + C) \, \|\partial_z \Pi_\Delta^* \mathbf{U}^e\|_{L^2(I)} \, \|\partial_z \widehat{\mathbf{U}}_\Delta^{n+1}\|_{L^2(I)},
\end{aligned}$$

where:

$$K = 2 \, K_1 \, \frac{Q_u + Q_v}{m} + 2 \, K_2 \, \frac{|Q_\rho|}{m} \leq \frac{C}{m(1+\overline{R})^3} \left(\frac{M^2}{m^2 \lambda} \right)^2 \left[\frac{(Q_u + Q_v)\overline{R} + 1}{Q_u^2 + Q_v^2} \right] (Q_u + Q_v + |Q_\rho|).$$

Thus, for large enough $|Q_\rho|$, we have $K < m$. Then, denoting $\widehat{m} = m - K$, we obtain:

$$\begin{aligned}
&\|\widehat{\mathbf{U}}_\Delta^{n+1}\|_{L^2(I)}^2 + 2 \, \widehat{m} \, \Delta t \, \|\partial_z \widehat{\mathbf{U}}_\Delta^{n+1}\|_{L^2(I)}^2 \\
\leq\ & \|\widehat{\mathbf{U}}_\Delta^{n}\|_{L^2(I)}^2 + 2\Delta t \, (K + M + C) \, \|\partial_z \Pi_\Delta^* \mathbf{U}^e\|_{L^2(I)} \, \|\partial_z \widehat{\mathbf{U}}_\Delta^{n+1}\|_{L^2(I)}.
\end{aligned}$$

Using Young's inequality:

$$\begin{aligned}\|\widehat{\mathbf{U}}_\Delta^{n+1}\|^2_{L^2(I)} + \widehat{m}\,\Delta t\,\|\partial_z\widehat{\mathbf{U}}_\Delta^{n+1}\|^2_{L^2(I)} &\leq \|\widehat{\mathbf{U}}_\Delta^{n}\|^2_{L^2(I)} + \Delta t\,\frac{(K+M+C)^2}{\widehat{m}}\,\|\partial_z\Pi_\Delta^*\mathbf{U}^e\|^2_{L^2(I)}\\ &\leq \|\widehat{\mathbf{U}}_\Delta^{n}\|^2_{L^2(I)} + C_1\,(\Delta z)^2\,\Delta t, \qquad (2.41)\end{aligned}$$

for some numerical constant $C_1 > 0$, where the last inequality follows from the finite element interpolation error estimate:

$$\|\partial_z\Pi_\Delta^*\mathbf{U}^e\|_{L^2(I)} \leq C_2\,\Delta z\|\partial^2_{zz}\mathbf{U}^e\|_{L^2(I)},$$

for some numerical constant C_2, and we use the fact that $\mathbf{U}^e \in [C^\infty(\overline{I})]^3$ from (1.25). Using Poincaré inequality $\|\widehat{\mathbf{U}}_\Delta^{n+1}\|^2_{L^2(I)} \leq C_3\,\|\partial_z\widehat{\mathbf{U}}_\Delta^{n+1}\|^2_{L^2(I)}$ for some constant $C_3 > 0$, we deduce from (2.41):

$$\left(1 + C_3^{-1}\,\widehat{m}\Delta t\right)\sigma_{n+1} \leq \sigma_n + C_1\,(\Delta z)^2\Delta t,$$

where we denote $\sigma_n = \|\widehat{\mathbf{U}}_\Delta^{n}\|^2_{L^2(I)}$. Let $\widehat{K} = \dfrac{1}{(1 + C_3^{-1}\,\widehat{m}\Delta t)}$, so we can write:

$$\sigma_{n+1} \leq \widehat{K}\sigma_n + \widehat{K}C_1(\Delta z)^2\Delta t = (1 - C_4\Delta t)\sigma_n + (1 - C_4\Delta t)\,C_1\,(\Delta z)^2\Delta t,$$

where we denote $C_4 = C_3^{-1}\,\widehat{K}\,\widehat{m}$. Then:

$$\sigma_{n+1} \leq (1 - C_4\Delta t)^{n+1}\sigma_0 + (C_1/C_4)(\Delta z)^2, \qquad (2.42)$$

and we conclude (2.37). ■

Corollary 2.15. *Under the hypotheses of Theorem 2.14, the sequence* $\{\mathbf{U}_\Delta^n\}_{n\in\mathbb{N}}$ *asymptotically converges to the continuous equilibrium* $\mathbf{U}^e$ *in* $[L^2(I)]^3$ *as* $(n, \Delta z) \to (+\infty, 0)$.

Remark 2.16. *Concerning Hypothesis (2.13), if the initial perturbation lies in the set S, to prove that its time iterates remain in it is still an open problem. However, in Section 3.2.3, we will perform some numerical tests for realistic initial and boundary conditions to analyze the asymptotic convergence of the time iterates computed with the numerical scheme (2.2) to the continuous equilibria, in order to numerically validate the thesis of Corollary 2.15.*

2.4 A Primitive Equations multidimensional LES for mixing layers

To investigate the finite-time stability of the algebraic MLM (1.17), (1.18) and (1.19) with respect to multidimensional perturbations, we introduce in this section a hydrostatic ocean model based on a LES approach. For computational efficiency, we choose a domain that represents a vertical section through the ocean in the $x - z$ plane, periodic in the $x-$direction, which is physically reasonable. Our procedure is to solve on this

domain a 2D Primitive Equations model of oceanic flow, whose data are 1D plus small 2D perturbations.

The Primitive Equations govern oceanic flows at large scales in space and time, and are often used as a physical-mathematical basic model to analyze global climate changes and oceanic bio-systems, usually in combination with turbulence models (*cf.* [18]). In their reduced formulation, they form a set of PDEs for horizontal velocity, surface pressure and density, arising from the Boussinesq Equations (1.8) together with the hydrostatic approximation (1.14).

Instead of the *free-surface condition*, we consider here the *rigid-lid assumption*, that states that the sea-surface is flat and the vertical velocity vanishes on it. Let us consider the 1D domain:

$$\omega = (0, L),\ L > 0,$$

that shall represent the rigid-surface domain of the flow. We define the 2D flow domain as:

$$\Omega = \left\{(x, z) \in \mathbb{R}^2 \text{ s.t. } x \in \omega,\ -h < z < 0\right\}.$$

We assume that the flow is homogeneous in the y direction and turbulent, and we represent by:

$$\mathbf{U} = (u(x, z; t), w(x, z; t)), \quad \rho = \rho(x, z; t), \quad p = p(x, z; t),$$

the mean velocity, density and pressure (rescaled by ρ_r) of the fluid, arising from a statistical Reynolds averaging of the 2D Boussinesq Equations. The averaged form of the Primitive Equations is:

$$\begin{cases} (a) & \partial_t u + (\mathbf{U}\cdot\nabla)u - a_1\Delta u + \partial_x p = -\nabla\cdot\left(\overline{\mathbf{U}'\,u'}\right) & \text{in} & \Omega\times(0,\mathcal{T}) \\ (b) & \partial_z p = -\dfrac{\rho}{\rho_r}g & \text{in} & \Omega\times(0,\mathcal{T}) \\ (c) & \nabla\cdot\mathbf{U} = 0 & \text{in} & \Omega\times(0,\mathcal{T}) \\ (d) & \partial_t\rho + (\mathbf{U}\cdot\nabla)\rho - a_2\Delta\rho = -\nabla\cdot\left(\overline{\mathbf{U}'\,\rho'}\right) & \text{in} & \Omega\times(0,\mathcal{T}) \end{cases} \tag{2.43}$$

As we are considering tropical seas, we neglect the Coriolis force. Also, the anisotropy of the domain ($L >> h$) permits to apply the hydrostatic approximation:

$$\partial_z p = -\frac{\rho}{\rho_r}g. \tag{2.44}$$

In system (2.43), $\mathbf{U}'$, u', and ρ' are respectively the fluctuations of the total velocity, the horizontal velocity and the density of the fluid, and a_1, a_2 are the laminar viscosity and diffusion. To solve the closure problem for model (2.43), we use the concept of eddy viscosity and diffusion. So, we set:

$$-\overline{\mathbf{U}'\,u'} = (\nu_h^t\,\partial_x u,\ \nu_v^t\,\partial_z u), \quad -\overline{\mathbf{U}'\,\rho'} = (K_h^t\,\partial_x\rho,\ K_v^t\,\partial_z\rho),$$

where ν_h^t and ν_v^t are the horizontal and vertical eddy viscosity coefficients, while K_h^t and K_v^t are the horizontal and vertical eddy diffusivity coefficients. We apply a Smagorinsky

turbulence model for the horizontal eddy viscosity and diffusivity coefficients ν_h^t and K_h^t. The Smagorinsky turbulence model is a LES model based upon the eddy viscosity and mixing length concepts, intrinsically linked to a discretization grid (*cf.* [56]). We consider:

$$\nu_h^t = (C_S\,\Delta x)^2\,|\partial_x u|, \quad K_h^t = \frac{a_2}{a_1}\,\nu_h^t,$$

where C_S is the Smagorinsky constant, estimated from experimental measurements (*cf.* [35]), and Δx is the horizontal turbulent mixing length, identified with the horizontal diameter of the elements of the grid considered on the computational domain Ω. As for the vertical eddy viscosity and diffusivity coefficients ν_v^t and K_v^t, we use the gradient Richardson number-based model of Bennis et al. (1.19). So, we consider:

$$\nu_v^t = \frac{b_1}{(1+5R)^2}, \quad K_v^t = \frac{a_1}{(1+5R)^2} + \frac{b_1}{(1+5R)^4},$$

where the gradient Richardson number R is now defined as:

$$R = -\frac{g}{\rho_r}\,\frac{\partial_z \rho}{(\partial_z u)^2}.$$

The hydrostatic and the rigid-lid assumptions allow to integrate the hydrostatic equation (2.44) from an arbitrary depth z up to the rigid-surface $z = 0$:

$$\int_z^0 \partial_s p(x,s;t)\,ds = -\frac{g}{\rho_r}\int_z^0 \rho(x,s;t)\,ds \Longrightarrow p(x,z;t) = p_s(x;t) + \frac{g}{\rho_r}\int_z^0 \rho(x,s;t)\,ds,$$

with p_s denoting the surface pressure. It follows that the horizontal gradient of the pressure is rewritten in terms of the horizontal gradient of the surface pressure, plus a baroclinic contribution:

$$\partial_x p(x,z;t) = \partial_x p_s(x;t) + \frac{g}{\rho_r}\partial_x \int_z^0 \rho(x,s;t)\,ds.$$

The reduced formulation of the Primitive Equations becomes:

$$\begin{cases} (a) \quad \partial_t u + (\mathbf{U}\cdot\nabla)u - \partial_x(\nu_h \partial_x u) - \partial_z(\nu_v \partial_z u) + \partial_x p_s + \dfrac{g}{\rho_r}\partial_x \displaystyle\int_z^0 \rho(x,s;t)\,ds = 0 \\ (b) \quad \partial_z w = -\partial_x u \\ (c) \quad \partial_t \rho + (\mathbf{U}\cdot\nabla)\rho - \partial_x(K_h \partial_x \rho) - \partial_z(K_v \partial_z \rho) = 0 \end{cases} \tag{2.45}$$

where $\nu_h = a_1 + \nu_h^t$, $\nu_v = a_1 + \nu_v^t$ respectively are the total horizontal and vertical viscosity, and $K_h = a_2 + K_h^t$, $K_v = a_2 + K_v^t$ respectively are the total horizontal and vertical diffusion.

Let us decompose the boundary of Ω into four pieces, $\partial\Omega = \Gamma_b \cup \Gamma_s \cup \Gamma_{\ell_1} \cup \Gamma_{\ell_2}$, where Γ_b is the domain bottom, Γ_s is the ocean surface, and Γ_{ℓ_1}, Γ_{ℓ_2} are artificial vertical sidewalls.

We shall consider the following initial and boundary conditions associated to problem (2.45):

$$\begin{cases} (d) & u_{|\Gamma_b} = u_b, \quad \rho_{|\Gamma_b} = \rho_b \\ (e) & w_{|\Gamma_b} = w_{|\Gamma_s} = 0 \\ (f) & u_{|\Gamma_{\ell_1}} = u_{|\Gamma_{\ell_2}}, \quad \rho_{|\Gamma_{\ell_1}} = \rho_{|\Gamma_{\ell_2}} \\ (g) & \nu_v \partial_z u_{|\Gamma_s} = Q_u, \quad K_v \partial_z \rho_{|\Gamma_s} = Q_\rho \\ (h) & u(t=0) = u_0, \quad \rho(t=0) = \rho_0, \quad w(t=0) = 0 \end{cases} \tag{2.46}$$

The boundary condition $(2.46) - (e)$ includes the rigid-lid assumption: $w = 0$ at the surface $z = 0$, while the boundary condition $(2.46) - (f)$ represents periodic boundary conditions that we impose on the sidewalls Γ_{ℓ_1}, Γ_{ℓ_2}. The remaining boundary conditions are those of the 1D model (1.16)-(1.20).

Remark 2.17. *If the initial conditions* $(2.46) - (h)$ *are 1D (do not depend on* x*), the solutions of the MLM are solutions of the Primitive Equations with a zero pressure gradient.*

We discretize model (2.45)-(2.46) with a Galerkin FEM in the spatial variables, and a semi-implicit Euler scheme for the temporal variable. In particular, we use a Taylor-Hood $(P2-P1)$ discretization for velocity-pressure. This ensures the stability of the discretization of the pressure (*cf.* [13]). We also use a $P1$ discretization for the density. Note that the integral appearing in equation $(2.45) - (a)$, related to the baroclinic contribution, is approximated by composite quadrature formulas (e.g., composite trapezoidal rule). As for the temporal discretization, we linearize the convective, viscous and diffusive terms appearing in the problem. Moreover, we solve decoupled problems for the pair velocity-pressure and density, by considering the baroclinic contribution at a previous time step. This yields a stable full discretization.

In Section 3.2.4, the approximated LES model (2.45)-(2.46) is integrated for characteristic times associated to the formation of mixing-layer profiles (almost constant density from the surface down to the depth where a sharp gradient appears), typically of the order of several days. The purpose is to test whether, in tropical seas, replacing a multidimensional model with a 1D MLM provides accurate results. We will observe that the finite-time solutions provided by the 2D model loose memory of 2D rather small initial perturbations, and are close to the solutions provided by the 1D MLM.

Chapter 3

Numerical Experiments by MLM

3.1 Introduction

In this chapter, we investigate the finite-time (characteristic times of formation of well-developed mixing layers) and asymptotic behavior of algebraic turbulent MLM by numerical simulations, using data corresponding to tropical seas as well as to polar regions. We start by comparing the performances given by the three different settings of the eddy viscosity previously introduced in Chapter 1, i.e. the Pacanowski-Philander model (1.17), the Gent model (1.18) and the Bennis et al. model (1.19). This comparison is performed for relatively large deviations of realistic initial conditions provided by the Tropical Atmosphere Ocean (TAO) array. These initial conditions correspond to states close to mixing-layer profiles, measured on the Equatorial Pacific region called West-Pacific Warm Pool. The applied initial perturbations admit meaningful physical interpretations: on one hand, we take into account strong heating or precipitation phenomena at the surface, while on another hand we consider the cooling or evaporation of surface waters. To run the numerical tests, the conservative FD discretization proposed in Section 2.2 is used in its semi-implicit form. This first numerical study allows to conclude that mixing-layer profiles could be considered as kinds of "absorbing configurations" in finite-time, that asymptotically evolve to steady states under the application of warming surface fluxes.

Moreover, we use the Primitive Equations LES model for mixing layer, introduced in Section 2.4, as a reference for a numerical investigation of the finite-time stability of MLM with respect to multidimensional perturbations. We will find that, in tropical seas, replacing a multidimensional model by a 1D MLM provides quite accurate results to predict the mixing-layer evolution.

To provide a more comprehensive numerical investigation, some results on different parameterizations of vertical mixing in polar regions are finally presented. We will clearly observe as strong cooling effects provide a rather different dynamics of the mixing layer with respect to typical dynamics in tropical regions. In particular, we focus the attention on two situations of interest: the mixed layer induced by wind stress in the Arctic Ocean, and the deep mixed regime in the Labrador Sea driven by buoyancy loss at the surface. The vertical mixing parameterizations that we test on realistic initial conditions extracted

from the World Ocean Atlas 2001 (WOA01) data are the first-order closure PP and KPP models, a modified version of Mellor and Yamada scheme, and the second-order closure model of Gaspar et al., as they are implemented in the MIT general circulation model (MITgcm).

In a first stage, the surface wind forcing and buoyancy fluxes are prescribed and constant during all time integration. This is obviously an idealized situation, since in more realistic cases time-dependent surface currents, sensible and latent heat fluxes as well as fresh-water fluxes/brine rejection during melting/sea-ice formation are involved, and can modify the ocean stratification. Furthermore, lateral advection processes too play an increasing important role as time progresses, and can dominate variability over seasonal and inter-annual time-scales (*cf.* [39]). For these reasons, we conclude that vertical (1D) MLM can be successfully used in general to represent the evolving mixed layer on short time scales, but to properly represent lateral exchanges for larger time scales, we have decided to move to a more meaningful 3D configuration. For computational efficiency, we use a regional Arctic Ocean configuration of the MITgcm global grid. We perform an intercomparison of the Arctic Ocean circulation simulated with PP and KPP models, driven by realistic (CORE-II, 1958-2007) forcing. Coordinated Ocean-ice Reference Experiments (COREs) are commonly used as a tool to explore the behavior of global ocean-ice models under forcing from a common atmospheric dataset (*cf.* [26])

The chapter is structured as follows: In Section 3.2, we investigate the finite-time and asymptotic behavior of algebraic turbulent MLM by numerical simulations, using data corresponding to the Equatorial Pacific region called West-Pacific Warm Pool (Test 1). In the framework of Test 1, we present four cases of study. Case 1 (Subsection 3.2.1) is devoted to test the ability of the various MLM introduced to reproduce the formation of well-mixed boundary layers, starting by a large negative deviation from realistic density initial conditions in absence of convection (i.e., $\partial_z \rho_0 < 0$ for any $z \in (-h, 0)$). The perturbation applied in this case intends to simulate strong initial heating or precipitation processes at the surface. With the same purpose, in Case 2 (Subsection 3.2.2) we consider an initialization of the code by a large positive surface deviation from a real density profile in presence of convection (i.e., $\partial_z \rho_0 > 0$ for some $z \in (-h, 0)$). The perturbation applied in this case simulates strong initial processes such as the cooling of surface waters or evaporation. Case 3 (Subsection 3.2.3) is devoted to the computational analysis of asymptotic stability of discrete equilibria, while in Case 4 (Subsection 3.2.4) we perform a numerical study of finite-time stability with respect to 2D perturbations. On another hand, in Section 3.3 we test the performances of MLM in various configurations pertaining to high latitudes of the Northern Hemisphere (Test 2). Within the setting of Test 2, we present two cases of study. Case 1 (Subsection 3.3.1) is related to the impact of different MLM driven by wind forcing and/or cooling at the surface, while Case 2 (Subsection 3.3.2) analyzes the sensitivity of the Arctic Ocean circulation simulated by a 3D coupled ocean - sea-ice model with two different mixed-layer physics.

The results of Test 2 have been carried out during my stay at the Alfred Wegener Institute (AWI, Bremerhaven, GERMANY, http://www.awi.de/en/) for the period from

15.09 to 15.12.2013, in close collaboration with Drs. Sergey Danilov, Martin Losch, and Jens Schröter of Climate Dynamics Section, and presented at the Section Seminar. The results of Test 1 can be found in [12], [10], [54].

3.2 Test 1: West-Pacific Warm Pool

In this section, we study the application of oceanic turbulent MLM in the Equatorial Pacific region, called West-Pacific Warm Pool. The West-Pacific Warm Pool is an area located at the equator between 120^oE and 180^oE (see Figure 3.1), where the temperature is high and almost constant along the year (oscillating between $28 - 30^o$ C). The precipitations are intense and, as consequence, the salinity is low.

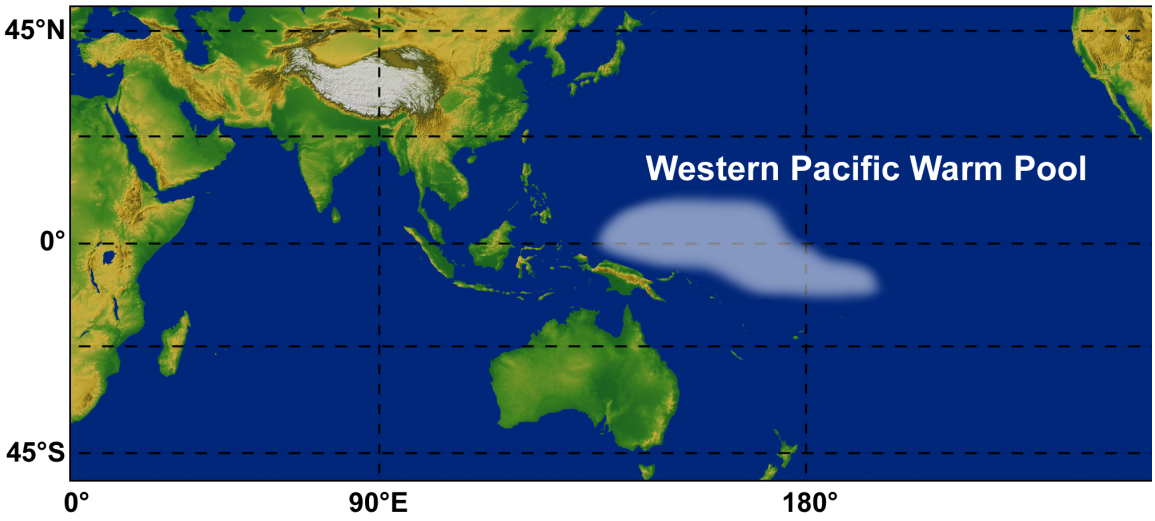

Figure 3.1:
West-Pacific Warm Pool location.

In particular, we are interested in perturbing real initial data available from the TAO array [42]. The TAO project aims at studying the exchange between tropical oceans and the atmosphere, source of phenomena such as ENSO (El Niño Southern Oscillation), and it provides data often used in many numerical simulations (see the TAO El Niño web-page http://www.pmel.noaa.gov/tao/elnino/simulation.html). These data correspond in general to profiles close to mixing-layer configurations, that have been analyzed in [2], [12], [54]. From these studies, one can conclude that by starting from initial conditions close to mixing-layer profiles it is possible to reach a well-developed surface turbulent mixing layer within two days, and mathematical stable equilibria within two months approximately. Here, as in [10], we are mainly interested in analyzing whether the formation of a homogeneous mixing layer first, and then of theoretical equilibria, are reachable even starting from initial conditions far away either from mixing-layer profiles and steady state solutions, within the respective characteristic times.

To obtain the actual initial profiles, we approximate the data measured at 0^oN, 165^oE by a linear interpolation, and we largely perturb the density at the surface, leaving unchanged the velocity profiles. We consider a warming flux acting on the sea-surface in accordance with [22], so that the only turbulence source is the wind stress. All the numerical experiments are grid-size and time-step independent, in the sense that the results remain practically unchanged as Δz and Δt decrease.

3.2.1 Case 1: Mixed layer induced by wind stress in absence of convection

In this test, we consider a perturbation of the initial conditions corresponding to the TAO's data for the 15th June 1991. The studied layer depth is 100 m. The initial profiles are displayed on Figure 3.2. The initial zonal velocity presents a westward current at the surface and, below it, an eastward undercurrent whose maximum is located at about - 55 m. Deepest, we observe a westward undercurrent. The initial meridional velocity presents a southward current whose maximum is located at about - 90 m. The initial density presents at the surface (first 20 m) a strong negative deviation of the original data, in order to move away the density profile from a (homogeneous) mixing-layer configuration. Physically, we are in absence of convection, since the initial density profile has negative derivative along the water column, and by the perturbation we are simulating an important initial increase of heating or precipitation phenomena. At the surface, we impose a zonal wind equal to 8.1 m s^{-1} (eastward wind) and a meridional wind equal to 2.1 m s^{-1} (northward wind). We consider a surface heat flux equal to -10^{-6} kg m^{-2} s^{-1}, which is consistent with the observations of Gent [22].

The formation of a well-developed mixing layer is achieved by integrating the various models for a time $\mathcal{T}$ = 192 hours (8 days). The grid spacing is Δz = 5 m and the time step is Δt = 60 s. The corresponding numerical results are displayed on Figure 3.3. We consider hereafter a standard definition of mixed layer (*cf.* [57], [51]), that states that the base of the mixed layer is the depth at which the density changes by 0.01 kg m^{-3}. The final density profile displays a similar mixed layer for $R213$, $R23$ and $R224$ models of about 20 m, in agreement with the observations reported by [4]. Furthermore, the pycnocline simulated by the three models is similar. In the upper oceanic layer, the surface currents for $R213$ and $R224$ models show almost the same behavior, while the $R23$ model underestimates these profiles, simulating a weaker surface current. Anyway, we notice an increase in the zonal and meridional surface currents in comparison with the initial profiles, which is in agreement with the application of a north-easterly wind. The surface current behavior can be explained by the final viscosity and diffusivity values, displayed on Figure 3.4 for all models, where in particular we observe that $R23$ model produces the strongest viscosity and diffusivity, and this mitigates the effect of surface winds.

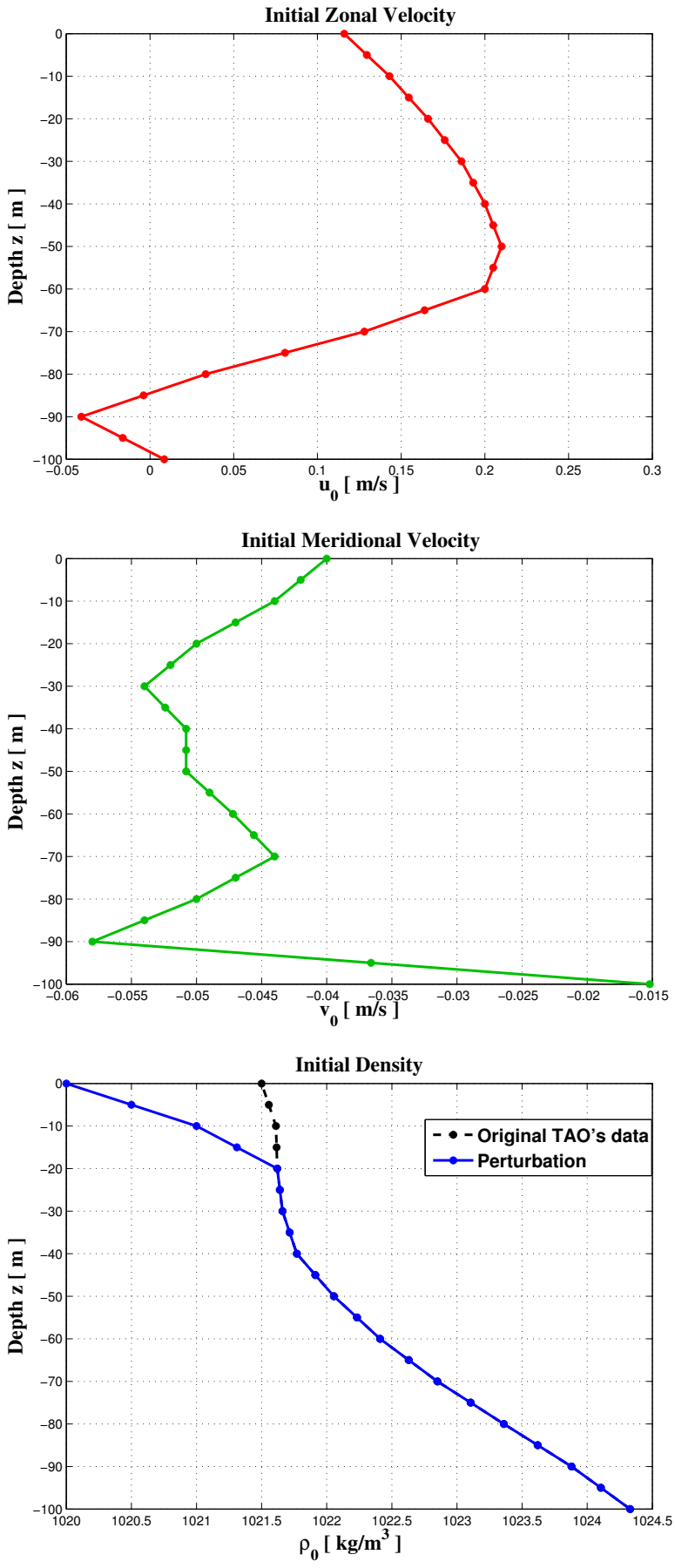

Figure 3.2:
Case 1: initial zonal velocity, meridional velocity and density profiles.

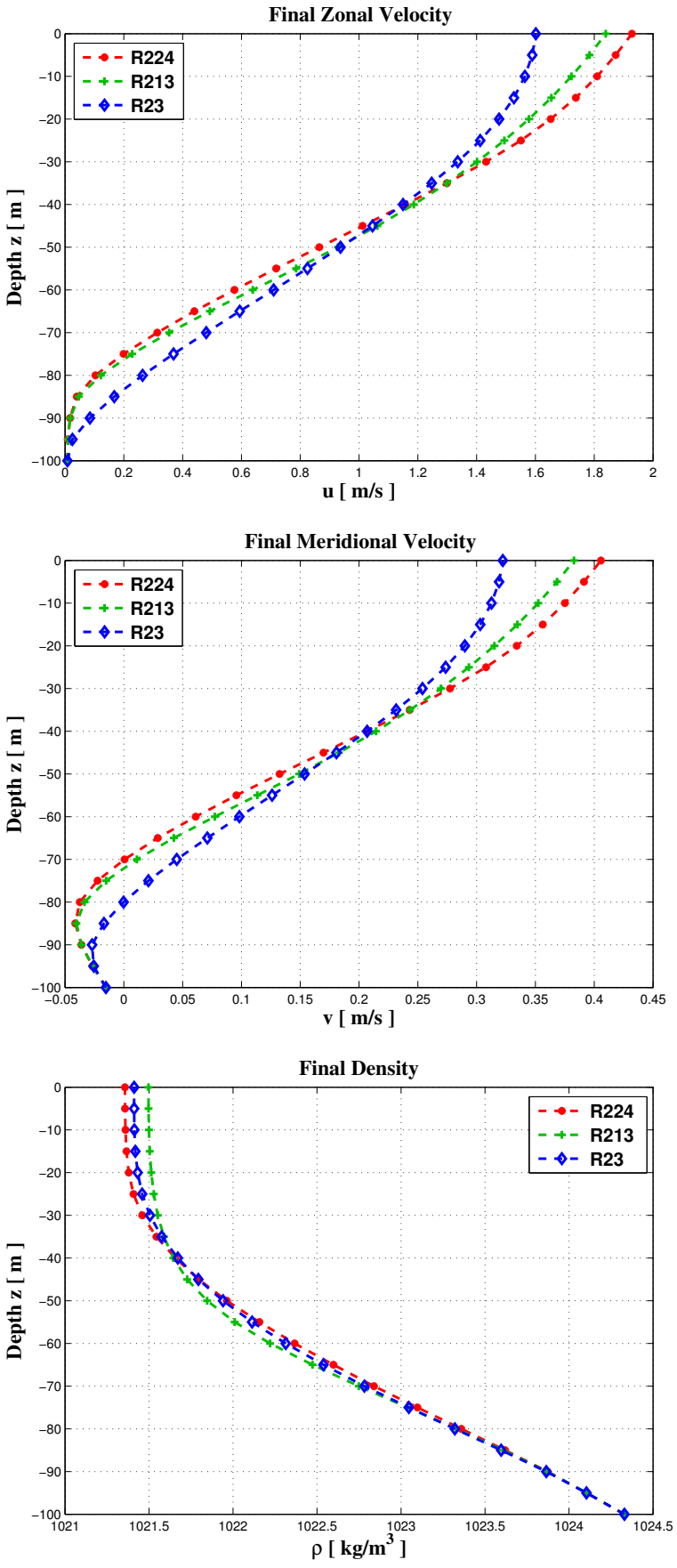

Figure 3.3:
Case 1: mixing-layer zonal velocity, meridional velocity and density profiles for models $R224$, $R213$ and $R23$.

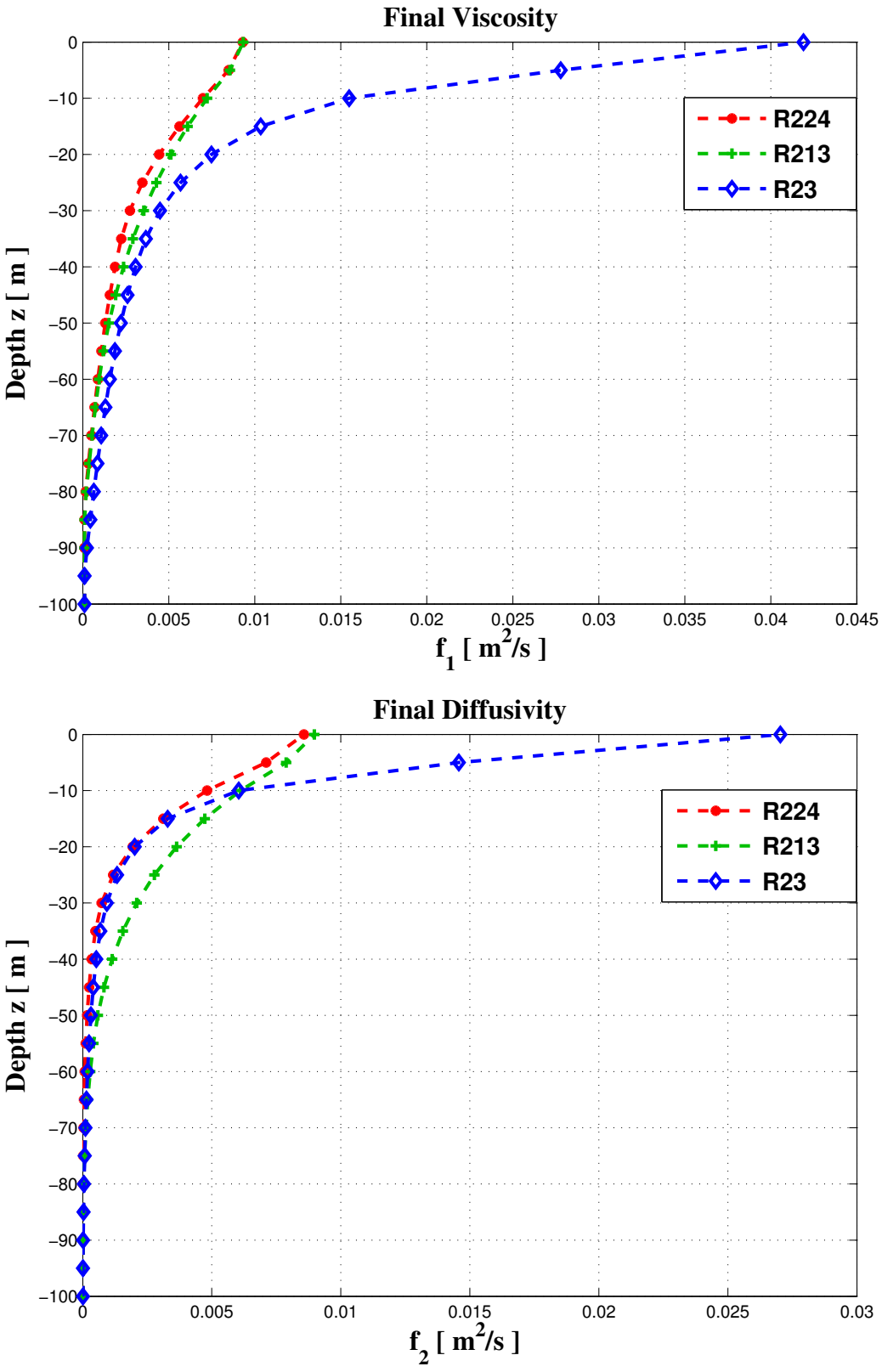

Figure 3.4:
Case 1: mixing-layer viscosity and diffusivity for models $R224$, $R213$ and $R23$.

3.2.2 Case 2: Mixed layer induced by wind stress in presence of convection

The code is initialized with a perturbation of the 15th November 1990 TAO's data (see Figure 3.5). The studied layer depth is 100 m. The initial zonal velocity profile displays an eastward current all along the water column, whose maximum is located at the sea-surface. The initial meridional velocity displays a southward current whose maximum is located at about 40 m of depth. The initial density profile displays at the surface (first 20 m) a strong positive deviation of the original data, in order to move away the density profile from a (not-homogeneous) mixing-layer configuration, and to create a deep (first 50 m) significant surface zone of negative initial gradient Richardson numbers. So, we are in presence of convection, where convection phenomena are in particular linked to physical processes such as the cooling of surface waters or evaporation. Note that the presence of static instabilities zones in the density profiles can be detected with a certain frequency in the TAO's data. We impose at the surface a zonal wind equal to 7.3 m s^{-1} (eastward wind) and a meridional wind equal to 2.1 m s^{-1} (northward wind), and we consider a surface heat flux equal to -10^{-6} kg m^{-2} s^{-1}, as in Case 1.

In Figure 3.6, we display the initial gradient Richardson number, that is effectively negative for the first 50 m of depth. This fact is reflected on the initial diffusivities of the various models, as shown in Figure 3.7, where in particular we observe negative values for models $R213$ and $R23$, while for model $R224$ we always have positive values. Physically, negative diffusivity can not exist, so we can not use here $R213$ and $R23$ models in their original formulations (see equations (1.17) and (1.18)), described in [49] and [22]. In practice, ocean modelers bypass this problem by extending the eddy diffusivities to these regions with positive constant values. Usually, a limited viscosity with typical value of 10^{-2} m^2 s^{-1} (*cf.* [58]) is applied to modify the Pacanowski-Philander and Gent models, in order to handle static instabilities. We compare hereafter the numerical results given by the Bennis et al. model $R224$ with the ones of the modified Pacanowski-Philander $R213$ and Gent $R23$ models. The Bennis et al. model $R224$ presents the advantage that it can be used here without needing any additional parameter, which is an important feature in situations where we have to simulate different turbulent regimes. The large value displayed by the initial $R224$ diffusivity corresponds to a negative gradient Richardson number near to its singularity, that is at $R = -0.2$.

The formation of a well-developed mixing layer is achieved by integrating the various models for $\mathcal{T} = 48$ hours (2 days). The grid-spacing is $\Delta z = 5$ m and the time-step is $\Delta t = 60$ s. The results are displayed on Figure 3.8. In particular, the final density profiles show a statically stable configuration, where the density increases with the depth. We observe that the Bennis et al. model $R224$ has approximately the same behavior of the modified PP model $R213$, but it performs a smoother and faster transition from static instabilities to a homogeneous mixed layer. In fact, it produces a mixed layer of 75 m, at least 10 m deeper with respect to the modified Gent model $R23$, i.e. the scheme that reacts slower. In any case, the application of a warming flux at the surface permits to stabilize the water column, creating a well-developed mixing layer even for initial condi-

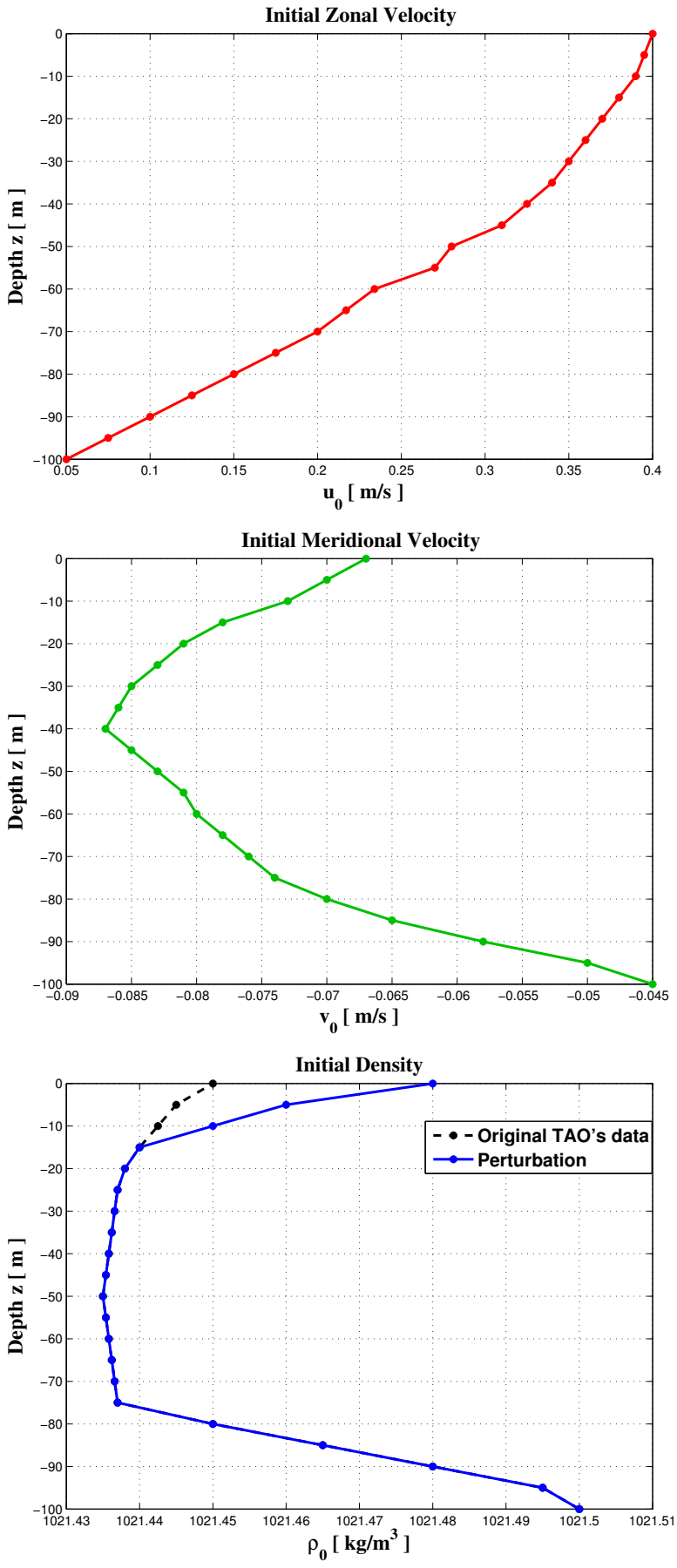

Figure 3.5:
Case 2: initial zonal velocity, meridional velocity and density profiles.

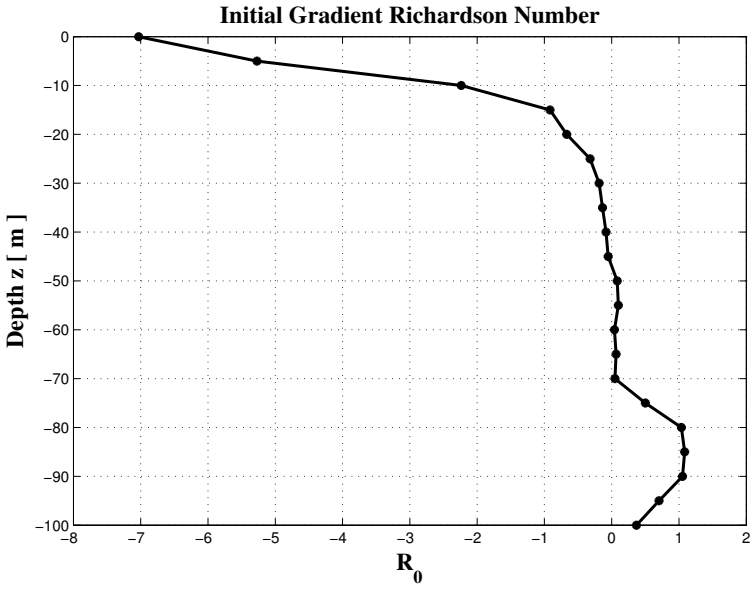

Figure 3.6:
Case 2: initial gradient Richardson number.

tions that present strong and deep vertical instabilities. Also, we notice an increase in the zonal surface current, by applying an eastward wind at the surface ($u_a > 0$). At the same time, an efficient northward wind at the surface ($v_a > 0$) causes an increase in the meridional surface current. These results are in agreement with the physical reality. As for the diffusivity, a simple calculation shows that the modified Pacanowski-Philander and Gent models limit the diffusivity respectively to 10^{-2} and 3×10^{-3} (units: $m^2\ s^{-1}$). During the computation, the Bennis et al. model is able to automatically adjusts the diffusivity, reducing the initial peak until converging to a range between 10^{-4} and 10^{-2} (units: $m^2\ s^{-1}$), which is in agreement with Osborn and Cox [48]. By estimating the diffusivity with measurements of very small scale vertical structures, they have shown that it fits in the range [$10^{-6}\ m^2\ s^{-1}$; $10^{-1}\ m^2\ s^{-1}$] in the studied region, i.e. the West-Pacific Warm Pool.

To sum up, Case 1 and 2 show that the analyzed algebraic MLM seem to have good stability properties in finite-time for warming surface fluxes, and that they provide accurate physical predictions of mixing-layer profiles, even with relatively large perturbations of the data, remaining in the respective characteristic times of formation.

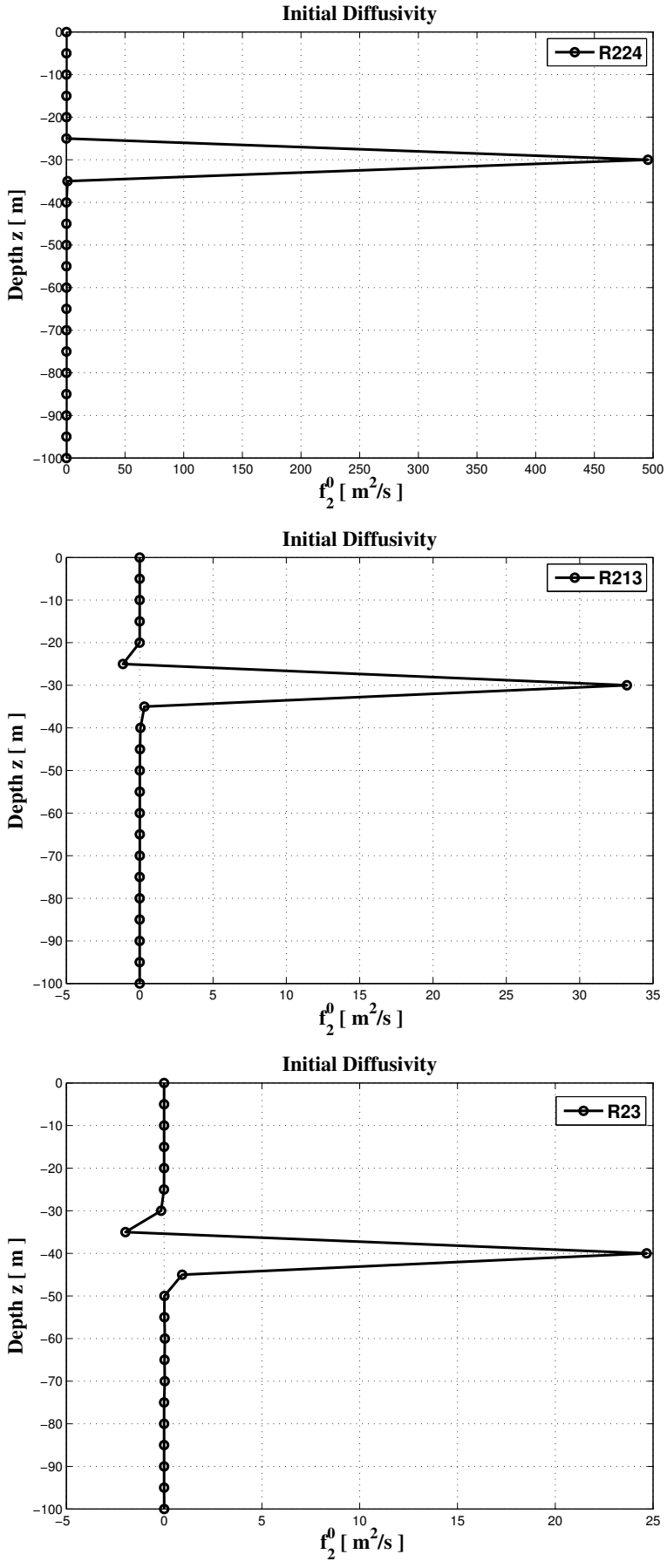

Figure 3.7:
Case 2: initial diffusivity for models $R224$, $R213$ and $R23$.

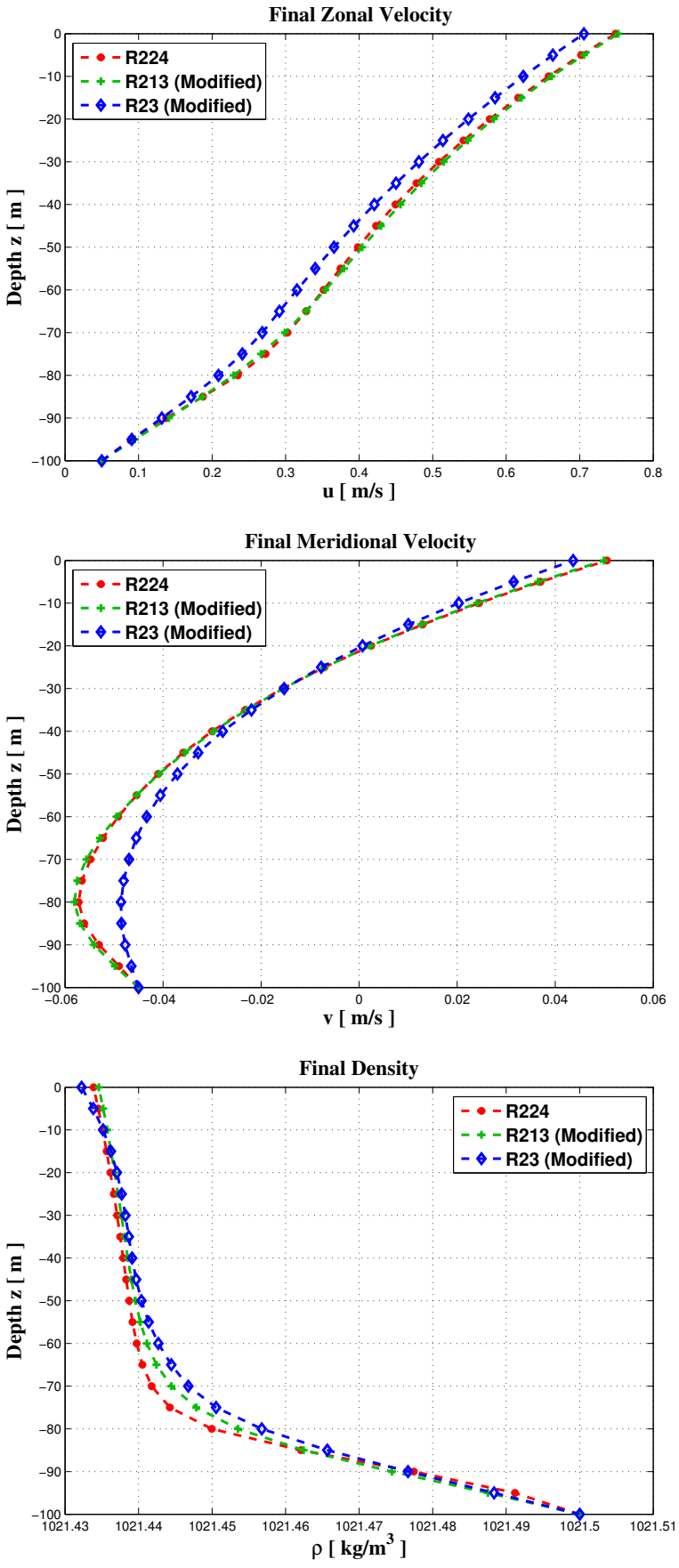

Figure 3.8:
Case 2: mixing-layer zonal velocity, meridional velocity and density profiles for models $R224$, $R213$ (Modified) and $R23$ (Modified).

3.2.3 Case 3: Analysis of asymptotic stability of discrete equilibria

In this case, we investigate the asymptotic behavior of algebraic turbulent MLM by numerical simulations. Firstly, we are interested in analyzing whether the formation of theoretical equilibria are reachable even starting from initial conditions far away either from mixing-layer profiles and steady-state solutions, by using the same initial data of Case 1 and 2.

Starting with the perturbed initial conditions of Case 1 (see Figure 3.2), and the same boundary conditions, we integrate the various models for $\mathcal{T} = 10\,000$ h (about 14 months), with $\Delta z = 5$ m and $\Delta t = 1$ h, to obtain the steady states of the flow. In practice, the discrete unsteady solutions corresponding to time $\mathcal{T} = 10\,000$ h change very little as time increases, so we consider them as steady solutions. In Figure 3.9, we can notice the formation of linear steady profiles for velocity and density, conforming to the theoretical expectations (*cf.* [2]). Similar numerical results are obtained for $R213$ and $R224$ models, while $R23$ model diverges from these results in all the water column. In Figure 3.10, we can observe for all models a monotonic numerical convergence to the steady states, corresponding to rather high levels of turbulent viscosity and diffusions due to the dissipative nature of the equations of the models. Model $R23$ reaches first a stable equilibrium (after about 3 000 hours, i.e. 4 months approximately), since it provides stronger eddy viscosity and diffusivity, as suggested by Figure 3.4. Here, we compute the residual values as:

$$r^n = \left[\sum_{i=0}^{N} |u_{z_i}^{n+1} - u_{z_i}^n|^2 + |v_{z_i}^{n+1} - v_{z_i}^n|^2 + |\rho_{z_i}^{n+1} - \rho_{z_i}^n|^2 \right]^{1/2},$$

and we refer to a stable equilibrium when $r^n < 10^{-6}$. Collecting data at time $\mathcal{T} = 10\,000$ h implies to consider a subsequent relaxation time, until to obtain $r^n < 10^{-10}$ for all models. This shows the non-linear stability of equilibrium solutions, that act as point-wise attractors, whenever we apply a warming flux at the surface as in this case. In particular, the steady states attract configurations corresponding to mixing layers, that appear as intermediate transient states reached by the asymptotic evolution of the flow to mathematical equilibria.

Also to obtain the steady states of the flow for the perturbed initial conditions of Case 2 (see Figure 3.5) and the same boundary conditions, we propose to integrate the various models for $\mathcal{T} = 10\,000$ h (about 14 months), with $\Delta z = 5$ m and $\Delta t = 1$ h. Recall that to apply $R213$ and $R23$ models in this case, where we have to handle initial negative gradient Richardson numbers, we must modify them by imposing a limited eddy viscosity as in Case 2. This forces the so-modified models to switch to positive gradient Richardson number during the computation to reach the theoretical equilibria. It implies that for all models considered the theoretical equilibrium solutions will be unique, as shown in Section 1.4.1. Remarkable is the fact that $R224$ model does not need any adjustment in order to ensure the uniqueness of the theoretical equilibria, to which the discrete numerical

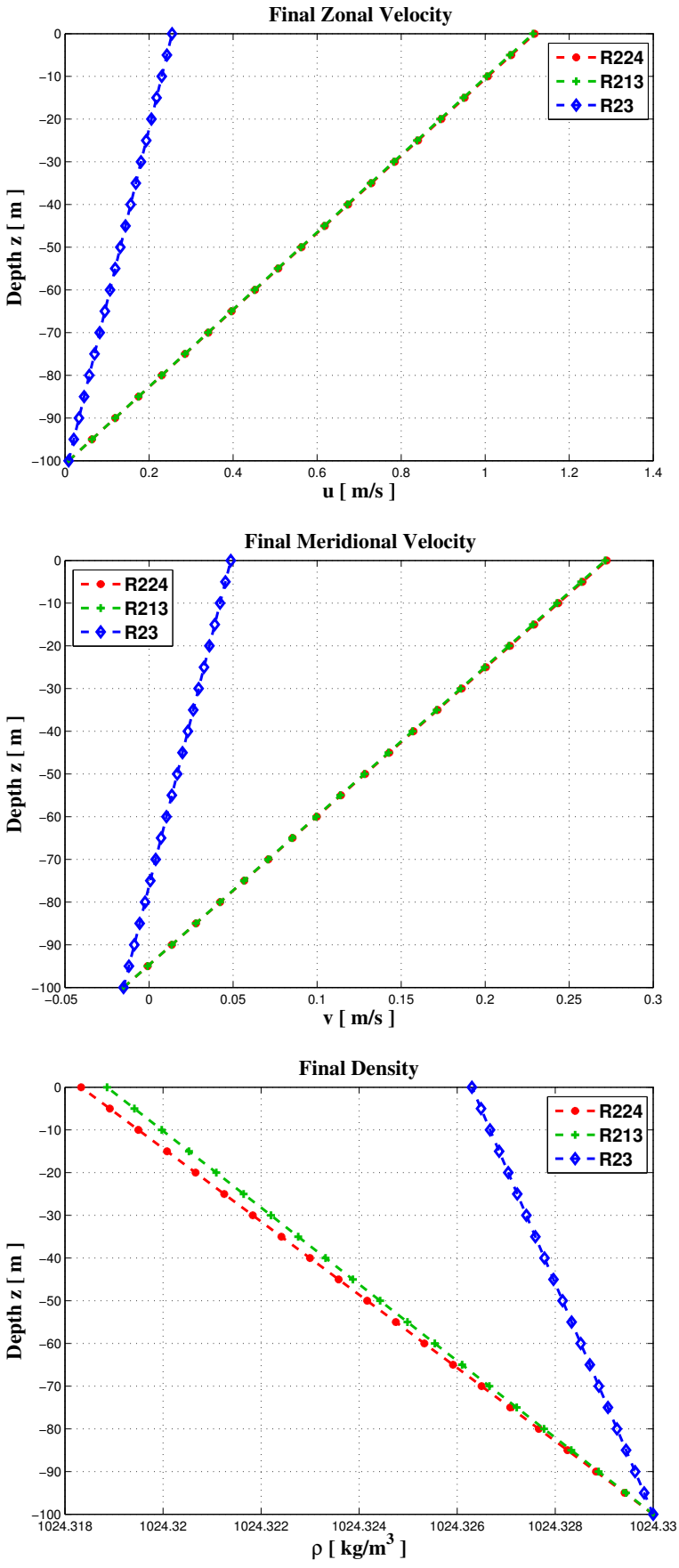

Figure 3.9:
Case 1: steady zonal velocity, meridional velocity and density profiles for models $R224$, $R213$ and $R23$.

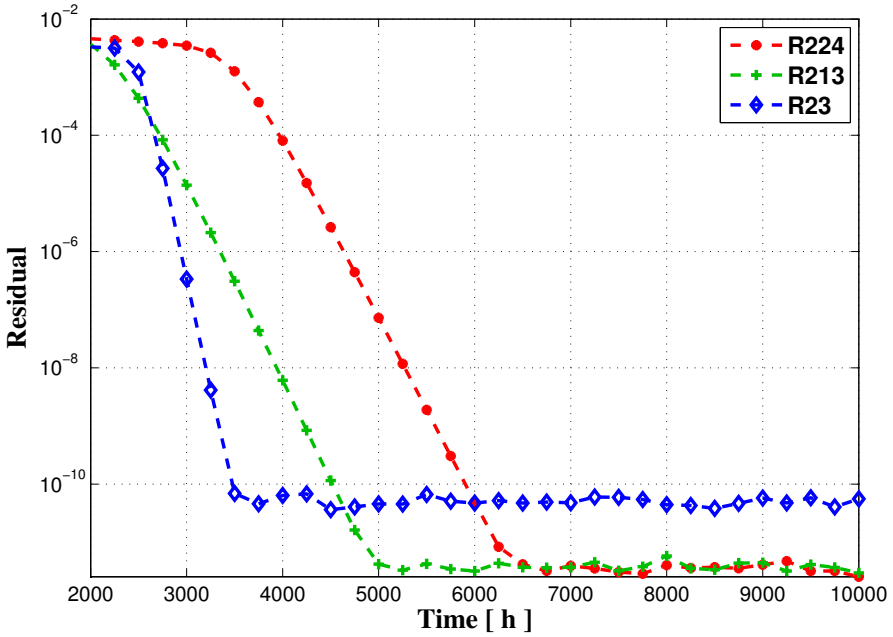

Figure 3.10:
Case 1: temporal evolution of residual values for models $R224$, $R213$ and $R23$.

equilibria will converge. In Figure 3.11, we observe that we obtain linear steady profiles for velocity and density, conforming to the theoretical expectations (*cf.* [2]). In Figure 3.12, the residual values display a good monotonic numerical convergence to the steady states. So, although physically stable equilibria correspond to positive gradient Richardson numbers, even initial conditions that present strong and deep vertical instabilities could asymptotically converge to those equilibria, i.e. these initial conditions too are in the range of attraction. We conclude that mixing-layer configurations act attracting the perturbed initial conditions in time scales of the order of several days, in agreement with the physics of the problem, and asymptotically evolve to the theoretical equilibria in time scales of the order of several months.

To further validate the stability properties for discrete equilibria, we propose another numerical test, where we directly perturb the equations of the models. We initialize the code with the 17th November 1991 original TAO's data (see Figure 3.13). The studied layer depth is 100 m. The initial density profile displays an instability zone between - 30 m and - 50 m, that corresponds to negative initial gradient Richardson numbers. As confirmed by Case 2, this is not an isolated situation. We directly apply the Bennis et al. model $R224$, that is more suitable to this kind of situation, as we have already seen. We impose the boundary conditions $u_a = 11.7$ m s^{-1} (eastward wind), $v_a = 0.4$ m s^{-1} (northward wind) and $Q_\rho = -10^{-6}$ kg m$^{-2}\cdot$ s^{-1} (heat flux). We set $\Delta z = 1$ m and $\Delta t = 1$ h. We consider the case $D_\rho = 0$ m s^{-2}, $D_u = D_v = D = constant$, with the following values: $D = 10^{-6}$ m s^{-2}, $D = 0$ m s^{-2}, where we recall that these quantities have been

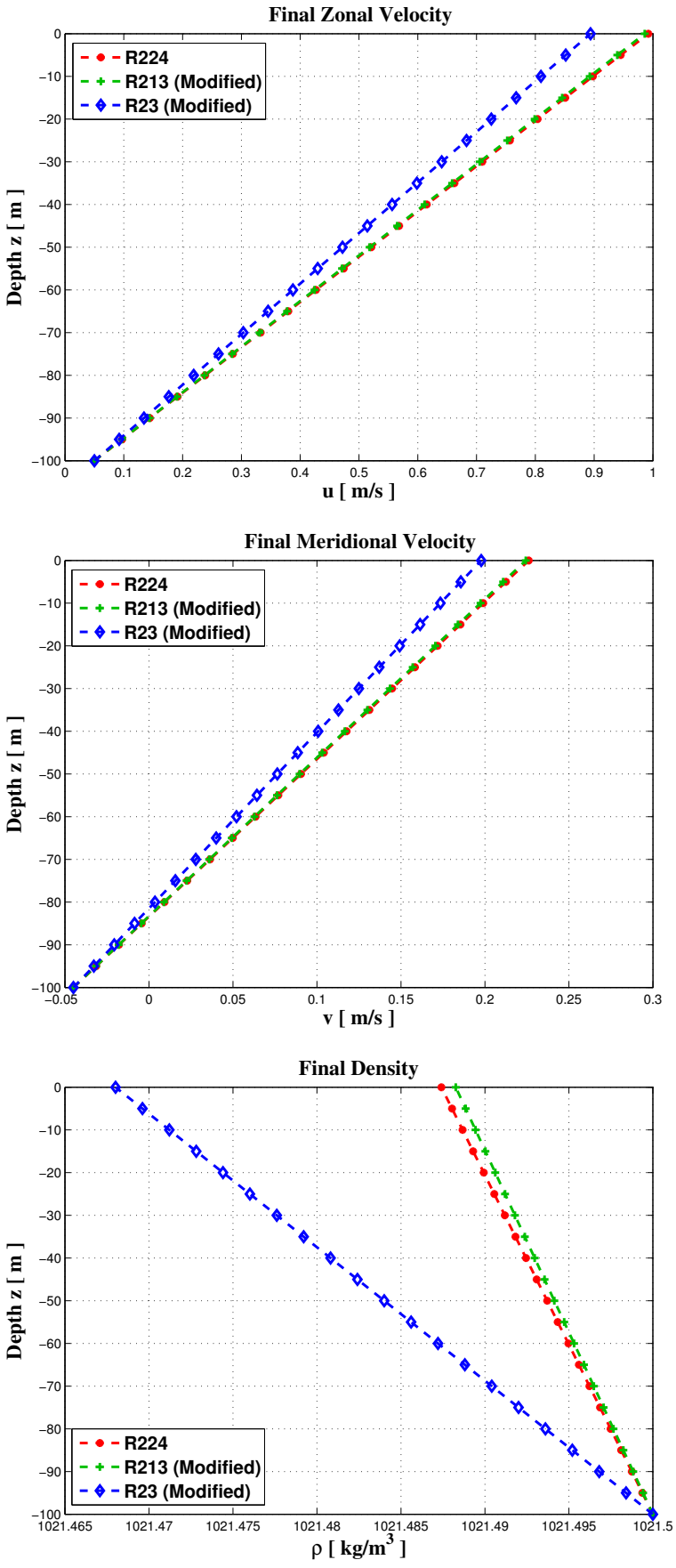

Figure 3.11:
Case 2: steady zonal velocity, meridional velocity and density profiles for models $R224$, $R213$ (Modified) and $R23$ (Modified).

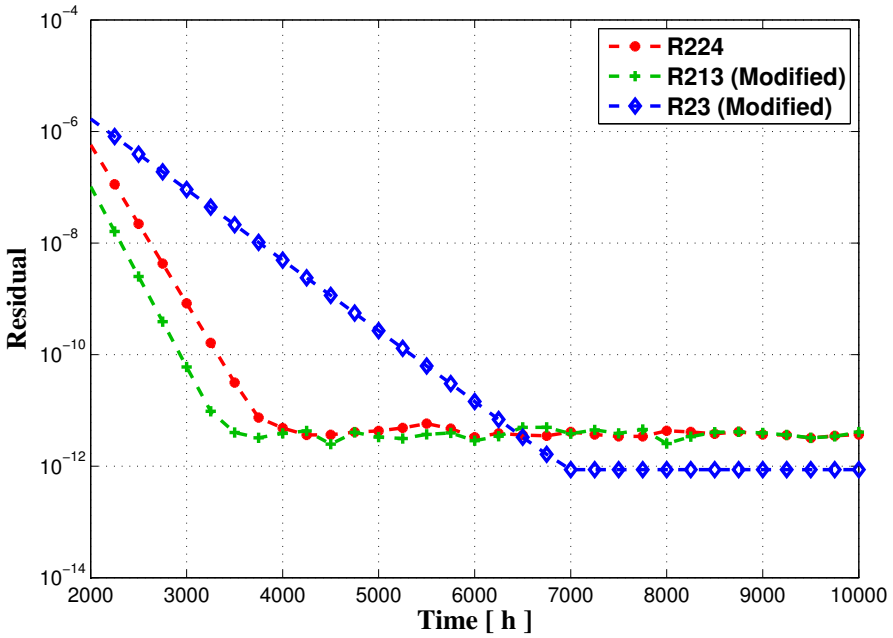

Figure 3.12:
Case 2: temporal evolution of residual values for models $R224$, $R213$ (Modified) and $R23$ (Modified).

introduced in the perturbed model (1.21). The results are presented in Figures 3.14 and 3.15. As the equilibrium solutions are unique in the case of model $R224$, we can compute the theoretical solutions and compare them with the numerical ones. In Figure 3.14, at first we observe that the theoretical and the numerical solutions are very close. Also, for $D = 0$ m s^{-2} we effectively obtain linear profiles for both equilibrium velocity and density, as in [2]. For $D = 10^{-6}$ m s^{-2} (and in general for small perturbation of D from 0 m s^{-2}) the density does not practically change its linear profile, while the zonal and the meridional velocities are largely changed. Looking at the residual values in Figure 3.15, we can observe in both cases a fast monotonic numerical convergence to the steady state.

We also test the convergence order of the numerical iterates to the continuous equilibria, as stated in Corollary 2.15. Note that this result is based upon the hypothesis that the time iterates lie in a small enough neighborhood of the equilibrium. Our results are presented in Table 3.1, where we confirm the thesis of Corollary 2.15: The time iterates of the numerical scheme approximate, for large enough time, the continuous equilibria, with order 1, in the sense that $\|\mathbf{U}^n_\Delta - \mathbf{U}^e\|_{L^2(I)} \simeq C\,\Delta z$ for large enough n. Actually, the convergence order deteriorates as Δz decreases, due to the error term coming from the time discretization in estimate (2.42).

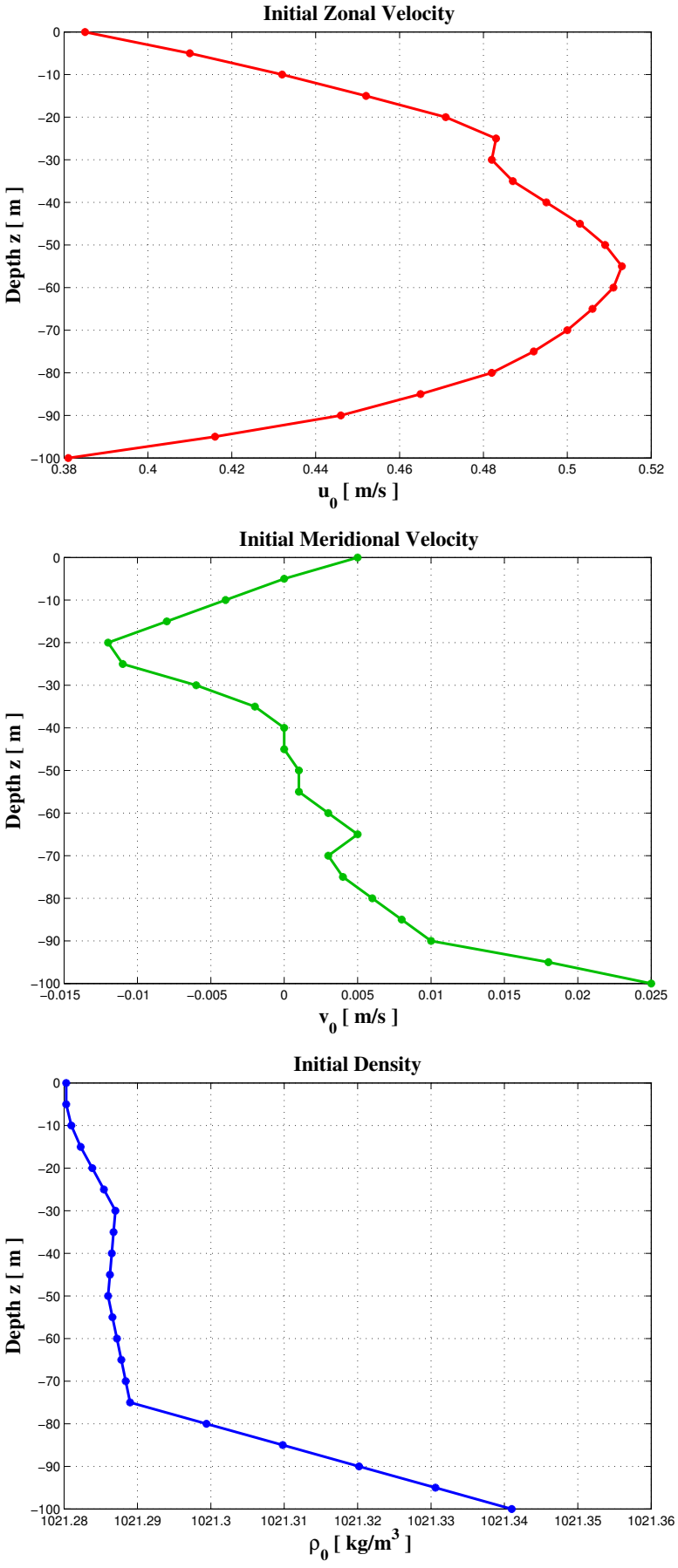

Figure 3.13:
Case 3: initial zonal velocity, meridional velocity and density profiles.

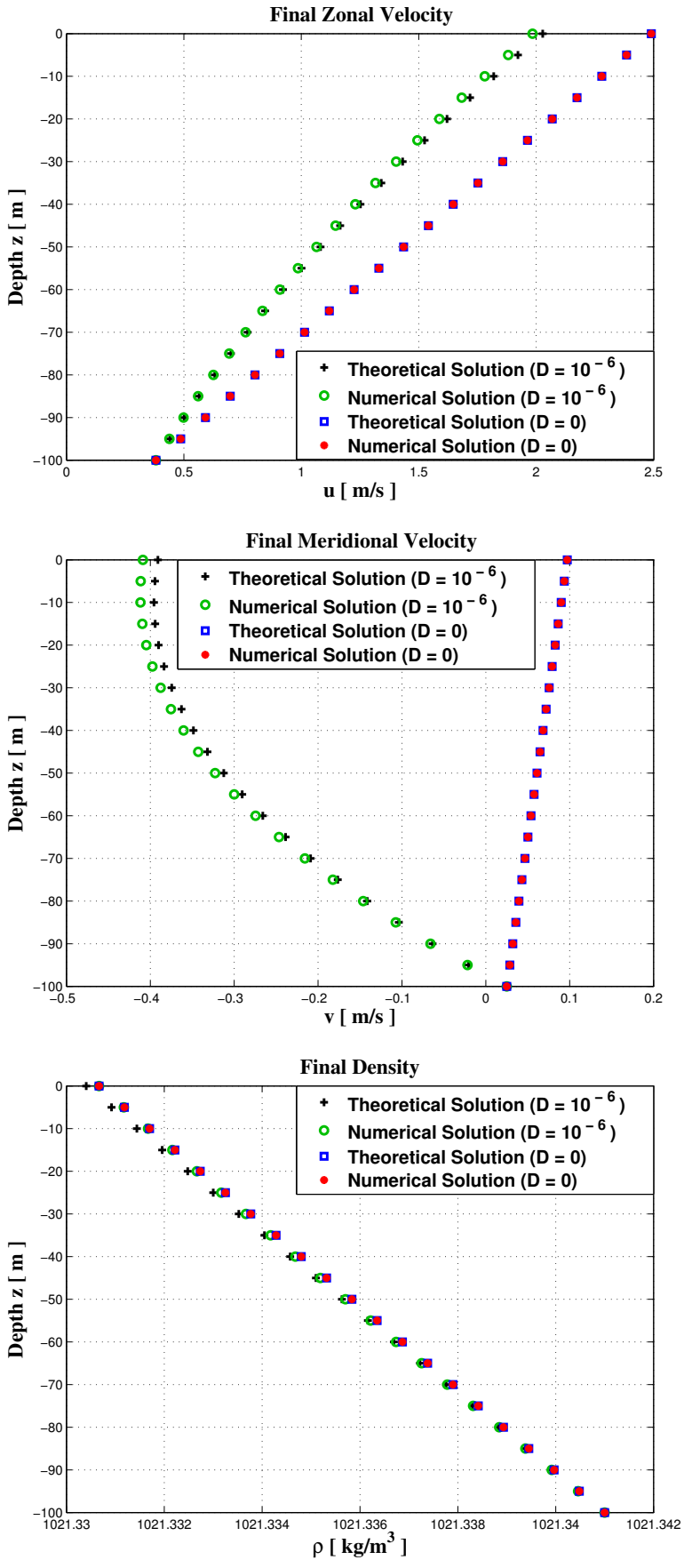

Figure 3.14:
Case 3: steady zonal velocity, meridional velocity and density profiles for models $R224$ (theoretical vs. numerical equilibria).

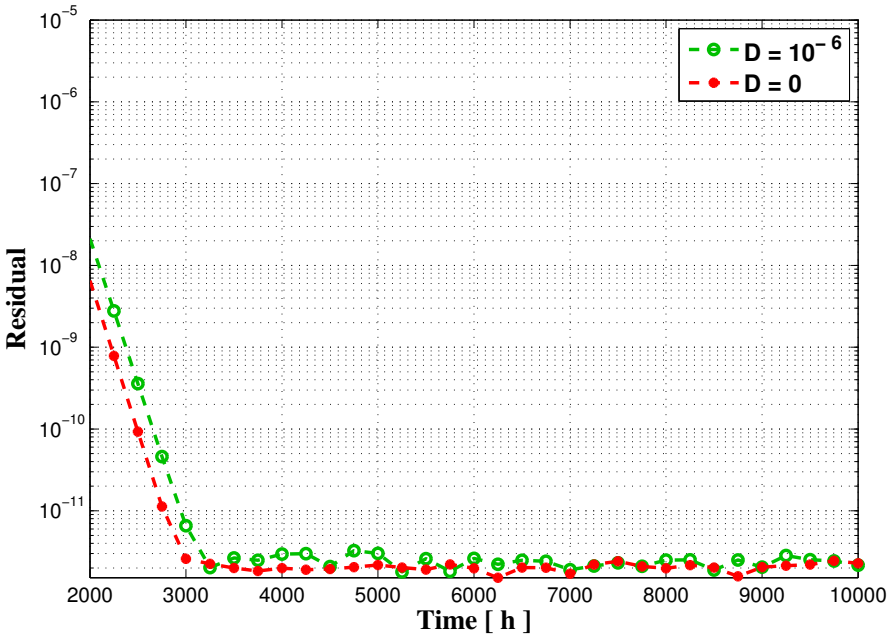

Figure 3.15:
Case 3: temporal evolution of residual values for model $R224$.

	Final time $\mathcal{T} = 10\,000$ h, $D = 10^{-6}$ m s^{-2}	
Δz (m)	$\|\mathbf{U}^n_\Delta - \mathbf{U}^e\|_{L^2(I)}$	Convergence order
8	0.7895	-
4	0.3893	1.02
2	0.2048	0.93
1	0.1149	0.83
0.5	0.0733	0.65

Table 3.1:
Case 3: estimated error and convergence order for model $R224$.

Remark 3.1. *In all numerical experiments, we have noticed that the convergence to steady states takes time of the order of several months. This time scale is much larger than that needed to generate a typical homogeneous mixed layer, which is of the order of a few days by applying steady boundary data. This may explain why these equilibria profiles are not found in real surface layers of tropical oceans, as the boundary data usually change in time scales of the order of hours. Even the formation of a homogeneous mixed layer is not possible if these data change too fast. From the numerical point of view, the investigation of the asymptotic behavior of algebraic turbulent MLM has been useful on one hand to show the effective good stability properties of these schemes for warming surface fluxes and, on another hand, to prove that the equilibria states behave as point-wise attractors for intermediate transient mixing-layer configurations, for which the analyzed models provide accurate physical predictions. In their turn, mixing-layer profiles act as "absorbing configurations" with characteristic times of a few days.*

3.2.4 Case 4: Analysis of finite-time stability with respect to 2D perturbations

We analyze here the finite-time stability of algebraic MLM with respect to 2D perturbations in tropical oceans. The strategy is described in Section 2.4. We solve the Primitive Equations (2.45)-(2.46), and we compare the corresponding numerical results with the ones of the algebraic MLM (1.21)-(1.22), with the Bennis et al. modeling (1.19) of the turbulent viscosity and diffusivity.

The Primitive Equations (2.45)-(2.46) are solved on the rectangular computational domain Ω, with a length $L = 3$ km, and a thickness $h = 100$ m, periodic in the horizontal direction. The grid spacing is $\Delta x = 15$ m and $\Delta z = 1$ m respectively in the horizontal and vertical directions. We perform two numerical simulations, respectively corresponding to physically unstable and physically stable initial conditions (inverse and favorable vertical density gradients). We set periodic horizontal perturbations of 1D (vertical) initial data, of the form:

$$u(t=0) = u_0(z) + \lambda\sigma(x), \quad \rho(t=0) = \rho_0(z) + \lambda\sigma(x) \text{ in } \Omega, \tag{3.1}$$

by choosing a small λ. It permits to set genuine 2D initial conditions for the current problem (2.45)-(2.46). The initial 1D zonal velocity (u_0) and density (ρ_0) profiles are taken from the TAO array. We use the software FreeFem++ [27] to compute the practical solution of problem (2.45)-(2.46).

Simulation 1

The initial 1D zonal velocity and density profiles are the same of Case 3 (see Figure 3.13), so that we have an instability zone below the ocean surface, where $\partial_z \rho > 0$. The initial fields are perturbed with random horizontal noise of small amplitude ($\lambda = 10^{-3}$) to start the convection.

We also apply the same boundary conditions of Case 3, i.e. we impose a warming surface flux $Q_\rho = -10^{-6}$ kg m^{-2} s^{-1}, and a zonal wind-stress $Q_u \simeq 10^{-1}$ m^2 s^{-2}. We integrate the 2D model for a final time $\mathcal{T} = 48$ h, with $\Delta t = 60$ s. After 48 h of integration lateral exchange between the convection site and the ambient fluid through advective processes (*cf.* [39]) is assumed to dominate. The lateral exchange can not be represented properly by our two-dimensional configuration and the integration is stopped. In order to perform a comparison with the results of the 1D model, we compute it with the same data, by neglecting the meridional velocity, which is usually smaller than the zonal one.

Figure 3.16 shows a comparison between the final zonal velocity and the final density computed by the 2D model (horizontally averaged), and the 1D model with $D_u = D = 10^{-7}$ m s^{-2}, and $D_u = D = 0$ m s^{-2}.

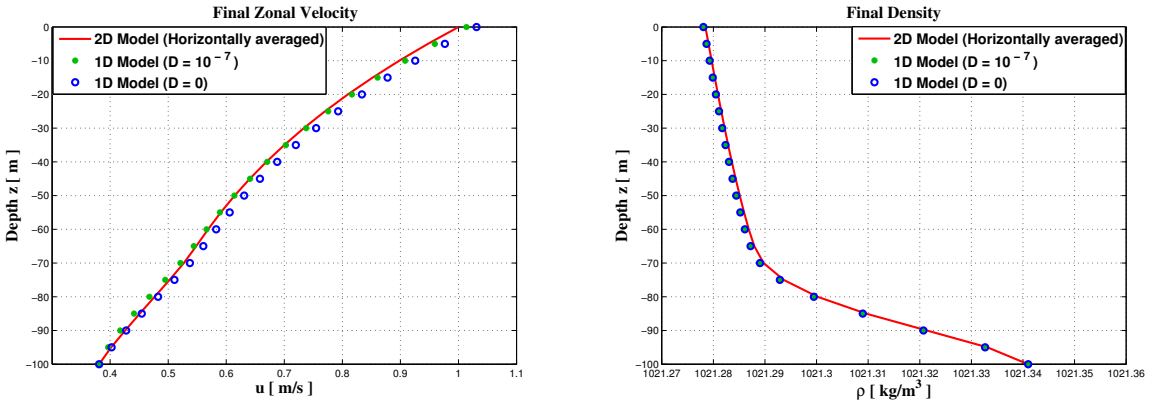

Figure 3.16:
Simulation 1: mixing-layer zonal velocity and density profiles (2D model vs. 1D model).

The order of magnitude for D is found by observing that it plays the role of a horizontal pressure gradient, that may compensate for a loss of incompressibility in the initial conditions. Indeed, it is computed by the well-known *Bernoulli's law* applied to the initial velocity field along flow lines:

$$\frac{1}{2}|\mathbf{U}(0)|^2 + p = C,$$

where C is a constant, and then:

$$|D| = |\partial_x p| = |u(t=0)\partial_x u(t=0)|.$$

From the final density profile, we observe the formation of a mixed layer (almost constant density) of about 70 m depth, by using either the 2D model or the 1D model with a zero and non-zero pressure gradient D. A pycnocline (high gradient of density) is formed immediately below, that is a characteristic density profile for a well-mixed layer.

The final fluid velocity and density obtained with the 2D model are horizontally homogeneous, even starting from 2D initial conditions (see Figure 3.17). Moreover, the vertical component of the velocity is almost zero. The final surface pressure assumes its values in the range $[-2 \cdot 10^{-7}, 2 \cdot 10^{-7}]$.

The results of Figure 3.16 stress that if we take into account a non-zero horizontal pressure gradient D in the 1D model, we barely improve the accuracy in the mixing-layer profiles, with respect to the mixing-layer profiles obtained with the 2D model. This not only shows the stability of the 1D model with respect to 2D perturbations, but also its accuracy to compute the mixing layer.

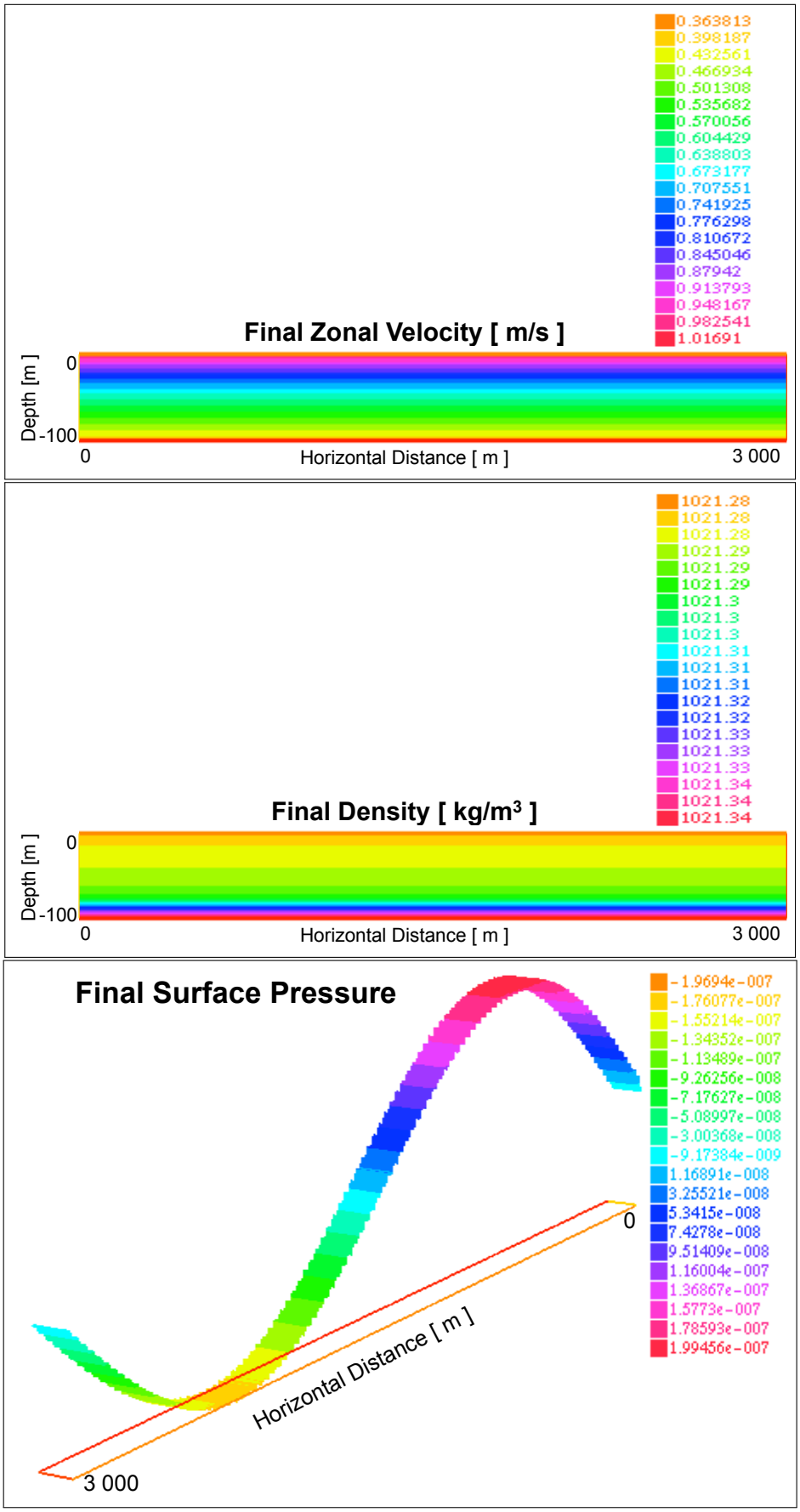

Figure 3.17:
Simulation 1: final zonal velocity, density and surface pressure (LES reference).

Simulation 2

The initial 1D zonal velocity and density profiles are the same of Case 1 (see Figure 3.2), so that this simulation corresponds to a stable initial density condition. The initial fields are perturbed with random horizontal noise of small amplitude ($\lambda = 10^{-3}$) to start the convection. We also apply the same boundary conditions of Case 1, i.e. we impose a warming surface flux $Q_\rho = -10^{-6}$ kg m^{-2} s^{-1}, and a zonal wind-stress $Q_u \simeq 10^{-1}$ m^2 s^{-2}. We integrate the 2D model for a final time $\mathcal{T} = 24$ h, with $\Delta t = 60$ s. In order to perform a comparison with the results of the 1D model, we compute it with the same data.

Figure 3.18 shows a comparison between the final zonal velocity and the final density computed by the 2D model (horizontally averaged), and the 1D model with the horizontal pressure gradient $D_u = D = 10^{-7}$ m s^{-2}, and $D_u = D = 0$ m s^{-2}.

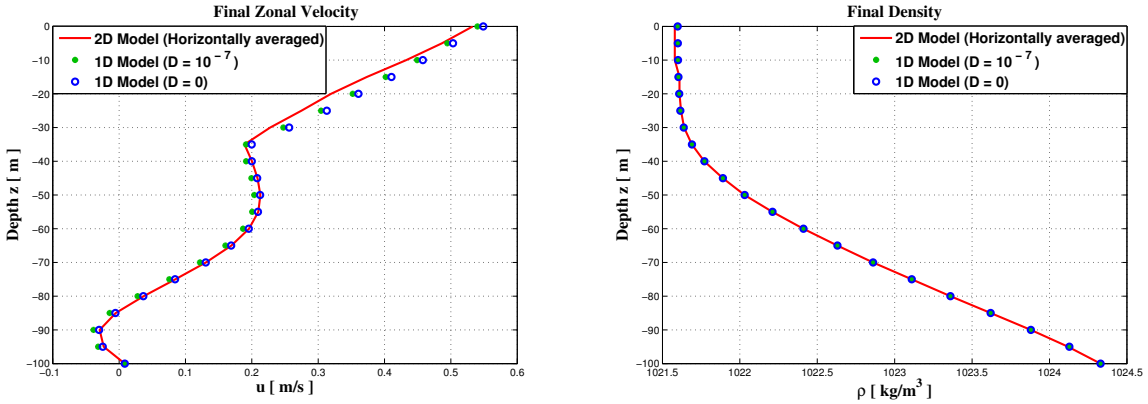

Figure 3.18:
Simulation 2: mixing-layer zonal velocity and density profiles (2D model vs. 1D model).

From the final density profile we observe the formation of a mixed layer of about 20 m depth, by using either the 2D model or the 1D model with a zero and non-zero pressure gradient D. A pycnocline is formed immediately below. This structure is quite similar to the one of Simulation 1, where the initial density presented an unstable configuration.

Again in this test, the final fluid velocity and density obtained with the 2D model are horizontally homogeneous (see Figure 3.19). Moreover, the vertical component of the velocity is almost zero. The final surface pressure assumes its values in the range $[-1 \cdot 10^{-3}, 1 \cdot 10^{-3}]$.

The results of Figure 3.18 stress that taking into account a non-zero horizontal pressure gradient in the 1D model does not improve the accuracy in the computation of the 2D mixing-layer profiles through the 1D MLM. Then, we could assert that the unsteady flow leading to mixing-layer configurations is also stable under 2D perturbations. The 1D model provide mixing-layer profiles on time scales of the order of a few days, which are accurate with respect to 2D perturbations of the initial conditions, and with respect to

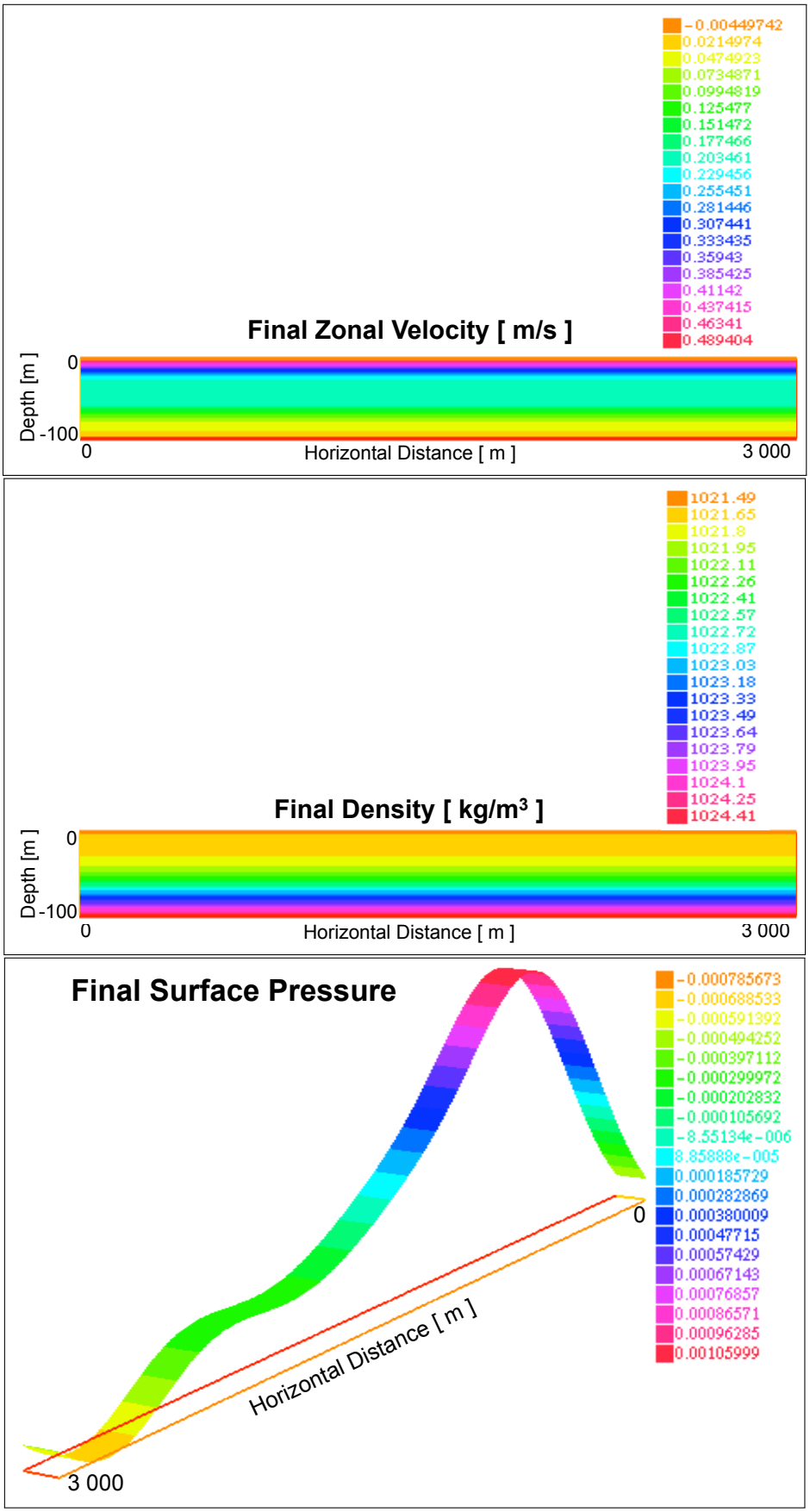

Figure 3.19:
Simulation 2: final zonal velocity, density and surface pressure (LES reference).

horizontal pressure gradients. We finally conclude that algebraic oceanic turbulent MLM applied to tropical seas bear excellent stability properties and provide good predictions of the formation of mixing-layer profiles and of flow equilibria, even with relatively large perturbations of the data.

3.3 Test 2: Arctic Ocean and Labrador Sea

In this section, we study the performances of oceanic turbulent MLM in various configurations pertaining to high latitudes of the Northern Hemisphere. In a first stage, we do inter-comparison of dynamics simulated by one of the models previously used with respect to more complex vertical (1D) mixing schemes, driven by wind forcing and/or cooling at the surface, by using the tools provided by the MIT general circulation model (MITgcm, [45]). Within the models already used, we choose to work with the Pacanowski-Philander model $R213$, as it gives similar results with respect to the Bennis et al. model $R224$, and it is the most used by physical oceanographers. Actually, we will use the modified version of $R213$, by limiting the eddy viscosities to 10^{-2} m^2 s^{-1} for all values of the gradient Richardson number smaller than the corresponding critical value in the present implementation of MITgcm. In this way, statically unstable stratifications are forced to return to a vertical stable stratification. To shorten the notation, we will denote hereafter the so modified version of the Pacanowski-Philander model simply by the acronym PP81. The other schemes to compare with are:

1. **KPP model of Large et al. (KPP)**. The more sophisticated K-Profile Parameterization is a first order turbulent closure scheme which models higher turbulent moments by means of a counter-gradient flux.

2. **Modified Level 2.5 model of Mellor and Yamada (MY82)**. In the present implementation of MITgcm, the turbulent kinetic energy is just parameterized, thus leading to an overall method of first order.

3. **Gaspar et al. model (GGL90)**. This is effectively implemented in MITgcm as a second order turbulent closure model.

In particular, we focus the attention on two situations of interest:

(a) Mixed layer induced by wind stress in the Arctic Ocean (see Figure 3.20).

(b) Deep mixed regime in the Labrador Sea (see Figure 3.21) driven by buoyancy loss at the surface.

To run these simulations, we use realistic initial conditions extracted from the WOA01 data (http://www.nodc.noaa.gov/OC5/WOA01/pr_woa01.html), and we prescribe constant surface wind forcing and buoyancy fluxes during all time integration.

This is obviously an idealized situation, but it gives some preliminary qualitative highlights on the impact of different parameterizations of vertical mixing in polar regions. Remarkable is the fact that the PP81 model is the one which gives inferior performances

Figure 3.20:
Arctic Ocean map.

Figure 3.21:
Labrador Sea location.

with respect to physical and observational expectations, while on the contrary the more sophisticated KPP model is the one which outperforms mixing by other models. Thus, in a second step, we decide to compare these two schemes in the context of a more meaningful 3D configuration focused on the Arctic Ocean, driven by realistic (CORE-II, 1958-2007) forcing (*cf.* [26]). We use a regional Arctic Ocean configuration of the MITgcm global grid, and we run a 3D coupled ocean - sea-ice model with the two different mixed-layer physics. The aim is to monitor the mixed-layer behavior in different seasons, and also the sea-ice concentration and thickness, and to analyze the sensitivity with respect to the different MLM.

3.3.1 Case 1: Impact of different parameterizations of vertical mixing

We present the numerical results on a systematic study that aims to compare the impact of different parameterizations of vertical mixing in northern polar oceanic areas.

(a) Mixed layer induced by wind stress in the Arctic Ocean

We use realistic initial conditions that correspond to the northern polar region of the Arctic Ocean. We select seven different coordinates in this area, whose latitudes range from 80.5^oN to 85.5^oN, and whose longitudes vary from 0.5^oE to 5^oW (anti-clockwise rotating), trying to distribute them well over the basin. We take into account the upper 1 km of the water column.

We consider the vertical profiles for the initial temperature and salinity extracted from the monthly averaged WOA01 *in-situ* data, corresponding to the period of September (typical condition of freezing). In order to get unique water-column vertical profiles, the selected data are horizontally averaged. The initial conditions are displayed in Figure 3.22, where we can discern the climatological profiles of potential temperature (Θ), salinity (S) and potential density (σ_0, normalized by subtracting 10^3 kg m^{-3}). The potential density is computed by using the accurate non-linear Equation Of State (E.O.S.) by McDougall et al. [41], as implemented in the MATLAB script contained in the utilities of MITgcm. Observe that the initial (potential) density profile does not present a mixed layer. An impulsive start is performed, i.e. the initial velocity condition is a zero velocity field. A Coriolis parameter $f = 1.4 \times 10^{-4}$ s^{-1} is considered for the rotational term, in accordance with [39]. The boundary conditions correspond to a constant wind stress of strong magnitude, much larger than the measured ones to force the formation of a mixed layer. Note that the simulations presented here do not contain any buoyancy effects, to isolate the action of wind forcing. A horizontal wind stress of 1 N m^{-2} is prescribed at the surface during the computation time. It corresponds to a zonal wind velocity of 32 m s^{-1} (eastward wind), i.e. to a violent storm of 11 Beaufort number.

A coarse vertical resolution is chosen to represent typical grids in numerical OGCM: the vertical grid spacing increases within 18 layers (18 Δz) from 10 m near the surface up to 100 m at 1 km depth. The various models are integrated for a relatively large

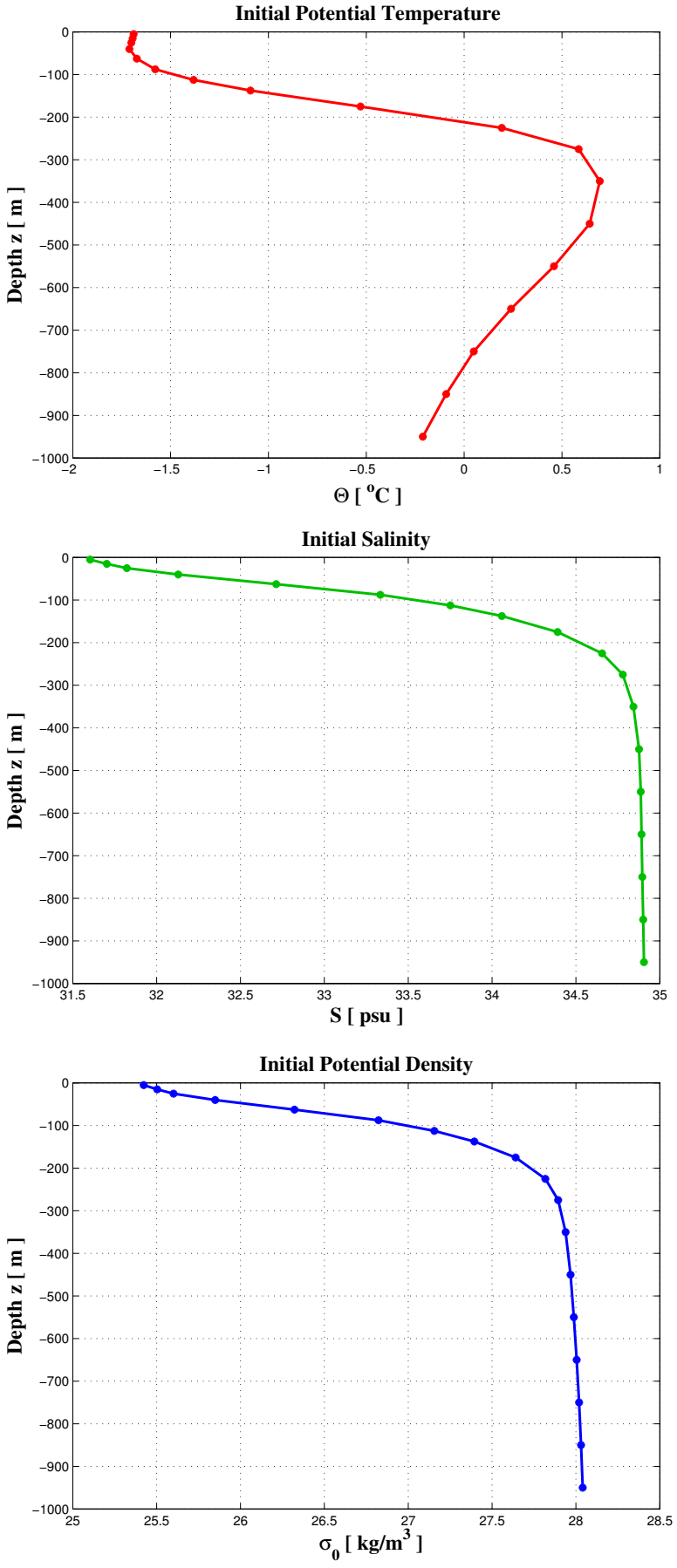

Figure 3.22:
Simulation (a): initial potential temperature, salinity and potential density profiles.

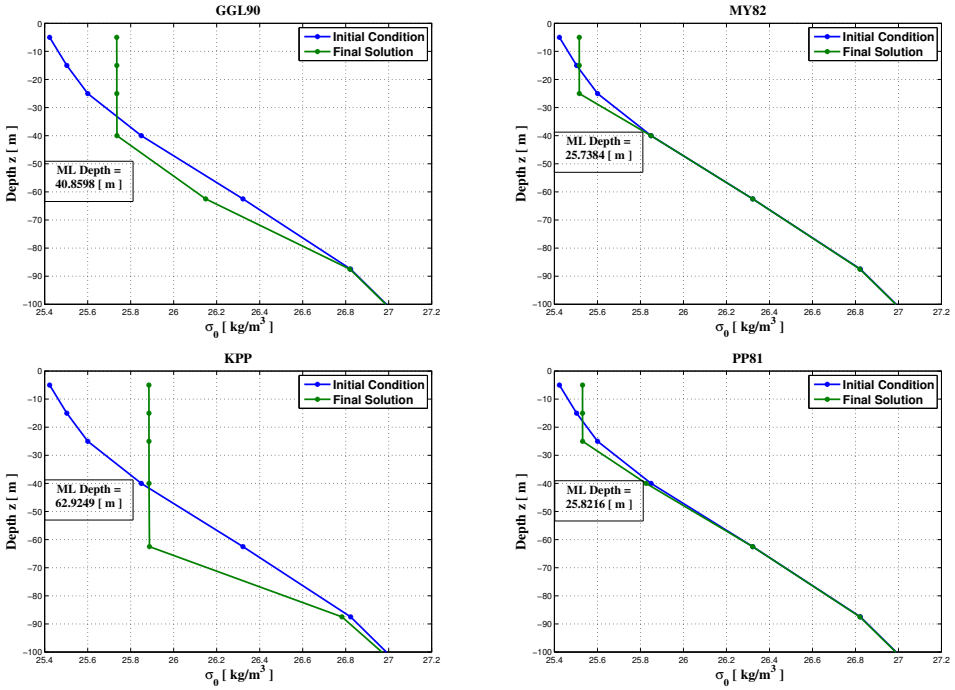

Figure 3.23:
Simulation (a): Comparison between initial and final potential density profiles.

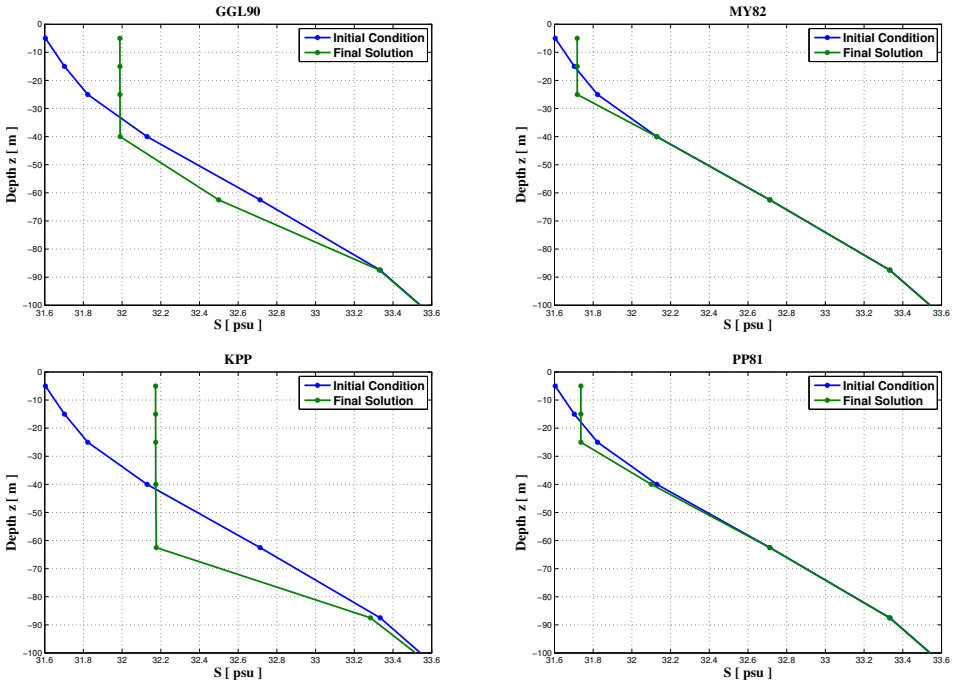

Figure 3.24:
Simulation (a): Comparison between initial and final salinity profiles.

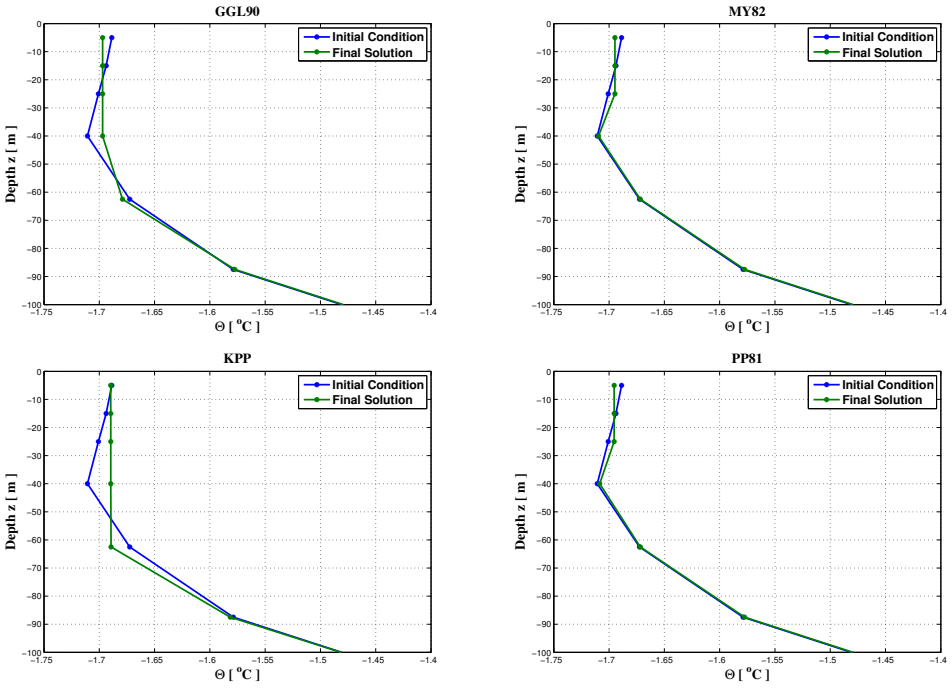

Figure 3.25:
Simulation (a): Comparison between initial and final potential temperature profiles.

time $\mathcal{T} = 10$ days with a time-step $\Delta t = 20$ minutes. We display the results for the upper 100 m of the water column. Figures 3.23, 3.24, 3.25 show respectively the final potential density, salinity and potential temperature. The hydrography is characterized for all models by the formation of a low-salinity ($S < 33$ psu) mixed layer, varying in depth depending on the model, overlying a cold (near freezing temperature) isothermal layer of the same thickness. In particular, the KPP model shows the deepest mixed layer, of about 63 m depth, the GGL90 shows a mixed layer of about 41 m depth, while the MY82 and PP81 models show the shallowest mixed layer, of about 26 m depth. Also, the latter show a certain vertical instability in the profile of final potential temperature. The upper cold mixed layer is followed by a cold halocline layer (CHL) down to the bottom of the studied water column, where the density change is dominated by increasing salinity. Below (not shown, as similar to the initial profiles), both Θ and S increase until a depth of about 250 m, both contributing to density variations. Warm water with $\Theta > 0$ ^{o}C is already found below 180 m, above temperature maxima at 280 m and 340 m separated by a well-mixed 60 m thick layer (see Figure 3.22). This is a physical stratification typical of the upper 1 km of the observed Arctic Ocean (*cf.* [55]).

(b) Deep mixed regime in the Labrador Sea driven by buoyancy loss at the surface

We use realistic initial conditions that correspond to the North-Atlantic Ocean region of the Labrador Sea, near 61^oN, 56^oW. For this test, we take into account the upper 2 km of

the water column, since we expect to obtain a deep mixed regime. Indeed, in this region, characterized by weak stratification and, in winter and early spring, exposed to intense buoyancy loss to the atmosphere, violent and deep-reaching motion mixes surface waters to great depth. Deep convection in this site feeds the thermohaline circulation, i.e. the global meridional overturning circulation (MOC) of the ocean responsible for roughly half of the heat transport demanded of the atmosphere-ocean system (*cf.* [37]).

The vertical profiles for the initial temperature and salinity are extracted from the monthly averaged WOA01 *in-situ* data, corresponding to the period of April, when rather large values of buoyancy loss at the sea-surface are registered. The initial conditions are displayed in Figure 3.26, where we can observe the climatological profiles of potential temperature, salinity and potential density. An impulsive start is performed, i.e. the initial velocity condition is a zero velocity field. The surface layer is stirred by the winds and undergoes a regular cycle of convection and re-stratification in response to the annual cycle of buoyancy fluxes at the sea-surface. The buoyancy flux is expressed in terms of heat and fresh-water fluxes as:

$$\mathcal{B} = \frac{g}{\rho_r}\frac{\alpha_\Theta}{c_w}\mathcal{H} + g\beta_S S_r(E-P) = \text{ Thermal Part } + \text{ Haline Part (units: m}^2\text{ s}^{-3}\text{)}.$$

Here, $\alpha_\Theta = 10^{-4}$ K^{-1} and $\beta_S = 8 \times 10^{-4}$ psu^{-1} are respectively the coefficient of thermal expansion and haline contraction, $S_r = 35$ psu is a constant reference salinity value, $c_w = 3\,900$ J kg^{-1} K^{-1} is the heat capacity of water, $\mathcal{H}$ is the surface heat flux and $(E-P)$ represents the fresh water flux (*evaporation minus precipitations*). In this experiment, a constant surface heat flux $\mathcal{H} = 200$ W m^{-2} out of the ocean is applied over the time of integration. The value is chosen to represent typical buoyancy loss in the Labrador Sea in early spring (see [36], [39]). The buoyancy contribution of precipitation is rather small compared with the magnitude of heat flux, so that we neglect haline effects in the simulations. The heat flux value leads to a buoyancy flux of the order of 0.5×10^{-7} m^2 s^{-3}, dictated by the thermal component. A constant weak wind stress of magnitude 4×10^{-2} N m^{-2}, typical of the period and the region considered, is prescribed at the sea-surface. A Coriolis parameter $f = 1.4 \times 10^{-4}$ s^{-1} leads to a deep mixed regime that is affected by rotation.

Also in this case, a coarse vertical resolution is chosen to represent typical grids in numerical OGCM: the vertical grid spacing increases within 25 layers (25 Δz) from 10 m near the surface up to 250 m at 2 km depth. The various models are integrated for a relatively large time $\mathcal{T} = 20$ days with a time-step $\Delta t = 1$ h, that is typical of a coarse, large-scale OGCM. We display the results all along the water column. Figures 3.27, 3.28, 3.29 show respectively the time evolution of the potential density, salinity and potential temperature after 20 days of surface cooling. The final density profiles show for all models, except for the PP81 model, that the buoyancy forcing is sufficiently large and strong enough to break the initial stratification and mix surface waters to great depth all along the water column, setting and maintaining the properties of the abyss.

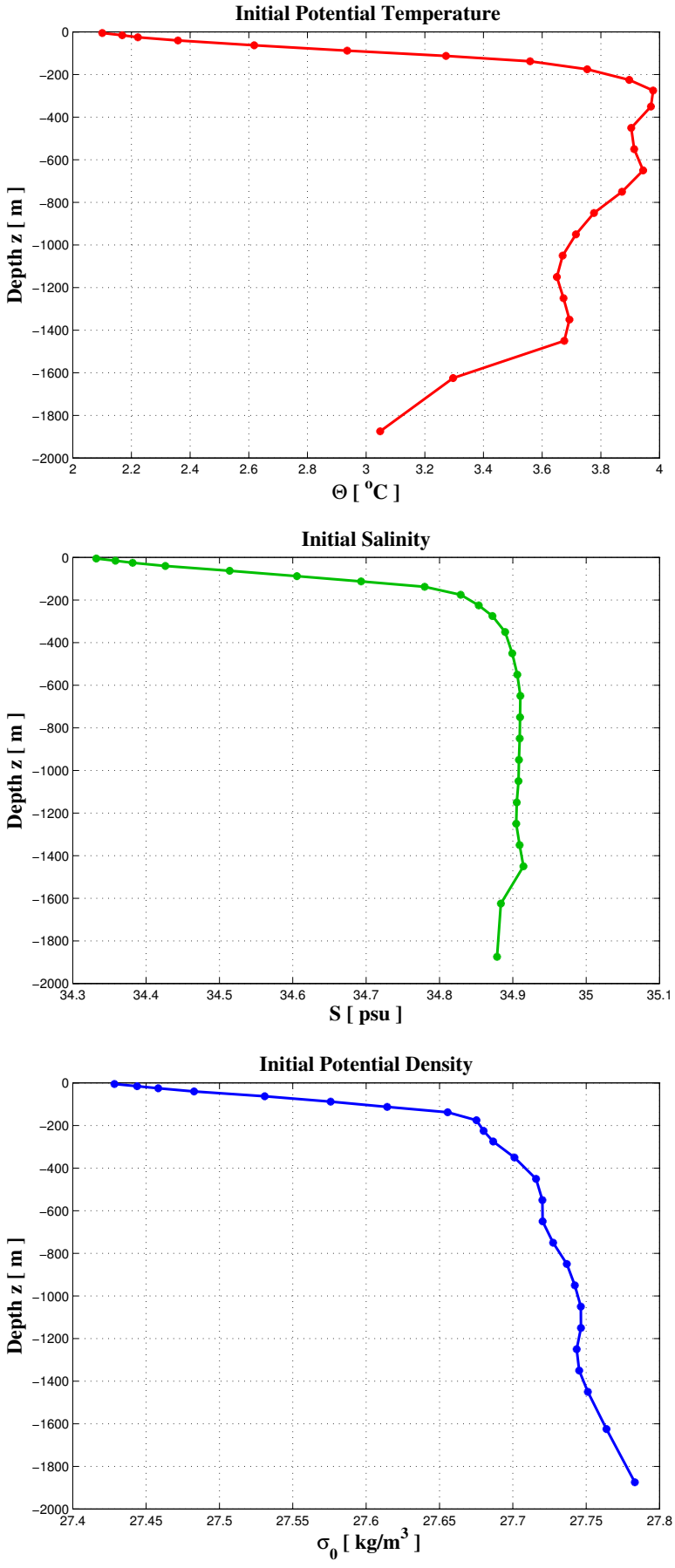

Figure 3.26:
Simulation (b): initial potential temperature, salinity and potential density profiles.

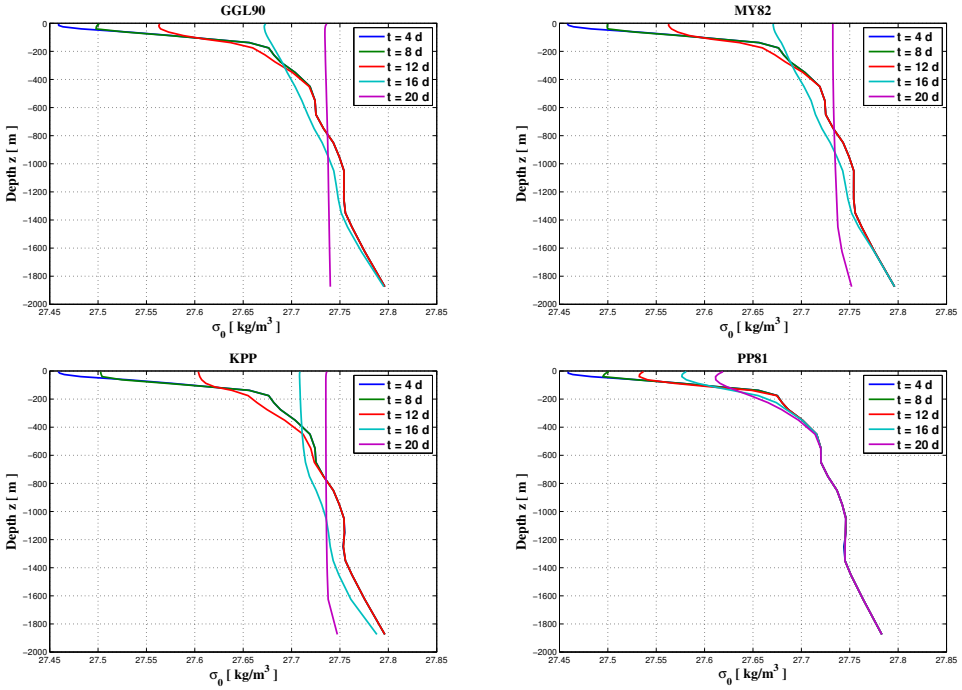

Figure 3.27:
Simulation (b): Time evolution of the potential density profiles.

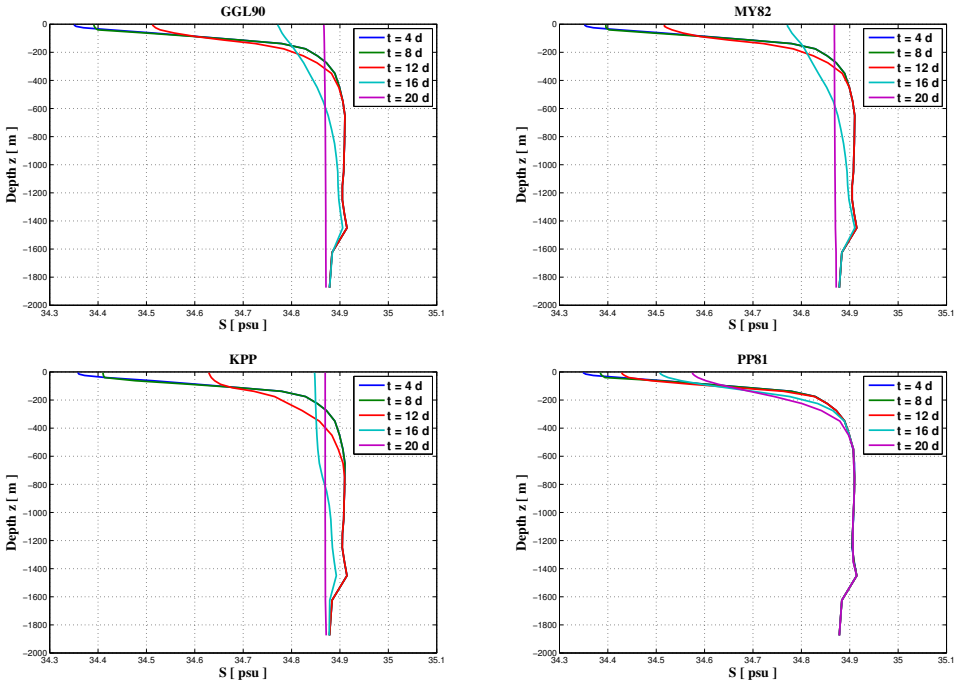

Figure 3.28:
Simulation (b): Time evolution of the salinity profiles.

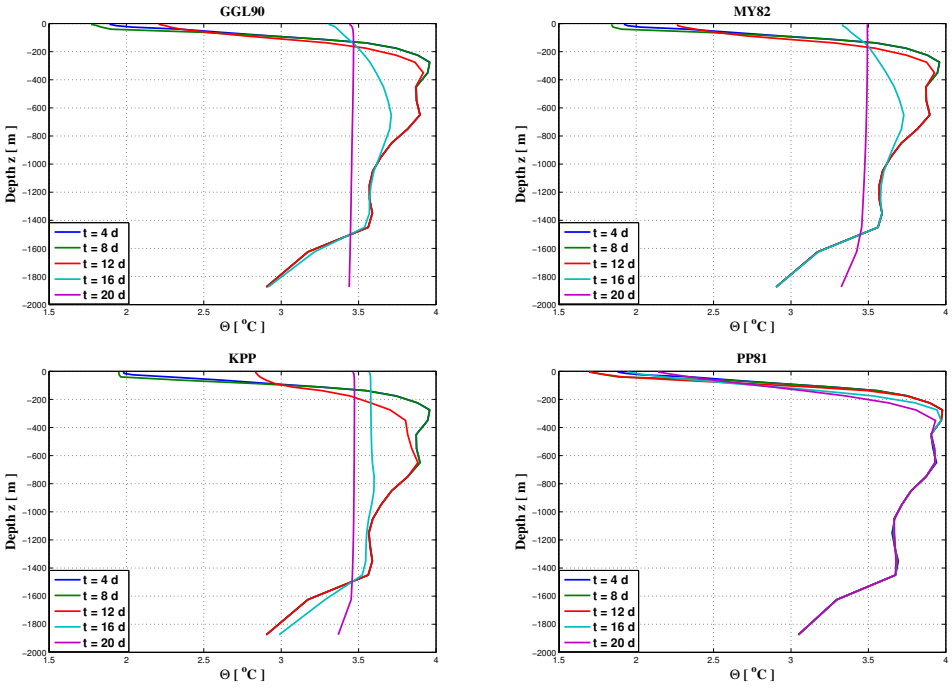

Figure 3.29:
Simulation (b): Time evolution of the potential temperature profiles.

Discussion

The numerical experiments presented show that the PP81 model is the one which gives inferior performances with respect to physical and observational expectations, that is not surprising, due to the simplicity of the model. On the contrary, the more sophisticated KPP model, despite being an overall turbulent closure scheme of first order, is the one which outperforms mixing by other models. This is probably due to the important role played by the non-local transport term (*cf.* [32]), i.e. the counter-gradient flux which models higher turbulent moments. This term is determined mostly from surface fluxes and therefore, in the case of heat loss at the surface of Simulation (b) for instance, it represents an additional up-ward heat flux over the entire boundary layer, which is not present in the other models.

More in detail, looking through the results of Simulation (a), we can conclude how the single application of wind forcing (neglecting buoyancy effects), although very strong, gives rise to a rather shallow mixed layer, suggesting that surface cooling fluxes lead the capability of deep mixing penetration for the various models during numerical simulations. This is clear looking through the results of Simulation (b), where we have to detach how the KPP model is the faster in mixing surface cold water until reaching a deep mixed layer of about 600 m after 16 days, even if vertical instabilities (negative gradient of temperature) are completely removed only after 20 days, when the entire water column is homogenized. So, not only the integral buoyancy supply is important, but also its timing.

On the contrary, the slowest method is precisely PP81 model, that even after 20 days has not removed yet the instabilities of the water column from the initial stratification, emphasizing the weakness of this model, probably resulting in a too crude parameterization of the vertical mixing.

3.3.2 Case 2: Vertical mixing schemes in a 3D sea-ice ocean circulation model

We aim to test the different parameterizations of vertical mixing given by KPP and PP81 models in a 3D MITgcm configuration. The MIT General Circulation Model (MITgcm) is a numerical model designed for study of the atmosphere, ocean and climate, based on a spatial finite-volume (FV) discretization. The model algorithm is described in Marshall et al. [40], for online documentation and access to the model code, see MITgcm Group [45]. The interest is focused on numerical simulation of the Arctic Ocean circulation. The Arctic Ocean depends on a delicate balance in which the magnitude and distribution of the oceanic vertical buoyancy flux are important. Thermal and mechanical forcing, ocean stratification, internal waves, and turbulent mixing have significant impact on this buoyancy flux (*cf.* [19]).

For computational efficiency, we use a regional Arctic Ocean configuration of the MITgcm global grid (see Figure 3.30), with open boundaries. The inter-comparison of the Arctic Ocean circulation simulated with KPP and PP81 models is driven by realistic (CORE-II, 1958-2007) forcing (*cf.* [26]). The algorithm presents as a tracer advection model a high (seventh) order monotonicity-preserving scheme (Daru and Tenaud [15]).

The simulation starts on January 1958, and it runs for 50 years, until December 2007. The analysis is centered on the mixed layer behavior in different seasons. In particular, as usual, we will compare the mean (over the last years of simulation, i.e. for the period 1979-2006) monthly averaged mixed layer depth in March (end of winter) and September (end of summer), and the corresponding mean sea-ice concentration and thickness, for the different models. The first diagnostic of this analysis is the mixed layer depth (MLD), shown in Figure 3.31. It is quite evident the formation of a rather large zone of deep convection in Labrador Sea in March. In September, a rather shallow mixed layer takes place, that in particular achieve the highest depths near the southeastern coast of Greenland washed by the waters of the open North Atlantic, i.e. in the so-called *Ammassalik area*. Indeed, this important area, which takes the name by the englobed Ammassalik Island, is subject to strong downslope wind events in winter, that increase convection phenomena (*cf.* [47]). Globally, the result are quite similar for both models, and the reason is probably given by the important role played by the prescribed high-order advection scheme, that homogenizes the performances of the different diffusion schemes. Nevertheless, in September, KPP model outperforms mixing by PP81 model. This fact shows one of the main deficiencies of this model, that is the simulation of unrealistically shallow mixed layers in summer. To avoid this problem, an additional positive constant (of magnitude 10^{-2} m^2 s^{-1}) vertical diffusivity (and viscosity) could be applied over a depth defined

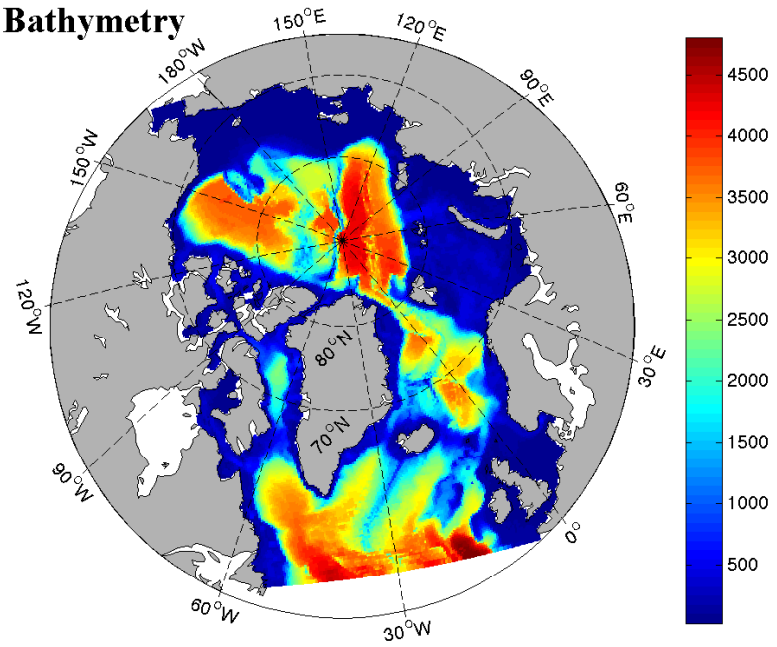

Figure 3.30:
Map of the Arctic Ocean sector of the MITgcm and water depth [m].

by the Monin-Obukhov length, as suggested by Timmermann and Beckmann [58]. The Monin-Obukhov length characterizes the oceanic surface boundary layer where the wind effects are strong, and it is computed from a diagnostic equation given by Lemke [33]. This leads to a modified PP81 model, that has been proved to give good results in the Antarctic geographical region of Weddell Sea (*cf.* [58]), where important convective phenomena occur. These results are comparable with the ones of more sophisticated models, such as KPP.

Maps of simulated sea-ice thickness and concentration are shown in Figure 3.32 and 3.33, respectively. They indicate the mean minimum (September) and maximum (March) ice coverage in the Arctic. Here, the results for the two models are practically identical, with almost undetectable differences. Actually, this is in partly due to the fact that the two models perform similar mixed layer depth, to which the sea-ice evolution is strictly correlated. However, this sensitivity is effectively more significant when considering global (and not regional, as in this case) coupled ocean - sea-ice models. Figure 3.34, taken from Timmermann et al. [59], permits to do a comparison with other numerical results and observed data. The numerical results are obtained by Timmermann et al. [59] using a Finite Element Sea-ice Ocean Model (FESOM), that implements in the vertical direction the modified Pacanowski-Philander scheme just described, while the observed fields are derived from the datasets of Cavalieri et al. [9] and Meier et al. [43]. In general, the MITgcm code used in this work agrees slightly better with the observed data respect to the FESOM code, probably due to the coarser resolution of the latter.

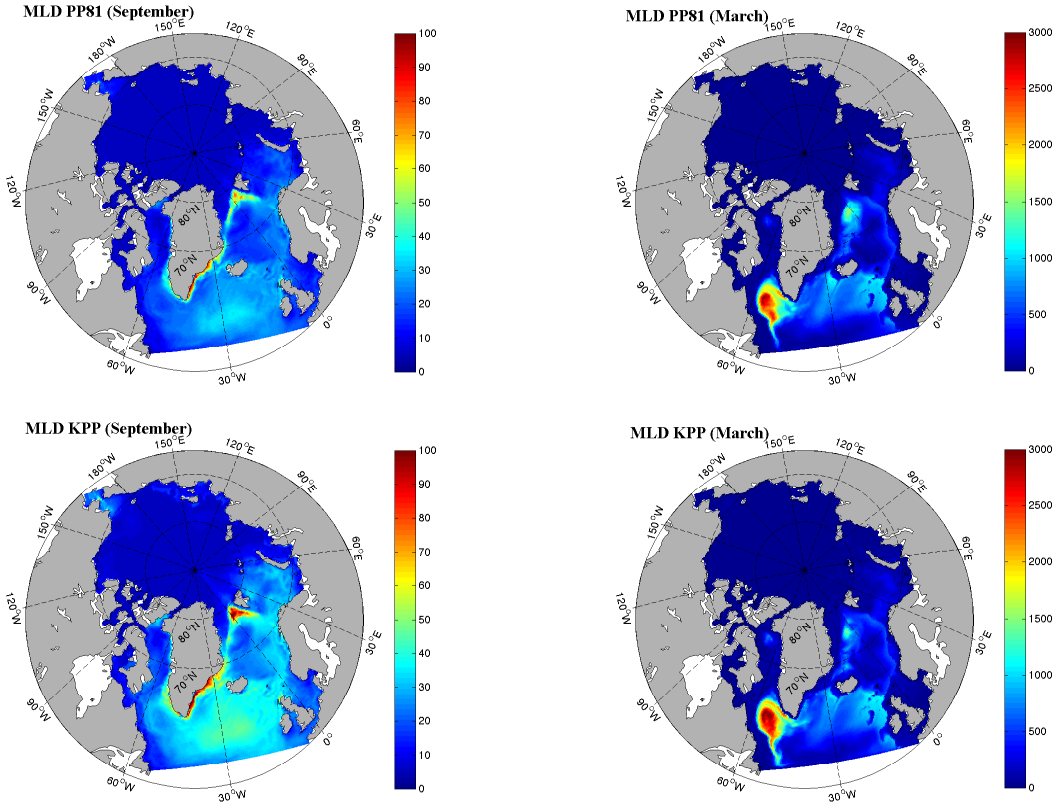

Figure 3.31:
Mean Mixed Layer Depth (MLD, in [m]) for the period 1979-2006 in September (*left*) and March (*right*), for PP81 model (*top*) and KPP model (*bottom*).

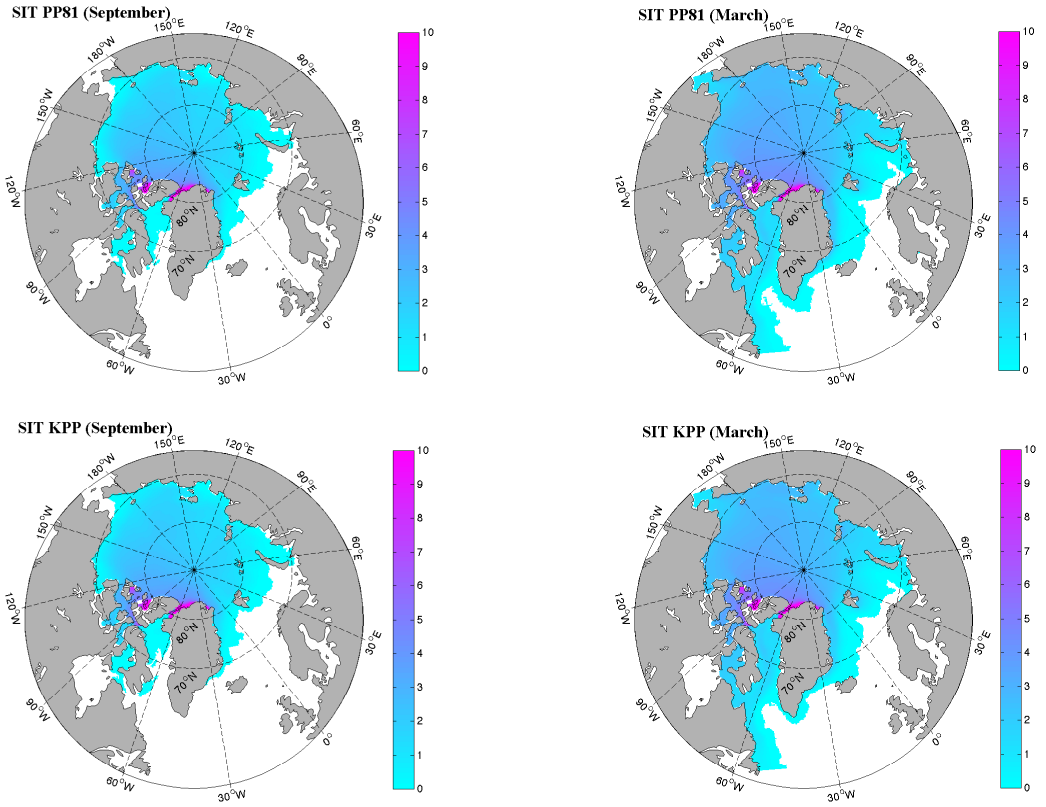

Figure 3.32:
Mean Sea-Ice Thickness (SIT, in [m]) for the period 1979-2006 in September (*left*) and March (*right*), for PP81 model (*top*) and KPP model (*bottom*).

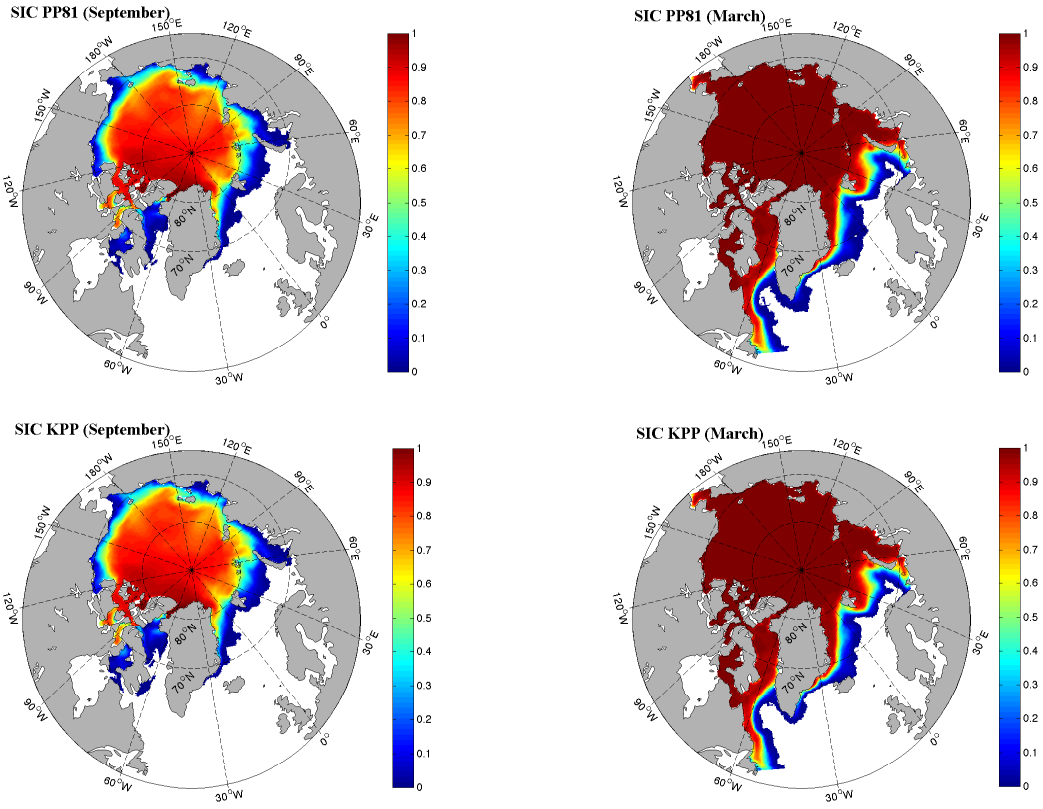

Figure 3.33:
Mean Sea-Ice Concentration (SIC) for the period 1979-2006 in September (*left*) and March (*right*), for PP81 model (*top*) and KPP model (*bottom*).

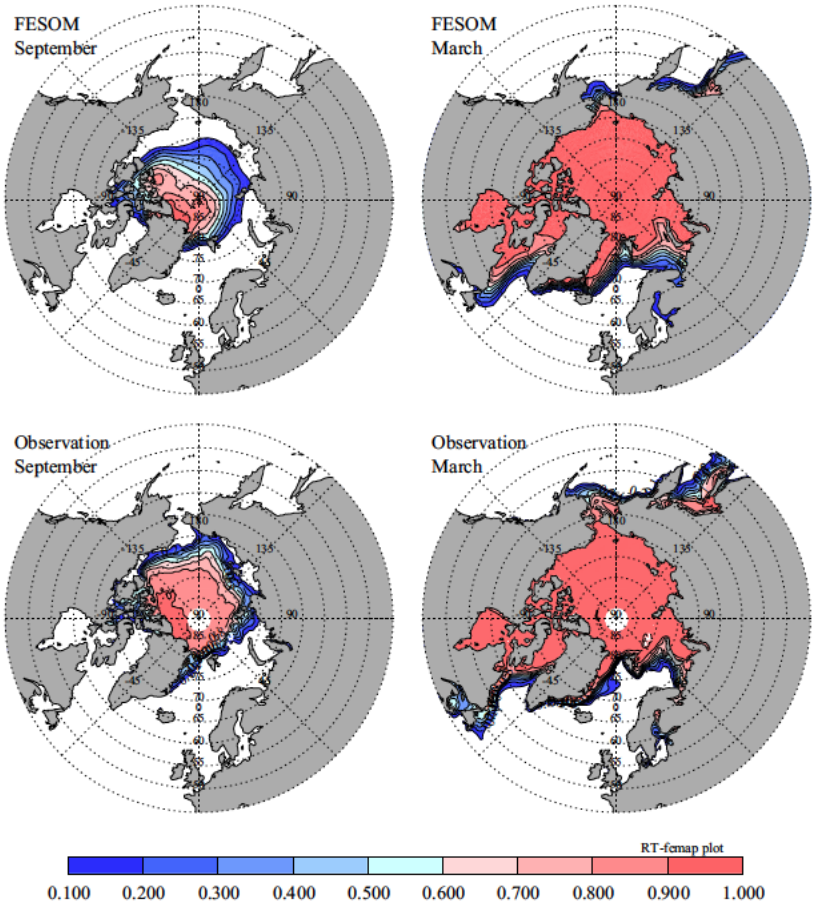

Figure 3.34:
Simulated (*top*) and observed (*bottom*) mean Sea-Ice Concentration (SIC) for the period 1979-2006 in September (*left*) and March (*right*) [From Timmermann et al. [59]].

The results presented in Case 2 are of interest to show non-trivial effects stemming from the difference in the mixed-layer physics, that could influence the ocean circulation as a whole in a global scale. They also put in evidence practical aspect of ocean numerical modeling, showing difficulties and compromises necessarily involved in modeling of such complex systems.

Part II: Finite Element Projection-based VMS Turbulence Models

Chapter 4

A Variational Multi-Scale Sub-Grid Model (VMS-SGM) for Laminar and Turbulent Incompressible Flows

4.1 Introduction

In this chapter, we firstly introduce a mixed boundary value problem for the steady incompressible Navier-Stokes equations, that includes Dirichlet and wall-law boundary conditions to take into account inflow and solid wall boundaries at the same time. After setting the variational formulation of the continuous problem, and establishing a mathematical analysis of wall-law functions, we approximate the weak formulation of the boundary value problem by a finite element projection-based VMS model that only needs a (fine) grid and interpolation operators on a (virtual) coarser grid. The large scales are represented in the (virtual) coarse grid, while the sub-filter scales are their complement into the fine grid. The interaction between the small un-resolved scales and the small resolved scales is assumed to be diffusive, and is modeled by the Smagorinsky sub-grid term with projection structure. We use high-order term-by-term stabilization to stabilize each single term that could lead to unstable discretizations (e.g., convection, pressure gradient), with high accuracy (*cf.* [19], [20], [22]). This allows in particular to use polynomials of the same degree to interpolate velocity and pressure.

The chapter is structured as follows: In Section 4.2, we present the continuous problem we work with, recalling its main properties, and we consider its variational formulation (Subsection 4.2.1). Section 4.3 is devoted to the mathematical analysis of wall-law functions. In Section 4.4, we derive the discrete approximation of the continuous problem by a projection-based VMS approach including wall laws. We construct specific finite element spaces that approximate the slip condition (Subsection 4.4.1), and we specify in details the sub-grid eddy viscosity form (Subsection 4.4.2). Finally, we establish a proper stabilization procedure (Subsection 4.4.3), in order to construct a more comprehensive and viable numerical method in view of its application in realistic turbulent situations.

4.2 Steady Navier-Stokes equations with wall - law boundary conditions

We introduce a mixed boundary value problem for the steady Navier-Stokes equations, that includes a wall-law boundary condition in combination with inflow boundary conditions. Let Ω be a bounded polyhedric connected domain in $\mathbb{R}^d$, $d = 2$ or 3, with a Lipschitz boundary split into $\Gamma = \overline{\Gamma}_D \cup \overline{\Gamma}_n$. We suppose Γ split as the union of the sides $\Sigma_1, \ldots, \Sigma_r$, that we assume to be closed $(d-1)-$dimensional sets (straight segments when $d = 2$ or polygons when $d = 3$), in such a way that $\overline{\Gamma}_D = \bigcup_{i=1}^{k-1} \Sigma_i$, $\quad \overline{\Gamma}_n = \bigcup_{i=k}^{r} \Sigma_i$, for some integer $k \in \{2, \ldots, r\}$.

We impose a Dirichlet inflow boundary condition on Γ_D and a wall-law boundary condition on Γ_n. The problem reads:

Find $\mathbf{u} : \Omega \longrightarrow \mathbb{R}^d$ *and* $p : \Omega \longrightarrow \mathbb{R}$ *such that:*

$$\left\{\begin{array}{rcll} \nabla \cdot (\mathbf{u} \otimes \mathbf{u}) - 2\nu \nabla \cdot D(\mathbf{u}) + \nabla p &=& \mathbf{f} & \text{in } \Omega, \\ \nabla \cdot \mathbf{u} &=& 0 & \text{in } \Omega, \\ -\left[\mathbf{n} \cdot 2\nu D(\mathbf{u})\right]_\tau &=& \mathbf{g}(\mathbf{u})_\tau & \text{on } \Gamma_n, \\ \mathbf{u} \cdot \mathbf{n} &=& 0 & \text{on } \Gamma_n, \\ \mathbf{u} &=& \mathbf{u}_D & \text{on } \Gamma_D, \end{array}\right. \tag{4.1}$$

where $\mathbf{u} \otimes \mathbf{u}$ is the tensor function of components $u_i u_j$, $D(\mathbf{u})$ is the symmetric deformation tensor given by $D(\mathbf{u}) = (1/2)(\nabla \mathbf{u} + (\nabla \mathbf{u})^t)$, $\mathbf{n}$ is the outer normal to Γ, the notation $_\tau$ represents the tangential component with respect to Γ defined as $\mathbf{u}_\tau = \mathbf{u} - (\mathbf{u} \cdot \mathbf{n})\mathbf{n}$, and $\mathbf{g} : \mathbb{R}^d \longrightarrow \mathbb{R}^d$ is a given function, specific of the chosen wall law. The unknowns are the velocity $\mathbf{u}$ and the pressure p of the incompressible fluid. The data are the source term $\mathbf{f}$, that represents a body force per mass unit (typically the gravity), the kinematic viscosity ν of the fluid, that is a positive constant, and the Dirichlet data $\mathbf{u}_D$. By a slight but technical adaptation of the analysis performed in this work, that we skip for brevity, it is possible to add free-normal-tension (also called "do-nothing") boundary conditions on outflow boundaries.

In a more general context, this problem may be set on domains with Lipschitz boundary. For homogeneous Dirichlet boundary conditions on the whole Γ, its numerical analysis has been extensively studied. Let us mention, for instance, the basic books of Girault and Raviart [42], and Temam [82], where in particular it is proved that it admits a solution $(\mathbf{u}, p) \in [H_0^1(\Omega)]^d \times L_0^2(\Omega)$, that continuously depends on the data $(\mathbf{f}, \nu)$. However, slip conditions on general Lipschitz domains must be treated by penalty, and solved by mixed finite elements (*cf.* [84]).

4.2.1 Variational formulation of the continuous problem

We consider the Sobolev spaces $H^s(\Omega)$, $s \in \mathbb{R}$, and $W^{m,p}(\Omega)$, $m \in \mathbb{N}$, $1 \leq p \leq \infty$, equipped with the standard norms and semi-norms. We denote by $\|\cdot\|_{m,p,\Omega}$ and $|\cdot|_{m,p,\Omega}$ respectively the standard norm and semi-norm in $W^{m,p}(\Omega)$. In order to give a variational formulation of problem (4.1), let us consider the spaces:

$$\mathbb{M} = L^2_0(\Omega) = \left\{ q \in L^2(\Omega) : \int_\Omega q \, d\mathbf{x} = 0 \right\},$$

$$\mathbf{W} = \left\{ \mathbf{w} \in [H^1(\Omega)]^d : \mathbf{w} = \mathbf{0} \text{ on } \Gamma_D, \mathbf{w} \cdot \mathbf{n} = 0 \text{ on } \Gamma_n \right\}.$$

The first one is the pressure space, which is isomorphic to the quotient space $L^2(\Omega)/\mathbb{R}$. The second one is the velocity space, which is a closed linear sub-space of $[H^1(\Omega)]^d$, and thus a Hilbert space endowed with the $[H^1(\Omega)]^d$-norm. Indeed, it is well known that the trace is a continuous mapping from $H^1(\Omega)$ into $L^2(\Gamma)$. Also, the normal component of $\mathbf{w}$ exists a.e. on Γ, as $\mathbf{n} \in [L^\infty(\Gamma)]^d$, and since $\mathbf{w} \in [H^1(\Omega)]^d$, by trace theorem and Sobolev injection (*cf.* [8]), its trace on Γ belongs to $[L^4(\Gamma)]^d$. Then, the mapping $\mathbf{w} \in \mathbf{W} \mapsto \mathbf{w} \cdot \mathbf{n} \in L^4(\Gamma_n)$ is continuous, as:

$$\|\mathbf{w} \cdot \mathbf{n}\|_{0,4,\Gamma_n} \leq \|\mathbf{w}\|_{0,4,\Gamma_n} \leq C \, \|\mathbf{w}\|_{1,2,\Omega}.$$

Thanks to Korn's inequalities (*cf.* [50]), the $[H^1(\Omega)]^d$-norm is equivalent on $\mathbf{W}$ to the norm:

$$\|\mathbf{w}\|_{\mathbf{W}} = \|D(\mathbf{w})\|_{0,2,\Omega}.$$

We assume the Dirichlet boundary data admissible, in the sense that there exists a divergence-free lifting $\mathbf{U}_D \in [H^1(\Omega)]^d$ such that $\mathbf{U}_{D_{|\Gamma_D}} = \mathbf{u}_D$ and $\mathbf{U}_D = 0$ on $\overline{\Gamma}_n$. Such a lifting exists if $\mathbf{u}_D \in [H^{1/2}_{00}(\Gamma_D)]^d$, as we assume hereafter, where:

$$H^{1/2}_{00}(\Gamma_D) = \left\{ \sigma \in L^2(\Gamma_D) : \widetilde{\sigma} \in H^{1/2}(\Gamma) \right\},$$

$\widetilde{\sigma}$ denoting the extension by zero of σ on the whole Γ. In this way, we search for a continuous solution $\mathbf{u} = \mathbf{u}_0 + \mathbf{U}_D$, with $\mathbf{u}_0 \in \mathbf{W}$ divergence-free. We shall consider the following variational formulation of (4.1):

Find $(\mathbf{u}, p) \in (\mathbf{U}_D + \mathbf{W}) \times \mathbb{M}$ *such that:*

$$\left\{ \begin{array}{rcl} b(\mathbf{u}; \mathbf{u}, \mathbf{v}) + a(\mathbf{u}, \mathbf{v}) - (p, \nabla \cdot \mathbf{v})_\Omega + \langle G(\mathbf{u}), \mathbf{v} \rangle & = & \langle \mathbf{f}, \mathbf{v} \rangle, \\ (\nabla \cdot \mathbf{u}, q)_\Omega & = & 0, \end{array} \right. \tag{4.2}$$

for any $(\mathbf{v}, q) \in \mathbf{W} \times \mathbb{M}$, where $\langle \cdot, \cdot \rangle$ stands for the duality pairing between $\mathbf{W}$ and its dual $\mathbf{W}'$. The forms b, a and G are given by:

$$b(\mathbf{w}; \mathbf{u}, \mathbf{v}) = \frac{1}{2} \left[(\mathbf{w} \cdot \nabla \mathbf{u}, \mathbf{v})_\Omega - (\mathbf{w} \cdot \nabla \mathbf{v}, \mathbf{u})_\Omega \right], \tag{4.3}$$

$$a(\mathbf{u}, \mathbf{v}) = 2\nu \, (D(\mathbf{u}), D(\mathbf{v}))_\Omega, \tag{4.4}$$

$$\langle G(\mathbf{u}), \mathbf{v} \rangle = (\mathbf{g}(\mathbf{u}), \mathbf{v})_{\Gamma_n}, \tag{4.5}$$

for $\mathbf{u}$, $\mathbf{v}$, $\mathbf{w} \in [H^1(\Omega)]^d$. Semicolons $(;)$ are used for forms that are non-linear with respect to its first argument. The function g is given in implicit form as:

$$\mathbf{g}(\mathbf{u}) = \begin{cases} \dfrac{\mathbf{u}}{|\mathbf{u}|}(u_\tau)^2 & \text{if } |\mathbf{u}| > 0, \\ \\ \mathbf{0} & \text{if } |\mathbf{u}| = 0, \end{cases} \tag{4.6}$$

where $u_\tau = u_\tau(|\mathbf{u}|)$ is the wall-friction velocity, computed as unique solution (see Lemma 4.1 in the next section) of the algebraic equation:

$$u^+ = L(y^+), \text{ with } u^+ = \frac{|\mathbf{u}|}{u_\tau} \text{ and } y^+ = \frac{u_\tau y}{\nu}. \tag{4.7}$$

Here, u^+ is a friction non-dimensional velocity, L is the wall-law function, obtained from an asymptotic analysis in the boundary layer, y^+ denotes a friction non-dimensional normal distance to the solid wall, and y denotes the normal distance to the solid wall. We suppose that the boundary layer is divided into two sub-layers (*cf.* [25]):

$$T_1^+ = \Gamma_n \times [0, y_0^+], \quad T_2^+ = \Gamma_n \times [y_0^+, A^+],$$

where y_0^+ denotes a fixed friction non-dimensional normal distance to the solid wall. The most common wall-law function is the logarithmic law of Prandtl [73] and Von Kármán [87]:

$$L(y^+) = \begin{cases} y^+ & \text{if } y^+ \in [0, y_0^+], \\ \\ \dfrac{1}{C_1}\log(y^+) + C_2 & \text{if } y^+ \in [y_0^+, A^+], \end{cases} \tag{4.8}$$

where $C_1 \simeq 0.41$ and $C_2 \simeq 5.5$ are constants, calculated from experimental measurements, and y_0^+ is chosen by preserving the continuity of L ($y_0^+ \simeq 11.5$). Actually, there exist other several possible settings of L (*cf.* [49], [81]). In all cases, the wall-law function L is non-negative, strictly increasing and continuous, L' admits a finite number of discontinuities, and there exist two positive constants K_1 and K_2 such that:

$$\lim_{z^+ \to 0^+} \frac{L(z^+)}{z^+} = K_1, \quad \lim_{z^+ \to \infty} \frac{L(z^+)}{\log z^+} = K_2. \tag{4.9}$$

4.3 Mathematical analysis of wall - law functions

In this section, we analyze the properties of the mapping G, defined by (4.5), that sets the wall-law boundary condition in the steady Navier-Stokes problem (4.2). We start by proving the existence and uniqueness of solution for the algebraic equation (4.7).

Lemma 4.1. *Let $L : \mathbb{R}_+ \to \mathbb{R}$ be a wall-law function. Let $\lambda > 0$ be a fixed parameter. Then, for any $\alpha \in \mathbb{R}_+$, the algebraic equation:*

$$\frac{\alpha}{\beta} = L(\beta\lambda), \tag{4.10}$$

admits a unique solution $\beta \in \mathbb{R}_+$.

Proof. Let us re-write equation (4.10) as:

$$\alpha = F(\beta), \quad \text{where } F(\beta) = \beta L(\beta\lambda).$$

As L is strictly increasing and continuous, then F is strictly increasing and continuous. Also, by (4.9), F is continuous at $\beta = 0$ with $F(0) = 0$, and $\lim_{\beta\to\infty} F(\beta) = +\infty$. Then, F is bijective from $\mathbb{R}_+$ onto $\mathbb{R}_+$. Consequently, the equation (4.10) admits a unique solution $\beta = F^{-1}(\alpha)$. ■

Lemma 4.2. *Let $h(\alpha) = \beta$ be the unique solution of (4.10). Then, h is a continuous bijection from $\mathbb{R}_+$ onto $\mathbb{R}_+$. Moreover, there exists a constant $C > 0$ such that:*

$$|h(\alpha)| \leq C(1 + |\alpha|), \quad \textit{for all } \alpha \in \mathbb{R}_+. \tag{4.11}$$

Proof. The function $h = F^{-1}$ is clearly bijective and continuous, since F is. Also, from (4.9):

$$\lim_{\alpha\to\infty} \frac{h(\alpha)}{\alpha} = \lim_{t\to\infty} \frac{t}{F(t)} = \lim_{t\to\infty} \frac{1}{L(\lambda t)} = \lim_{t\to\infty} \frac{1}{\log(\lambda t)} \frac{\log(\lambda t)}{L(\lambda t)} = 0.$$

As h is continuous, (4.11) follows. ■

We now prove the main properties of the function $\mathbf{g}$, given by (4.6), that appears in the definition of the mapping G.

Lemma 4.3. *Let $\mathbf{g} : \mathbb{R}^d \to \mathbb{R}^d$ the function defined by:*

$$\mathbf{g}(\mathbf{v}) = \begin{cases} \dfrac{\mathbf{v}}{|\mathbf{v}|} h^2(|\mathbf{v}|)^2 & \textit{if } |\mathbf{v}| > 0, \\ \\ \mathbf{0} & \textit{if } |\mathbf{v}| = 0. \end{cases}$$

Then, $\mathbf{g} \in [W^{1,\infty}_{loc}(\mathbb{R}^d \setminus \{\mathbf{0}\}) \cap C^0(\mathbb{R}^d)]^d$ and is monotone. Moreover, $\mathbf{g}$ satisfies the growth property:

$$|\mathbf{g}(\mathbf{v})| \leq C(1 + |\mathbf{v}|^2), \quad \textit{for all } \mathbf{v} \in \mathbb{R}^d, \tag{4.12}$$

for some constant $C > 0$. Also, $\nabla\mathbf{g}$ satisfies the growth property:

$$|\nabla\mathbf{g}(\mathbf{v})| \leq C(1 + |\mathbf{v}|), \quad \textit{a.e. in } \mathbb{R}^d, \tag{4.13}$$

for some constant $C > 0$.

Proof. The continuity of $\mathbf{g}$ over $\mathbb{R}^d \setminus \{\mathbf{0}\}$ follows from the continuity of h in $\mathbb{R}_+$. Also, as $h(\alpha) \to 0$ as $\alpha \to 0^+$, we have that $\mathbf{g}(\mathbf{v}) \to 0$ as $|\mathbf{v}| \to 0^+$. Therefore, $\mathbf{g}$ is a continuous function over $\mathbb{R}^d$. To prove that $\mathbf{g} \in [W^{1,\infty}_{loc}(\mathbb{R}^d \setminus \{\mathbf{0}\})]^d$, we first note that $F \in W^{1,\infty}_{loc}(\mathbb{R}_+)$. Then, if $\beta = F^{-1}(\alpha) = h(\alpha)$:

$$h'(\alpha) = \frac{1}{F'(\beta)} = \frac{1}{L(\beta\lambda) + \beta\lambda L'(\beta\lambda)} \leq \frac{1}{L(\beta\lambda)} \quad \text{a.e. in } \mathbb{R}_+,$$

as L is strictly increasing. Then, as L' admits a finite number of discontinuities, so does h', which is non-negative. From (4.9), $\lim_{\alpha\to\infty} h(\alpha) = 0$, and consequently $h' \in L^\infty(\mathbb{R}_+)$. As the application $\mathbf{v} \to |\mathbf{v}|$ belongs to $C^\infty(\mathbb{R}^d \setminus \{\mathbf{0}\})$, we conclude $\mathbf{g} \in [W^{1,\infty}_{loc}(\mathbb{R}^d \setminus \{\mathbf{0}\})]^d$.

To prove that $\mathbf{g}$ is monotone, it is sufficient to prove that it is the gradient of a convex function in $\mathbb{R}^d$ (*cf.* [36]). Let us define the functions:

$$H(\alpha) = \int_0^\alpha h^2(v)\, dv, \quad C(\mathbf{v}) = H(|\mathbf{v}|).$$

Then, $\mathbf{g}(\mathbf{v}) = \nabla C(\mathbf{v})$ for any $\mathbf{v} \in \mathbb{R}^d$. Indeed, on one hand the function C is differentiable and $\nabla C \in [W^{1,\infty}_{loc}(\mathbb{R}^d \setminus \mathbf{0})]^d$, since H is differentiable in $\mathbb{R}$ with $H' \in W^{1,\infty}_{loc}(\mathbb{R})$. Moreover:

$$\partial_i C(\mathbf{v}) = \partial_i(|\mathbf{v}|)H'(|\mathbf{v}|) = \frac{v_i}{|\mathbf{v}|}\, h^2(|\mathbf{v}|) = g_i(\mathbf{v}), \quad i = 1, \ldots, d \quad \text{if } \mathbf{v} \in \mathbb{R}^d \setminus \mathbf{0}.$$

On another hand, $\nabla C(\mathbf{0}) = \mathbf{g}(\mathbf{0})$. Indeed:

$$\frac{C(\mathbf{v})}{|\mathbf{v}|} = \frac{1}{|\mathbf{v}|} \int_0^{|\mathbf{v}|} h^2(v)\, dv \le \max_{0\le v\le|\mathbf{v}|} h^2(v),$$

and then $\lim_{\mathbf{v}\to\mathbf{0}} C(\mathbf{v})/|\mathbf{v}| = 0$. C is convex, as it is the composition of convex functions. Indeed:

$$H''(\alpha) = 2\, h(\alpha)\, h'(\alpha) \ge 0 \quad \text{a.e. in } \mathbb{R}_+,$$

as $h = F^{-1} \in W^{1,\infty}_{loc}(\mathbb{R}_+)$, is non-negative and strictly increasing.

To determine the growth property of $\mathbf{g}$, observe that $|\mathbf{g}(\mathbf{v})| = h^2(|\mathbf{v}|)$ if $\mathbf{v} \neq 0$, hence (4.12) follows from (4.11). We investigate the growth property of $\nabla\mathbf{g}$. We have $\mathbf{g}(\mathbf{v}) = (\mathbf{v}/|\mathbf{v}|)\, H'(|\mathbf{v}|)$ if $\mathbf{v} \neq 0$. A straightforward calculation yields:

$$\partial_j g_i(\mathbf{v}) = \left(\frac{\delta_{i,j}}{|\mathbf{v}|} - \frac{v_i v_j}{|\mathbf{v}|^3}\right) H'(|\mathbf{v}|) + \frac{v_i v_j}{|\mathbf{v}|^2}\, H''(|\mathbf{v}|), \tag{4.14}$$

with $\delta_{i,j}$ the Kronecker delta. We easily deduce from (4.11) that:

$$\left|\left(\frac{\delta_{i,j}}{|\mathbf{v}|} - \frac{v_i v_j}{|\mathbf{v}|^3}\right) H'(|\mathbf{v}|)\right| \le C(1 + |\mathbf{v}|). \tag{4.15}$$

It remains to investigate the term involving $H''(|\mathbf{v}|)$. From the relation $\beta = F^{-1}(\alpha) = h(\alpha)$, we deduce:

$$H''(\alpha) = 2F^{-1}(\alpha)\frac{1}{F'(\beta)} = \frac{2\beta}{L(\beta\lambda) + \beta\lambda L'(\beta\lambda)} \quad \text{a.e. in } \mathbb{R}_+.$$

Thus, as $\beta = \alpha/L(\beta\lambda)$, we get:

$$\frac{H''(\alpha)}{\alpha} = \frac{2}{L(\beta\lambda)(L(\beta\lambda) + \beta\lambda L'(\beta\lambda))} \le \frac{2}{[L(\beta\lambda)]^2} \quad \text{a.e. in } \mathbb{R}_+.$$

Then, $\lim_{\alpha\to\infty} H''(\alpha)/\alpha = 0$. Also, H'' is bounded in compact sets as $h \in W^{1,\infty}_{loc}(\mathbb{R}_+)$. Consequently, there exists a constant $C > 0$ such that:

$$|H''(\alpha)| \leq C(1+\alpha) \quad \text{a.e. in } \mathbb{R}_+. \tag{4.16}$$

Combining (4.14), (4.15) and (4.16), we obtain:

$$|\partial_j g_i(\mathbf{v})| \leq C(1+|\mathbf{v}|)\text{a.e. in } \mathbb{R}^d,$$

which yields (4.13). ■

We are now in a position to prove the following properties of the mapping G, essential for the subsequent analysis in Chapter 5.

Lemma 4.4. *The functional G given by (4.5) is well defined from $\mathbf{W}$ into its dual $\mathbf{W}'$, is monotone, compact and satisfies the estimates: $\forall \mathbf{v}, \mathbf{w} \in \mathbf{W}$,*

$$\begin{aligned} \|G(\mathbf{v})\|_{\mathbf{W}'} &\leq C\,(1+\|\mathbf{v}\|^2_{1,2,\Omega}), & (4.17)\\ \|G(\mathbf{v})-G(\mathbf{w})\|_{\mathbf{W}'} &\leq C\,(1+\|\mathbf{v}\|_{1,2,\Omega}+\|\mathbf{w}\|_{1,2,\Omega})\,\|\mathbf{v}-\mathbf{w}\|_{1,2,\Omega}, & (4.18)\end{aligned}$$

where C is a positive constant only depending on d, Ω and Γ_n.

Proof. Consider $\mathbf{v} \in \mathbf{W}$. By trace theorem and Sobolev injection, its trace on Γ belongs to $[L^4(\Omega)]^d$. Moreover, $\|\mathbf{v}\|_{0,4,\Gamma_n} \leq \|\mathbf{v}\|_{0,4,\Gamma} \leq C\|\mathbf{v}\|_{1,2,\Omega}$. Thus, the duality $\langle G(\mathbf{v}), \mathbf{w}\rangle$ expressed by (4.5) is well defined following (4.12), and satisfies:

$$|\langle G(\mathbf{v}), \mathbf{w}\rangle| \leq \|\mathbf{g}(\mathbf{v})\|_{0,2,\Gamma_n}\|\mathbf{w}\|_{0,2,\Gamma_n} \leq C(1+\|v\|^2_{1,2,\Omega})\|\mathbf{w}\|_{1,2,\Omega}.$$

Hence, (4.17) follows. As $\mathbf{g} \in W^{1,\infty}_{loc}(\mathbb{R}^d \setminus \{\mathbf{0}\}) \cap C^0(\mathbb{R}^d)$, the Taylor's formula with integral reminder leads to:

$$\mathbf{g}(\mathbf{v}(\mathbf{x})) - \mathbf{g}(\mathbf{w}(\mathbf{x})) = \int_0^1 \nabla\mathbf{g}(\theta\mathbf{v}(\mathbf{x}) + (1-\theta)\mathbf{w}(\mathbf{x})) \cdot (\mathbf{v}(\mathbf{x}) - \mathbf{w}(\mathbf{x}))\, d\theta.$$

Using estimate (4.13), we obtain:

$$|\mathbf{g}(\mathbf{v}(\mathbf{x})) - \mathbf{g}(\mathbf{w}(\mathbf{x}))| \leq (1+|\mathbf{v}(\mathbf{x})|+|\mathbf{w}(\mathbf{x})|)|\mathbf{v}(\mathbf{x})-\mathbf{w}(\mathbf{x})|, \tag{4.19}$$

which in conjunction with Hölder's inequality leads to:

$$\begin{aligned} \|\mathbf{g}(\mathbf{v})-\mathbf{g}(\mathbf{w})\|_{0,2,\Gamma_n} &\leq C\|1+|\mathbf{v}|+|\mathbf{w}|\|_{0,4,\Gamma_n}\|\mathbf{v}-\mathbf{w}\|_{0,4,\Gamma_n} \\ &\leq C(1+\|\mathbf{v}\|_{1,2,\Omega}+\|\mathbf{w}\|_{1,2,\Omega})\|\mathbf{v}-\mathbf{w}\|_{1,2,\Omega}, \qquad (4.20)\end{aligned}$$

where the last inequality follows by trace theorem and Sobolev injection. Estimate (4.18) follows from (4.20). Also, G is monotone as $\mathbf{g}$ is monotone.

To prove the compactness of G, it is enough to prove that for any sequence $\{\mathbf{v}_n\}_{n\in\mathbb{N}}$ weakly convergent to some $\mathbf{v} \in \mathbf{W}$, then, up to a sub-sequence, $\{G(\mathbf{v}_n)\}_{n\in\mathbb{N}}$ strongly converges to $G(\mathbf{v})$ in $\mathbf{W}'$. Let $\mathbf{w} \in \mathbf{W}$. By Hölder's inequality and (4.19), we have:

$$\begin{aligned} |\langle G(\mathbf{v}_n) - G(\mathbf{v}), \mathbf{w}\rangle| &\leq C\|(1 + |\mathbf{v}_n| + |\mathbf{v}|)|\mathbf{v}_n - \mathbf{v}|\|_{0,3/2,\Gamma_n}\|\mathbf{w}\|_{0,3,\Gamma_n} \\ &\leq C\|1 + |\mathbf{v}_n| + |\mathbf{v}|\|_{0,3,\Gamma_n}\|\mathbf{v}_n - \mathbf{v}\|_{0,3,\Gamma_n}\|\mathbf{w}\|_{1,2,\Omega} \\ &\leq C'\|\mathbf{v}_n - \mathbf{v}\|_{0,3,\Gamma_n}\|\mathbf{w}\|_{1,2,\Omega}, \end{aligned}$$

where C' depends on Ω, $\|\mathbf{v}\|_{0,3,\Gamma_n}$ and $\sup_{n\in\mathbb{N}}(\|\mathbf{v}_n\|_{0,3,\Gamma_n})$. In particular:

$$\|G(\mathbf{v}_n) - G(\mathbf{v})\|_{\mathbf{W}'} \leq C'\|\mathbf{v}_n - \mathbf{v}\|_{0,3,\Gamma_n}. \tag{4.21}$$

As $\{\mathbf{v}_n\}_{n\in\mathbb{N}}$ weakly converges to $\mathbf{v}$ in $\mathbf{W}$, the corresponding traces sequence weakly converges to $\mathbf{v}$ in $[H^{1/2}(\Gamma)]^d$. Since the embedding $[H^{1/2}(\Gamma)]^d \hookrightarrow [L^3(\Gamma)]^d$ is compact, up to a sub-sequence, $\|\mathbf{v}_n - \mathbf{v}\|_{0,3,\Gamma_n} \to 0$ for $n \to \infty$, hence the result by estimate (4.21). ■

4.4 A projection-based VMS approach including wall laws

We approximate the weak formulation (4.2) of the boundary value problem (4.1) for the steady Navier-Stokes equations by a Variational Multi-Scale Sub-Grid Model (VMS-SGM). To state it, we decompose the spaces $\mathbf{W}$ and $\mathbb{M}$ as:

$$\mathbf{W} = \overline{\mathbf{X}}_h \oplus \mathbf{X}', \quad \mathbb{M} = \overline{\mathbb{M}}_h \oplus \mathbb{M}',$$

where $\overline{\mathbf{X}}_h$, $\overline{\mathbb{M}}_h$ respectively are the large scale finite-dimensional spaces for velocity and pressure, and $\mathbf{X}'$, $\mathbb{M}'$ are small scale complementary spaces. The sum is assumed to be direct (i.e., $\overline{\mathbf{X}}_h \cap \mathbf{X}' = \{\mathbf{0}\}$, $\overline{\mathbb{M}}_h \cap \mathbb{M}' = \{0\}$), to ensure a proper separation between large and small scales. Moreover, we subdivide the lifting $\mathbf{U}_D$ between large and small scales, by considering a suitable interpolant $\overline{\mathbf{U}}_{Dh}$ on a foreground large scale space, and denoting by $\mathbf{U}'_D$ its small scale complement.

The solution of the steady Navier-Stokes equations (4.1) is decomposed into:

$$(\mathbf{u}, p) = (\overline{\mathbf{u}}_h, \overline{p}_h) + (\mathbf{u}', p'), \text{ with } (\overline{\mathbf{u}}_h, \overline{p}_h) \in (\overline{\mathbf{U}}_{Dh} + \overline{\mathbf{X}}_h) \times \overline{\mathbb{M}}_h, (\mathbf{u}', p') \in (\mathbf{U}'_D + \mathbf{X}') \times \mathbb{M}'.$$

The pairs $(\overline{\mathbf{u}}_h, \overline{p}_h)$ and $(\mathbf{u}', p')$ satisfy the following set of coupled equations:

$$\left\{ \begin{array}{rcl} b(\mathbf{u}; \overline{\mathbf{u}}_h, \overline{\mathbf{v}}_h) + a(\overline{\mathbf{u}}_h, \overline{\mathbf{v}}_h) - (\overline{p}_h, \nabla\cdot\overline{\mathbf{v}}_h)_\Omega + \langle G(\mathbf{u}), \overline{\mathbf{v}}_h\rangle &=& -\langle R(\mathbf{u}; \mathbf{u}', p'), \overline{\mathbf{v}}_h\rangle, \\ (\nabla\cdot\overline{\mathbf{u}}_h, \overline{q}_h)_\Omega &=& -(\nabla\cdot\mathbf{u}', \overline{q}_h)_\Omega, \end{array} \right. \tag{4.22}$$

for all $(\overline{\mathbf{v}}_h, \overline{q}_h) \in \overline{\mathbf{X}}_h \times \overline{\mathbb{M}}_h$, and:

$$\left\{ \begin{array}{rcl} b(\mathbf{u}; \mathbf{u}', \mathbf{v}') + a(\mathbf{u}', \mathbf{v}') - (p', \nabla\cdot\mathbf{v}')_\Omega + \langle G(\mathbf{u}), \mathbf{v}'\rangle &=& -\langle R(\mathbf{u}; \overline{\mathbf{u}}_h, \overline{p}_h), \mathbf{v}'\rangle, \\ (\nabla\cdot\mathbf{u}', q')_\Omega &=& -(\nabla\cdot\overline{\mathbf{u}}_h, q')_\Omega, \end{array} \right. \tag{4.23}$$

for all $(\mathbf{v}', q') \in \mathbf{X}' \times \mathbb{M}'$, where:

$$\langle R(\mathbf{u}; \mathbf{z}, r), \mathbf{w} \rangle = b(\mathbf{u}; \mathbf{z}, \mathbf{w}) + a(\mathbf{z}, \mathbf{w}) - (r, \nabla \cdot \mathbf{w})_\Omega - \langle \mathbf{f}, \mathbf{w} \rangle.$$

In the coupled set of equations (4.22)-(4.23), the large scales are driven by the residual associated to the small scales $R(\mathbf{u}; \mathbf{u}', p')$, while the small scales are driven by the residual associated to the large scales $R(\mathbf{u}; \overline{\mathbf{u}}_h, \overline{p}_h)$.

The VMS-SGM modeling is a discretization of this set of macro-micro scales equations, based upon the following procedure:

(i) Approximate the small scales spaces $\mathbf{X}'$ and $\mathbb{M}'$ by finite-dimensional sub-spaces of *small resolved scales* $\mathbf{X}'_h$ and $\mathbb{M}'_h$, respectively. Then, $\mathbf{X}' = \mathbf{X}'_h \oplus \mathbf{X}''$, $\mathbb{M}' = \mathbb{M}'_h \oplus \mathbb{M}''$, where $\mathbf{X}''$ and $\mathbb{M}''$ are complementary spaces of *small un-resolved scales* of infinite dimension. As the sum is assumed to be direct, this yields the unique decompositions:

$$\begin{array}{rcll} \mathbf{v} & = & \overline{\mathbf{v}}_h + \mathbf{v}'_h + \mathbf{v}'' & \text{for all} \quad \mathbf{v} \in \mathbf{W}, \\ q & = & \overline{q}_h + q'_h + q'' & \text{for all} \quad q \in \mathbb{M}, \end{array}$$

with obvious notation.

(ii) Neglect the interactions between large and small un-resolved scales. It is assumed that the interaction large - small un-resolved scales is weak whenever these are inside the inertial spectrum.

(iii) Model the action of small un-resolved scales on small resolved scales in problem (4.23) by an eddy viscosity procedure.

(iv) Neglect the small un-resolved scales in the modeling of wall laws. This is justified since wall laws apply to the mean flow, and we can identify it with the resolved flow.

Let us decompose $\mathbf{u} = \overline{\mathbf{u}}_h + \mathbf{u}'_h + \mathbf{u}'' \in (\mathbf{U}_D + \mathbf{W})$, and similarly $p = \overline{p}_h + p'_h + p'' \in \mathbb{M}$. We denote:

$$(\mathbf{U}_{Dh} + \mathbf{X}_h) = (\overline{\mathbf{U}}_{Dh} + \overline{\mathbf{X}}_h) \oplus (\mathbf{U}'_{Dh} + \mathbf{X}'_h), \quad \mathbb{M}_h = \overline{\mathbb{M}}_h \oplus \mathbb{M}'_h,$$

with $\mathbf{U}'_{Dh}$ a suitable interpolant of $\mathbf{U}'_D$ on a foreground small scale space, and:

$$\mathbf{u}_h = \overline{\mathbf{u}}_h + \mathbf{u}'_h \in (\mathbf{U}_{Dh} + \mathbf{X}_h), \quad p_h = \overline{p}_h + p'_h \in \mathbb{M}_h. \tag{4.24}$$

The equations (4.22) for $(\overline{\mathbf{u}}_h, \overline{p}_h)$ are modeled as follows: By (ii) and (iv), we approximate

$$b(\mathbf{u}; \overline{\mathbf{u}}_h, \overline{\mathbf{v}}_h) \simeq b(\mathbf{u}_h; \overline{\mathbf{u}}_h, \overline{\mathbf{v}}_h), \qquad \langle G(\mathbf{u}), \overline{\mathbf{v}}_h \rangle \simeq \langle G(\mathbf{u}_h), \overline{\mathbf{v}}_h \rangle,$$

$$\langle R(\mathbf{u}; \mathbf{u}', p'), \overline{\mathbf{v}}_h \rangle \simeq \langle R(\mathbf{u}_h; \mathbf{u}'_h, p'_h), \overline{\mathbf{v}}_h \rangle, \qquad (\nabla \cdot \mathbf{u}', \overline{q}_h)_\Omega \simeq (\nabla \cdot \mathbf{u}'_h, \overline{q}_h)_\Omega.$$

This suggests the following modeled equations for $(\overline{\mathbf{u}}_h, \overline{p}_h)$:

$$\left\{ \begin{array}{rcl} b(\mathbf{u}_h; \overline{\mathbf{u}}_h, \overline{\mathbf{v}}_h) + a(\overline{\mathbf{u}}_h, \overline{\mathbf{v}}_h) - (\overline{p}_h, \nabla \cdot \overline{\mathbf{v}}_h)_\Omega + \langle G(\mathbf{u}_h), \overline{\mathbf{v}}_h \rangle & = & -\langle R(\mathbf{u}_h; \mathbf{u}'_h, p'_h), \overline{\mathbf{v}}_h \rangle, \\ (\nabla \cdot \overline{\mathbf{u}}_h, \overline{q}_h)_\Omega & = & -(\nabla \cdot \mathbf{u}'_h, \overline{q}_h)_\Omega, \end{array} \right. \tag{4.25}$$

for all $(\overline{\mathbf{v}}_h, \overline{q}_h) \in \overline{\mathbf{X}}_h \times \overline{\mathbb{M}}_h$.

The modeling of equations (4.23) is more involved. Set $\mathbf{v}' = \mathbf{v}'_h \in \mathbf{X}'_h$ and $p' = p'_h \in \mathbb{M}'_h$. By (ii) and (iv), we approximate:

$$b(\mathbf{u}; \mathbf{u}', \mathbf{v}'_h) \simeq b(\mathbf{u}_h; \mathbf{u}'_h, \mathbf{v}'_h) + b(\mathbf{u}'_h; \mathbf{u}'', \mathbf{v}'_h) + b(\mathbf{u}''; \mathbf{u}'_h, \mathbf{v}'_h) + b(\mathbf{u}''; \mathbf{u}'', \mathbf{v}'_h),$$

$$\langle G(\mathbf{u}), \mathbf{v}'_h \rangle \simeq \langle G(\mathbf{u}_h), \mathbf{v}'_h \rangle, \quad \langle R(\mathbf{u}; \overline{\mathbf{u}}_h, \overline{p}_h), \mathbf{v}'_h \rangle \simeq \langle R(\mathbf{u}_h; \overline{\mathbf{u}}_h, \overline{p}_h), \mathbf{v}'_h \rangle.$$

Equations (4.23) become:

$$\left\{ \begin{array}{rcl} b(\mathbf{u}_h; \mathbf{u}'_h, \mathbf{v}'_h) + a(\mathbf{u}'_h, \mathbf{v}'_h) - (p'_h, \nabla \cdot \mathbf{v}'_h)_\Omega + \langle G(\mathbf{u}_h), \mathbf{v}'_h \rangle = & - & \langle R(\mathbf{u}_h; \overline{\mathbf{u}}_h, \overline{p}_h), \mathbf{v}'_h \rangle \\ & - & \langle T(\mathbf{u}'_h; \mathbf{u}'', p''), \mathbf{v}'_h \rangle, \\ \\ (\nabla \cdot \mathbf{u}'_h, q'_h)_\Omega = & - & (\nabla \cdot \overline{\mathbf{u}}_h, q'_h)_\Omega \\ & - & (\nabla \cdot \mathbf{u}'', q'_h)_\Omega, \end{array} \right. \tag{4.26}$$

for all $(\mathbf{v}'_h, q'_h) \in \mathbf{X}'_h \times \mathbb{M}'_h$, where:

$$\langle T(\mathbf{u}'_h; \mathbf{u}'', p''), \mathbf{v}'_h \rangle = b(\mathbf{u}'_h; \mathbf{u}'', \mathbf{v}'_h) + b(\mathbf{u}''; \mathbf{u}'_h, \mathbf{v}'_h) + b(\mathbf{u}''; \mathbf{u}'', \mathbf{v}'_h) + a(\mathbf{u}'', \mathbf{v}'_h) - (p'', \nabla \cdot \mathbf{v}'_h)_\Omega.$$

We sum up the two equations in (4.26), and we call:

$$\langle T(\mathbf{u}'_h; \mathbf{u}'', p''), (\mathbf{v}'_h, q'_h) \rangle = \langle T(\mathbf{u}'_h; \mathbf{u}'', p''), \mathbf{v}'_h \rangle + (\nabla \cdot \mathbf{u}'', q'_h)_\Omega.$$

Applying (iii), we approximate $\langle T(\mathbf{u}'_h; \mathbf{u}'', p''), (\mathbf{v}'_h, q'_h) \rangle \simeq c'(\mathbf{u}_h; \mathbf{u}_h, \mathbf{v}_h)$, where:

$$c'(\mathbf{u}_h; \mathbf{u}_h, \mathbf{v}_h) = c(\mathbf{u}'_h; \mathbf{u}'_h, \mathbf{v}'_h) = 2(\nu_T(\mathbf{u}'_h) D(\mathbf{u}'_h), D(\mathbf{v}'_h))_\Omega, \tag{4.27}$$

and ν_T is a turbulent viscosity that we will specify later on. Thus, we deduce the following modeled equations for $(\mathbf{u}'_h, p'_h)$:

$$\left\{ \begin{array}{rcl} b(\mathbf{u}_h; \mathbf{u}'_h, \mathbf{v}'_h) + a(\mathbf{u}'_h, \mathbf{v}'_h) + c'(\mathbf{u}_h; \mathbf{u}_h, \mathbf{v}_h) - (p'_h, \nabla \cdot \mathbf{v}'_h)_\Omega & + & \langle G(\mathbf{u}_h), \mathbf{v}'_h \rangle \\ & = & -\langle R(\mathbf{u}_h; \overline{\mathbf{u}}_h, \overline{p}_h), \mathbf{v}'_h \rangle, \\ \\ (\nabla \cdot \mathbf{u}'_h, q'_h)_\Omega & = & -(\nabla \cdot \overline{\mathbf{u}}_h, q'_h)_\Omega, \end{array} \right. \tag{4.28}$$

for all $(\mathbf{v}'_h, q'_h) \in \mathbf{X}'_h \times \mathbb{M}'_h$. Reunifying the large scale equations (4.25) and the small resolved scale equations (4.28), the model may be simplified to a single problem for the unknowns $(\mathbf{u}_h, p_h) \in (\mathbf{U}_{Dh} + \mathbf{X}_h) \times \mathbb{M}_h$ defined by (4.24). This problem reads as follows:

$$\left\{ \begin{array}{rcl} b(\mathbf{u}_h; \mathbf{u}_h, \mathbf{v}_h) + a(\mathbf{u}_h, \mathbf{v}_h) + c'(\mathbf{u}_h; \mathbf{u}_h, \mathbf{v}_h) - (p_h, \nabla \cdot \mathbf{v}_h)_\Omega + \langle G(\mathbf{u}_h), \mathbf{v}_h \rangle & = & \langle \mathbf{f}, \mathbf{v}_h \rangle, \\ \\ (\nabla \cdot \mathbf{u}_h, q_h)_\Omega & = & 0, \end{array} \right. \tag{4.29}$$

for all $(\mathbf{v}_h, q_h) \in \mathbf{X}_h \times \mathbb{M}_h$. This is a preliminary version of the VMS-SGM model that we will analyze in the sequel.

4.4.1 Velocity finite element spaces

In problem (4.29), we are searching for a resolved velocity in the affine variety $(\mathbf{U}_{Dh}+\mathbf{X}_h)$. In this work, we identify the finite-dimensional space $\mathbf{X}_h$ with a finite element (FE) space. This subsection focuses on the construction of FE spaces that approximate the slip condition $\mathbf{u}\cdot\mathbf{n}=0$ on Γ_n.

Let $\{\mathcal{T}_h\}_{h>0}$ be a family of affine-equivalent and conforming (i.e, without hanging nodes) triangulations of $\overline{\Omega}$, formed by triangles or quadrilaterals ($d=2$), tetrahedra or hexaedra ($d=3$). As usual, the parameter h is the largest diameter h_K among the elements K of $\mathcal{T}_h$. We shall assume that the family of triangulations $\{\mathcal{T}_h\}_{h>0}$ is also admissible in the following sense:

Definition 4.5. *The family of triangulations $\{\mathcal{T}_h\}_{h>0}$ is admissible if $\overline{\Gamma}_D$ and $\overline{\Gamma}_n$ are the union of whole sides of elements of $\mathcal{T}_h$, $h>0$.*

Here, we call "side"either an edge (when $d=2$) or a face (when $d=3$). Given an integer $l\geq 0$, and an element $K\in\mathcal{T}_h$, denote by $\mathbb{R}_l(K)$ either $\mathbb{P}_l(K)$ (i.e., the space of Lagrange polynomials of degree $\leq l$, defined on K), if the grids are formed by triangles ($d=2$) or tetrahedra ($d=3$), or $\mathbb{Q}_l(K)$ (i.e., the space of Lagrange polynomials of degree $\leq l$ on each variable, defined on K), if the family of triangulations is formed by quadrilaterals ($d=2$) or hexaedra ($d=3$). We consider the following FE spaces for the velocity:

$$\begin{cases} Y_h^l = V_h^l(\Omega) = \{v_h\in C^0(\overline{\Omega}) : v_{h_{|_K}}\in\mathbb{R}_l(K),\ \forall K\in\mathcal{T}_h\}, \\ \mathbf{Y}_h^l = [Y_h^l]^d = \{\mathbf{v}_h\in[C^0(\overline{\Omega})]^d : \mathbf{v}_{h_{|_K}}\in[\mathbb{R}_l(K)]^d,\ \forall K\in\mathcal{T}_h\}, \\ \mathbf{X}_h = \{\mathbf{v}_h\in\mathbf{Y}_h^l : \mathbf{v}_h=\mathbf{0} \text{ on } \overline{\Gamma}_D, \mathbf{v}_h\cdot\mathbf{n}_i=0 \text{ on } \Sigma_i, i=k,\dots,r\}\subset\mathbf{Y}_h^l, \end{cases} \tag{4.30}$$

where $\mathbf{n}_i$ is the outer normal to Σ_i for $i=k,\dots,r$, and we recall that $\overline{\Gamma}_n=\bigcup_{i=k}^{r}\Sigma_i$. Hereafter, $\mathbf{Y}_h^l$ (Y_h^l) will constitute the discrete foreground vectorial (scalar) spaces in which we will work on. We prove that the family of spaces $\{\mathbf{X}_h\}_{h>0}$ is effectively an internal approximation of $\mathbf{W}$, i.e. a family of finite-dimensional sub-spaces of $\mathbf{W}$ such that for any $\mathbf{v}\in\mathbf{W}$:

$$\lim_{h\to 0} d_{1,2,\Omega}(\mathbf{v},\mathbf{X}_h)=0,$$

where:

$$d_{1,2,\Omega}(\mathbf{v},\mathbf{X}_h)=\inf_{\mathbf{v}_h\in\mathbf{X}_h}\|\mathbf{v}-\mathbf{v}_h\|_{1,2,\Omega}.$$

To do it, let us consider the uniformly stable and convergent Bernardi-Maday-Rapetti (BMR, [6]) interpolation operator $\mathbb{P}_h$ from $[H^1(\Omega)]^d$ on $\mathbf{Y}_h^l$ as follows. Let us denote by $\mathcal{A}_h$ the set of Lagrange interpolation nodes for space $\mathbf{Y}_h^l$. Then:

$$\mathbb{P}_h\mathbf{v}=\sum_{\alpha\in\mathcal{A}_h}\overline{\mathbf{v}}_\alpha\,\lambda_\alpha(\mathbf{x})\quad\text{for }\mathbf{x}\in\overline{\Omega}, \tag{4.31}$$

where λ_α are the canonic basis functions of the Lagrange interpolation, given by:

$$\lambda_\alpha \in Y_h^l, \quad \lambda_\alpha(\beta) = \delta_{\alpha,\beta} \quad \text{for all } \alpha, \beta \in \mathcal{A}_h,$$

with $\delta_{\alpha,\beta}$ the Kronecker delta and $\overline{\mathbf{v}}_\alpha$ an averaged value of $\mathbf{v}$ in a neighborhood of node α. Following Chacón and Lewandowski [26], it may be proved that if the family of triangulations is admissible, then the values $\overline{\mathbf{v}}_\alpha$ may be chosen to preserve both the no-slip and slip boundary conditions: If $\mathbf{v} \in \mathbf{W}$, then

$$\left\{ \begin{array}{rcl} \overline{\mathbf{v}}_\alpha \cdot \mathbf{n}_{|_F} & = & 0 \quad \text{for any } F \in \partial\mathcal{T}_h(\alpha) \text{ if } \alpha \in \mathcal{A}_h \cap \overline{\Gamma}_n, \\ \overline{\mathbf{v}}_\alpha & = & \mathbf{0} \quad \text{if } \alpha \in \mathcal{A}_h \cap \overline{\Gamma}_D, \end{array} \right.$$

where:

$$\partial\mathcal{T}_h(\alpha) = \{ F \subset \Gamma \,:\, F \text{ is a side of some element of } \mathcal{T}_h \text{ such that } \alpha \in F \},$$

and $\mathbf{n}_{|_F}$ denotes the outer normal to Ω on F. Indeed, let us define the vector regularization operator $\overrightarrow{\pi}_\alpha$ as follows:

1. If α lies in the interior of Ω, let K_α be any element of $\mathcal{T}_h$ that contains α.

2. Else, either if $\alpha \in \overline{\Gamma}_D$ or α lies in the interior of some Σ_i, $i = k, \ldots, r$, let K_α be a side of some element of $\mathcal{T}_h$ such that $\alpha \in K_\alpha \subset \Sigma_i$, $i = 1, \ldots, r$.

   The vector regularization operator $\overrightarrow{\pi}_\alpha : [L^1(K_\alpha)]^d \to [\mathbb{R}_l(K_\alpha)]^d$ is defined componentwise as:

   $$\overrightarrow{\pi}_\alpha \mathbf{v} = (\pi_\alpha v_1, \ldots, \pi_\alpha v_d)^t, \tag{4.32}$$

   where $\pi_\alpha : L^1(K_\alpha) \to \mathbb{R}_l(K_\alpha)$ is given by:

   $$\int_{K_\alpha} (v - \pi_\alpha v) q = 0, \quad \text{for all } q \in \mathbb{R}_l(K_\alpha). \tag{4.33}$$

3. Else, α must belong to the intersection of (at least) two Σ_i, $i = k, \ldots, r$, say Σ_1 and Σ_2 for simplicity of notation. We associate to α two sets $K_{\alpha,1} \subset \Sigma_1$ and $K_{\alpha,2} \subset \Sigma_2$, both of them a side of some element of $\mathcal{T}_h$, and such that both contain α. Additionally, in 3D we associate one more set $K_{\alpha,3}$ defined as either $K_{\alpha,1}$ or $K_{\alpha,2}$.

   Let us respectively denote by $\mathbf{n}_1$ and $\mathbf{n}_2$ the normal vectors to Σ_1 and Σ_2, and $\mathbf{n}_3 = \mathbf{n}_1 \times \mathbf{n}_2$, $\mathbf{m}_2 = \mathbf{n}_1 \times \mathbf{n}_3$. Then, $\{\mathbf{n}_1, \mathbf{m}_2, \mathbf{n}_3\}$ is an orthogonal basis of $\mathbb{R}^3$ (in 2D, $\mathbf{n}_3 = \mathbf{0}$), and there exist two non-zero constants $a, b \in \mathbb{R}$ such that $\mathbf{n}_2 = a\,\mathbf{n}_1 + b\,\mathbf{m}_2$. We set:

   $$\begin{array}{rcl} \overrightarrow{\pi}_\alpha \mathbf{v} & = & \pi_\alpha^{(1)}(\mathbf{v} \cdot \mathbf{n}_1)\,\mathbf{n}_1 + \dfrac{1}{b}\left[\pi_\alpha^{(2)}(\mathbf{v} \cdot \mathbf{n}_2) - a\,\pi_\alpha^{(1)}(\mathbf{v} \cdot \mathbf{n}_1)\right]\,\mathbf{m}_2 \\ & + & \pi_\alpha^{(3)}(\mathbf{v} \cdot \mathbf{n}_3)\,\mathbf{n}_3, \text{ for } \mathbf{v} \in [H^1(\Delta_\alpha)]^d, \end{array} \tag{4.34}$$

   where $\pi_\alpha^{(1)}$, $\pi_\alpha^{(2)}$ and $\pi_\alpha^{(3)}$ are the regularization operators defined by (4.33) with K_α respectively equal to $K_{\alpha,1}$, $K_{\alpha,2}$ and $K_{\alpha,3}$, and Δ_α is the union of the elements of $\mathcal{T}_h$ that contain α.

Note that in the last case we assume $\mathbf{v} \in [H^1(\Delta_\alpha)]^d$, as then $(\mathbf{v}\cdot\mathbf{n})_{|_{K_{\alpha,i}}} \in L^4(K_{\alpha,i})$, $i = 1, 2$, and so $\overrightarrow{\pi}_\alpha \mathbf{v}$ is well defined. We can thus set:

$$\overline{\mathbf{v}}_\alpha = \overrightarrow{\pi}_\alpha \mathbf{v}(\alpha). \tag{4.35}$$

and then we have:

Lemma 4.6. *Assume that the family of triangulations $\{\mathcal{T}_h\}_{h>0}$ is admissible. Then, $\mathbb{P}_h\mathbf{v} \in \mathbf{X}_h$ if $\mathbf{v} \in \mathbf{W}$.*

Proof. Let $\mathbf{v} \in \mathbf{W}$, $\alpha \in \mathcal{A}_h$.

(i) If $\alpha \in \overline{\Gamma}_D$, then $K_\alpha \subset \overline{\Gamma}_D$, and by (4.33) we deduce $\overrightarrow{\pi}_\alpha \mathbf{v}(\alpha) = 0$. As $\{\mathcal{T}_h\}_{h>0}$ is admissible, from (4.31) we obtain:

$$\mathbb{P}_h\mathbf{v}(\mathbf{x}) = \sum_{\alpha\in\mathcal{A}_h\cap\overline{\Gamma}_D} \overrightarrow{\pi}_\alpha \mathbf{v}(\alpha)\, \lambda_\alpha(\mathbf{x}), \text{ for any } \mathbf{x} \in \overline{\Gamma}_D.$$

Consequently, $\mathbb{P}_h\mathbf{v} = 0$ on $\overline{\Gamma}_D$.

(ii) If α lies in the interior of some Σ_i, $i = k, \ldots, r$, from (4.33) we deduce:

$$\int_{K_\alpha} [\mathbf{v}\cdot\mathbf{n} - (\overrightarrow{\pi}_\alpha \mathbf{v})\cdot\mathbf{n}]\; q = 0, \text{ for all } q \in \mathbb{R}_l(K_\alpha),$$

where $\mathbf{n}$ is the normal to K_α. As $\mathbf{n}$ is constant, then $(\overrightarrow{\pi}_\alpha \mathbf{v})\cdot\mathbf{n} \in \mathbb{R}_l(K_\alpha)$. Consequently, $\overrightarrow{\pi}_\alpha \mathbf{v}\cdot\mathbf{n} = 0$ and, in particular, $(\overrightarrow{\pi}_\alpha \mathbf{v}(\alpha))\cdot\mathbf{n} = 0$.

(iii) Assume that α lies in the intersection of two Σ_i, $i = k, \ldots, r$, say Σ_1 and Σ_2 for simplicity of notation. Let us denote by $\mathbf{n}_i$ the normal to Σ_i, $i = 1, 2$. From (4.34) we readily deduce:

$$(\overrightarrow{\pi}_\alpha \mathbf{v})\cdot\mathbf{n}_1 = \pi_\alpha^{(1)}(\mathbf{v}\cdot\mathbf{n}_1), \quad (\overrightarrow{\pi}_\alpha \mathbf{v})\cdot\mathbf{n}_2 = \pi_\alpha^{(2)}(\mathbf{v}\cdot\mathbf{n}_2).$$

As $\mathbf{v} \in \mathbf{W}$, then $\mathbf{v}\cdot\mathbf{n}_i = 0$ a.e. on $K_{\alpha,i}$, $i = 1, 2$. Thus, $\pi_\alpha^{(i)}(\mathbf{v}\cdot\mathbf{n}_i)(\alpha) = 0$, $i = 1, 2$, reasoning as in the item (ii) above. As a consequence, $(\overrightarrow{\pi}_\alpha \mathbf{v}(\alpha))\cdot\mathbf{n}_i = 0$, $i = 1, 2$.

In sum, items (ii) and (iii) above prove that for any Σ_i, $i = k, \ldots, r$, and for any $\alpha \in \mathcal{A}_h \cap \Sigma_i$, it holds $(\overrightarrow{\pi}_\alpha \mathbf{v}(\alpha))\cdot\mathbf{n}_i = 0$, where $\mathbf{n}_i$ denotes the normal to Σ_i. As $\{\mathcal{T}_h\}_{h>0}$ is admissible, from (4.31) we obtain:

$$\mathbb{P}_h\mathbf{v}(\mathbf{x})\cdot\mathbf{n}_i = \sum_{\alpha\in\mathcal{A}_h\cap\Sigma_i} (\overrightarrow{\pi}_\alpha \mathbf{v}(\alpha))\cdot\mathbf{n}_i\, \lambda_\alpha(\mathbf{x}), \text{ for any } \mathbf{x} \in \Sigma_i.$$

Consequently, $(\mathbb{P}_h\mathbf{v})\cdot\mathbf{n}_i = 0$ on Σ_i, $i = k, \ldots, r$. ∎

Lemma 4.6 and the convergence in $H^1(\Omega)$ of the BMR interpolation operator $\mathbb{P}_h$ permits easily to conclude that the family $\{\mathbf{X}_h\}_{h>0}$ is an internal approximation of $\mathbf{W}$ if we consider a regular and admissible family of triangulations $\{\mathcal{T}_h\}_{h>0}$ of $\overline{\Omega}$.

4.4.2 Sub-grid eddy viscosity modeling

In this subsection, we detail the form c' appearing in the VMS-SGM discretization (4.29). To do so, let us introduce the space:

$$\overline{\mathbf{X}}_h = \{\mathbf{v}_h \in \mathbf{Y}_h^{l-1} : \mathbf{v}_h = \mathbf{0} \text{ on } \overline{\Gamma}_D, \mathbf{v}_h \cdot \mathbf{n}_i = 0 \text{ on } \Sigma_i, i = k, \ldots, r\}, \tag{4.36}$$

and consider a uniformly stable (in $H^1(\Omega)$-norm) interpolation operator Π_h on $\overline{\mathbf{Y}}_h$, where:

$$\overline{\mathbf{Y}}_h = [V_h^{l-1}(\Omega)]^d, \tag{4.37}$$

or:

$$\overline{\mathbf{Y}}_h = [V_H^{l}(\Omega)]^d, \tag{4.38}$$

and $V_H^l(\Omega)$ in (4.38) is a sub-space of $V_h^l(\Omega)$ with larger grid size $H > h$ (typically, $H = 2h$ or $H = 3h$). The considered interpolation operator Π_h must satisfy optimal error estimates (see Proposition 4.8 in the next section), and preserve both the no-slip and slip boundary conditions when restricted to $\mathbf{X}_h$. Thus, we define:

$$\mathbf{X}'_h = (Id - \Pi_h)\mathbf{X}_h,$$

where Id is the identity operator. In accordance to (4.37), we identify $\overline{\mathbf{X}}_h = \Pi_h \mathbf{X}_h \subset \overline{\mathbf{Y}}_h = [V_h^{l-1}(\Omega)]^d$ as the large scales velocity space, and $\mathbf{X}'_h$ as the sub-filter scales velocity space. Space $\mathbf{X}'_h$ does not need to be explicitly constructed, only the operator Π_h is needed. In accordance to (4.38), another possible definition of $\overline{\mathbf{X}}_h$ is:

$$\overline{\mathbf{X}}_h = \{\mathbf{v}_h \in [V_H^l(\Omega)]^d : \mathbf{v}_h = \mathbf{0} \text{ on } \overline{\Gamma}_D, \mathbf{v}_h \cdot \mathbf{n}_i = 0 \text{ on } \Sigma_i, i = k, \ldots, r\} \subset \overline{\mathbf{Y}}_h = [V_H^l(\Omega)]^d. \tag{4.39}$$

In practical implementations, we consider a standard nodal Lagrange interpolation operator Π_h for its simplicity and its efficiency with respect to other choices. This provides quite stable and accurate results. However, there exist other possibilities: we may mention the Scott-Zhang interpolation operator (*cf.* [79]), or the already cited BMR (*cf.* [6]). Also, the L^2-projection is used by John in [61] to define the large scales.

We take the form c' in (4.29) as a multi-scale Smagorinsky modeling of the eddy viscosity, given by:

$$c'(\mathbf{u}_h; \mathbf{u}_h, \mathbf{v}_h) = 2(\nu_T(\mathbf{u}'_h)D(\mathbf{u}'_h), D(\mathbf{v}'_h))_\Omega, \tag{4.40}$$

where:

$$\mathbf{u}'_h = \Pi_h^* \mathbf{u}_h, \quad \mathbf{v}'_h = \Pi_h^* \mathbf{v}_h, \quad \Pi_h^* = Id - \Pi_h,$$

and the eddy viscosity ν_T is defined as:

$$\nu_T(\mathbf{v})(\mathbf{x}) = (C_S h_K)^2 |D(\mathbf{v}_{|K})(\mathbf{x})| \quad \text{for } \mathbf{x} \in K, \tag{4.41}$$

where $|\cdot|$ denoties the Frobenius norm on $\mathbb{R}^{d\times d}$, and C_S is a (theoretically) universal constant. However, in practical applications, depending on the flow, the value of C_S may vary between 0.065 (*cf.* [69]) and 0.25 (*cf.* [67]). Here, we shall use an intermediate value

$C_S = 0.1$. Actually, it can be dynamically adapted in a time-dependent computation (see e.g. [40], [65]), to better fit the dissipation balance of the flow. It can also be adjusted close to solid walls, in order to avoid over-diffusion phenomena. This is usually done either by wall laws, or by "damping functions", that adjust the constant to the normal distance to the wall, so that (4.41) is changed to the expression (see Van Driest [83]):

$$\nu_T(\mathbf{v})(\mathbf{x}) = f(y^+)(C_S h_K)^2 |D(\mathbf{v}_{|K})(\mathbf{x})|, \quad \text{with } f(y^+) = 1 - \exp(-y^+/A^+), \tag{4.42}$$

where A^+ is the Van Driest constant, i.e. a constant distance located inside the logarithmic layer, that sets the intensity of the damping (typically, $A^+ = 26$).

Note that model (4.29) includes three grid levels: large resolved scales (those of $\overline{\mathbf{X}}_h$), sub-filter scales (those of $\mathbf{X}'_h$), and un-resolved scales (the remaining scales, that are taken into account by means of the eddy viscosity term). In the terminology of VMS methods, this corresponds to the *Small-Small* setting of the eddy viscosity (*cf.* [53]). Another possibility is to set the turbulent viscosity as a function of the whole resolved velocity field (the *Small-All* setting of the eddy viscosity in the terminology of VMS methods):

$$c'(\mathbf{u}_h; \mathbf{u}_h, \mathbf{v}_h) = 2(\nu_T(\mathbf{u}_h) D(\mathbf{u}'_h), D(\mathbf{v}'_h))_\Omega. \tag{4.43}$$

However, the *Small-Small* setting seems to be more meaningful from a physical point of view, and it provides in general more accurate results, so that we will use it hereafter.

In any case, the eddy viscosity only acts on the small resolved scales $\mathbf{u}'_h$ of the velocity. The role of the high frequency components $\mathbf{u}'_h$ is to absorb the energy consumed in the formation of small eddies in the inertial range. So, the basic grid to build space $\mathbf{X}_h$ should be fine enough to ensure that this space covers the large scales and an initial segment of the inertial range.

In Berselli et al. (*cf.* [7], Chapter 11), the eddy viscosity term (4.40) is reformulated as an eddy viscosity acting on the resolved small scales of the deformation tensor. This applies when the restriction operator is the elliptic projection Π_h on $\overline{\mathbf{Y}}_h$. This allows to rewrite the term c' as:

$$c'(\mathbf{u}_h; \mathbf{u}_h, \mathbf{v}_h) = 2(\nu_T(\widetilde{\Pi}^*_h D(\mathbf{u}_h)) \widetilde{\Pi}^*_h D(\mathbf{u}_h), \widetilde{\Pi}^*_h D(\mathbf{v}_h))_\Omega, \tag{4.44}$$

where $\widetilde{\Pi}^*_h = Id - \widetilde{\Pi}_h$, and we have denoted by $\widetilde{\Pi}_h$ the $[L^2(\Omega)]^{d\times d}$-orthogonal projection on the space:

$$L_h = D(\overline{\mathbf{Y}}_h) = \{d_h \in [L^2(\Omega)]^{d\times d} : d_h = D(\overline{\mathbf{w}}_h), \text{ for some } \overline{\mathbf{w}}_h \in \overline{\mathbf{Y}}_h\}.$$

Then, to compute the eddy viscosity, filtering the small scales of the velocity is equivalent to filter the small scale component of the deformation tensor. This allows in practice to replace the eddy viscosity term (4.40) by (4.44). However, this assumes that Π_h is the elliptic projection operator. This idea is also used by John in his works [58], [59], [60], [62].

Remark 4.7. *The standard Smagorinsky model was introduced in 1963 in the context of atmospheric weather prediction (cf. [80]). It is a LES model that relies on modeling the eddy viscosity effects by the form c defined by:*

$$c(\mathbf{u}_h; \mathbf{u}_h, \mathbf{v}_h) = 2(\nu_T(\mathbf{u}_h)D(\mathbf{u}_h), D(\mathbf{v}_h))_\Omega. \tag{4.45}$$

This form does not include the restriction term, so the eddy viscosity acts on both large and small resolved scales. This usually produces an over-diffusive effect, that the restriction term intends to correct.

4.4.3 Stabilization procedure

Remaining in the context of FEM, a more coherent VMS formulation to reproduce properly turbulent flows, when the convection term is dominant, must take into account also stabilizing terms (*cf.* [45]). Indeed, even choosing a pair of FE spaces for velocity-pressure satisfying the well-known uniform discrete inf-sup condition (*cf.* [9]), it has to be emphasized that a practical multi-scale implementation does not need to be stable "per se", unless using very fine grids, due to the dominant convection that generates spurious instabilities. On the contrary, most of the approaches rather demand for additional stabilization to represent a viable numerical method.

Stabilized discretizations were introduced by Hughes, Franca and co-workers. These discretizations are based upon an "augmented" variational formulation of the flow equations, that includes additional terms to the standard Galerkin discretization. Let us mention, for instance, the stabilized Galerkin-Least Squares (GALS) method, introduced in [52]. There exist several modifications of the GALS discretization for steady and unsteady flows: the Streamline Upwind Galerkin (SUPG) method (*cf.* [14]), the Adjoint-Stabilized (also called USFEM, Unusual Stabilized) method (*cf.* [38]), and the projection-stabilized methods (*cf.* [13], [15], [30], [32], [47]), that also increase the precision of the former. All of them share the properties of using equal-order interpolation in velocity and pressure (no additional degrees of freedom in velocity are needed, really, to achieve the stability of the pressure discretization), and of stabilizing the convection-dominance effects. Also, they are residual-based methods, in the sense that the stabilizing terms are products of the residual by some convenient test functions. As a consequence, the continuous solution exactly satisfies the discrete equations, whenever it is smooth enough.

An alternative is provided by the penalty-stabilized methods, that have a simpler and less expensive structure, but are only approximately consistent. Let us mention, in particular, the penalty term-by-term stabilized method (*cf.* [16]), that provides a separate stabilization of each single operator that could lead to unstable discretizations (e. g., convection, pressure gradient). An accurate and easy-to-implement stabilized method could be provided by the combination of projection-stabilized methods and penalty-stabilized methods. This is the high-order term-by-term stabilized method, that provides the separate stabilization of each single operator that could lead to unstable discretizations (e.g., convection, pressure gradient) as the penalty term-by-term stabilized method, but with higher accuracy (*cf.* [19], [20], [22]). This is a particular type of projection-stabilized

method, where each operator that needs stabilization is stabilized by least-squares interpolation penalty terms added to the Galerkin formulation.

The discretization of the VMS-SGM model (4.29) by the high-order term-by-term stabilized method reads as follows:

Find $(\mathbf{u}_h, p_h) \in (\mathbf{U}_{Dh} + \mathbf{X}_h) \times \mathbb{M}_h$ *such that:*

$$\left\{\begin{array}{rcl} b(\mathbf{u}_h;\mathbf{u}_h,\mathbf{v}_h) + a(\mathbf{u}_h,\mathbf{v}_h) + c'(\mathbf{u}_h;\mathbf{u}_h,\mathbf{v}_h) - (p_h, \nabla\cdot\mathbf{v}_h)_\Omega & + & \langle G(\mathbf{u}_h), \mathbf{v}_h\rangle \\ +s_{conv}(\mathbf{u}_h;\mathbf{v}_h) & = & \langle \mathbf{f}, \mathbf{v}_h\rangle, \\ \\ (\nabla\cdot\mathbf{u}_h, q_h)_\Omega + s_{pres}(p_h, q_h) & = & 0, \end{array}\right. \tag{4.46}$$

for all $(\mathbf{v}_h, q_h) \in \mathbf{X}_h \times \mathbb{M}_h$, where $\mathbf{X}_h$ is given by (4.30). As we can use the same interpolation for velocity and pressure, we consider the following FE pressure spaces:

$$\mathbb{M}_h = Y_h^l \cap L_0^2(\Omega),$$

where we recall that $Y_h^l = V_h^l(\Omega)$ is the foreground scalar space already given in (4.30). Let us also define the space:

$$\mathbf{Y}_{0h}^{l+1} = \{\mathbf{v}_h \in \mathbf{Y}_h^{l+1} : \mathbf{v}_h = \mathbf{0} \text{ on } \overline{\Gamma}\} \subset \mathbf{Y}_h^{l+1},$$

and consider an approximation $\mathbf{U}_{Dh} \in \mathbf{Y}_h^{l+1}$ of $\mathbf{U}_D$ such that $\mathbf{U}_{Dh} = \mathbf{0}$ on $\overline{\Gamma}_n$, given by the Stokes projection:

$$\left\{\begin{array}{rcl} (D(\mathbf{U}_{Dh}), D(\mathbf{v}_h))_\Omega - (r_h, \nabla\cdot\mathbf{v}_h)_\Omega & = & (D(\mathbf{U}_D), D(\mathbf{v}_h))_\Omega, \\ \\ (\nabla\cdot\mathbf{U}_{Dh}, q_h)_\Omega & = & 0, \end{array}\right. \tag{4.47}$$

for all $(\mathbf{v}_h, q_h) \in \mathbf{Y}_{0h}^{l+1} \times \mathbb{M}_h$, and some associated pressure $r_h \in \mathbb{M}_h$. As the family of pairs of FE spaces $\{(\mathbf{Y}_{0h}^{l+1}, \mathbb{M}_h)\}_{h>0}$ satisfies the so-called uniform discrete inf-sup condition (exhaustively described, for instance, in Brezzi and Fortin [9]), it is well-known that this problem admits a unique solution that satisfies:

$$\|D(\mathbf{U}_{Dh})\|_{0,2,\Omega} \leq C\|D(\mathbf{U}_D)\|_{0,2,\Omega}, \tag{4.48}$$

$$\|\mathbf{U}_D - \mathbf{U}_{Dh}\|_{1,2,\Omega} \leq C d_{1,2,\Omega}(\mathbf{U}_D, \mathbf{Y}_h^{l+1}), \tag{4.49}$$

for some constant $C > 0$ independent of h. In (4.46), we search really for a solution $\mathbf{u}_h = \mathbf{u}_{0h} + \mathbf{U}_{Dh}$, with $\mathbf{u}_{0h} \in \mathbf{X}_h$, and $\mathbf{U}_{Dh}$ given by (4.47).

Coming back to (4.46), the forms s_{conv} and s_{pres} correspond to the high-order term-by-term stabilized method, and are given by:

$$s_{conv}(\mathbf{u}_h;\mathbf{v}_h) = \sum_{K\in\mathcal{T}_h} \tau_{\nu,K}(\sigma_h^*(\mathbf{u}_h\cdot\nabla\mathbf{u}_h), \sigma_h^*(\mathbf{u}_h\cdot\nabla\mathbf{v}_h))_K,$$

$$s_{pres}(p_h, q_h) = \sum_{K\in\mathcal{T}_h} \tau_{p,K}(\sigma_h^*(\nabla p_h), \sigma_h^*(\nabla q_h))_K.$$

Here, $\tau_{\nu,K}$ and $\tau_{p,K}$ are stabilization coefficients for convection and pressure gradient, respectively, and $\sigma_h^* = Id - \sigma_h$, where σ_h is some locally stable (in $L^2(\Omega)$-norm) projection or interpolation operator on the foreground vectorial space $\mathbf{Y}_h^{l-1}$ (also called "buffer space" in this context). The proposed method provides a separate stabilization of convection and pressure gradient with high accuracy. In practical implementations, we choose σ_h as a Scott-Zhang-like interpolation operator on space $\mathbf{Y}_h^{l-1}$ (*cf.* [79]). This gives rise to a discretization with a reduced computational cost, but that maintains the same high-order accuracy with respect to standard projection-stabilized methods. Furthermore, if needed, specific stabilizations for convection and pressure gradient may be used, via different approximation operators and stabilization coefficients. Note that the case $\sigma_h^* = Id$ corresponds to the pure penalty-stabilized method.

The interpolation operators σ_h and Π_h must satisfy the following properties (*cf.* [6]), that we will use in the sequel:

Proposition 4.8. *Consider a regular family of triangulations $\{\mathcal{T}_h\}_{h>0}$ of $\overline{\Omega}$, and an integer $l \geq 1$. Then, there exists an interpolation operator $L_h : L^1(\Omega) \to V_h^l(\Omega)$ satisfying:*

(i) **Stability.** *For any $v \in L^p(\Omega)$, $1 \leq p < +\infty$:*

$$\|L_h(v)\|_{0,p,K} \leq C\|v\|_{0,p,\omega_K} \quad \forall K \in \mathcal{T}_h, \tag{4.50}$$

where, for any $K \in \mathcal{T}_h$, we denote by ω_K the union of all elements of $\mathcal{T}_h$ that intersect K. In addition:

$$\|L_h(v)\|_{0,p,\Omega} \leq C\|v\|_{0,p,\Omega}. \tag{4.51}$$

Moreover, for any $v \in W^{1,p}(\Omega)$:

$$\|L_h(v)\|_{1,p,\Omega} \leq C\|v\|_{1,p,\Omega}, \tag{4.52}$$

where $C > 0$ is a constant only depending on p, Ω, d and the aspect ratio of the family of triangulations.

(ii) **Error estimates.** *Let $m = 0$ or $m = 1$. If $v \in H^s(\Omega)$ for $m + 1 \leq s \leq l + 1$, then:*

$$\|v - L_h(v)\|_{m,p,K} \leq C h_K^{s-m+d/p-d/2} |v|_{s,2,\omega_K}, \quad \forall K \in \mathcal{T}_h. \tag{4.53}$$

In addition:

$$\|v - L_h(v)\|_{m,p,\Omega} \leq C h^{s-m+d/p-d/2} |v|_{k,2,\Omega}, \tag{4.54}$$

where $C > 0$ is a constant only depending on m, p, s, Ω, d and the aspect ratio of the family of triangulations.

Note that the standard nodal Lagrange interpolation operator satisfies the properties of Proposition 4.8 for functions that additionally belongs to $C^0(\overline{\Omega})$.

For the subsequent numerical analysis of model (4.46), we also need the following technical hypothesis on the stabilization coefficients:

Hypothesis 4.9. *The stabilization coefficients $\tau_{\nu,K}$, $\tau_{p,K}$ appearing in the stabilization terms s_{conv}, s_{pres}, respectively, satisfy the following condition:*

$$\alpha_1 h_K^2 \leq \tau_{\nu,K},\, \tau_{p,K} \leq \alpha_2 h_K^2, \quad \forall K \in \mathcal{T}_h, \tag{4.55}$$

for some positive constants α_1 and α_2, independent of h.

We will work with the following expression for the stabilization coefficients:

$$\tau_{\nu,K} = \tau_{p,K} = \left[\left(c_1 \frac{\nu + \overline{\nu}_{T|_K}}{h_K^2} \right) + \left(c_2 \frac{U_K}{h_K} \right) \right]^{-1}, \tag{4.56}$$

by adapting the form of Codina (*cf.* [29]), designed by asymptotic scaling arguments applied to the framework of stabilized methods. In (4.56), c_1 and c_2 are experimental positive constants, $\overline{\nu}_{T|_K}$ is some local eddy viscosity on element K, and U_K is some local speed on element K. We assume U_K uniformly bounded from below and from above for technical reasons. This ensures (4.55). We are now ready to start the numerical analysis of model (4.46) in Chapter 5.

Chapter 5

Numerical Analysis of VMS-SGM

5.1 Introduction

In this chapter, we perform the numerical analysis of the approximation of steady laminar and turbulent flows by model (4.46), with the *Small-Small* setting of the eddy viscosity term c' defined by (4.40)-(4.41). In the sequel, we will call this model VMS-S model. This analysis may be extended to other definitions of the eddy viscosity term c' already cited in Chapter 4, with slight modifications.

We first introduce some technical results that are required for the numerical analysis. Then, we prove stability in natural norms and perform a convergence analysis to the Navier-Stokes equations with rather realistic boundary conditions, that include wall laws and inflow boundary conditions, in steady regime. We obtain weak convergence in natural norms, and we prove that a result of strong convergence for solutions with natural minimal regularity is obtained by the use of the Galerkin method, together with the subsequent asymptotic energy balance. Moreover, we analyze the approximation of diffusion-dominated flows by the stabilized VMS-S method, through the computation of error estimates. The error analysis strengthen the fact that the proposed model is suitable both for laminar and turbulent flows. We obtain optimal error estimates with respect to the polynomial interpolation for laminar smooth flows. This results permits to prove the strong convergence of the stabilized VMS-S method for slightly smooth flows, and a consequent asymptotic energy balance of the system, in which the deformation and the friction boundary energy are asymptotically conserved, and the dissipated eddy energy so as the sub-grid energy due to stabilizing terms tend to zero. For technical reasons, we will assume throughout the work that the family of triangulations $\{\mathcal{T}_h\}_{h>0}$ is uniformly regular. Actually, this technical hypothesis may be relaxed to the more general case of regular grids, but we keep it to focus the analysis on the new aspects of the method, and to not unnecessarily lengthen it.

The chapter is structured as follows: In Section 5.2, we establish some technical considerations, essential for the numerical analysis of the VMS-S method, which is the core of the chapter. This analysis deals with existence (Section 5.3) and weak convergence (Section 5.4) for solutions with the natural minimal regularity. This implies in particular

the existence of weak solutions of problem (4.1), so as its stability with respect to FE multi-scale discretizations. We also insert the proof of strong convergence for solutions with the natural minimal regularity in the context of mixed methods (Subsection 5.4.1), that allows to study the asymptotic energy balance of the corresponding system for any solutions, without needing further regularity. Finally, in Section 5.5, we come back to the stabilized VMS-S method, and perform the error analysis. The VMS-S method attempts optimal accuracy for laminar regular flows, and the order decreases with the regularity. The error analysis allows to conclude the strong convergence of VMS-S method for slightly smooth flows, and to study the corresponding asymptotic energy balance of the system (Subsection 5.5.1). We obtain that the total energy balance is asymptotically maintained in such a way that the deformation energy and the energy dissipated at the wall pass to the limit. In addition, the dissipated sub-grid energy due to the eddy viscosity and the stabilizing terms asymptotically vanish.

The main results presented in this chapter can be found in [23].

5.2 Technical background

We state in this section some technical results that are required for the numerical analysis. We shall denote hereafter by C, C_0, C_1, C_2, ... constants that may vary from a line to another, but which are always independent of h.

We first establish the main properties of the main operators involved in the weak formulation of the steady Navier-Stokes equations (4.1), i.e. the transport operator defined by the form b and the diffusion operator defined by the form a.

Lemma 5.1. *The form b defined by (4.3) verifies the following properties:*

(i) b is trilinear and bounded in $[H^1(\Omega)]^d$:

$$|b(\mathbf{z};\mathbf{v},\mathbf{w})| \leq C\|\mathbf{z}\|_{1,2,\Omega}\|\mathbf{v}\|_{1,2,\Omega}\|\mathbf{w}\|_{1,2,\Omega}, \tag{5.1}$$

for all $\mathbf{z}$, $\mathbf{v}$, $\mathbf{w} \in [H^1(\Omega)]^d$, and some constant $C > 0$ only depending on Ω.

(ii) b is antisymmetric:

$$b(\mathbf{z};\mathbf{v},\mathbf{w}) = -b(\mathbf{z};\mathbf{w},\mathbf{v}), \tag{5.2}$$

for all $\mathbf{z}$, $\mathbf{v}$, $\mathbf{w} \in [H^1(\Omega)]^d$.

Proof.

(i) The form b is obviously trilinear. The boundedness in $[H^1(\Omega)]^d$ follows by Sobolev embedding theorem and Hölder's inequality. Indeed, let $\mathbf{z}$, $\mathbf{v}$, $\mathbf{w} \in [H^1(\Omega)]^d$. We have:

$$|(\mathbf{z}\cdot\nabla\mathbf{v},\mathbf{w})_\Omega| \leq \|\mathbf{z}\|_{0,4,\Omega}\|\nabla\mathbf{v}\|_{0,2,\Omega}\|\mathbf{w}\|_{0,4,\Omega} \leq C\|\mathbf{z}\|_{1,2,\Omega}\|\mathbf{v}\|_{1,2,\Omega}\|\mathbf{w}\|_{1,2,\Omega},$$

where C is a constant only depending on Ω, by using the injection $H^1(\Omega) \hookrightarrow L^4(\Omega)$. Then (5.1) follows.

(ii) Property (5.2) directly follows from definition (4.3) of form b.

■

Lemma 5.2. *The form a defined by (4.4) is bilinear and bounded in $[H^1(\Omega)]^d$.*

Proof. The form a is obviously bilinear. Let $\mathbf{v}$, $\mathbf{w} \in [H^1(\Omega)]^d$. By Cauchy-Schwarz inequality, we get:

$$|a(\mathbf{v},\mathbf{w})| \leq 2\nu \|D(\mathbf{v})\|_{0,2,\Omega} \|D(\mathbf{w})\|_{0,2,\Omega},$$

hence the continuity of a. ■

The following well-known local inverse inequalities (*cf.* [6]) will be frequently used in the sequel. Their proof consists in a standard application of norm equivalence on finite-dimensional spaces.

Lemma 5.3. *Let q_1, q_2 be two real numbers such that $1 \leq q_1, q_2 \leq +\infty$. Let k_1, k_2 be two non-negative integer numbers. Assume that $k_2 \leq k_1$ and $k_2 - d/q_2 \leq k_1 - d/q_1$. For each non-negative integer l there exists a constant $C > 0$ such that:*

$$\forall K \in \mathcal{T}_h, \quad \forall p \in \mathbb{R}_l(K), \quad |p|_{k_1,q_1,K} \leq C \rho_K^{k_2-k_1-\frac{d}{q_2}} h_K^{\frac{d}{q_1}} |p|_{k_2,q_2,K}, \tag{5.3}$$

where ρ_K is the diameter of the ball inscribed in K.

If in addition the family of triangulations $\{\mathcal{T}_h\}_{h>0}$ is regular (i.e., $h_K \leq s\rho_K$, for s positive constant independent of h), then there exists a constant $C > 0$ such that:

$$\forall K \in \mathcal{T}_h, \quad \forall p \in \mathbb{R}_l(K), \quad |p|_{k_1,q_1,K} \leq C h_K^{k_2-k_1-\frac{d}{q_2}+\frac{d}{q_1}} |p|_{k_2,q_2,K}, \tag{5.4}$$

for all $\mathcal{T}_h$, where the constant C only depends on q_1, q_2, k_1, k_2, d, l, and the aspect ratio of the family of triangulations.

We now define the scalar products:

$$\begin{aligned} (\cdot,\cdot)_{\tau_\nu} : L^2(\Omega) \times L^2(\Omega) &\longrightarrow \mathbb{R}, \\ (f,g)_{\tau_\nu} &\longrightarrow \sum_{K\in\mathcal{T}_h} \tau_{\nu,K}(f,g)_K, \\ (\cdot,\cdot)_{\tau_p} : L^2(\Omega) \times L^2(\Omega) &\longrightarrow \mathbb{R}, \\ (f,g)_{\tau_p} &\longrightarrow \sum_{K\in\mathcal{T}_h} \tau_{p,K}(f,g)_K, \end{aligned}$$

and their associated norms:

$$\|f\|_{\tau_\nu} = (f,f)_{\tau_\nu}^{1/2}, \quad \|f\|_{\tau_p} = (f,f)_{\tau_p}^{1/2}.$$

Lemma 5.4. *Assume that Hypothesis 4.9 holds. Then, the following conditions are satisfied:*

$$\forall z \in L^2(\Omega), \quad C_1 \sum_{K\in\mathcal{T}_h} h_K^2 \|z\|_{0,2,K}^2 \leq \|z\|_\tau^2 \leq C_2 \sum_{K\in\mathcal{T}_h} h_K^2 \|z\|_{0,2,K}^2, \tag{5.5}$$

where τ denotes either τ_ν or τ_p, and:

$$\forall g \in L^2(\Omega), \quad ||\sigma_h^*(g)||_\tau \leq C\, h ||g||_{0,2,\Omega}. \tag{5.6}$$

Proof. Estimates (5.5) immediately follow from Hypothesis 4.9. Now, let $g \in L^2(\Omega)$. By applying the second part of (5.5) to $\sigma_h^*(g)$, we obtain:

$$\|\sigma_h^*(g)\|_\tau^2 \leq C_2 \sum_{K\in\mathcal{T}_h} h_K^2 \|\sigma_h^*(g)\|_{0,2,K}^2 \leq C_2 h^2 \|\sigma_h^*(g)\|_{0,2,\Omega}^2 \leq Ch^2 \|g\|_{0,2,\Omega}^2,$$

where we have used the global stability property (4.51) of σ_h, due to the regularity of the mesh. Thus, we conclude:

$$\|\sigma_h^*(g)\|_\tau \leq Ch\|g\|_{0,2,\Omega}.$$

■

We next state a specific discrete inf-sup condition for stabilized approximations, that is essential for the stability of method (4.46). The main difficulty in its proof stems from the fact that the interpolation operator σ_h takes value in $\mathbf{Y}_h^{l-1}$, thus reducing the effective number of degrees of freedom (d.o.f.) of the foreground velocity space $\mathbf{Y}_h^l$.

Lemma 5.5. *Assume that Hypothesis 4.9 holds. Then, we have the following inf-sup condition:*

$$\forall q_h \in \mathbb{M}_h, \quad \|q_h\|_{0,2,\Omega} \leq C \left(\sup_{\mathbf{v}_h\in\mathbf{X}_h} \frac{|(\nabla\cdot\mathbf{v}_h, q_h)_\Omega|}{\|D(\mathbf{v}_h)\|_{0,2,\Omega}} + \|\sigma_{p,h}^*(\nabla q_h)\|_{\tau_p} \right), \tag{5.7}$$

for some positive constant C independent of h.

The proof of this Lemma can be derived from [19], and consists in an adaptation of a discrete inf-sup condition obtained by Verfürth (*cf.* [84]). Actually, in [19] the discrete inf-sup condition (5.7) is proved with the discrete velocity space $\mathbf{X}_{0h} = [V_h^l(\Omega) \cap H_0^1(\Omega)]^d$, but since $\mathbf{X}_{0h} \subset \mathbf{X}_h$, then it is trivially valid also in our case. Moreover, note that the discrete inf-sup condition (5.7) can be extended to a more complex condition, that holds for regular family of triangulations, as proved in [19]. However, in that case, the analysis becomes quite lengthy, and here we restrict it to uniformly regular grids.

Our analysis also needs some properties of the eddy viscosity ν_T defined by (4.41) and the form c' defined by (4.40), that we state next.

Lemma 5.6. *There exists a constant $C > 0$ only depending on d, Ω and the aspect ratio of the family of triangulations such that:*

$$\|\nu_T(\mathbf{v}_h')\|_{0,\infty,\Omega} \leq C\, h^{2-d/2}\, \|D(\mathbf{v}_h)\|_{0,2,\Omega}, \tag{5.8}$$

$$|c'(\mathbf{v}_h; \mathbf{v}_h, \mathbf{w}_h)| \leq C\, h^{2-d/2}\, \|D(\mathbf{v}_h)\|_{0,2,\Omega}^2 \|D(\mathbf{w}_h)\|_{0,2,\Omega}. \tag{5.9}$$

Proof. As $\nabla\mathbf{v}_h'$ is piecewise discontinuous, then there exists $K \in \mathcal{T}_h$ such that:

$$\|\nu_T(\mathbf{v}_h')\|_{0,\infty,\Omega} = \|\nu_T(\mathbf{v}_h')\|_{0,\infty,K} \leq C_S^2\, h_K^2\, \|D(\mathbf{v}_h')\|_{0,\infty,K}.$$

By the local inverse estimate (5.4):

$$\|\nabla\mathbf{v}_h'\|_{0,\infty,K} \leq C\, h_K^{-d/2}\, \|\nabla\mathbf{v}_h'\|_{0,2,K},$$

for some constant $C > 0$ only depending on d and the aspect ratio of the family of triangulations. Then:

$$\begin{aligned}\|\nu_T(\mathbf{v}'_h)\|_{0,\infty,\Omega} &\leq CC_S^2\, h_K^{2-d/2}\, \|D(\mathbf{v}'_h)\|_{0,2,K} \leq C\, h^{2-d/2}\, \|D(\mathbf{v}'_h)\|_{0,2,\Omega} \\ &\leq C\, h^{2-d/2}\, \|D((Id-\Pi_h)\mathbf{v}_h)\|_{0,2,\Omega} \leq C\, h^{2-d/2}\, \|D(\mathbf{v}_h)\|_{0,2,\Omega} \quad (5.10)\end{aligned}$$

where the last inequality follows from the (H^1-)uniform stability property (4.52) of the interpolation operator Π_h. By estimate (5.8) and the (H^1-)uniform stability of the interpolation operator Π_h:

$$\begin{aligned}|c'(\mathbf{v}_h;\mathbf{v}_h,\mathbf{w}_h)| &\leq 2\|\nu_T(\mathbf{v}'_h)\|_{0,\infty,\Omega}\, \|D(\mathbf{v}'_h)\|_{0,2,\Omega}\|D(\mathbf{w}'_h)\|_{0,2,\Omega} \\ &\leq C\, h^{2-d/2}\, \|D(\mathbf{v}_h)\|_{0,2,\Omega}^2\|D(\mathbf{w}_h)\|_{0,2,\Omega}.\end{aligned}$$

■

Also, the convection stabilizing term s_{conv} satisfies the following estimate:

Lemma 5.7. *Assume that Hypothesis 4.9 holds. Then:*

$$|s_{conv}(\mathbf{u}_h;\mathbf{v}_h)| \leq Ch^{2-d/2}\|D(\mathbf{u}_h)\|_{0,2,\Omega}^3\|D(\mathbf{v}_h)\|_{0,2,\Omega}, \quad (5.11)$$

for some constant $C > 0$ only depending on d, Ω and the aspect ratio of the family of triangulations.

Proof. By the definition of the form s_{conv}, we have:

$$\begin{aligned}|s_{conv}(\mathbf{u}_h;\mathbf{v}_h)| &= \left|\sum_{K\in\mathcal{T}_h} \tau_{\nu,K}(\sigma_h^*(\mathbf{u}_h\cdot\nabla\mathbf{u}_h),\sigma_h^*(\mathbf{u}_h\cdot\nabla\mathbf{v}_h))_K\right| \\ &\leq C\sum_{K\in\mathcal{T}_h} h_K^2\|\sigma_h^*(\mathbf{u}_h\cdot\nabla\mathbf{u}_h)\|_{0,2,K}\|\sigma_h^*(\mathbf{u}_h\cdot\nabla\mathbf{v}_h)\|_{0,2,K},\end{aligned}$$

where we have applied Hypothesis 4.9 and Cauchy-Schwarz inequality.

By using the (L^2-)local stability property (4.50) of the interpolation operator σ_h, we obtain:

$$\begin{aligned}|s_{conv}(\mathbf{u}_h;\mathbf{v}_h)| &\leq C\sum_{K\in\mathcal{T}_h} h_K^2\|\mathbf{u}_h\cdot\nabla\mathbf{u}_h\|_{0,2,\omega_K}\|\mathbf{u}_h\cdot\nabla\mathbf{v}_h\|_{0,2,\omega_K} \\ &\leq C\|\mathbf{u}_h\|_{0,4,\Omega}^2\sum_{K\in\mathcal{T}_h} h_K^2\|D(\mathbf{u}_h)\|_{0,4,\omega_K}\|D(\mathbf{v}_h)\|_{0,4,\omega_K},\end{aligned}$$

where we have applied Hölder's inequality. By Sobolev embedding theorem, we can write:

$$\begin{aligned}|s_{conv}(\mathbf{u}_h;\mathbf{v}_h)| &\leq C\|D(\mathbf{u}_h)\|_{0,2,\Omega}^2\sum_{K\in\mathcal{T}_h} h_K^2\|D(\mathbf{u}_h)\|_{0,4,\omega_K}\|D(\mathbf{v}_h)\|_{0,4,\omega_K} \\ &\leq C\|D(\mathbf{u}_h)\|_{0,2,\Omega}^2\sum_{K\in\mathcal{T}_h} h_K^{2-d/2}\|D(\mathbf{u}_h)\|_{0,2,\omega_K}\|D(\mathbf{v}_h)\|_{0,2,\omega_K},\end{aligned}$$

where in the last inequality we have applied the local inverse estimate (5.4) and the local uniform regularity of the grid, which is implied by the regularity. Using again the regularity of the grid, which implies that $card(\omega_K) \leq N$ bounded for any K, we finally obtain:

$$\begin{aligned} |s_{conv}(\mathbf{u}_h;\mathbf{v}_h)| &\leq Ch^{2-d/2}\|D(\mathbf{u}_h)\|_{0,2,\Omega}^2 \left(\sum_{K\in\mathcal{T}_h}\|D(\mathbf{u}_h)\|_{0,2,\omega_K}^2\right)^{1/2}\left(\sum_{K\in\mathcal{T}_h}\|D(\mathbf{v}_h)\|_{0,2,\omega_K}^2\right)^{1/2} \\ &\leq Ch^{2-d/2}\|D(\mathbf{u}_h)\|_{0,2,\Omega}^3\|D(\mathbf{v}_h)\|_{0,2,\Omega}. \end{aligned}$$

■

5.3 Existence and stability results

Problem (4.46) is equivalent to a system of algebraic non-linear equations in finite dimension. The non-linearity is due to several effects: the convection operator, the VMS-eddy viscosity, the convection stabilizing term, and the wall-law boundary condition. We use the Brouwer fixed point theorem to prove that it admits a solution (*cf.* [8]). In particular, we have the following stability result:

Theorem 5.8. *Assume that Hypothesis 4.9 holds. Let* $\mathbf{f}\in\mathbf{W}'$. *Then, if* $\|D(\mathbf{U}_D)\|_{0,2,\Omega}$ *is small enough, problem (4.46) admits at least a solution, that satisfies the estimate:*

$$\|D(\mathbf{u}_{0h})\|_{0,2,\Omega}+\|\sigma_h^*(\mathbf{u}_{0h}\cdot\nabla\mathbf{u}_{0h})\|_{\tau_\nu}+\|\sigma_h^*(\nabla p_h)\|_{\tau_p}+\|p_h\|_{0,2,\Omega}\leq C\left(\|\mathbf{f}\|_{\mathbf{W}'};\|D(\mathbf{U}_D)\|_{0,2,\Omega}\right), \tag{5.12}$$

where $C>0$ *is an increasing function of the data norms* $\|\mathbf{f}\|_{\mathbf{W}'}$, $\|D(\mathbf{U}_D)\|_{0,2,\Omega}$, *independent of* h.

Proof. We prove the existence and stability of solutions in 4 steps.

Step 1. Linearization of (4.46).
Let $\mathbf{w}_h=\mathbf{w}_{0h}+\mathbf{U}_{Dh}$, with $\mathbf{w}_{0h}\in\mathbf{X}_h$ such that $\|D(\mathbf{w}_{0h})\|_{0,2,\Omega}\leq R$ (where R is a positive constant independent of h to be determined later), and consider the following linearized problem:

Given $\mathbf{f}\in\mathbf{W}'$, find $(\mathbf{u}_{0h},p_h)\in\mathbf{X}_h\times\mathbb{M}_h$ such that:

$$B_T(\mathbf{w}_h,(\mathbf{u}_{0h},p_h),(\mathbf{v}_h,q_h))=\langle\widetilde{\mathbf{f}},\mathbf{v}_h\rangle, \tag{5.13}$$

for all $(\mathbf{v}_h,q_h)\in\mathbf{X}_h\times\mathbb{M}_h$, where:

$$\begin{aligned} B_T(\mathbf{w}_h,(\mathbf{u}_{0h},p_h),(\mathbf{v}_h,q_h)) &= b(\mathbf{w}_h,\mathbf{u}_{0h},\mathbf{v}_h)+a(\mathbf{u}_{0h},\mathbf{v}_h)+c'(\mathbf{w}_h,\mathbf{u}_{0h},\mathbf{v}_h) \\ -(p_h,\nabla\cdot\mathbf{v}_h)_\Omega+\widehat{s}_{conv}(\mathbf{u}_{0h},\mathbf{v}_h) &+ \langle\widehat{G}(\mathbf{u}_{0h}),\mathbf{v}_h\rangle+(\nabla\cdot\mathbf{u}_{0h},q_h)_\Omega+s_{pres}(p_h,q_h), \end{aligned}$$

and:

$$\langle\widetilde{\mathbf{f}},\mathbf{v}_h\rangle=\langle\mathbf{f},\mathbf{v}_h\rangle-b(\mathbf{w}_h,\mathbf{U}_{Dh},\mathbf{v}_h)-a(\mathbf{U}_{Dh},\mathbf{v}_h)-c'(\mathbf{w}_h,\mathbf{U}_{Dh},\mathbf{v}_h)-\widehat{s}_{conv}(\mathbf{U}_{Dh},\mathbf{v}_h).$$

The symbol $\widehat{\ }$ denotes the linearization of the corresponding terms with respect to $\mathbf{w}_h$, i.e.:

$$\begin{aligned}\widehat{s}_{conv}(\mathbf{u}_{0h},\mathbf{v}_h) &= \sum_{K\in\mathcal{T}_h}\tau_{\nu,K}(\sigma_h^*(\mathbf{w}_h\cdot\nabla\mathbf{u}_{0h}),\sigma_h^*(\mathbf{w}_h\cdot\nabla\mathbf{v}_h))_K,\\ \langle\widehat{G}(\mathbf{u}_{0h}),\mathbf{v}_h\rangle &= \int_{\Gamma_n}\mathbf{u}_{0h}\cdot\mathbf{v}_h\,e(|\mathbf{w}_h|)\,ds,\end{aligned}$$

where the function $e:\mathbb{R}_+\to\mathbb{R}$ is defined by:

$$e(|\mathbf{u}|)=\begin{cases}\dfrac{[u_\tau(|\mathbf{u}|)]^2}{|\mathbf{u}|} & \text{if } |\mathbf{u}|>0,\\[2ex] \dfrac{1}{(y/\nu)K_1} & \text{if } |\mathbf{u}|=0,\end{cases}\tag{5.14}$$

and K_1 is given by (4.9). We recall that u_τ is the unique solution (see Lemma 4.1) of the implicit equation (4.7). We prove that e is continuous. Indeed, let us re-write equation (4.7) as:

$$|\mathbf{u}| = u_\tau L(u_\tau y/\nu) = F(u_\tau).$$

The wall-law function L is strictly increasing and continuous, then F is strictly increasing and continuous. Due to (4.9), $\lim_{u_\tau\to 0^+}F(u_\tau)=0$ and $\lim_{u_\tau\to\infty}F(u_\tau)=+\infty$. It implies that $u_\tau=F^{-1}(|\mathbf{u}|)$ is continuous, and so e is continuous at any $|\mathbf{u}|\neq 0$. To prove the continuity at $|\mathbf{u}|=0$, we set $t=u_\tau(|\mathbf{u}|)$. Then, $|\mathbf{u}|=tL(\lambda t)$, with $\lambda=y/\nu$, and:

$$\lim_{|\mathbf{u}|\to 0}e(|\mathbf{u}|)=\lim_{t\to 0}\frac{t^2}{tL(\lambda t)}=\lim_{t\to 0}\frac{t}{L(\lambda t)}=\frac{1}{\lambda K_1},$$

where the last identity follows from (4.9). We deduce that $e(|\mathbf{w}_h|)$ is bounded on $\overline{\Omega}$:

$$\max_{\mathbf{x}\in\overline{\Omega}}e(|\mathbf{w}_h(\mathbf{x})|)\le M(\|\mathbf{w}_h\|_{0,\infty,\Omega}),\ \text{where } M(r)=\max_{x\in[0,r]}e(x).$$

The estimate for the form $\widehat{G}$ becomes:

$$\begin{aligned}\langle\widehat{G}(\mathbf{u}_{0h}),\mathbf{v}_h\rangle &\le M(\|\mathbf{w}_h\|_{0,\infty,\Omega})\|\mathbf{u}_{0h}\|_{0,2,\Gamma_n}\|\mathbf{v}_h\|_{0,2,\Gamma_n}\\ &\le CM(\|\mathbf{w}_h\|_{0,\infty,\Omega})\|D(\mathbf{u}_{0h})\|_{0,2,\Omega}\|D(\mathbf{v}_h)\|_{0,2,\Omega}.\end{aligned}\tag{5.15}$$

Step 2. Existence of solution of problem (5.13).
Problem (5.13) is equivalent to a linear system with $dim(\mathbf{X}_h)+dim(\mathbb{M}_h)$ unknowns and equations. Then, the existence of solutions is equivalent to its uniqueness. To prove uniqueness, let us assume that problem (5.13) admits a solution $(\mathbf{u}_{0h},p_h)\in\mathbf{X}_h\times\mathbb{M}_h$, that we next estimate in terms of the data.

- Velocity estimate.

Take $\mathbf{v}_h = \mathbf{u}_{0h}$ and $q_h = p_h$ in (5.13) as test functions. This yields:

$$2\nu\|D(\mathbf{u}_{0h})\|^2_{0,2,\Omega}+c'(\mathbf{w}_h,\mathbf{u}_{0h},\mathbf{u}_{0h})+\widehat{s}_{conv}(\mathbf{u}_{0h},\mathbf{u}_{0h})+\langle\widehat{G}(\mathbf{u}_{0h}),\mathbf{u}_{0h}\rangle+s_{pres}(p_h,p_h)=\langle\widetilde{\mathbf{f}},\mathbf{u}_{0h}\rangle,$$

as the form b is antisymmetric. Since the form c' and $\widehat{G}$ are non-negative, we have:

$$2\nu\|D(\mathbf{u}_{0h})\|^2_{0,2,\Omega}+\widehat{s}_{conv}(\mathbf{u}_{0h},\mathbf{u}_{0h})+s_{pres}(p_h,p_h)\leq\langle\widetilde{\mathbf{f}},\mathbf{u}_{0h}\rangle. \tag{5.16}$$

From the boundedness of the forms b and a in $[H^1(\Omega)]^d$, and (5.9), it follows:

$$\begin{aligned}\langle\widetilde{\mathbf{f}},\mathbf{u}_{0h}\rangle &\leq (\|\mathbf{f}\|_{\mathbf{W}'}+\delta)\|D(\mathbf{u}_{0h})\|_{0,2,\Omega}+C_0R\|D(\mathbf{U}_D)\|_{0,2,\Omega}\|D(\mathbf{u}_{0h})\|_{0,2,\Omega}\\ &+ C_1[diam(\Omega)]^{2-d/2}(R+\|D(\mathbf{U}_D)\|_{0,2,\Omega})\|D(\mathbf{U}_D)\|_{0,2,\Omega}+|\widehat{s}_{conv}(\mathbf{U}_{Dh},\mathbf{u}_{0h})|,\end{aligned}$$

where $\delta=(C_0\|D(\mathbf{U}_D)\|_{0,2,\Omega}+2\nu)\|D(\mathbf{U}_D)\|_{0,2,\Omega}$, and we have used (4.48). By applying Hypothesis 4.9 and Young's inequality, we have:

$$|\widehat{s}_{conv}(\mathbf{U}_{Dh},\mathbf{u}_{0h})|\leq C_2\left(\sum_{K\in\mathcal{T}_h}\frac{h_K^2}{2}\|\sigma_h^*(\mathbf{w}_h\cdot\nabla\mathbf{U}_{Dh})\|^2_{0,2,K}\right)+\frac{1}{2}\widehat{s}_{conv}(\mathbf{u}_{0h},\mathbf{u}_{0h})=I+II.$$

Using the (L^2-)local stability property (4.50) of the interpolation operator σ_h on the first summand I, we obtain:

$$\begin{aligned}I &\leq C_3\sum_{K\in\mathcal{T}_h}h_K^2(\|\mathbf{w}_{0h}\cdot\nabla\mathbf{U}_{Dh}\|^2_{0,2,\omega_K}+\|\mathbf{U}_{Dh}\cdot\nabla\mathbf{U}_{Dh}\|^2_{0,2,\omega_K})\\ &\leq C_3\sum_{K\in\mathcal{T}_h}h_K^2(\|\mathbf{w}_{0h}\|^2_{0,\infty,\omega_K}+\|\mathbf{U}_{Dh}\|^2_{0,\infty,\omega_K})\|D(\mathbf{U}_{Dh})\|^2_{0,2,\omega_K},\end{aligned}$$

where we have used Hölder's inequality in the last line. By the local inverse estimate (5.4), the regularity of the grid, and the Sobolev embedding theorem, we can write:

$$\begin{aligned}I &\leq C_4\sum_{K\in\mathcal{T}_h}h_K^{2(1-d/4)}(\|\mathbf{w}_{0h}\|^2_{0,4,\omega_K}+\|\mathbf{U}_{Dh}\|^2_{0,4,\omega_K})\|D(\mathbf{U}_{Dh})\|^2_{0,2,\omega_K}\\ &\leq C_5\,h^{2(1-d/4)}(R^2+\|D(\mathbf{U}_D)\|^2_{0,2,\Omega})\|D(\mathbf{U}_D)\|^2_{0,2,\Omega}\leq M(R),\end{aligned}$$

with $M(R)=C_5\,[diam(\Omega)]^{2(1-d/4)}(R^2+\|D(\mathbf{U}_D)\|^2_{0,2,\Omega})\|D(\mathbf{U}_D)\|^2_{0,2,\Omega}$. Collecting all these estimates, from (5.16) we obtain:

$$\begin{aligned}&2\nu\|D(\mathbf{u}_{0h})\|^2_{0,2,\Omega}+\frac{1}{2}\widehat{s}_{conv}(\mathbf{u}_{0h},\mathbf{u}_{0h})+s_{pres}(p_h,p_h)\\ \leq\ &\left[\|\mathbf{f}\|_{\mathbf{W}'}+\widetilde{\delta}(R)\right]\|D(\mathbf{u}_{0h})\|_{0,2,\Omega}+M(R),\end{aligned}$$

where we have denoted:

$$\widetilde{\delta}(R)=\delta+\{C_0R+C_1[diam(\Omega)]^{2-d/2}(R+\|D(\mathbf{U}_D)\|_{0,2,\Omega})\}\|D(\mathbf{U}_D)\|_{0,2,\Omega}.$$

Using Young's inequality:

$$\nu\|D(\mathbf{u}_{0h})\|^2_{0,2,\Omega} + \frac{1}{2}\,\widehat{s}_{conv}(\mathbf{u}_{0h},\mathbf{u}_{0h}) + s_{pres}(p_h,p_h) \leq \frac{\Big[\|\mathbf{f}\|_{\mathbf{W}'} + \widetilde{\delta}(R)\Big]^2}{4\nu} + M(R).$$

Finally, we conclude:

$$\|D(\mathbf{u}_{0h})\|_{0,2,\Omega} \leq \frac{\Big[\|\mathbf{f}\|_{\mathbf{W}'} + \widetilde{\delta}(R)\Big]}{2\nu} + \sqrt{\frac{M(R)}{\nu}}; \tag{5.17}$$

$$\|\sigma^*_h(\mathbf{w}_h\cdot\nabla\mathbf{u}_{0h})\|_{\tau_\nu} \leq \frac{\Big[\|\mathbf{f}\|_{\mathbf{W}'} + \widetilde{\delta}(R)\Big]}{\sqrt{2\,\nu}} + \sqrt{2\,M(R)}; \tag{5.18}$$

$$\|\sigma^*_{p,h}(\nabla p_h)\|_{\tau_p} \leq \frac{\Big[\|\mathbf{f}\|_{\mathbf{W}'} + \widetilde{\delta}(R)\Big]}{2\sqrt{\nu}} + \sqrt{M(R)}. \tag{5.19}$$

Observe that the bound (5.17) may be written as:

$$\|D(\mathbf{u}_{0h})\|_{0,2,\Omega} \leq \mathcal{K} + \frac{\mathcal{A}}{2}\|D(\mathbf{U}_D)\|_{0,2,\Omega}R, \tag{5.20}$$

with:

$$\mathcal{K} = \frac{[\|\mathbf{f}\|_{\mathbf{W}'} + \delta]}{2\nu} + \frac{\left(C_1 + 2\sqrt{C_5\nu}\right)[diam(\Omega)]^{2-d/2}}{2\nu}\,\|D(\mathbf{U}_D)\|^2_{0,2,\Omega}, \tag{5.21}$$

and:

$$\mathcal{A} = \frac{C_0 + \left(C_1 + 2\sqrt{C_5\nu}\right)[diam(\Omega)]^{2-d/2}}{\nu}. \tag{5.22}$$

As we want $\mathbf{w}_{0h}$ in the same ball of $\mathbf{u}_{0h}$, we impose $R = 2\mathcal{K}$, so that it must be:

$$\|D(\mathbf{u}_{0h})\|_{0,2,\Omega} \leq \mathcal{K} + \mathcal{A}\|D(\mathbf{U}_D)\|_{0,2,\Omega}\mathcal{K} \leq 2\mathcal{K}, \tag{5.23}$$

thai is satisfied if:

$$\|D(\mathbf{U}_D)\|_{0,2,\Omega} \leq \mathcal{A}^{-1}.$$

- Pressure estimate.

Take $q_h = 0$ in (5.13). Using the previous estimates, this yields:

$$\begin{aligned} |(p_h,\nabla\cdot\mathbf{v}_h)_\Omega| &\leq |-\langle\widetilde{\mathbf{f}},\mathbf{v}_h\rangle + b(\mathbf{w}_h,\mathbf{u}_{0h},\mathbf{v}_h) + a(\mathbf{u}_{0h},\mathbf{v}_h) + c'(\mathbf{w}_h,\mathbf{u}_{0h},\mathbf{v}_h) \\ &+ \widehat{s}_{conv}(\mathbf{u}_{0h},\mathbf{v}_h) + \langle\widehat{G}(\mathbf{u}_{0h}),\mathbf{v}_h\rangle| \end{aligned}$$

$$\leq C\left\{\|\widetilde{\mathbf{f}}\|_{\mathbf{W}'} + \left[1 + h^{2-d/2} + 2\nu + M(\|\mathbf{w}_h\|_{0,\infty,\Omega})\right]\|D(\mathbf{u}_{0h})\|_{0,2,\Omega}\right\}\|D(\mathbf{v}_h)\|_{0,2,\Omega}$$

$$\leq C\left\{\|\widetilde{\mathbf{f}}\|_{\mathbf{W}'} + [1 + \nu + M(\|\mathbf{w}_h\|_{0,\infty,\Omega})]\,\mathcal{K}\right\}\|D(\mathbf{v}_h)\|_{0,2,\Omega},$$

where the second inequality follows from the boundedness of the forms b and a in $[H^1(\Omega)]^d$, and we have used properties (5.9), (5.11) and (5.15) to estimate respectively the forms c', $\widehat{s}_{conv}$ and $\widehat{G}$, while the last inequality follows from (5.23). By the discrete inf-sup condition (5.7) and the fact that $\|\sigma^*_{p,h}(\nabla p_h)\|_{\tau_p} \leq 2\sqrt{\nu}\mathcal{K}$, we obtain:

$$\begin{aligned}\|p_h\|_{0,2,\Omega} &\leq C\left(\sup_{\mathbf{v}_h\in\mathbf{X}_h}\frac{|(\nabla\cdot\mathbf{v}_h,p_h)_\Omega|}{\|D(\mathbf{v}_h)\|_{0,2,\Omega}}+\|\sigma^*_{p,h}(\nabla p_h)\|_{\tau_p}\right)\\ &\leq C\left\{\|\widetilde{\mathbf{f}}\|_{\mathbf{W}'}+\left[1+\nu+\sqrt{\nu}+M(\|\mathbf{w}_h\|_{0,\infty,\Omega})\right]\mathcal{K}\right\}.\end{aligned}$$

Step 3. Existence of solution of problem (4.46).
We use Brouwer fixed point theorem to prove existence of solution of problem (4.46). Let us define the mapping $\mathcal{F}:\mathbf{X}_h\mapsto\mathbf{X}_h$, that transforms $\mathbf{w}_{0h}\in\mathbf{X}_h$ into $\mathbf{u}_{0h}$, the unique solution of problem (5.13). The previous estimates and the uniqueness of solution of (5.13) allow to prove the continuity of $\mathcal{F}$. Indeed, let $\{\mathbf{w}_n\}_{n\in\mathbb{N}}\subset\mathbf{X}_h$ be a sequence convergent to $\mathbf{w}\in[H^1(\Omega)]^d$. Let us consider the sequence of images $\{\mathcal{F}(\mathbf{w}_n)\}_{n\in\mathbb{N}}=\{\mathbf{u}_n\}_{n\in\mathbb{N}}\subset\mathbf{X}_h$. The previous estimates allow to extract a sub-sequence, that we denote in the same way, strongly convergent (as $\mathbf{X}_h$ is of finite dimension) to $\mathbf{t}\in\mathbf{X}_h$. Also, there exists a sub-sequence $\{p_n\}_{n\in\mathbb{N}}\subset\mathbb{M}_h$ strongly convergent to $p\in\mathbb{M}_h$. We take the limit $n\to+\infty$ in:

$$B_T(\mathbf{w}_n,(\mathbf{u}_n,p_n),(\mathbf{v}_h,q_h))=\langle\widetilde{\mathbf{f}},\mathbf{v}_h\rangle,\quad\forall(\mathbf{v}_h,q_h)\in\mathbf{X}_h\times\mathbb{M}_h.$$

Note that, as we are working in finite dimension, B_T is a continuous function, as all terms appearing in the definition of B_T are continuous functions of the d.o.f. of their arguments. We can conclude that:

$$B_T(\mathbf{w},(\mathbf{t},p),(\mathbf{v}_h,q_h))=\langle\widetilde{\mathbf{f}},\mathbf{v}_h\rangle,\quad\forall(\mathbf{v}_h,q_h)\in\mathbf{X}_h\times\mathbb{M}_h.$$

Thus, $\mathcal{F}(\mathbf{w})=\mathbf{t}$. As the limit problem satisfied by $\mathbf{t}$ admits a unique solution, then the whole sequence $\{\mathcal{F}(\mathbf{w}_n)\}_{n\in\mathbb{N}}$ converges to it, by *reductio ad absurdum*. The previous estimates (5.23) also prove that $\mathcal{F}$ transforms the closed ball $\overline{B}_{\mathbf{X}_h}(0,2\mathcal{K})$ into itself. Then, by Brouwer fixed point theorem, the mapping $\mathcal{F}$ admits a fixed point. This fixed point is a solution of (4.46), satisfying the estimate (5.12) for the first three summands.

Step 4. Estimate (5.12).
It remains just to prove that the estimate for $\|p_h\|_{0,2,\Omega}$ does not depend on h for the non-linear problem (4.46). Note that the dependence on h in the linear case is due to estimate (5.15) of the form $\widehat{G}$, where M depends on $\|\mathbf{w}_h\|_{0,\infty,\Omega}$, and thus on h. Instead, in the non-linear case, we can directly apply (4.17) to estimate the form G, and thus the pressure estimate does not depend on h. Indeed, we have:

$$\begin{aligned}|(p_h,\nabla\cdot\mathbf{v}_h)_\Omega| &\leq |-\langle\widetilde{\mathbf{f}},\mathbf{v}_h\rangle+b(\mathbf{u}_h;\mathbf{u}_{0h},\mathbf{v}_h)+a(\mathbf{u}_{0h},\mathbf{v}_h)+c'(\mathbf{u}_h;\mathbf{u}_{0h},\mathbf{v}_h)\\ &+ s_{conv}(\mathbf{u}_h;\mathbf{u}_{0h},\mathbf{v}_h)+\langle G(\mathbf{u}_{0h}),\mathbf{v}_h\rangle|\end{aligned}$$

where now:

$$\langle\widetilde{\mathbf{f}},\mathbf{v}_h\rangle=\langle\mathbf{f},\mathbf{v}_h\rangle-b(\mathbf{u}_h;\mathbf{U}_{Dh},\mathbf{v}_h)-a(\mathbf{U}_{Dh},\mathbf{v}_h)-c'(\mathbf{u}_h;\mathbf{U}_{Dh},\mathbf{v}_h)-s_{conv}(\mathbf{u}_h;\mathbf{U}_{Dh},\mathbf{v}_h).$$

Following the proof of the previous error estimate for the linear problem (5.13), and applying (4.17) to estimate the form G, we obtain:

$$\begin{aligned} |(p_h, \nabla \cdot \mathbf{v}_h)_\Omega| &\leq C \left\{ \|\mathbf{f}\|_{\mathbf{W}'} + \left(1 + h^{2-d/2} + 2\nu\right) \|D(\mathbf{u}_{0h})\|_{0,2,\Omega} \right\} \|D(\mathbf{v}_h)\|_{0,2,\Omega} \\ &+ C \left\{ (1 + h^{2-d/2})(1 + \|D(\mathbf{u}_{0h})\|_{0,2,\Omega}^2) \right\} \|D(\mathbf{v}_h)\|_{0,2,\Omega} \\ &\leq C \left\{ \|\mathbf{f}\|_{\mathbf{W}'} + (1+\nu)\mathcal{K} + (1+\mathcal{K}^2) \right\} \|D(\mathbf{v}_h)\|_{0,2,\Omega}. \end{aligned}$$

By the discrete inf-sup condition (5.7) and the fact that $\|\sigma_{p,h}^*(\nabla p_h)\|_{\tau_p} \leq 2\sqrt{\nu}\mathcal{K}$, we obtain:

$$\begin{aligned} \|p_h\|_{0,2,\Omega} &\leq C \left(\sup_{\mathbf{v}_h \in \mathbf{X}_h} \frac{|(\nabla \cdot \mathbf{v}_h, p_h)_\Omega|}{\|D(\mathbf{v}_h)\|_{0,2,\Omega}} + \|\sigma_{p,h}^*(\nabla p_h)\|_{\tau_p} \right) \\ &\leq C \left\{ \|\mathbf{f}\|_{\mathbf{W}'} + (1 + \nu + \sqrt{\nu})\mathcal{K} + (1+\mathcal{K}^2) \right\}, \end{aligned}$$

and we have no more dependence on h. ■

Remark 5.9. *The estimate for the convective stabilization term makes apparent a certain stabilization of the convective derivative. We next give an interpretation of this mechanism.*

In convection-dominated flows, the velocities provided by the Galerkin method lose stability in L^∞. Small-period oscillations appear, unless the grid size is small enough. For practical applications, where Reynolds number may reach the value of 10^4 (or greater), this restriction is frequently unaffordable, and stabilization procedures are needed.

This phenomenon seemingly is due to an accumulation of sub-grid energy: when the grid is not fine enough, the initial viscosity ν of the problem can not dissipate all the energy, and the flow produces short-period (or high-frequency) oscillations. This accumulation of energy is only in part counter-balanced in method (4.46) by the eddy diffusion term c', deriving from a multi-scale sub-grid discretization, because without the stabilizing terms, this method is in practice a Galerkin method (cf. [21]). So, while the pressure stabilization term is used to estimate the pressure by means of the specific discrete inf-sup condition introduced, the convective stabilization term, as indeed is a diffusive term, helps to counter-balance the accumulation of energy. We are thus adding some numerical diffusion, that together with the one provided by the sub-grid eddy viscosity, permits to replace the sub-grid dissipation of energy which is not present at all in a simple multi-scale sub-grid discretization. The space of high frequencies of the numerical velocity is given by the operator σ_h^*. So that, $\sigma_h^*(\mathbf{u}_h \cdot \nabla \mathbf{u}_h)$ represents the high-frequency component of the convective derivative. The estimate of the convective stabilization term guarantees an extra-control on the high frequencies of the convective derivative, which is not obtained by the standard VMS-SGM method (4.29).

Some of these ideas are used in [18] to elaborate a post-processing of oscillating solutions of the steady Navier-Stokes equations, discretized by a standard Galerkin FE method.

5.4 Convergence analysis

The convergence analysis is based upon the theory developed in [17], that enables to extend to stabilized methods the standard techniques for the numerical analysis of mixed methods.

We shall need a technical result that allows to represent formulation (4.2) as an internal approximation of an "augmented" variational formulation.

Definition 5.10. *A FE space $\mathbb{Z}_h$, constructed on a triangulation $\mathcal{T}_h$, is called a* **bubble FE space** *if, for all $b_h \in \mathbb{Z}_h$, for all $K \in \mathcal{T}_h$, $b_h \in H^1_0(K)$.*

A similar definition applies for vectorial bubble FE spaces.

Lemma 5.11. *There exists a family $\{\mathbb{Z}_h\}_{h>0}$ of bubble FE sub-spaces of $[H^1_0(\Omega)]^d$ and a family $\{\mathcal{S}_h\}_{h>0}$ of bilinear uniformly continuous and uniformly coercive forms on $[H^1_0(\Omega)]^d$ such that:*

$$s_{pres}(p_h, q_h) = \mathcal{S}_h(\mathcal{R}_h(\sigma^*_{p,h}(\nabla p_h)), \mathcal{R}_h(\sigma^*_{p,h}(\nabla q_h))), \quad \forall p_h, q_h \in \mathbb{M}_h, \tag{5.24}$$

where $\mathcal{R}_h : [H^{-1}(\Omega)]^d \to \mathbb{Z}_h$ is the "static condensation" operator on $\mathbb{Z}_h$ defined as follows:

Given $\varphi \in [H^{-1}(\Omega)]^d$, $\mathcal{R}_h(\varphi)$ is the only element of $\mathbb{Z}_h$ that satisfies:

$$\mathcal{S}_h(\mathcal{R}_h(\varphi), z_h) = \langle \varphi, z_h \rangle, \quad \forall z_h \in \mathbb{Z}_h.$$

This result is proved in [17]. We shall also need the following property of bubble FE spaces (*cf.* [17]):

Lemma 5.12. *If a sequence $\{\mathbb{Z}_h\}_{h>0}$ of bubble FE sub-spaces of $[H^1_0(\Omega)]^d$ is uniformly bounded in $[H^1_0(\Omega)]^d$, then it weakly converges to zero in $[H^1_0(\Omega)]^d$.*

We now state the weak convergence of solutions provided by method (4.46) to a weak solution of the Navier-Stokes boundary value problem (4.2).

Theorem 5.13. *Assume that Hypothesis 4.9 holds. Then, the sequence $\{(\mathbf{u}_h, p_h)\}_{h>0}$ of solutions of the VMS-S approximation (4.46) contains a sub-sequence which is weakly convergent in $[H^1(\Omega)]^d \times L^2(\Omega)$ to a solution of the steady Navier-Stokes equations (4.2). If this solution is unique, then the whole sequence converges to it.*

Proof. The proof is divided into various steps.

Step 1. Extracting sub-sequences.
Due to estimate (5.12), the sequence $\{(\mathbf{u}_{0h}, p_h)\}_{h>0}$ is uniformly bounded in the space $\mathbf{W} \times \mathbb{M}$, which is a Hilbert space. Then, it contains a sub-sequence, that we still denote in the same way, weakly convergent in that space to some pair $(\mathbf{u}_0, p)$. As the injection of $H^1(\Omega)$ in $L^q(\Omega)$ is compact for $1 \leq q < q^* = 2d/(d-2)$, by the Rellich-Kondrakov compactness theorem (*cf.* [8]) we may assume that the sub-sequence $\{\mathbf{u}_{0h}\}_{h>0}$ is strongly convergent in $[L^q(\Omega)]^d$, and so, in particular, in $[L^4(\Omega)]^d$. Also, the operator G is compact

from $\mathbf{W}$ to its dual $\mathbf{W}'$, by Lemma 4.4. Then, we may assume that the sub-sequence $\{G(\mathbf{u}_{0h})\}_{h>0}$ is strongly convergent in $\mathbf{W}'$. We recall that by (4.49) $\mathbf{U}_{Dh}$ is strongly converges to $\mathbf{U}_D$ in $[H^1(\Omega)]^d$. Let us prove that $(\mathbf{u}, p)$ is a solution of problem (4.2), where $\mathbf{u} = \mathbf{u}_0 + \mathbf{U}_D$.

Step 2. Limit of convection terms.
Let us consider a pair of test functions $(\mathbf{v}, q)$ such that $\mathbf{v} \in \mathbf{W}$, $q \in \mathcal{D}(\Omega) \cap \mathbb{M}$, where $\mathcal{D}(\Omega)$ is the space of $C_0^\infty(\Omega)$-functions (i.e., smooth functions with compact support), which is dense in $L^2(\Omega)$ (*cf.* [66]). As $\mathbf{X}_h$ is an internal approximation of $\mathbf{W}$ (see Subsection 4.4.1), then there exists a sequence $\{\mathbf{v}_h\}_{h>0} \in \mathbf{X}_h$ strongly convergent to $\mathbf{v}$ in $\mathbf{W}$. Moreover, as $\mathbb{M}_h$ is an internal approximation of $H^1(\Omega) \cap \mathbb{M}$, then there exists a sequence $\{q_h\}_{h>0} \in \mathbb{M}_h$ strongly convergent to q in particular in $\mathbb{M}$. We have:

$$\begin{aligned}
& |(\mathbf{u}_h \cdot \nabla \mathbf{u}_h, \mathbf{v}_h)_\Omega - (\mathbf{u} \cdot \nabla \mathbf{u}, \mathbf{v})_\Omega| \\
\leq\ & |((\mathbf{u}_h - \mathbf{u}) \cdot \nabla \mathbf{u}_h, \mathbf{v}_h)_\Omega| + |(\mathbf{u} \cdot \nabla (\mathbf{u}_h - \mathbf{u}), \mathbf{v})_\Omega| + |(\mathbf{u} \cdot \nabla \mathbf{u}_h, \mathbf{v}_h - \mathbf{v})_\Omega| \\
\leq\ & \|\mathbf{u}_h - \mathbf{u}\|_{0,4,\Omega} \|\nabla \mathbf{u}_h\|_{0,2,\Omega} \|\mathbf{v}_h\|_{0,4,\Omega} + \sum_{i,j=1}^{d} |(\partial_j (u_{h,i} - u_i), u_j v_i)_\Omega| \\
+\ & \|\mathbf{u}_h\|_{0,4,\Omega} \|\nabla \mathbf{u}_h\|_{0,2,\Omega} \|\mathbf{v}_h - \mathbf{v}\|_{0,4,\Omega},
\end{aligned}$$

where we have denoted $\mathbf{u}_h = (u_{h,1}, \ldots, u_{h,d})$. All terms in the r.h.s. of the last inequality vanish in the limit because $\{\mathbf{u}_h\}_{h>0}$ is strongly convergent in $[L^4(\Omega)]^d$, $\{\partial_i u_{h,i}\}_{h>0}$ is weakly convergent in $L^2(\Omega)$, and $\{\mathbf{v}_h\}_{h>0}$ is strongly convergent in $[H^1(\Omega)]^d$. Then:

$$\lim_{h \to 0} (\mathbf{u}_h \cdot \nabla \mathbf{u}_h, \mathbf{v}_h)_\Omega = (\mathbf{u} \cdot \nabla \mathbf{u}, \mathbf{v})_\Omega.$$

Similarly:

$$\lim_{h \to 0} (\mathbf{u}_h \cdot \nabla \mathbf{v}_h, \mathbf{u}_h)_\Omega = (\mathbf{u} \cdot \nabla \mathbf{v}, \mathbf{u})_\Omega,$$

and then:

$$\lim_{h \to 0} b(\mathbf{u}_h; \mathbf{u}_h, \mathbf{v}_h) = b(\mathbf{u}; \mathbf{u}, \mathbf{v}).$$

Moreover, by (5.11), for the convection stabilizing term we have:

$$|s_{conv}(\mathbf{u}_h; \mathbf{v}_h)| \leq C h^{2-d/2} \|D(\mathbf{u}_h)\|_{0,2,\Omega}^3 \|D(\mathbf{v}_h)\|_{0,2,\Omega}.$$

Since the sequences $\{\mathbf{u}_h\}_{h>0}$ and $\{\mathbf{v}_h\}_{h>0}$ are bounded in $[H^1(\Omega)]^d$, we deduce:

$$\lim_{h \to 0} s_{conv}(\mathbf{u}_h; \mathbf{v}_h) = 0.$$

Step 3. Limit of diffusion terms.
As a is bilinear and continuous:

$$\lim_{h \to 0} a(\mathbf{u}_h, \mathbf{v}_h) = a(\mathbf{u}, \mathbf{v}).$$

Next, since the sequences $\{\mathbf{u}_h\}_{h>0}$ and $\{\mathbf{v}_h\}_{h>0}$ are bounded in $[H^1(\Omega)]^d$, we deduce from Lemma 5.6:

$$\lim_{h\to 0} c'(\mathbf{u}_h;\mathbf{u}_h,\mathbf{v}_h) = 0.$$

Step 4. Limit of pressure terms.
Since $\{\nabla\cdot\mathbf{u}_h\}_{h>0}$ is weakly convergent in $L^2(\Omega)$ to $\nabla\cdot\mathbf{u}$ and $\{q_h\}_{h>0}$ is strongly convergent in $L^2(\Omega)$ to q:

$$\lim_{h\to 0}(\nabla\cdot\mathbf{u}_h, q_h)_\Omega = (\nabla\cdot\mathbf{u}, q)_\Omega.$$

Also, we obviously have:

$$\lim_{h\to 0}(p_h, \nabla\cdot\mathbf{v}_h)_\Omega = (p, \nabla\cdot\mathbf{v})_\Omega.$$

The pressure stabilizing term also vanishes in the limit. To prove this, we use the representation formula (5.24). This yields:

$$\begin{aligned}\|\sigma^*_{p,h}(\nabla p_h)\|^2_{\tau_p} = s_{pres}(p_h,p_h) &= \mathcal{S}_h(\mathcal{R}_h(\sigma^*_{p,h}(\nabla p_h)),\mathcal{R}_h(\sigma^*_{p,h}(\nabla p_h)))\\ &\geq \mu_S\|\mathcal{R}_h(\sigma^*_{p,h}(\nabla p_h))\|^2_{H^1_0(\Omega)},\end{aligned}$$

using the uniform coercivity of the forms $\mathcal{S}_h$. Then, using the fact that $\|\sigma^*_{p,h}(\nabla p_h)\|_{\tau_p} \leq 2\sqrt{\nu}\mathcal{K}$, we deduce that the sequence $\{\mathcal{R}_h(\sigma^*_{p,h}(\nabla p_h))\}_{h>0}$ is uniformly bounded in $[H^1_0(\Omega)]^d$ and, by Lemma 5.12, as:

$$s_{pres}(p_h,q_h) = \mathcal{S}_h(\mathcal{R}_h(\sigma^*_{p,h}(\nabla p_h)),\mathcal{R}_h(\sigma^*_h(\nabla q_h))) = \langle\sigma^*_{p,h}(\nabla q_h),\mathcal{R}_h(\sigma^*_{p,h}(\nabla p_h))\rangle,$$

we conclude:

$$\lim_{h\to 0} s_{pres}(p_h,q_h) = 0.$$

Consequently, the pair $(\mathbf{u},p)$ is a weak solution of the Navier-Stokes equations (4.2).

Step 5. Uniqueness.
As this weak convergence follows from a compactness argument, it is standard to prove, by *reductio ad absurdum*, that if the limit is unique, then the whole sequence converges to it, in the same weak sense. ■

5.4.1 Convergence analysis for mixed methods

In this subsection, we prove a result of strong convergence for solutions with natural minimal regularity that holds for mixed methods. To approximate problem (4.1), let us consider the following mixed formulation:

Find $(\mathbf{u}_h,p_h)\in(\mathbf{U}_{Dh}+\mathbf{X}_h)\times\mathbb{M}_h$ *such that:*

$$\left\{\begin{array}{rcl} b(\mathbf{u}_h;\mathbf{u}_h,\mathbf{v}_h)+a(\mathbf{u}_h,\mathbf{v}_h)+c'(\mathbf{u}_h;\mathbf{u}_h,\mathbf{v}_h)-(p_h,\nabla\cdot\mathbf{v}_h)_\Omega+\langle G(\mathbf{u}_h),\mathbf{v}_h\rangle &=& \langle\mathbf{f},\mathbf{v}_h\rangle,\\ (\nabla\cdot\mathbf{u}_h,q_h)_\Omega &=& 0,\end{array}\right. \tag{5.25}$$

for all $(\mathbf{v}_h, q_h) \in \mathbf{X}_h \times \mathbb{M}_h$, where now $\{(\mathbf{X}_h, \mathbb{M}_h)\}_{h>0}$ is a family of pairs of FE spaces that is an internal approximation of $\mathbf{W} \times \mathbb{M}$, and at the same time satisfies the uniform discrete inf-sup condition (*cf.* [9]):

$$\forall q_h \in \mathbb{M}_h, \quad \|q_h\|_{0,2,\Omega} \leq C \sup_{\mathbf{v}_h \in \mathbf{X}_h} \frac{|(\nabla \cdot \mathbf{v}_h, q_h)_\Omega|}{\|D(\mathbf{v}_h)\|_{0,2,\Omega}}, \tag{5.26}$$

for some positive constant C independent of h. As for the stabilized VMS-S method (4.46), problem (5.25) admits at least a solution $(\mathbf{u}_h, p_h)$ uniformly bounded in $[H^1(\Omega)]^d \times L^2(\Omega)$. This result is the key to prove the following:

Theorem 5.14. *Assume that Hypothesis 4.9 holds. Then, the sequence $\{(\mathbf{u}_h, p_h)\}_{h>0}$ of solutions of the mixed approximation (5.25) contains a sub-sequence which is strongly convergent in $[H^1(\Omega)]^d \times L^2(\Omega)$ to a solution of the steady Navier-Stokes equations (4.2).*

Proof. The weak convergence of a sub-sequence (that we denote in the same way) is proved analogously to Theorem 5.13, so that we directly prove the strong convergence.

- Strong convergence of the velocities.

Set $\mathbf{v}_h = \mathbf{u}_{0h}$ in (5.25). Then:

$$\begin{aligned} 2\nu\|D(\mathbf{u}_{0h})\|^2_{0,2,\Omega} &= \langle \mathbf{f}, \mathbf{u}_{0h} \rangle - b(\mathbf{U}_{Dh}; \mathbf{U}_{Dh}, \mathbf{u}_{0h}) - b(\mathbf{u}_{0h}; \mathbf{U}_{Dh}, \mathbf{u}_{0h}) - a(\mathbf{U}_{Dh}, \mathbf{u}_{0h}) \\ &- c'(\mathbf{u}_h; \mathbf{u}_h, \mathbf{u}_{0h}) - \langle G(\mathbf{u}_h), \mathbf{u}_{0h} \rangle. \end{aligned}$$

From (5.9), since the sequence $\{\mathbf{u}_h\}_{h>0}$ is uniformly bounded in $[H^1(\Omega)]^d$, we have:

$$\lim_{h \to 0} c'(\mathbf{u}_h; \mathbf{u}_h, \mathbf{u}_{0h}) = 0.$$

Moreover, as a is bilinear and continuous:

$$\lim_{h \to 0} a(\mathbf{U}_{Dh}, \mathbf{u}_{0h}) = a(\mathbf{U}_D, \mathbf{u}_0),$$

and by standard arguments already used in the proof of Theorem 5.13 (Step 2), we deduce (up to a sub-sequence):

$$\lim_{h \to 0} b(\mathbf{U}_{Dh}; \mathbf{U}_{Dh}, \mathbf{u}_{0h}) + b(\mathbf{u}_{0h}; \mathbf{U}_{Dh}, \mathbf{u}_{0h}) = b(\mathbf{U}_D; \mathbf{U}_D, \mathbf{u}_0) + b(\mathbf{u}_0; \mathbf{U}_D, \mathbf{u}_0).$$

Therefore, as G is compact by Lemma 4.4, we obtain (up to a sub-sequence):

$$\begin{aligned} \lim_{h \to 0} 2\nu\|D(\mathbf{u}_{0h})\|^2_{0,2,\Omega} &= \langle \mathbf{f}, \mathbf{u}_0 \rangle - b(\mathbf{U}_D; \mathbf{U}_D, \mathbf{u}_0) - b(\mathbf{u}_0; \mathbf{U}_D, \mathbf{u}_0) - a(\mathbf{U}_D, \mathbf{u}_0) - \langle G(\mathbf{u}), \mathbf{u}_0 \rangle \\ &= 2\nu\|D(\mathbf{u}_0)\|^2_{0,2,\Omega}, \end{aligned}$$

where the last equality holds because $(\mathbf{u}, p)$ is a weak solution of the Navier-Stokes equations (4.1). As $\mathbf{W}$ is a Hilbert space, and $\{\mathbf{u}_{0h}\}_{h>0}$ is weakly convergent to $\mathbf{u}_0$ in $\mathbf{W}$, this proves the strong convergence of the velocities.

- Strong convergence of the pressures.

We use the discrete inf-sup condition (5.26) to estimate $\|p_h - p\|_{0,2,\Omega}$. As $\mathbb{M}_h$ is an internal approximation of $\mathbb{M}$, there exists a sequence $\{P_h\}_{h>0} \in \mathbb{M}_h$ strongly convergent to p in $\mathbb{M}$. We shall show that:

$$\lim_{h\to 0} \|p_h - P_h\|_{0,2,\Omega} = 0.$$

Let $\mathbf{v}_h \in \mathbf{X}_h$. Then, (4.2) holds with $\mathbf{v} = \mathbf{v}_h$. Let us write:

$$(p, \nabla\cdot\mathbf{v})_\Omega = (P_h, \nabla\cdot\mathbf{v})_\Omega + (p - P_h, \nabla\cdot\mathbf{v})_\Omega,$$

so that (4.2) becomes:

$$\left\{\begin{array}{rcl} b(\mathbf{u};\mathbf{u},\mathbf{v}) + a(\mathbf{u},\mathbf{v}) - (P_h, \nabla\cdot\mathbf{v})_\Omega - (p - P_h, \nabla\cdot\mathbf{v})_\Omega + \langle G(\mathbf{u}),\mathbf{v}\rangle &=& \langle \mathbf{f},\mathbf{v}\rangle, \\ (\nabla\cdot\mathbf{u}, q)_\Omega &=& 0, \end{array}\right. \tag{5.27}$$

for any $(\mathbf{v}, q) \in \mathbf{W}\times\mathbb{M}$. We subtract the first equation of (5.27) with $\mathbf{v} = \mathbf{v}_h$ from the first equation of (5.25). This yields:

$$\begin{array}{rcl} (p_h - P_h, \nabla\cdot\mathbf{v}_h)_\Omega &=& b(\mathbf{u}_h;\mathbf{u}_h,\mathbf{v}_h) - b(\mathbf{u};\mathbf{u},\mathbf{v}_h) + a(\mathbf{u}_h - \mathbf{u},\mathbf{v}_h) + c'(\mathbf{u}_h;\mathbf{u}_h,\mathbf{v}_h) \\ &+& \langle G(\mathbf{u}_h) - G(\mathbf{u}),\mathbf{v}_h\rangle + (p - P_h, \nabla\cdot\mathbf{v}_h)_\Omega. \end{array}$$

As:

$$\begin{array}{rcl} b(\mathbf{u}_h;\mathbf{u}_h,\mathbf{v}_h) - b(\mathbf{u};\mathbf{u},\mathbf{v}_h) &=& b(\mathbf{u}_h;\mathbf{u}_h - \mathbf{u},\mathbf{v}_h) + b(\mathbf{u}_h - \mathbf{u};\mathbf{u},\mathbf{v}_h) \\ &\le& C\|D(\mathbf{u}_h - \mathbf{u})\|_{0,2,\Omega}(\|D(\mathbf{u}_h)\|_{0,2,\Omega} + \|D(\mathbf{u})\|_{0,2,\Omega})\|D(\mathbf{v}_h)\|_{0,2,\Omega}, \end{array}$$

using the continuity of a, and estimates (5.9), (4.18), we deduce:

$$\begin{array}{rcl} (p_h - P_h, \nabla\cdot\mathbf{v}_h)_\Omega &\le& C[(\|D(\mathbf{u}_h)\|_{0,2,\Omega} + \|D(\mathbf{u})\|_{0,2,\Omega} + 2\nu + 1)\|D(\mathbf{u}_h - \mathbf{u})\|_{0,2,\Omega} \\ &+& h^{2-d/2}\|D(\mathbf{u}_h)\|^2_{0,2,\Omega} + \|p - P_h\|_{0,2,\Omega}]\|D(\mathbf{v}_h)\|_{0,2,\Omega}. \end{array}$$

Then, by the discrete inf-sup condition (5.26), there exists a constant $C > 0$ such that:

$$\begin{array}{rcl} \|p_h - P_h\|_{0,2,\Omega} &\le& C \sup\limits_{\mathbf{v}_h\in\mathbf{X}_h} \dfrac{|(\nabla\cdot\mathbf{v}_h, p_h - P_h)_\Omega|}{\|D(\mathbf{v}_h)\|_{0,2,\Omega}} \\ &\le& C\left(\|D(\mathbf{u}_h - \mathbf{u})\|_{0,2,\Omega} + \|p - P_h\|_{0,2,\Omega}\right). \end{array}$$

As $\{P_h\}_{h>0}$ strongly converges to p in $L^2(\Omega)$, and we have proved the strong convergence of the velocities, we have:

$$\lim_{h\to 0} \|p_h - P_h\|_{0,2,\Omega} = 0.$$

It follows that p_h strongly converges to p in $L^2(\Omega)$. ■

The proof of Theorem 5.14, and more concretely the proof of the strong convergence of the velocities, contains as a sub-product the asymptotic energy balance of the mixed

approximation (5.25). Indeed, let us respectively define the deformation energy E_D, the boundary friction energy E_F, and the sub-grid eddy dissipation energy E_S by:

$$\begin{aligned} E_D(\mathbf{u}) &= a(\mathbf{u},\mathbf{u}) &&= 2\nu\|D(\mathbf{u})\|^2_{0,2,\Omega}, \\ E_F(\mathbf{u}) &= \langle G(\mathbf{u}),\mathbf{u}\rangle &&= \int_{\Gamma_n} \mathbf{g}(\mathbf{u})\cdot\mathbf{u}\, ds, \\ E_S(\mathbf{u}_h) &= c'(\mathbf{u}_h;\mathbf{u}_h,\mathbf{u}_h) &&= 2\sum_{K\in\mathcal{T}_h}(C_S h_K)^2 \int_K |D(\mathbf{u}_{h'})|^3\, d\mathbf{x}. \end{aligned}$$

Then, it holds:

Corollary 5.15. *Let $\{(\mathbf{u}_h,p_h)\}_{h>0}$ be a sub-sequence of solutions of the mixed method (5.25) strongly convergent in $[H^1(\Omega)]^d\times L^2(\Omega)$ to a weak solution $(\mathbf{u},p)$ of the steady Navier-Stokes equations (4.1). Then:*

$$\lim_{h\to 0}[E_D(\mathbf{u}_h)+E_F(\mathbf{u}_h)+E_S(\mathbf{u}_h)] = E_D(\mathbf{u})+E_F(\mathbf{u}),$$

as:

$$\lim_{h\to 0} E_D(\mathbf{u}_h) = E_D(\mathbf{u}), \quad \lim_{h\to 0} E_F(\mathbf{u}_h) = E_F(\mathbf{u}),$$

and:

$$\lim_{h\to 0} E_S(\mathbf{u}_h) = 0.$$

Thus, the total energy balance is asymptotically maintained in such a way that the deformation energy and the energy dissipated at the wall pass to the limit. In addition, the dissipated eddy energy asymptotically vanish.

Remark 5.16. *Following the same strategy to initially prove the strong convergence of the velocities for the stabilized VMS-S method, it is easy to check that one can only conclude:*

$$\lim_{h\to 0} 2\nu\|D(\mathbf{u}_{0h})\|^2_{0,2,\Omega} + \|\sigma^*_{p,h}(\nabla p_h)\|^2_{\tau_p} = 2\nu\|D(\mathbf{u}_0)\|^2_{0,2,\Omega},$$

so that in this case we can not achieve a strong convergence result for solutions with natural minimal regularity, neither the corresponding asymptotic energy balance of the system, because we can not separate the deformation energy E_D from the sub-grid energy related to the pressure stabilizing term when passing to the limit.

However, assuming a slightly increased regularity of the solution for the steady Navier-Stokes equations (4.1) leads to a strong convergence result also in the context of the stabilized VMS-S method by an error estimate analysis, as we will show in the next section. This will guarantees the corresponding asymptotic energy balance of the system.

5.5 Error estimates

In this section, we derive error estimates for the VMS-S discretization (4.46) for diffusion-dominated flows. The interest of this analysis is to remark the fact that the VMS-S

method proposed may be used to approximate both laminar and turbulent flows. About the former, if they are regular enough, we obtain convergence of optimal order, and the order decreases with the regularity. As a consequence, we also obtain an asymptotic energy balance of the system for slightly smooth flows. Similar error estimates may be obtained in a more general framework, when the solution of Navier-Stokes equations is located in a branch of non-singular Reynolds numbers, in the sense that at these Reynolds numbers there are not bifurcations to more complex flows (*cf.* [10], [11], [12]). Roughly speaking, the mathematical concept of non-singular flow is closer to the physical concept of laminar flow than just the diffusion-dominated one. Here, we consider the diffusion-dominated regime (much more restrictive than non-singular flow) to determine the accuracy of VMS-S method. The same accuracy will hold for non-singular flows, but the related analysis, that makes mainly use of the implicit function theorem in Banach spaces, is quite involved.

We start by setting a condition that ensures the uniqueness of solutions of the steady Navier-Stokes equations (4.2). As b is a bounded trilinear form, then the quantity:

$$\beta := \sup_{\mathbf{z},\mathbf{v},\mathbf{w}\in\mathbf{W}} \frac{b(\mathbf{z};\mathbf{v},\mathbf{w})}{\|D(\mathbf{z})\|_{0,2,\Omega}\,\|D(\mathbf{v})\|_{0,2,\Omega}\,\|D(\mathbf{w})\|_{0,2,\Omega}},$$

is finite.

Theorem 5.17. *Assume that:*

$$2\nu > \beta(2\mathcal{K} + \|D(\mathbf{U}_D)\|_{0,2,\Omega}), \tag{5.28}$$

where $\mathcal{K}$ is the quantity defined by (5.21). Then, the solution of the steady Navier-Stokes equations (4.2) is unique.

Proof. Consider two solutions $\mathbf{w}, \mathbf{z} \in (\mathbf{U}_D + \mathbf{W})$ of (4.2). Let $\mathbf{e} = \mathbf{w} - \mathbf{z}$, and subtract the equations satisfied by $\mathbf{w}$ and $\mathbf{z}$ with $\mathbf{v} = \mathbf{e}$. Then:

$$\begin{aligned} & 2\nu\|D(\mathbf{e})\|^2_{0,2,\Omega} + \langle G(\mathbf{w}) - G(\mathbf{z}), \mathbf{e}\rangle = b(\mathbf{w};\mathbf{w},\mathbf{e}) - b(\mathbf{z};\mathbf{z},\mathbf{e}) \\ = \;& b(\mathbf{w};\mathbf{w},\mathbf{e}) \pm b(\mathbf{z};\mathbf{w},\mathbf{e}) - b(\mathbf{z};\mathbf{z},\mathbf{e}) = b(\mathbf{e};\mathbf{w},\mathbf{e}) \\ \leq \;& \beta(\|D(\mathbf{w}_0)\|_{0,2,\Omega} + \|D(\mathbf{U}_D)\|_{0,2,\Omega})\|D(\mathbf{e})\|^2_{0,2,\Omega}. \end{aligned}$$

By the monotonicity of G, $\langle G(\mathbf{w}) - G(\mathbf{z}), \mathbf{e}\rangle \geq 0$. As estimate (5.23) holds for $\mathbf{w}$ solution of (4.2), we have:

$$2\nu\|D(\mathbf{e})\|^2_{0,2,\Omega} \leq \beta(2\mathcal{K} + \|D(\mathbf{U}_D)\|_{0,2,\Omega})\|D(\mathbf{e})\|^2_{0,2,\Omega}.$$

Then, condition (5.28) implies $\mathbf{e} = \mathbf{0}$. ■

Remark 5.18. *The condition (5.28) means that the flow is diffusion-dominated. The viscosity ν is large enough to balance the convection effects relatively to the data* $\mathbf{f}$ *and* $\mathbf{U}_D$.

Theorem 5.19. *Assume that Hypothesis 4.9 and estimate (5.28) hold, and that, for smooth enough data, the (unique) solution* $(\mathbf{u}, p)$ *of the steady Navier-Stokes equations (4.2) has augmented regularity, i.e.* $(\mathbf{u}, p) \in [H^{s+1}(\Omega)]^d \times H^s(\Omega)$, $2 \leq s \leq l$. *Then, the following error estimates for a solution* $(\mathbf{u}_h, p_h)$ *of the VMS-S method (4.46) hold:*

$$\|D(\mathbf{u} - \mathbf{u}_h)\|_{0,2,\Omega} + \|p - p_h\|_{0,2,\Omega} \leq C \left(h^s + h^{2-d/2+2\eta}\right), \tag{5.29}$$

for some constant C *independent of* h, *and* $2 \leq \eta \leq (l-1)$ *if* Π_h *takes values in* $\overline{\mathbf{Y}}_h$ *defined by (4.37), while* $2 \leq \eta \leq l$ *if* Π_h *takes values in* $\overline{\mathbf{Y}}_h$ *defined by (4.38),* l *denoting the degree of the polynomial interpolation.*

Proof. We consider an approximation $\widetilde{\mathbf{u}}_{0h} = R_h \mathbf{u}_0 \in \mathbf{X}_h \subset \mathbf{Y}_h^l$ of $\mathbf{u}_0 = \mathbf{u} - \mathbf{U}_D \in \mathbf{W}$ satisfying:

$$(\mathbf{u}_0 - \widetilde{\mathbf{u}}_{0h}, \mathbf{v}_h)_\Omega = 0, \quad \forall \mathbf{v}_h \in \mathbf{Y}_h^{l-1}. \tag{5.30}$$

Note that such interpolant R_h exists, and satisfies the stability and optimal approximation properties of Proposition 4.8 (*cf.* [19]). Also, let $\widetilde{p}_h = T_h p \in \mathbb{M}_h$ with T_h the standard FE interpolation operator, that satisfies the properties of Proposition 4.8. We set $\widetilde{\mathbf{u}}_h = \widetilde{\mathbf{u}}_{0h} + \mathbf{U}_{Dh}$, where $\mathbf{U}_{Dh}$ is given by (4.47). From (4.2), we have:

$$\begin{aligned} b(\widetilde{\mathbf{u}}_h; \widetilde{\mathbf{u}}_h, \mathbf{v}) + a(\widetilde{\mathbf{u}}_h, \mathbf{v}) - (\widetilde{p}_h, \nabla \cdot \mathbf{v})_\Omega + \langle G(\widetilde{\mathbf{u}}_h), \mathbf{v} \rangle + (\nabla \cdot \widetilde{\mathbf{u}}_h, q)_\Omega &= \langle \mathbf{f}, \mathbf{v} \rangle \\ &+ \langle \varepsilon_{vh}, \mathbf{v} \rangle + \langle \varepsilon_{qh}, q \rangle, \end{aligned} \tag{5.31}$$

for all $(\mathbf{v}, q) \in \mathbf{W} \times \mathbb{M}_h$, where $\varepsilon_{vh} \in \mathbf{W}'$ and $\varepsilon_{qh} \in \mathbb{M}_h'$ define the consistency error:

$$\begin{aligned} \varepsilon_{vh} &= b(\widetilde{\mathbf{u}}_h; \widetilde{\mathbf{u}}_h, \mathbf{v}) - b(\mathbf{u}; \mathbf{u}, \mathbf{v}) + a(\widetilde{\mathbf{u}}_h - \mathbf{u}, \mathbf{v}) + \langle G(\widetilde{\mathbf{u}}_h) - G(\mathbf{u}), \mathbf{v} \rangle + (p - \widetilde{p}_h, \nabla \cdot \mathbf{v})_\Omega, \\ \varepsilon_{qh} &= -(\nabla \cdot (\mathbf{u} - \widetilde{\mathbf{u}}_h), q)_\Omega. \end{aligned}$$

Set $\mathbf{e}_h = \widetilde{\mathbf{u}}_h - \mathbf{u}_h$, $\lambda_h = \widetilde{p}_h - p_h$. Taking $\mathbf{v} = \mathbf{v}_h \in \mathbf{X}_h$, $q = q_h \in \mathbb{M}_h$, and subtracting (5.31) from (4.46), we obtain the error equation:

$$\begin{aligned} & b(\mathbf{e}_h; \mathbf{e}_h, \mathbf{v}_h) + a(\mathbf{e}_h, \mathbf{v}_h) - (\lambda_h, \nabla \cdot \mathbf{v}_h)_\Omega + \langle G(\widetilde{\mathbf{u}}_h) - G(\mathbf{u}_h), \mathbf{v}_h \rangle + (\nabla \cdot \mathbf{e}_h, q_h)_\Omega \\ = \; & \langle \varepsilon_{vh}, \mathbf{v}_h \rangle + \langle \varepsilon_{qh}, q_h \rangle - b(\mathbf{u}_h; \mathbf{e}_h, \mathbf{v}_h) - b(\mathbf{e}_h; \mathbf{u}_h, \mathbf{v}_h) + c'(\mathbf{u}_h; \mathbf{u}_h, \mathbf{v}_h) \\ + \; & s_{conv}(\mathbf{u}_h; \mathbf{v}_h) + s_{pres}(p_h, q_h), \end{aligned} \tag{5.32}$$

where we have used the identity:

$$b(\widetilde{\mathbf{u}}_h; \widetilde{\mathbf{u}}_h, \mathbf{v}_h) - b(\mathbf{u}_h; \mathbf{u}_h, \mathbf{v}_h) = b(\mathbf{e}_h; \mathbf{e}_h, \mathbf{v}_h) + b(\mathbf{u}_h; \mathbf{e}_h, \mathbf{v}_h) + b(\mathbf{e}_h; \mathbf{u}_h, \mathbf{v}_h).$$

Set $\mathbf{v}_h = \mathbf{e}_h$, $q_h = \lambda_h$. As $\langle G(\widetilde{\mathbf{u}}_h) - G(\mathbf{u}_h), \mathbf{e}_h \rangle \geq 0$ by the monotonicity of G, we deduce:

$$\begin{aligned} 2\nu \|D(\mathbf{e}_h)\|_{0,2,\Omega}^2 &\leq \langle \varepsilon_{vh}, \mathbf{e}_h \rangle + \langle \varepsilon_{qh}, \lambda_h \rangle - b(\mathbf{e}_h; \mathbf{u}_h; \mathbf{e}_h) \\ &+ c'(\mathbf{u}_h; \mathbf{u}_h, \mathbf{e}_h) + s_{conv}(\mathbf{u}_h; \mathbf{e}_h) + s_{pres}(p_h, \lambda_h) \\ &\leq \|\varepsilon_{vh}\|_{\mathbf{W}'} \|D(\mathbf{e}_h)\|_{0,2,\Omega} + \beta \|D(\mathbf{e}_h)\|_{0,2,\Omega}^2 \|D(\mathbf{u}_h)\|_{0,2,\Omega} \\ &+ c'(\mathbf{u}_h; \mathbf{u}_h, \mathbf{e}_h) + s_{conv}(\mathbf{u}_h; \mathbf{e}_h) + s_{pres}(p_h, \lambda_h) + \langle \varepsilon_{qh}, \lambda_h \rangle \\ &\leq \|\varepsilon_{vh}\|_{\mathbf{W}'} \|D(\mathbf{e}_h)\|_{0,2,\Omega} + \beta(2\mathcal{K} + \|D(\mathbf{U}_D)\|_{0,2,\Omega}) \|D(\mathbf{e}_h)\|_{0,2,\Omega}^2 \\ &+ c'(\mathbf{u}_h; \mathbf{u}_h, \mathbf{e}_h) + s_{conv}(\mathbf{u}_h; \mathbf{e}_h) + s_{pres}(p_h, \lambda_h) + \langle \varepsilon_{qh}, \lambda_h \rangle. \end{aligned}$$

By (5.28), $\delta = 2\nu - \beta(2\mathcal{K} + \|D(\mathbf{U}_D)\|_{0,2,\Omega}) > 0$. Using Young's inequality:

$$\begin{aligned}\delta\|D(\mathbf{e}_h)\|_{0,2,\Omega}^2 &\leq \frac{1}{2\delta}\|\varepsilon_{vh}\|_{\mathbf{W}'}^2 + \frac{\delta}{2}\|D(\mathbf{e}_h)\|_{0,2,\Omega}^2 \\ &+ c'(\mathbf{u}_h;\mathbf{u}_h,\mathbf{e}_h) + s_{conv}(\mathbf{u}_h;\mathbf{e}_h) + s_{pres}(p_h,\lambda_h) + \langle\varepsilon_{qh},\lambda_h\rangle.\end{aligned}$$

Then:

$$\delta\|D(\mathbf{e}_h)\|_{0,2,\Omega}^2 \leq \frac{1}{\delta}\|\varepsilon_h\|_{\mathbf{W}'}^2 + 2\left(c'(\mathbf{u}_h;\mathbf{u}_h,\mathbf{e}_h) + s_{conv}(\mathbf{u}_h;\mathbf{e}_h) + s_{pres}(p_h,\lambda_h) + \langle\varepsilon_{qh},\lambda_h\rangle\right). \tag{5.33}$$

From Lemma (5.6), we have:

$$c'(\mathbf{u}_h;\mathbf{u}_h,\mathbf{e}_h) \leq Ch^{2-d/2}\|D(\mathbf{u}_h')\|_{0,2,\Omega}^2\|D(\mathbf{e}_h')\|_{0,2,\Omega}. \tag{5.34}$$

Set $\widetilde{\mathbf{u}}_h' = (Id - \Pi_h)\widetilde{\mathbf{u}}_h$, $\mathbf{e}_h' = \widetilde{\mathbf{u}}_h' - \mathbf{u}_h'$, $\mathbf{u}' = (Id - \Pi_h)\mathbf{u}$. Then, by the stability property (4.52) satisfied by Π_h:

$$\begin{aligned}\|D(\mathbf{u}_h')\|_{0,2,\Omega} &\leq \|D(\mathbf{e}_h')\|_{0,2,\Omega} + \|D(\widetilde{\mathbf{u}}_h' - \mathbf{u}')\|_{0,2,\Omega} + \|D(\mathbf{u}')\|_{0,2,\Omega} \\ &\leq C\left(\|D(\mathbf{e}_h)\|_{0,2,\Omega} + \|D(\widetilde{\mathbf{u}}_h - \mathbf{u})\|_{0,2,\Omega} + \|D(\mathbf{u}')\|_{0,2,\Omega}\right) \\ &\leq C(\|D(\mathbf{e}_h)\|_{0,2,\Omega} + h^s + h^\eta),\end{aligned}$$

where in the last inequality we have used the optimal error estimates (4.54) for the interpolation operators R_h and Π_h. Inserting this last inequality in (5.34), we have:

$$c'(\mathbf{u}_h;\mathbf{u}_h,\mathbf{e}_h) \leq Ch^{2-d/2}\left(\|D(\mathbf{e}_h)\|_{0,2,\Omega}^3 + \left(h^s + h^\eta\right)^2\|D(\mathbf{e}_h)\|_{0,2,\Omega}\right).$$

Observe that:

$$\|D(\mathbf{e}_h)\|_{0,2,\Omega} \leq \|D(\mathbf{u}_h)\|_{0,2,\Omega} + \|D(\widetilde{\mathbf{u}}_h)\|_{0,2,\Omega} \leq C(2\mathcal{K} + \|D(\mathbf{u}_0)\|_{0,2,\Omega} + \|D(\mathbf{U}_D)\|_{0,2,\Omega}) \leq C,$$

and then:

$$\|D(\mathbf{e}_h)\|_{0,2,\Omega}^3 \leq C\|D(\mathbf{e}_h)\|_{0,2,\Omega}^2,$$

so that we obtain the following estimate for the form c':

$$c'(\mathbf{u}_h;\mathbf{u}_h,\mathbf{e}_h) \leq Ch^{2-d/2}\left(\|D(\mathbf{e}_h)\|_{0,2,\Omega}^2 + \left(h^s + h^\eta\right)^2\|D(\mathbf{e}_h)\|_{0,2,\Omega}\right). \tag{5.35}$$

From Hypothesis 4.9 and Hölder's inequality, for the form s_{conv} we have:

$$\begin{aligned}s_{conv}(\mathbf{u}_h;\mathbf{e}_h) &= \sum_{K\in\mathcal{T}_h}\tau_{\nu,K}(\sigma_h^*(\mathbf{u}_h\cdot\nabla\mathbf{u}_h),\sigma_h^*(\mathbf{u}_h\cdot\nabla\mathbf{e}_h))_K \\ &\leq C\sum_{K\in\mathcal{T}_h}h_K^2\|\sigma_h^*(\mathbf{u}_h\cdot\nabla\mathbf{u}_h)\|_{0,2,K}\|\sigma_h^*(\mathbf{u}_h\cdot\nabla\mathbf{e}_h)\|_{0,2,K}.\end{aligned}$$

Then, by the local stability property (4.50) satisfied by σ_h:

$$\begin{aligned}\|\sigma_h^*(\mathbf{u}_h\cdot\nabla\mathbf{u}_h)\|_{0,2,K} &\leq C\left(\|\mathbf{u}_h\cdot\nabla\mathbf{e}_h\|_{0,2,\omega_K} + \|\mathbf{u}_h\cdot\nabla(\widetilde{\mathbf{u}}_h - \mathbf{u})\|_{0,2,\omega_K} + \|\sigma_h^*(\mathbf{u}_h\cdot\nabla\mathbf{u})\|_{0,2,\omega_K}\right) \\ &\leq C\left(\|\mathbf{u}_h\cdot\nabla\mathbf{e}_h\|_{0,2,\omega_K} + \|\mathbf{u}_h\cdot\nabla(\widetilde{\mathbf{u}}_h - \mathbf{u})\|_{0,2,\omega_K} + \|\mathbf{e}_h\cdot\nabla\mathbf{u}\|_{0,2,\omega_K}\right) \\ &+ C\left(\|(\widetilde{\mathbf{u}}_h - \mathbf{u})\cdot\nabla\mathbf{u}\|_{0,2,\omega_K} + \|\sigma_h^*(\mathbf{u}\cdot\nabla\mathbf{u})\|_{0,2,\omega_K}\right).\end{aligned}$$

The standard application of local inverse estimates (see Lemma 5.3), the regularity of the grid, and Sobolev injections yields:

$$\begin{aligned}
s_{conv}(\mathbf{u}_h;\mathbf{e}_h) &\leq C\sum_{K\in\mathcal{T}_h} h_K^2\|\sigma_h^*(\mathbf{u}_h\cdot\nabla\mathbf{u}_h)\|_{0,2,K}\|\sigma_h^*(\mathbf{u}_h\cdot\nabla\mathbf{e}_h)\|_{0,2,K}\\
&\leq Ch^{2-d/3}(\|D(\mathbf{u}_h)\|_{0,2,\Omega}^2+\|D(\mathbf{u})\|_{0,2,\Omega}\|D(\mathbf{u}_h)\|_{0,2,\Omega})\|D(\mathbf{e}_h)\|_{0,2,\Omega}^2\\
&+ Ch^{2-d/3}\|D(\mathbf{u}_h)\|_{0,2,\Omega}^2\|D(\widetilde{\mathbf{u}}_h-\mathbf{u})\|_{0,2,\Omega}\|D(\mathbf{e}_h)\|_{0,2,\Omega}\\
&+ Ch^{2-d/6}\|D(\mathbf{u})\|_{0,2,\Omega}\|\widetilde{\mathbf{u}}_h-\mathbf{u}\|_{0,\infty,\Omega}\|D(\mathbf{u}_h)\|_{0,2,\Omega}\|D(\mathbf{e}_h)\|_{0,2,\Omega}\\
&+ Ch^{2-d/6}\|\sigma_h^*(\mathbf{u}\cdot\nabla\mathbf{u})\|_{0,2,\Omega}\|D(\mathbf{u}_h)\|_{0,2,\Omega}\|D(\mathbf{e}_h)\|_{0,2,\Omega}\\
&\leq Ch^{2-d/3}\|D(\mathbf{e}_h)\|_{0,2,\Omega}^2+C(h^{2-d/3+s}+h^{3-2d/3+s}+h^{2-d/6+s})\|D(\mathbf{e}_h)\|_{0,2,\Omega}\\
&\leq Ch^{2-d/3}\|D(\mathbf{e}_h)\|_{0,2,\Omega}^2+Ch^{2-d/3+s}\|D(\mathbf{e}_h)\|_{0,2,\Omega}, \qquad (5.36)
\end{aligned}$$

where we have used the optimal error estimates (4.54) for the interpolation operators R_h and σ_h, and assumed $h\leq 1$. For clarity, we detail, for instance, the bound for the following term appearing estimating the form $s_{conv}(\mathbf{u}_h;\mathbf{e}_h)$:

$$\sum_{K\in\mathcal{T}_h} h_K^2\|\mathbf{u}_h\cdot\nabla(\widetilde{\mathbf{u}}_h-\mathbf{u})\|_{0,2,\omega_K}\|\mathbf{u}_h\cdot\nabla\mathbf{e}_h\|_{0,2,\omega_K}.$$

Similarly, we have worked for the other terms. By Hölder's inequality, we have:

$$\begin{aligned}
&\sum_{K\in\mathcal{T}_h} h_K^2\|\mathbf{u}_h\cdot\nabla(\widetilde{\mathbf{u}}_h-\mathbf{u})\|_{0,2,\omega_K}\|\mathbf{u}_h\cdot\nabla\mathbf{e}_h\|_{0,2,\omega_K}\\
\leq\ &\sum_{K\in\mathcal{T}_h} h_K^2\|\mathbf{u}_h\|_{0,\infty,\omega_K}^2\|\nabla(\widetilde{\mathbf{u}}_h-\mathbf{u})\|_{0,2,\omega_K}\|\nabla\mathbf{e}_h\|_{0,2,\omega_K}\\
\leq\ &C\sum_{K\in\mathcal{T}_h} h_K^{2-d/3}\|\mathbf{u}_h\|_{0,6,\omega_K}^2\|\nabla(\widetilde{\mathbf{u}}_h-\mathbf{u})\|_{0,2,\omega_K}\|\nabla\mathbf{e}_h\|_{0,2,\omega_K}, \qquad (5.37)
\end{aligned}$$

where in the last inequality we have applied the local inverse estimate (5.4) and the local uniform regularity of the grid, which is implied by the regularity. By Cauchy-Schwarz inequality, from (5.37) we obtain:

$$\begin{aligned}
&\sum_{K\in\mathcal{T}_h} h_K^2\|\mathbf{u}_h\cdot\nabla(\widetilde{\mathbf{u}}_h-\mathbf{u})\|_{0,2,\omega_K}\|\mathbf{u}_h\cdot\nabla\mathbf{e}_h\|_{0,2,\omega_K}\\
\leq\ &Ch^{2-d/3}\|\mathbf{u}_h\|_{0,6,\Omega}^2\left(\sum_{K\in\mathcal{T}_h}\|\nabla(\widetilde{\mathbf{u}}_h-\mathbf{u})\|_{0,2,\omega_K}^2\right)^{1/2}\left(\sum_{K\in\mathcal{T}_h}\|\nabla\mathbf{e}_h\|_{0,2,\omega_K}^2\right)^{1/2}\\
\leq\ &Ch^{2-d/3}\|D(\mathbf{u}_h)\|_{0,2,\Omega}^2\|D(\widetilde{\mathbf{u}}_h-\mathbf{u})\|_{0,2,\Omega}\|D(\mathbf{e}_h)\|_{0,2,\Omega},
\end{aligned}$$

where in the last inequality we have used again the regularity of the grid, and the Sobolev injection $H^1(\Omega)\hookrightarrow L^6(\Omega)$.

Combining (5.33) with (5.35) and (5.36), we obtain:

$$\begin{aligned}(\delta - Ch^{2-d/2})\|D(\mathbf{e}_h)\|^2_{0,2,\Omega} &\leq \frac{1}{\delta}\|\varepsilon_{vh}\|^2_{\mathbf{W}'} + C(h^{2-d/2+2\eta} + h^{2-d/3+s})\|D(\mathbf{e}_h)\|_{0,2,\Omega} \\ &+ 2[\langle \varepsilon_{qh}, \lambda_h\rangle + s_{pres}(p_h, \lambda_h)].\end{aligned}$$

Using Young's inequality, we deduce:

$$\begin{aligned}\left(\frac{\delta}{2} - Ch^{2-d/2}\right)\|D(\mathbf{e}_h)\|^2_{0,2,\Omega} &\leq \frac{1}{\delta}\|\varepsilon_{vh}\|^2_{\mathbf{W}'} + \frac{C^2\left(h^{2(2-d/2+2\eta)} + h^{2(2-d/3+s)}\right)}{2\delta} \\ &+ 2[\langle \varepsilon_{qh}, \lambda_h\rangle + s_{pres}(p_h, \lambda_h)].\end{aligned}$$

For h small enough, say $h < (\delta/4C)^{1/(2-d/2)}$, we have:

$$\begin{aligned}\frac{\delta}{4}\|D(\mathbf{e}_h)\|^2_{0,2,\Omega} &\leq \frac{1}{\delta}\|\varepsilon_{vh}\|^2_{\mathbf{W}'} + \frac{C}{\delta}\left(h^{2(2-d/2+2\eta)} + h^{2(2-d/3+s)}\right) \\ &+ 2[\langle \varepsilon_{qh}, \lambda_h\rangle + s_{pres}(p_h, \lambda_h)].\end{aligned}$$

To estimate ε_{vh}, consider that:

$$\begin{aligned}|b(\widetilde{\mathbf{u}}_h; \widetilde{\mathbf{u}}_h, \mathbf{v}) - b(\mathbf{u}; \mathbf{u}, \mathbf{v})| &= |b(\widetilde{\mathbf{u}}_h; \widetilde{\mathbf{u}}_h - \mathbf{u}, \mathbf{v}) + b(\widetilde{\mathbf{u}}_h - \mathbf{u}; \mathbf{u}, \mathbf{v})| \\ &\leq C(\|D(\widetilde{\mathbf{u}}_h)\|_{0,2,\Omega} + \|D(\mathbf{u})\|_{0,2,\Omega})\|D(\widetilde{\mathbf{u}}_h - \mathbf{u})\|_{0,2,\Omega}\|D(\mathbf{v})\|_{0,2,\Omega};\end{aligned}$$

$$|a(\widetilde{\mathbf{u}}_h - \mathbf{u}, \mathbf{v})| \leq C\|D(\widetilde{\mathbf{u}}_h - \mathbf{u})\|_{0,2,\Omega}\|D(\mathbf{v})\|_{0,2,\Omega};$$

$$|(p - \widetilde{p}_h, \nabla\cdot\mathbf{v})_\Omega| \leq C\|p - \widetilde{p}_h\|_{0,2,\Omega}\|D(\mathbf{v})\|_{0,2,\Omega}.$$

Then, using estimate (4.18), we have $\|\varepsilon_{vh}\|_{\mathbf{W}'} \leq Ch^s$, so that we obtain:

$$\begin{aligned}\|D(\mathbf{e}_h)\|^2_{0,2,\Omega} &\leq C\left[h^{2s} + h^{2(2-d/2+2\eta)} + h^{2(2-d/3+s)} + \langle \varepsilon_{qh}, \lambda_h\rangle + s_{pres}(p_h, \lambda_h)\right] \\ &\leq C\left[h^{2s} + h^{2(2-d/2+2\eta)} + \langle \varepsilon_{qh}, \lambda_h\rangle + s_{pres}(p_h, \lambda_h)\right]. \qquad (5.38)\end{aligned}$$

Note that by divergence theorem and (5.30) it follows:

$$\langle \varepsilon_{qh}, \lambda_h\rangle = -(\nabla\cdot(\mathbf{u} - \widetilde{\mathbf{u}}_h), \lambda_h)_\Omega = (\mathbf{u} - \widetilde{\mathbf{u}}_h, \sigma^*_h(\nabla\lambda_h))_\Omega,$$

By using Hypothesis (4.9), we estimate:

$$\begin{aligned}\langle \varepsilon_{qh}, \lambda_h\rangle = (\mathbf{u} - \widetilde{\mathbf{u}}_h, \sigma^*_h(\nabla\lambda_h))_\Omega &\leq \sum_{K\in\mathcal{T}_h}\|\mathbf{u} - \widetilde{\mathbf{u}}_h\|_{0,2,K}\|\sigma^*_h(\nabla\lambda_h)\|_{0,2,K} \\ &\leq \|\sigma^*_h(\nabla\lambda_h)\|_{\tau_p}\left(\sum_{K\in\mathcal{T}_h}\frac{1}{\tau_{p,K}}\|\mathbf{u} - \widetilde{\mathbf{u}}_h\|^2_{0,2,K}\right)^{1/2} \\ &\leq \frac{1}{\alpha_1}\|\sigma^*_h(\nabla\lambda_h)\|_{\tau_p}\left(\sum_{K\in\mathcal{T}_h}\frac{1}{h^2_K}\|\mathbf{u} - \widetilde{\mathbf{u}}_h\|^2_{0,2,K}\right)^{1/2} \\ &\leq \frac{C}{\alpha_1}\|\sigma^*_h(\nabla\lambda_h)\|_{\tau_p}h^s \leq \frac{C}{4}\|\sigma^*_h(\nabla\lambda_h)\|^2_{\tau_p} + Ch^{2s},\end{aligned}$$

where we have used the local error estimate (4.53) for the interpolant R_h, the regularity of the grid, and Young's inequality in the last line. As $p_h = \widetilde{p}_h - \lambda_h$, we have:

$$s_{pres}(p_h, \lambda_h) = s_{pres}(\widetilde{p}_h, \lambda_h) - \|\sigma_h^*(\nabla\lambda_h)\|_{\tau_p}^2.$$

Thus, (5.38) becomes:

$$\|D(\mathbf{e}_h)\|_{0,2,\Omega}^2 + \frac{C}{2}\|\sigma_h^*(\nabla\lambda_h)\|_{\tau_p}^2 \leq C\left\{h^{2s} + h^{2(2-d/2+2\eta)} + \|\sigma_h^*(\nabla\widetilde{p}_h)\|_{\tau_p}^2\right\}, \tag{5.39}$$

where we have used Young's inequality to estimate $s_{pres}(\widetilde{p}_h, \lambda_h)$. It remains to bound the last term in (5.39). To do it, we add and subtract ∇p; This yields:

$$\begin{aligned}\|\sigma_h^*(\nabla\widetilde{p}_h)\|_{\tau_p} &\leq \|\sigma_h^*(\nabla(\widetilde{p}_h - p))\|_{\tau_p} + \|\sigma_{p,h}^*(\nabla p)\|_{\tau_p} \\ &\leq Ch\|\nabla(\widetilde{p}_h - p)\|_{0,2,\Omega} + Ch\|\sigma_h^*(\nabla p)\|_{0,2,\Omega} \leq Ch^s,\end{aligned} \tag{5.40}$$

by applying Lemma 5.4 and the optimal error estimates (4.54) for the interpolation operators T_h and σ_h. Combining this estimate with (5.39), we obtain:

$$\|D(\mathbf{e}_h)\|_{0,2,\Omega} + \|\sigma_h^*(\nabla\lambda_h)\|_{\tau_p} \leq C\left(h^s + h^{2-d/2+2\eta}\right). \tag{5.41}$$

The estimate (5.29) for the velocity follows from (5.41) using:

$$\|D(\mathbf{u} - \mathbf{u}_h)\|_{0,2,\Omega} \leq \|D(\mathbf{u} - \widetilde{\mathbf{u}}_h)\|_{0,2,\Omega} + \|D(\mathbf{e}_h)\|_{0,2,\Omega}.$$

To obtain the estimate for the pressure error, set $q_h = 0$ in error equation (5.32). By similar arguments, we deduce:

$$(\lambda_h, \nabla\cdot\mathbf{v}_h)_\Omega \leq C\left(h^s + h^{2-d/2+2\eta}\right)\|D(\mathbf{v}_h)\|_{0,2,\Omega}.$$

Thus, by the discrete inf-sup condition (5.7) and (5.41):

$$\|\lambda_h\|_{0,2,\Omega} \leq C(h^s + h^{2-d/2+2\eta} + \|\sigma_{p,h}^*(\nabla\lambda_h)\|_{\tau_p}) \leq C\left(h^s + h^{2-d/2+2\eta}\right). \tag{5.42}$$

Again, the estimate (5.29) for the pressure follows from (5.42) using:

$$\|p - p_h\|_{0,2,\Omega} \leq \|p - \widetilde{p}_h\|_{0,2,\Omega} + \|\lambda_h\|_{0,2,\Omega}.$$

This concludes the proof. ■

Remark 5.20. *To obtain optimal estimates with respect to the polynomial interpolation, we must take $s = l$. This yields:*

$$\|D(\mathbf{u} - \mathbf{u}_h)\|_{0,2,\Omega} + \|p - p_h\|_{0,2,\Omega} \leq C\left(h^l + h^{2-d/2+2\eta}\right).$$

If the interpolation operator Π_h that defines the sub-grid eddy viscosity takes values in $\overline{\mathbf{Y}}_h$ defined by (4.37), we have $2 - d/2 + 2\eta \geq l$, since we can take (at most) $\eta = (l-1)$, and it must be $l \geq 3$ as $\eta \geq 2$, so that we need at least piecewise cubic FE. Else, if Π_h takes values in $\overline{\mathbf{Y}}_h$ defined by (4.38), we again obtain $2 - d/2 + 2\eta \geq l$, since we can take (at most) $\eta = l$, and it must be $l \geq 2$ as $\eta \geq 2$, thus piecewise quadratic FE are sufficient.

Note that the assumption $s \geq 2$, and hence $\eta \geq 2$, is necessary to use optimal error estimates (4.54) for the interpolation operator σ_h in (5.40). In any case, the convergence order of the VMS-S method (4.46) is optimal with respect to the polynomial interpolation for laminar smooth flows.

Decreasing the regularity of the solution $(\mathbf{u}, p)$ of the steady Navier-Stokes equations (at most) to $[H^2(\Omega)]^d \times H^1(\Omega)$ implies that the convergence order of the VMS-S method is limited to one, due to the estimate of the pressure stabilizing term. However, this slightly augmented regularity already guarantees the strong convergence of the VMS-S method, and it is enough to prove the corresponding asymptotic energy balance in the next subsection.

Also, it is easy to check that the use of the Small-All setting (4.43) of the eddy viscosity instead of the Small-Small setting (4.40) used in the proof leads to an optimal method only if Π_h takes values in $\overline{\mathbf{Y}}_h$ defined by (4.38), while it leads to a sub-optimal method (in 3D), of order $(l - 1/2)$ with respect to the polynomial interpolation, if Π_h takes values in $\overline{\mathbf{Y}}_h$ defined by (4.37). The use of the standard Smagorinsky model (4.45) limits the order to $h^{2-d/2}$. In this case, there is no interest in increasing the accuracy of the interpolation, as this would requires a larger computational effort without increasing the accuracy of the numerical solution. This low convergence order appears linked to the diffusive nature of the Smagorinsky model, that extends the eddy diffusion to all wave-numbers.

5.5.1 Asymptotic energy balance

The proof of Theorem 5.19, that implies more concretely the strong convergence, in particular, of the velocities, contains as a sub-product the asymptotic energy balance of the VMS-S model (4.46). Indeed, let us define the deformation energy E_D, the boundary friction energy E_F, the sub-grid eddy dissipation energy E_S, and the energy E_{SC} and E_{SP} respectively corresponding to the convection and the pressure stabilization terms by:

$$\begin{aligned} E_D(\mathbf{u}) &= a(\mathbf{u},\mathbf{u}) &&= 2\nu\|D(\mathbf{u})\|^2_{0,2,\Omega}, \\ E_F(\mathbf{u}) &= \langle G(\mathbf{u}),\mathbf{u}\rangle &&= \int_{\Gamma_n} \mathbf{g}(\mathbf{u})\cdot\mathbf{u}\, ds, \end{aligned}$$

$$E_S(\mathbf{u}_h) = c'(\mathbf{u}_h;\mathbf{u}_h,\mathbf{u}_h) = 2\sum_{K\in\mathcal{T}_h}(C_S h_K)^2 \int_K |D(\mathbf{u}'_h)|^3\, d\mathbf{x},$$

$$E_{SC}(\mathbf{u}_h) = s_{conv}(\mathbf{u}_h;\mathbf{u}_h) = \|\sigma^*_h(\mathbf{u}_h\cdot\nabla\mathbf{u}_h)\|^2_{\tau_\nu},$$

$$E_{SP}(p_h) = s_{pres}(p_h,p_h) = \|\sigma^*_h(\nabla p_h)\|^2_{\tau_p}.$$

Then, it holds:

Corollary 5.21. *Let $\{(\mathbf{u}_h, p_h)\}_{h>0}$ be a sequence of solutions of the VMS-S model (4.46) strongly convergent in $[H^1(\Omega)]^d \times L^2(\Omega)$ to a solution $(\mathbf{u}, p)$ of the Navier-Stokes equations (4.2) with regularity $[H^2(\Omega)]^d \times H^1(\Omega)$ (at least). Then:*

$$\lim_{h\to 0}[E_D(\mathbf{u}_h) + E_F(\mathbf{u}_h) + E_S(\mathbf{u}_h) + E_{SC}(\mathbf{u}_h) + E_{SP}(p_h)] = E_D(\mathbf{u}) + E_F(\mathbf{u}),$$

as:

$$\lim_{h\to 0} E_D(\mathbf{u}_h) = E_D(\mathbf{u}), \quad \lim_{h\to 0} E_F(\mathbf{u}_h) = E_F(\mathbf{u}),$$

and:

$$\lim_{h\to 0} E_S(\mathbf{u}_h) = \lim_{h\to 0} E_{SC}(\mathbf{u}_h) = \lim_{h\to 0} E_{SP}(p_h) = 0.$$

Thus, the total energy balance is asymptotically maintained in such a way that the deformation energy and the energy dissipated at the wall pass to the limit. In addition, the dissipated eddy energy so as the sub-grid energy due to stabilizing terms asymptotically vanish.

Chapter 6

Numerical Experiments by VMS-SGM

6.1 Introduction

This section is devoted to analyze the numerical performances of the projection-based VMS model (4.46) applied to the computation of laminar and turbulent flows, with and without wall-law boundary conditions. We address simulations of two relevant 3D steady flows, for which there exists an extensive literature providing experimental measurements and reliable numerical results:

- Test 1: 3D lid-driven cavity flow - No-slip boundary conditions (Section 6.3).
- Test 2: 3D turbulent channel flow - Wall-law boundary conditions (Section 6.4).

Note that both of them are examples of flows possessing one direction of inhomogeneity. Turbulent flow examples may be distinguished in view of the number of directions of inhomogeneity, according to Sagaut [77], Chapter 13. The computer resources needed for an adequate resolution usually increase with every additional direction of inhomogeneity, so that, under this consideration, the focus is on flows possessing one direction of inhomogeneity, which provides a good balance between degree of interest in the context of practical applications and computational affordability.

First of all, we discuss the basic aspects of the practical implementation of the discrete model (4.46). We test this model with the different settings of the eddy viscosity term already introduced in Chapter 4, and compare the corresponding practical performances. The steady state of both flows under consideration is reached through unsteady time discretizations, where in particular the Crank-Nicolson scheme together with a linearization by a fixed point like iteration is used. Once clarified the basic aspects of the practical implementation, we introduce the most relevant features of the analyzed flows.

The first numerical test concerns the 3D lid-driven cavity flow, that is one of the most studied problem in computational fluid dynamics, that exhibits one direction of inhomogeneity. We address three significant Reynolds numbers ($Re = 3\,200,\ 7\,500,\ 10\,000$), that

cover the laminar, transient and turbulent regimes. As usual, we set a unit horizontal velocity on the top boundary layer, while no-slip boundary conditions are prescribed on the rest of the boundary. After introducing the setup for numerical solutions, we present simulations on coarse grids, in order to validate the proposed model. A comparison of first and second-order statistics with experimental data so as to other numerical results justifies the interest of our approach.

The second numerical test concerns the 3D turbulent channel flow, that is one of the most popular test problem for the investigation of wall-bounded turbulent flows. We present simulations of turbulent channel flows at friction Reynolds number $Re_\tau = 180$ on coarse grids. Here, the interest is mainly focused on comparing the use of no-slip boundary conditions at the walls *versus* the use of wall-law boundary conditions. We provide some qualitative and quantitative highlights on the the application of wall laws. Compared to direct numerical simulations and other numerical results, we obtain a good prediction of first and second-order statistics of the flow, with a substantial reduction of the computation time with the use of wall laws.

The numerical experiments confirm the ability of the proposed model to simulate both laminar and turbulent flows. They also show a reasonable accuracy with respect to the coarse discretization at hand, as well as the efficiency based on the fact that only a single mesh and nodal interpolation operators are needed to implement the algorithm. Similar errors levels are obtained with respect to more complex VMS models. Moreover, the use of wall laws permits to maintain a rather good accuracy, with a significant reduction of the computational cost. So that, the proposed projection-based VMS method, even in combination with wall laws, seems to provide a promising tool to simulate laminar and turbulent flows, which guarantees a good compromise between accuracy and computational complexity. This is an important feature, especially in view of its use in industrial, environmental and other practical applications.

The chapter is structured as follows: In Section 6.2, we discuss the basic aspects of the discrete model (4.46), that we will use to perform the numerical tests. In Section 6.3, we address the simulation of a 3D lid-driven cavity flow at Reynolds numbers 3 200, 7 500, and 10 000, to cover the spectrum from laminar to turbulent regime. In this context, we fix the setup for the numerical simulations (Subsection 6.3.1), and we display the numerical results obtained for coarse grids by comparing with experimental data and numerical solutions obtained by other authors (Subsection 6.3.2). In Section 6.4, we address the simulation of a 3D turbulent channel flow at friction Reynolds number $Re_\tau = 180$. For this problem, we fix the setup for the numerical simulations (Subsection 6.4.1), where in addition we propose to perform a comparison between the application of standard no-slip boundary conditions at the walls and non-standard wall laws. Finally, the numerical results are also compared with direct numerical simulations and VMS-LES performed by other authors (Subsection 6.4.2).

6.2 Practical implementation

In all numerical experiments performed, we test the projection-based VMS model (4.46) with the following different settings of the eddy viscosity term:

- VMS-S model: The *Small-Small* VMS-Smagorinsky setting, given by (4.40);
- VMS-B model: The Berselli-Iliescu-Layton setting of Ref. [7], given by (4.44), in which we replace the $[L^2(\Omega)]^{d\times d}$ orthogonal projection $\widetilde{\Pi}_h$ on space L_h by an interpolation operator on a coarser (e.g., $P0$) FE space, much faster to compute;
- SMA model: The Smagorinsky setting, given by (4.45).

Moreover, to reach a (quasi-)steady state, an unsteady time discretization is used. In particular, we consider the Crank-Nicolson scheme for the temporal discretization.
We solve in practice the following linearized system in each time step:

$$\left\{\begin{array}{rcl} \left(\dfrac{\mathbf{u}_h^{n+1}-\mathbf{u}_h^n}{\Delta t},\mathbf{v}_h\right)_\Omega + b(\mathbf{u}_h^n,\mathbf{u}_h^{n+\theta},\mathbf{v}_h) + a(\mathbf{u}_h^{n+\theta},\mathbf{v}_h) & + & c'(\mathbf{u}_h^n,\mathbf{u}_h^{n+\theta},\mathbf{v}_h) \\ -(p_h^{n+\theta},\nabla\cdot\mathbf{v}_h)_\Omega + \langle\widehat{G}(\mathbf{u}_h^{n+\theta}),\mathbf{v}_h\rangle + \widehat{s}_{conv}(\mathbf{u}_h^{n+\theta},\mathbf{v}_h) & = & (\mathbf{f}_h,\mathbf{v}_h)_\Omega, \\ (\nabla\cdot\mathbf{u}_h^{n+\theta},q_h)_\Omega + \widetilde{s}_{pres}(p_h^{n+\theta},q_h) + \varepsilon(p_h^{n+1},q_h)_\Omega & = & 0, \end{array}\right. \tag{6.1}$$

where:

$$\mathbf{u}_h^{n+\theta} = \theta\mathbf{u}_h^{n+1} + (1-\theta)\mathbf{u}_h^n, \quad p_h^{n+\theta} = \theta p_h^{n+1} + (1-\theta)p_h^n, \quad \theta = 1/2.$$

In (6.1), the form c' denotes the linearized (with respect to the convection velocity at a previous time step $\mathbf{u}_h^n$) eddy diffusion term defined by either VMS-S, VMS-B or SMA models, and the term with factor ε denotes a penalty term, that permits to fix the constant the pressure is determined up through the formulation, for a small positive value of ε (e.g., $\varepsilon = 10^{-10}$ in the numerical simulations). The boundary term is linearized as:

$$\langle\widehat{G}(\mathbf{u}_h^{n+\theta}),\mathbf{v}_h\rangle = \int_{\Gamma_n} \mathbf{u}_h^{n+\theta}\cdot\mathbf{v}_h\, e(|\mathbf{u}_h^n|)ds,$$

where the function e is given by (5.14). Moreover, the stabilizing terms are defined by:

$$\widehat{s}_{conv}(\mathbf{u}_h^{n+\theta},\mathbf{v}_h) = \sum_{K\in\mathcal{T}_h} (\tau_{\nu,K}^n\,\sigma_h^*(\mathbf{u}_h^n\cdot\nabla\mathbf{u}_h^{n+\theta}),\sigma_h^*(\mathbf{u}_h^n\cdot\nabla\mathbf{v}_h)),$$

$$\widetilde{s}_{pres}(p_h^{n+\theta},q_h) = \sum_{K\in\mathcal{T}_h} (\tau_{p,K}^n\,\widetilde{\sigma}_h^*(\nabla p_h^{n+\theta}),\widetilde{\sigma}_h^*(\nabla q_h)),$$

where $\widetilde{\sigma}_h^* = Id$. The choice $\widetilde{\sigma}_h^* = \sigma_h^*$ gives raise to small oscillations, that could bring to small numerical instabilities during the computation. Our choice limits the accuracy

order of method (6.1) to one, but in practice it provides accurate results. The stabilization coefficients are given by the adapted Codina's form (4.56):

$$\tau^n_{\nu,K} = \tau^n_{p,K} = \left[\left(c_1 \frac{\nu + \overline{\nu}^n_T}{h_k^2}\right) + \left(c_2 \frac{U^n_K}{h_k}\right)\right]^{-1},$$

where $U^n_K = \|\mathbf{u}^n_h\|_{0,2,K}/|K|^{1/2}$, and $\overline{\nu}^n_T = (C_S h_K)^2 U^{*,n}_K$, with:

- $U^{*,n}_K = \|D(\Pi^*_h \mathbf{u}^n_h)\|_{0,2,K}/|K|^{1/2}$ for the VMS-S model;
- $U^{*,n}_K = \|\widetilde{\Pi}^*_h D(\mathbf{u}^n_h)\|_{0,2,K}/|K|^{1/2}$ for the VMS-B model;
- $U^{*,n}_K = \|D(\mathbf{u}^n_h)\|_{0,2,K}/|K|^{1/2}$ for the SMA model.

The value for the constants c_1 and c_2 are $c_1 = 16$ (as we will use quadratic elements), and $c_2 = \sqrt{c_1}$ (*cf.* [31]). For simplicity of implementation, we define the element size $h_K = \sqrt[3]{|K|}$, for all $K \in \mathcal{T}_h$. Problem (6.1) is implemented on a FreeFem++ (*cf.* [48]) numerical code, and the corresponding system is solved by a GMRES (Generalized Minimal Residual) method (*cf.* [76]). The interested reader may consult the FreeFem++ numerical code [24] used for the computations in Chacón and Lewandowski [26], where some hints on the algorithm strategy are included in the form of comments.

Remark 6.1. *The semi-implicit Crank-Nicolson scheme (6.1) produces less numerical diffusion with respect to a simple semi-implicit Euler scheme (*cf. *[21]), and thus it does not tend to artificially increment the turbulent diffusion. Furthermore, it is less expensive in terms of storage requirements with respect to two-step schemes (e.g., Adams-Bashfort method), that could achieve a second-order accuracy in time. So that, the temporal discretization used provides a good compromise between accuracy and computational cost. Also, it is crucial to discretize the convective term by an anti-symmetric form $b(\mathbf{u}^n_h, \cdot, \cdot)$ to obtain a good stability in time. This ensures the conservation of the kinetic energy in the absence of diffusive effects and source terms.*

6.3 Test 1: 3D lid-driven cavity flow

The lid-driven cavity flow is one of the most studied problem in computational fluid dynamics, that exhibits one direction of inhomogeneity. It consists in computing the flow induced in a cavity by an external flow, parallel to its lid. This flow presents the occurrence of some genuine 3D features, even at relatively low Reynolds numbers. One of the most remarkable is the formation of Taylor-Görtler-like (TGL) vortices at the corners of the cavity bottom, i.e. small counter-rotating vortices formed as a result of the curvature of the streamlines due to the main vortex in the middle of the cavity (*cf.* [78]). Zang et al. [89] report the numerical simulation of the 3D cavity flow by a LES model in a Finite Volume Method (FVM), using the dynamic procedure of Germano et al. (*cf.* [40]). Based on experimental experiences performed in Prasad and Koseff [74], they describe the flow at Reynolds number 3 200 to be essentially laminar, although an inherent unsteadiness may occur. For Reynolds number 7 500, a transitional stage is reached, since the flow

becomes unstable near the downstream eddies at Reynolds numbers higher than about 6 000. With even higher Reynolds numbers at about 10 000, the flow becomes fully turbulent. Thus, laminar, transient, and turbulent regimes are covered by the choice of these three cases.

The primary goal of the simulation of the 3D cavity flow is to obtain a bounded kinetic energy as time increases, during the complete simulation time needed to reach a stable equilibrium (*cf.* [68]). This may look a simple requirement, but some turbulence models violate it. Indeed, Iliescu et al. [57] reported the numerical results obtained with three subgrid-scale models: The Smagorinsky model, a traditional Taylor LES model of Clark et al. [28], and two variants of a new rational LES model developed in Galdi and Layton [39]. It was shown that the Taylor LES model produces an energy blow-up in finite time. The two rational LES models dis not cause an energy blow-up, but exhibited important oscillations. The standard Smagorinsky model (with the Smagorinsky constant $C_S = 0.1$) turned out to be notably more diffusive, as expected. These results were obtained for a Reynolds number of 10^4, using $8 \times 8 \times 8$ elements with biquadratic velocity interpolation and discontinuous bilinear pressure interpolation. These elements are known to fulfill the standard inf-sup condition and, moreover, they are considered to be the most stable and best performing elements for FE discretizations of the Navier-Stokes equations fulfilling the inf-sup condition (see Fortin [37], Gresho and Sani [46]).

6.3.1 Setup for numerical simulations

We simulate the 3D cavity flow at Reynolds numbers ($Re = 1/\nu$) 3 200, 7 500, and 10 000, following the works of Gravemeier [43] and Zang et al. [89]. In his PhD thesis [43], Gravemeier analyzes (among others) the performances of two types of VMS models, based on the Residual Free Bubbles (RFB) method, and the use of several nested meshes. These are called two-level method (VMS-2L) and three-level method (VMS-3L), where the latter is the most similar to our scheme, as it includes three grid levels, and it takes into account the effect of small un-resolved scales onto small resolved scales by a sub-grid viscosity approach in Smagorinsky's form. However, it is more complicated to implement and requires an higher computational cost. The numerical results of these VMS models are compared by Gravemeier with the ones of the Adjoint-Stabilized FEM (also called USFEM, Uncommon-Stabilized FEM), and of the Smagorinsky model on a PSPG (Pressure Stabilizing Petrov-Galerkin) FE discretization, and with the experimental results of Prasad and Koseff [74].

Dirichlet boundary conditions are used: On the top boundary layer a unit horizontal velocity is prescribed, while no-slip boundary conditions are set on the rest of the boundary. We compare the solution provided by model (4.46) with the different settings of the eddy viscosity term specified in Section 6.2, where in all cases we use a static modeling of the Smagorinsky constant C_S, by imposing $C_S = 0.1$ (see Iliescu et al. [57], Gravemeier [43]), in order to avoid further complexity. Actually, in the VMS-3L method of Gravemeier [43] also the possibility of dynamic modeling is investigated in the numerical simulations for Reynolds numbers 3 200 and 7 500.

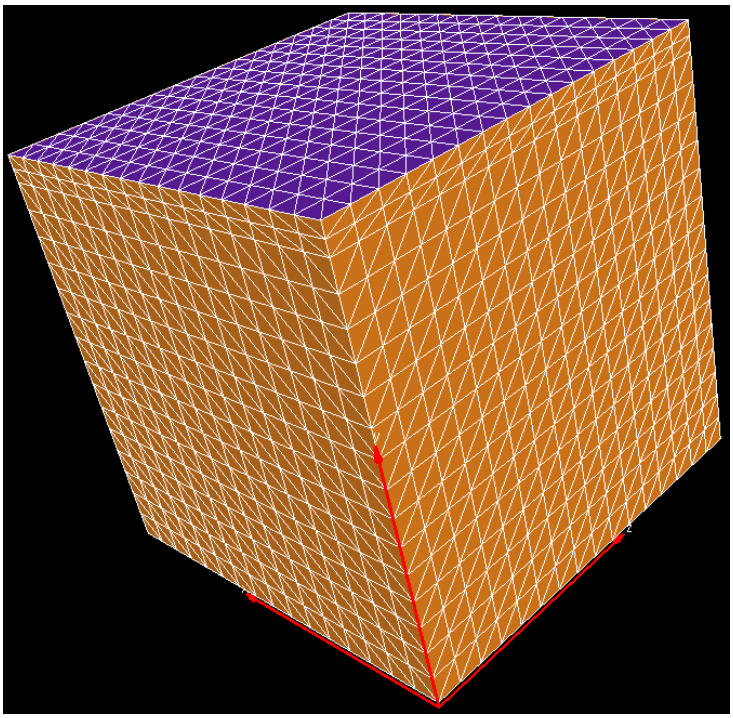

Figure 6.1:
3D lid-driven cavity flow mesh (refined top boundary layer).

The difficulty we face in the numerical simulations is to obtain a good accuracy with relatively coarse basic discretizations (i.e., low computational cost), for all flow situations. The computational grid consists of a uniform $16 \times 16 \times 16$ partition of the unit cube, where in addition we refine the grid-line corresponding to the top boundary layer (see Figure 6.1), in order to handle large velocity gradients. This already provides a large improvement in the accuracy of the numerical results. On this mesh (26 112 tetrahedra), we consider three-dimensional $P2$ FE for velocity and pressure. Actually, we are considering less d.o.f. with respect to the VMS-3L numerical simulation of Gravemeier [43], as its sub-mesh consists of a $3 \times 3 \times 3$ isotropic subdivision of the coarse basic discretization ($16 \times 16 \times 16$ trilinear hexahedral elements).

Following Gravemeier [43], we solve the 3D steady Navier-Stokes equations through an evolution approach, by using the linearized Crank-Nicolson temporal scheme (6.1) with a time step $\Delta t = 0.1$. An impulsive start is performed, i.e. the initial condition is a zero velocity field. A characteristic time scale T_{cav} is defined in Zang et al. [89] to be the estimated time for a fluid particle at the edge of the top boundary layer to turn and travel back to its starting position in the cavity. This time scale is roughly estimated to be about 10 time units for the current calculation. Initially, the simulation is run for five time scales T_{cav}, i.e. 50 time units or 500 time steps. Within this time period (*cf.* [43]), the flow is expected to develop to full extent, including a subsequent relaxation time.

Afterwards, statistics are collected for another five time scales T_{cav}.

6.3.2 Numerical results

All results are graphically compared to the experimental data of Prasad and Koseff [74], and numerical results of Gravemeier [43]. The experimental data for the flow at Reynolds number 7 500 have only been evaluated for half of the cavity.

The temporal evolution of the total kinetic energy subject to:

$$E_{kin}(\mathbf{u}_h^n) = \frac{1}{2}\int_\Omega \mathbf{u}_h^n \cdot \mathbf{u}_h^n \, d\mathbf{x},$$

for the three cases $Re = 3\,200$, $Re = 7\,500$, $Re = 10\,000$ is displayed on Figure 6.2. The flows become roughly stationary at $t \simeq 5\,T_{cav}$ (i.e., at 50 time units about), as expected. Method SMA, which is supposed to introduce the highest amount of numerical viscosity, also exhibits the highest values of the total kinetic energy throughout the simulation, for all three Reynolds numbers considered, which is physically reasonable. Indeed, it is well-known that the higher the physical viscosity of the flow the larger is the zone of influence of the prescribed velocity at the top boundary of the cavity. Both the VMS-S and the VMS-B methods produce similar amount levels of numerical viscosity, with the VMS-B method being slightly less viscous for every case under consideration. These results are in good agreement with the ones obtained in Gravemeier [43]. In particular, our SMA method is less diffusive than the Smagorinsky model (SM) of Gravemeier, discretized by a Pressure Stabilizing Petrov-Galerkin (PSPG) FE method. The energy curves for the VMS-S and VMS-B methods are located between the energy curves of the VMS-3L and VMS-2L methods of Gravemeier, being this last one the method that introduces the least numerical viscosity in the Gravemeier's simulations, for every case under consideration.

The mean velocities $\langle u_1 \rangle$ and $\langle u_3 \rangle$ are computed as a discrete time average according to:

$$\langle u_i \rangle(\mathbf{x}) = \frac{1}{N/2}\sum_{n=N/2}^{N-1} u_i(\mathbf{x}, t_n), \quad i = 1, 3, \quad N = \#\text{ time steps} = 1\,000.$$

Figure 6.3 shows the mean velocity $\langle u_1 \rangle$ on the centerline $z = 0.5$ of the longitudinal mid-plane $y = 0.5$, for the various Reynolds numbers under consideration. Both the VMS-S and the VMS-B methods show a good agreement with the experimental data of Prasad and Koseff [74], even with the coarse basic discretization at hand, and compare well also to the VMS-3L method [43], which is the method Gravemeier states working better in its simulations. A similar accuracy is found for the mean velocity $\langle u_3 \rangle$ on the centerline $x = 0.5$ of the longitudinal mid-plane $y = 0.5$ (see Figure 6.4). The SMA model is the one that presents the largest distance from the experimental curves. In Table 6.1, we perform a quantitative comparison between our numerical results and the ones of the VMS-3L method, by evaluating the deviation $e_0^{\langle u_1 \rangle}$, $e_0^{\langle u_3 \rangle}$ for the mean velocities profiles from the

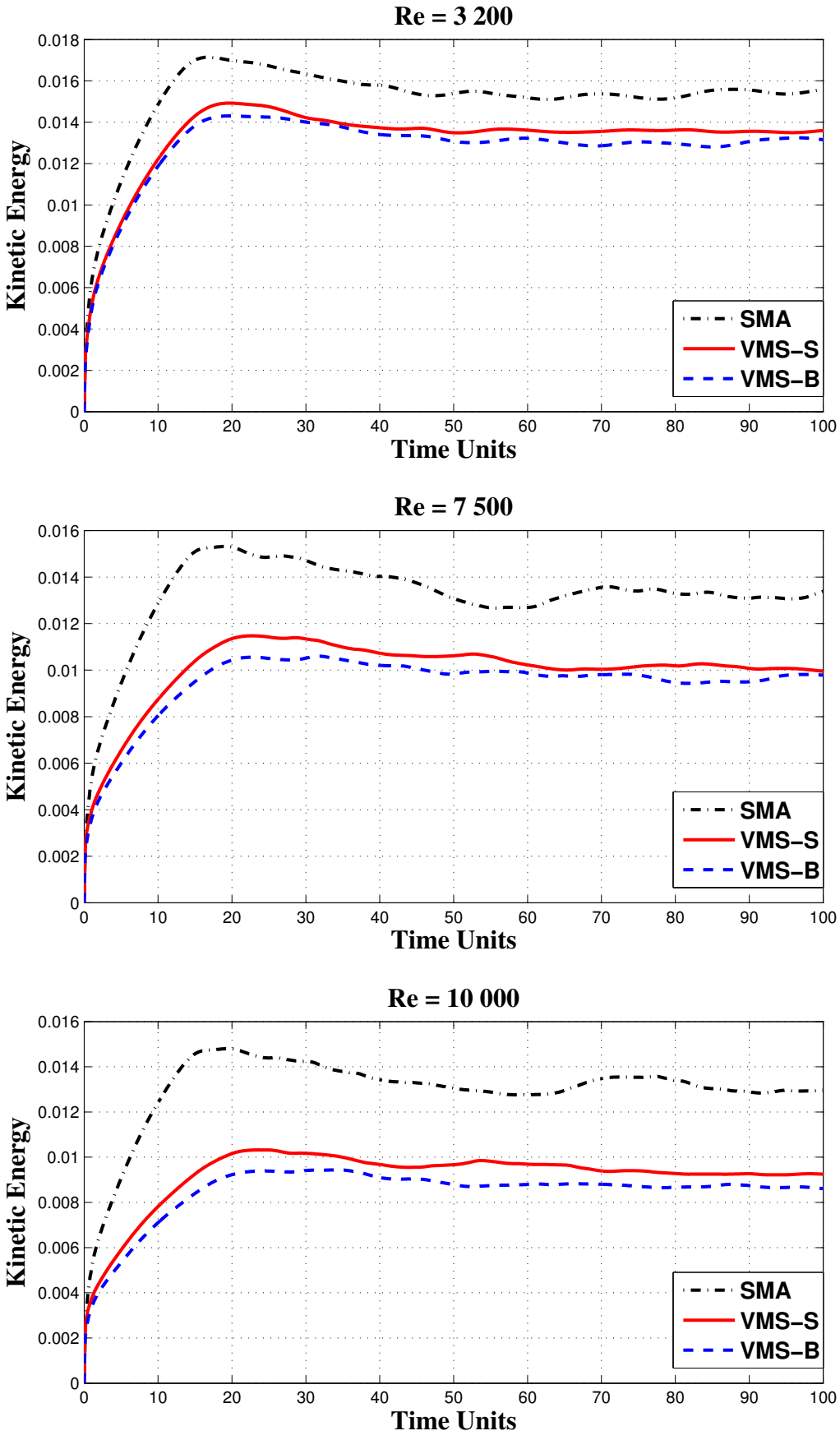

Figure 6.2:
Temporal evolution of the total kinetic energy for $Re = 3\,200$ (top), $Re = 7\,500$ (middle), $Re = 10\,000$ (bottom).

respective experimental data in a normalized discrete L^2-norm subject to:

$$e_0^{\langle u_1 \rangle} = \left[\frac{\int_{z=0}^{z=1} |(\langle u_1 \rangle_h - \langle u_1 \rangle_{exp})(0.5, 0.5, z)|^2 dz}{\int_{z=0}^{z=1} |\langle u_1 \rangle_{exp}(0.5, 0.5, z)|^2 dz} \right]^{1/2}, \tag{6.2}$$

$$e_0^{\langle u_3 \rangle} = \left[\frac{\int_{x=0}^{x=1} |(\langle u_3 \rangle_h - \langle u_3 \rangle_{exp})(x, 0.5, 0.5)|^2 dx}{\int_{x=0}^{x=1} |\langle u_3 \rangle_{exp}(x, 0.5, 0.5)|^2 dx} \right]^{1/2}. \tag{6.3}$$

We may observe that the errors due to the SMA method deteriorate as Re increases, while the errors due to all VMS methods remain within the same levels, between 15% to 30%.

	$e_0^{\langle u_1 \rangle}$			$e_0^{\langle u_3 \rangle}$		
Methods	$Re = 3\,200$	$Re = 7\,500$	$Re = 10\,000$	$Re = 3\,200$	$Re = 7\,500$	$Re = 10\,000$
VMS-S	0.1497	0.1221	0.2692	0.2188	0.1710	0.2862
VMS-B	0.1676	0.1828	0.2230	0.2399	0.1566	0.2682
SMA	0.1790	0.2627	0.4231	0.2870	0.2066	0.4147
VMS-3L	0.2434	0.3529	0.2962	0.6522	0.1428	0.2153

Table 6.1:
L^2-norm of the deviation from the experimental profiles for the mean velocities.

Also, higher-order moments $\langle \tilde{\mathbf{u}}^n \rangle$, with $n > 1$ and $\tilde{\mathbf{u}}$ denoting the fluctuating part of $\mathbf{u}$, are achieved by collecting values in the sense of a discrete time average, which is an appropriate procedure for stationary turbulence. In particular, we have considered the variance ($n = 2$) for the first and third component of the velocity, that reads $\langle \tilde{u}_i^2 \rangle = \langle u_i^2 \rangle - \langle u_i \rangle^2$, with the standard deviation (root-mean-square, r.m.s.) defined as $\sqrt{\langle \tilde{u}_i^2 \rangle}$ ($i = 1, 3$). Finally, the off-diagonal component $\langle \tilde{u}_1 \tilde{u}_3 \rangle = \langle u_1 u_3 \rangle - \langle u_1 \rangle \langle u_3 \rangle$ of the Reynolds stress tensor is depicted. As in Prasad and Koseff [74], the r.m.s. values and the off-diagonal Reynolds stress component are multiplied by the amplification factors 10 and 500, respectively, in order to ensure a reasonable visual impression of these values within the respective graphs. With respect to the experimental data, larger errors appear for the r.m.s. values and the crossed component of the Reynolds stress tensor in particular. These deviations are shown for $Re = 10\,000$ in Figures 6.5, 6.6 and in Table 6.2, that presents the normalized discrete L^2-norm of the errors. Mispredictions of various peaks of these curves may also be found in the numerical results of Zang et al. [89], achieved with a four-times finer discretization in every coordinate direction. This underlines the difficulty in predicting these sensitive measures.

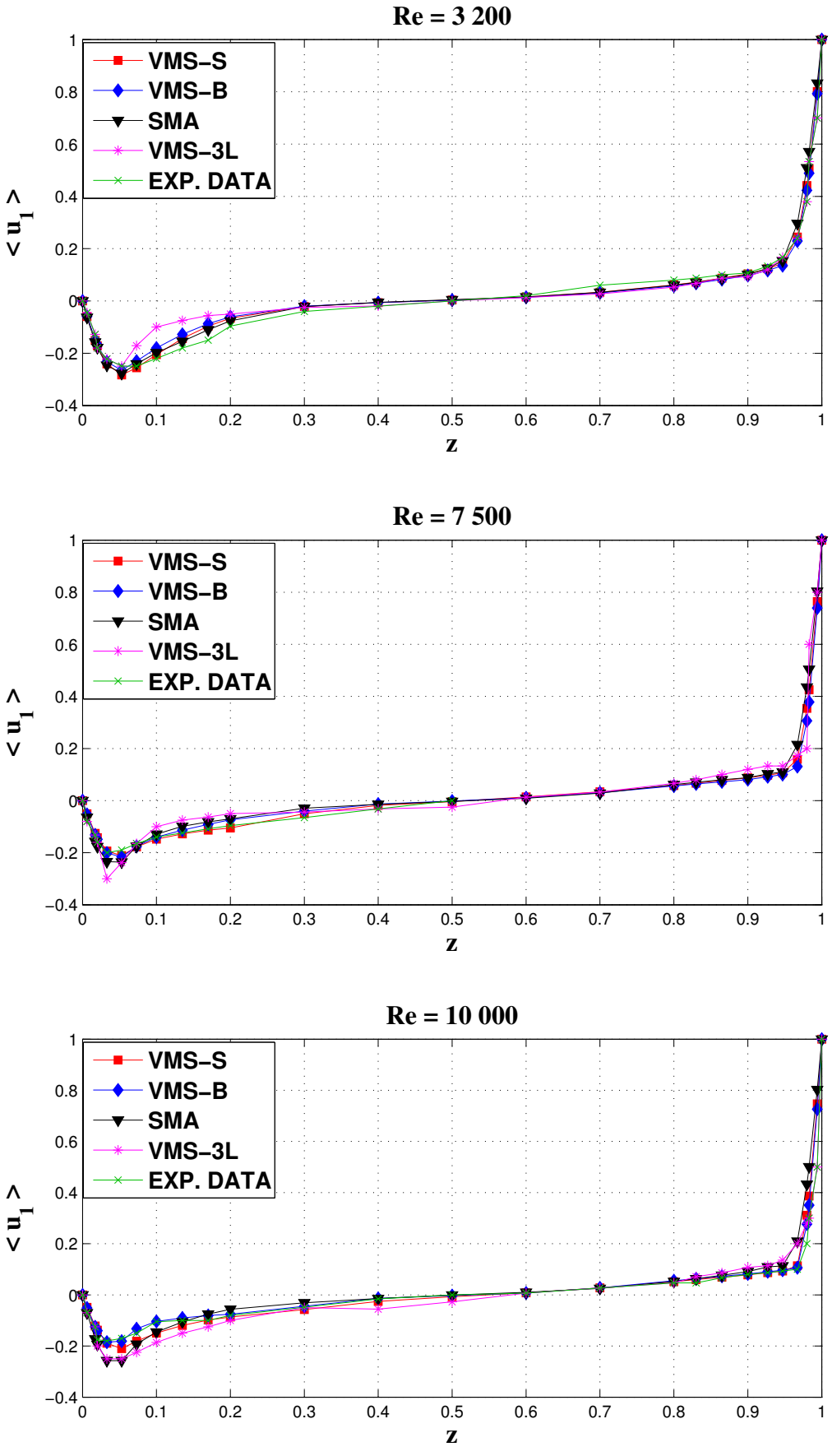

Figure 6.3:
$\langle u_1 \rangle$ on the vertical centerline ($z = 0.5$) of the mid-plane $y = 0.5$ for $Re = 3\,200$, $Re = 7\,500$, $Re = 10\,000$.

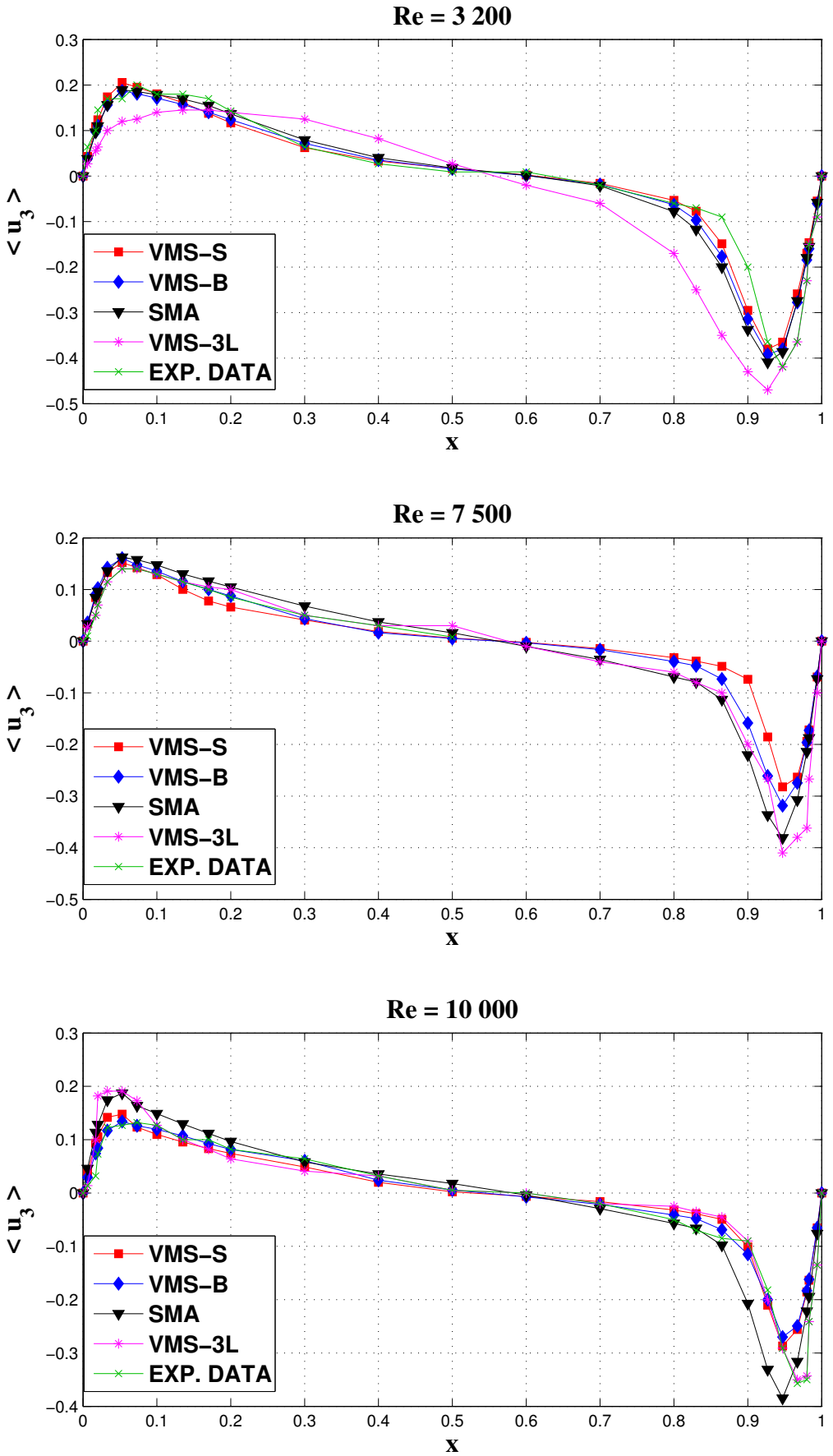

Figure 6.4:
$\langle u_3 \rangle$ on the horizontal centerline ($x = 0.5$) of the mid-plane $y = 0.5$ for $Re = 3\,200$, $Re = 7\,500$, $Re = 10\,000$.

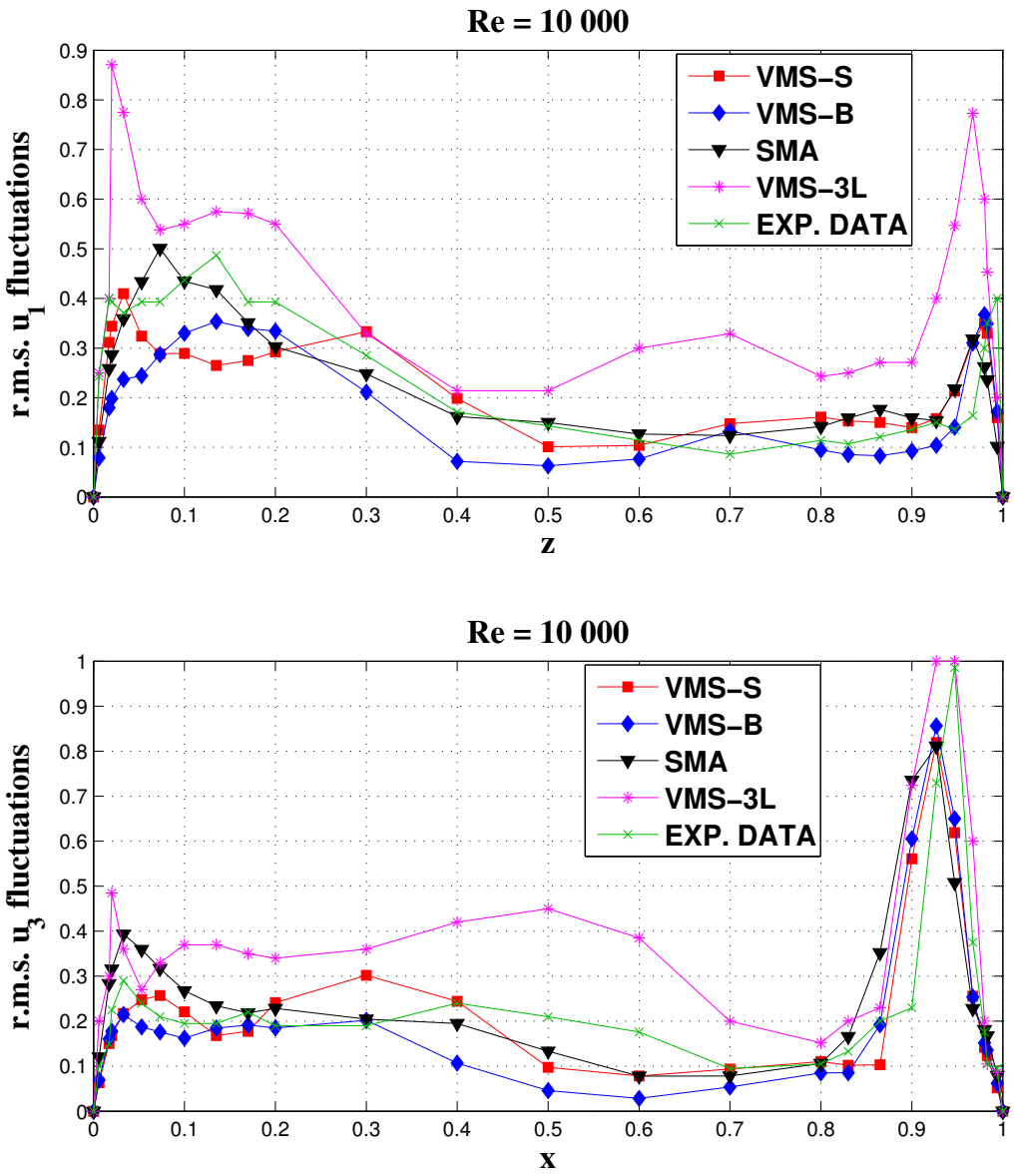

Figure 6.5:
$\sqrt{\langle \tilde{u}_1^2 \rangle}$ and $\sqrt{\langle \tilde{u}_3^2 \rangle}$ on the centerlines of the mid-plane $y = 0.5$ for $Re = 10\,000$.
(factor 10)

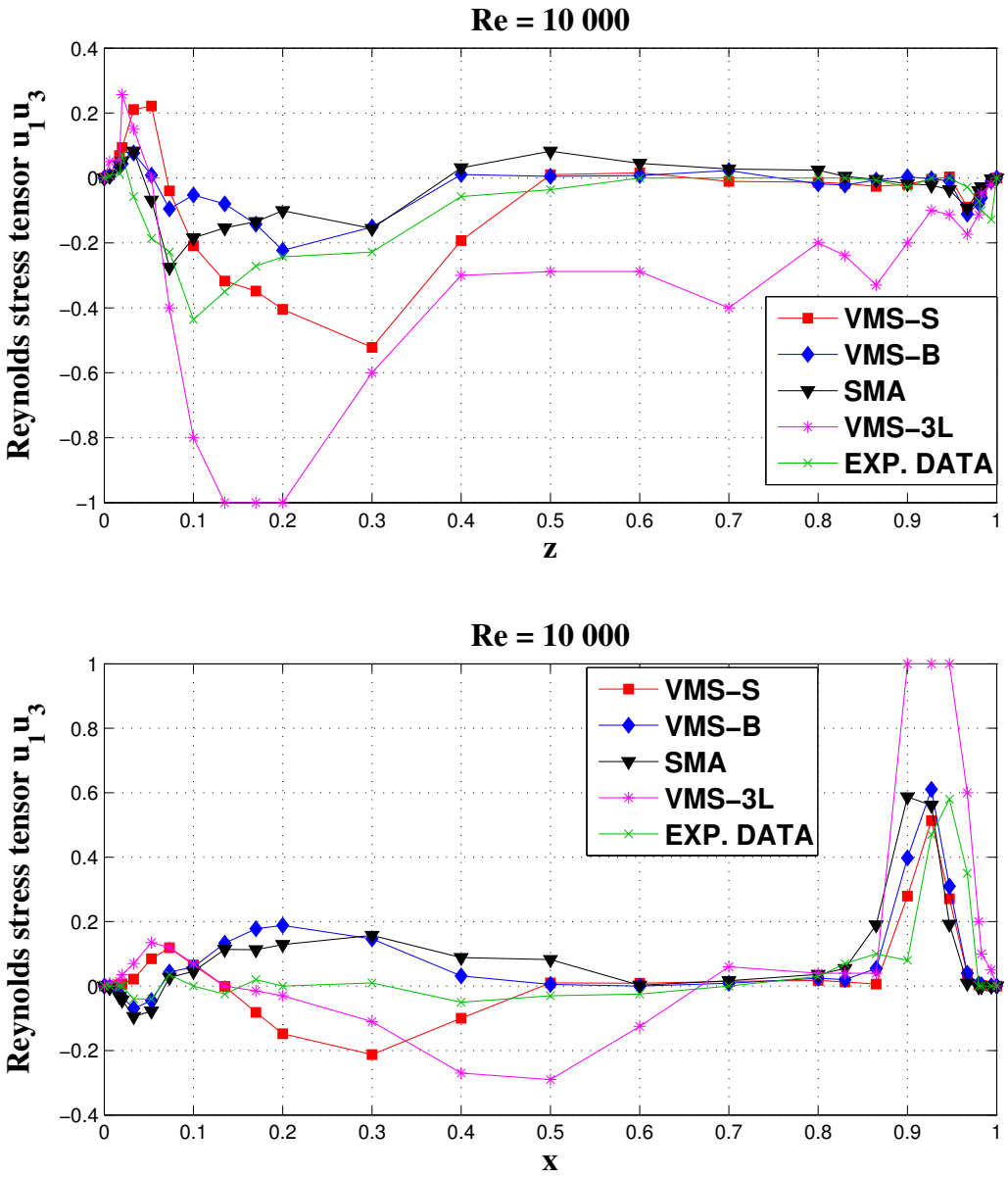

Figure 6.6:
$\langle \tilde{u}_1 \tilde{u}_3 \rangle$ on the centerlines of the mid-plane $y = 0.5$ for $Re = 10\,000$.
(factor 500)

	$Re = 10\,000$			
Methods	$e_0^{\sqrt{\langle \tilde{u}_1^2 \rangle}}$	$e_0^{\sqrt{\langle \tilde{u}_3^2 \rangle}}$	$e_0^{\langle \tilde{u}_1 \tilde{u}_3 \rangle (z)}$	$e_0^{\langle \tilde{u}_1 \tilde{u}_3 \rangle (x)}$
VMS-S	0.3256	0.4046	0.9251	0.8836
VMS-B	0.3426	0.4696	0.6856	0.8971
SMA	0.2424	0.5109	0.6195	1.1532
VMS-3L	0.7808	0.6975	2.3415	1.8805

Table 6.2:
L^2-norm of the deviation for the r.m.s. and the crossed component of the Reynolds stress tensor.

Qualitatively, we have observed that the flow exhibits effectively the formation of three-dimensional TGL corner vortices at the cavity end walls, that interact with the primary circulation vortex, thus influencing the distribution of momentum within the entire cavity (see Figure 6.7). In the case $Re = 3\,200$, in accordance to Prasad and Koseff [74], it is possible to discern these vortices as organized structures, while for higher Re, increasing turbulent effects cause the breakdown of these organized structures, resulting in a "weaker" flow when compared with the pure two-dimensional flow (see, for example, the numerical simulations of Ghia et al. [41]), in which it is not possible to discern at all the presence of TGL vortices. This suggests that the high-frequency turbulent fluctuations become dominant, and they partially destroy the integrity (or coherence) of the TGL vortices.

6.3.3 Conclusions

As a conclusion, in the case of the 3D cavity flow, both VMS-S and VMS-B methods act in general like a RFB-based VMS method with three grid levels (VMS-3L of Gravemeier [43]), with errors levels similar, or even smaller in some cases. Actually, both VMS-S and VMS-B methods are methods with three grid levels: Resolved large scales, resolved small scales and un-resolved small scales, whose action on the resolved small scales is modeled through the sub-grid eddy turbulence projection term.

From the computational point of view, the use of RFB-based VMS methods is quite involved. Several simplifying assumptions and modeling procedures are needed, but the more questionable point is the usefulness of the computed resolved small scales, because of the dominating influence of the viscosity model in the numerical solution of these equations on very coarse local grids (*cf.* [62]). To sum up, RFB-based VMS methods seem to need further improvement to be efficiently used, while the projection-based VMS-S method seems to be more promising in terms of accuracy, with reduced modeling issues, and also easier from the computational point of view.

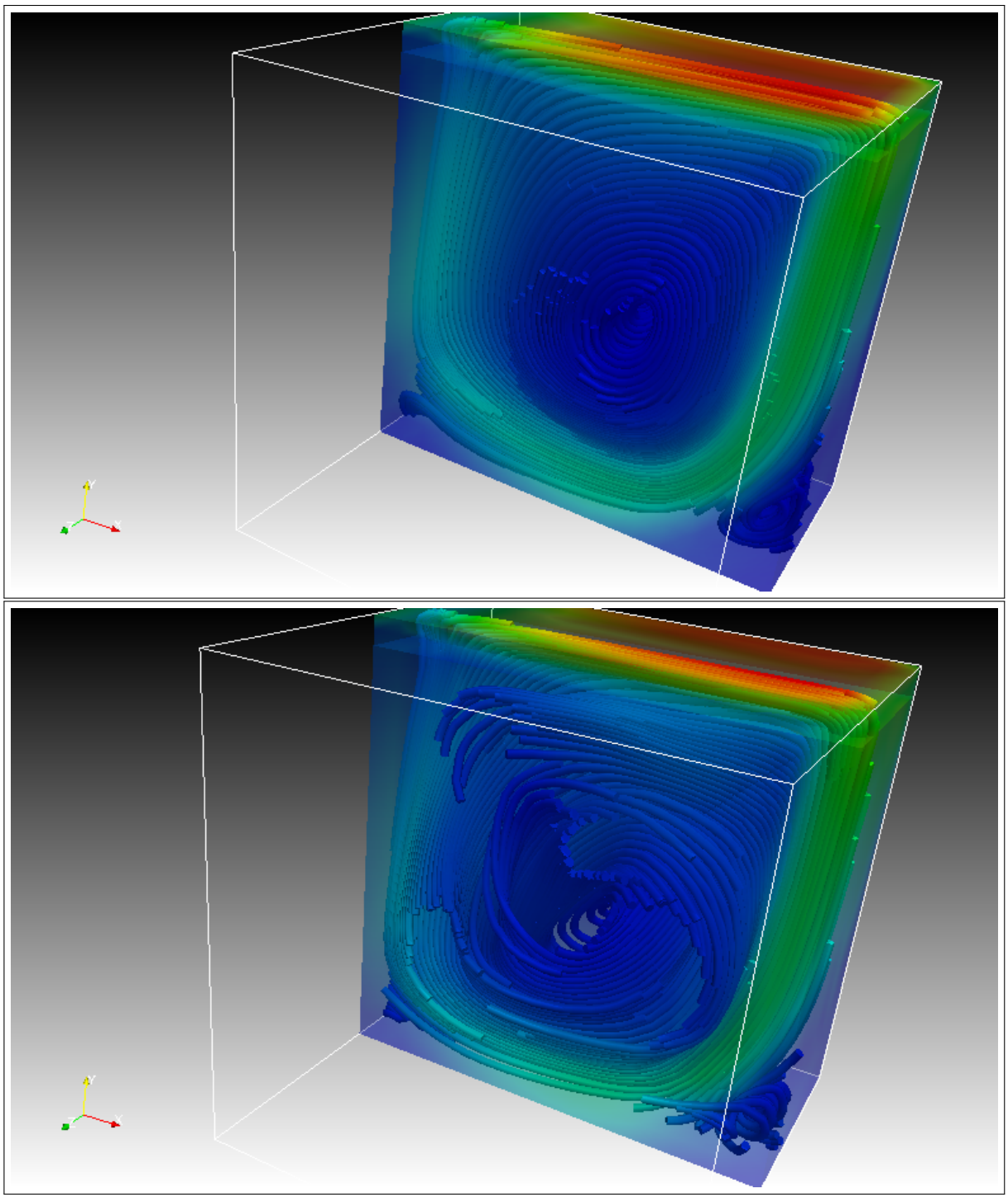

Figure 6.7:
Flow streamlines at $Re = 3\,200$ (top) and $Re = 7\,500$ (bottom); results for VMS-S method.

6.4 Test 2: 3D turbulent channel flow

The 3D channel flow is one of the most popular test problems for the investigation of wall bounded turbulent flows. It was pioneered as a LES test problem by Moin and Kim (*cf.* [69]), and more recently has been extensively used to test several versions of LES models. Let us mention, for instance, the simulation carried out by Iliescu and Fischer [56] using a Rational LES (RLES) model, in the context of a spectral element code. A number of numerical studies on turbulent channel flow has also been performed applying VMS methods. Among others, Bazilevs et al. [2] tested a Residual-based VMS (RB-VMS) turbulence model on a channel flow, employing linear, quadratic and cubic NURBS (Non-Uniform Rational B-Splines), while John and Kindl [62] compared the performances of two types of VMS methods, where one uses bubble functions to model resolved small scales (RFB-based method), whereas the other one contains the definition of the resolved small scales by an explicit projection in its set of equations (Projection-based method). For the setup of our numerical simulations, we choose to follow the guidelines given by Gravemeier in [45], where different scale-separating operators for a VMS-LES of a turbulent channel flow in the context of a FV method are tested. As a benchmark, we will use the fine Direct Numerical Simulations (DNS) of Moser, Kim and Mansour [70].

6.4.1 Setup for numerical simulations

The simulations concern a fully developed 3D turbulent channel flow at $Re_\tau = 180$. We test model (4.46) with the different settings of the eddy viscosity term specified in Section 6.2.

We use a setup similar to the one of Gravemeier [45]. The computational domain (see Figure 6.8) is $\Omega = (0, L_1) \times (-\delta_c, \delta_c) \times (0, L_3)$, with $\delta_c = 1$ (wall-normal direction), $L_1 = 2\pi$ (stream-wise direction), and $L_3 = (4/3)\pi$ (span-wise direction). The boundary conditions are periodic in both the stream-wise and span-wise directions, commonly referred to as homogeneous directions. We perform a comparison between the application of no-slip and wall-law boundary conditions at the walls. The viscosity is $\nu = 1/180 = 5.5 \times 10^{-3}$. The turbulent wall-shear velocity $u_\tau = \sqrt{\tau}$, where τ denotes the wall-shear stress, and the channel half-width δ_c define the Reynolds number:

$$Re_\tau = \frac{u_\tau \, \delta_c}{\nu},$$

besides the kinematic viscosity ν. The Reynolds number based on a unit friction velocity reachable at a steady state is $Re_\tau = 180$.

Our strategy is as follows: to reach a statistically steady state, we use an evolution approach starting by an initial parabolic velocity profile perturbed by a random velocity fluctuation. We first run a simulation with no-slip boundary conditions at the walls, in order to stabilize u_τ near a unitary value. Random velocity fluctuations of 10%-amplitude

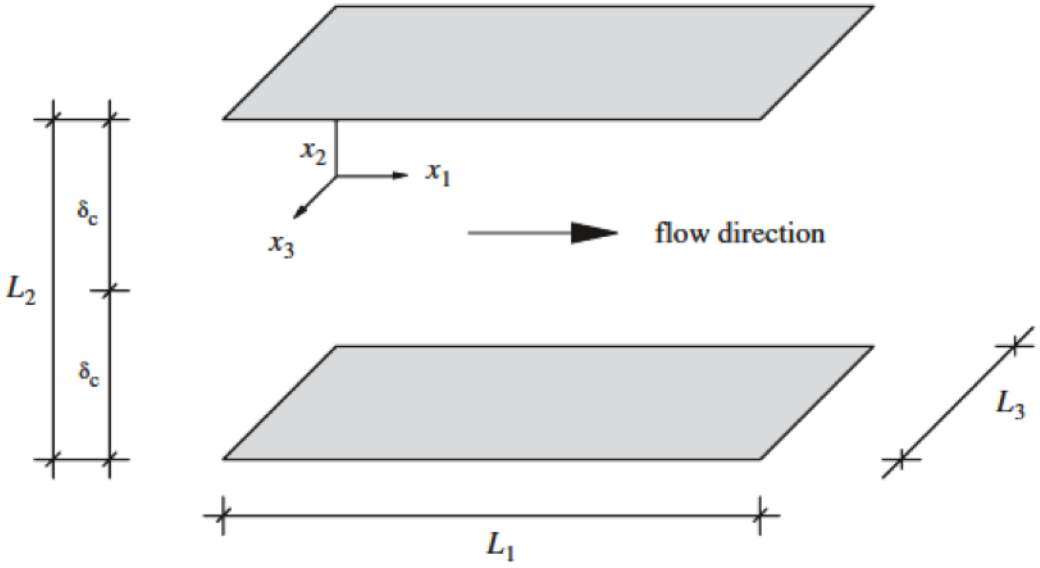

Figure 6.8:
Sketch of channel geometry [From Gravemeier [45]].

of the bulk mean stream-wise velocity perturb the initial condition for the velocity field:

$$\begin{cases} u_1(y, t=0) &= u_{1,c}(1-y^2) + 0.1 u_{1,m}\psi_{ran}, \\ u_2(y, t=0) &= 0.1 u_{1,m}\psi_{ran}, \\ u_3(y, t=0) &= 0.1 u_{1,m}\psi_{ran}, \end{cases}$$

where $u_{1,c}$ denotes the stream-wise velocity at the centerline of the channel, $u_{1,m}$ the bulk mean stream-wise velocity, and $\psi_{ran} \in [-1, 1]$ a random number. We choose $u_{1,c} = 25$, and hence $u_{1,m} = \int_0^{\delta_c} u_{1,c}(1-y^2)\, dy = 2u_{1,c}/3 = 16.7$. So, the corresponding Reynolds number based on the bulk mean stream-wise velocity ($Re_m = u_{1,m} 2\delta_c/\nu$, see [63]) is $Re_m = 6\,012$. The flow is driven by a constant forcing $\mathbf{f} = (f_p, 0, 0) = (1, 0, 0)$, that models an imposed pressure gradient in the stream-wise direction. The specific choice of a unit value for f_p aims at obtaining a unit value for u_τ in the statistically steady state, subject to the relation $u_\tau = \sqrt{f_p \delta_c}$ (*cf.* [35]). We choose to work with Van Driest damping [83], so that the Smagorinsky constant is changed to the expression $C_S(1 - \exp(-y^+/A^+))$, where $C_S = 0.1$ according to the original choice in [34], $y^+ = (\delta_c - |y|)u_\tau/\nu$ is the non-dimensional distance from the wall, and $A^+ = 26$ is the Van Driest constant.

The difficulty we face in the numerical simulations is to obtain a good accuracy with a relatively coarse spatial resolution. Our grid consists of a 16^3 partition of the channel, uniform in the homogeneous directions. The distribution of nodes in the wall-normal direction is non-uniform, and obeys the cosine function of Gauss-Lobatto:

$$y_i = -\cos\left(\frac{i\pi}{N_y}\right), \quad i = 0, \ldots, N_y = 16.$$

We use three-dimensional $P2$ FE for velocity and pressure. These choices give rise to 4 096 mesh cells (i.e., 24 576 tetrahedra), 33 792 d.o.f. for each scalar variable, and a distance of the d.o.f. next to the walls $y^+_{min} = 1.7293$. In Gravemeier [45], a VMS-Smagorinsky model, based on projection/averaging operators and the use of two nested meshes, is used in a FV method with 32 control volumes in all coordinate directions for Reynolds number $Re_\tau = 180$. A simulation equivalent in number of d.o.f. to our discretization for a turbulent channel flow at $Re_\tau = 180$ has been carried out by Akkerman in his PhD thesis [1], by using a RB-VMS turbulence model. Indeed, his coarsest computation consists on $Q1$ FE applied on a 32^3 partition of the computational domain, that results in a number of d.o.f. equivalent to our value, obtained by using $P2$ FE on a 16^3 partition of the channel. Note that the data from the fine DNS of Moser, Kim and Mansour [70] are obtained by a subdivision of the channel of 128^3.

We use the semi-implicit Crank-Nicolson scheme (6.1) for the temporal discretization. The discretized scheme (6.1) is first integrated for 1 250 time steps, with $\Delta t = 0.004$. This time step is smaller than the Kolmogorov time scale, and it fits into the range proposed in [27] to ensure numerical stability. Within this time period, the flow is expected to develop to full extent, including a subsequent relaxation time.

Afterwards, we further integrate in parallel the scheme (6.1) either with no-slip boundary conditions and wall-law boundary conditions, within another 1250 time steps, in order to collect statistics and perform a comparison. We choose to show the application of wall-law boundary conditions only to VMS-S method as it is the model that gives the most promising results. We consider the logarithmic wall-law of Prandtl and Von Kármán (4.8), where we fix $y^+ = 11.5$, and we use a uniform mesh with 12 grid-lines in wall-normal direction, neglecting the use of Van Driest damping too. This permits to avoid the quite costly calculation of the flow near the walls, reducing the number of d.o.f. to 25 600 for each scalar variable, with a saving in computing time of about 34% compared with the use of no-slip boundary conditions. Note that before the flow becomes (quasi-)stationary, the value of u_τ changes a lot in time (see Figure 6.10), and this implies a dynamic development of the boundary layer thickness, due to the definition of y^+. This requires a dynamic adaptation in the use of wall laws. Here, we choose a simpler procedure, letting the flow develop until reaching a stable configuration before applying wall laws in a static way. Actually, there exist flows for which the modeling of the boundary layer turbulence by means of wall laws yields good and accurate results near the solid walls without needing further adaptations. This is the case, for instance, of the backward step flow (*cf.* [22]), since this flow recirculates and then the boundary layer thickness is approximately constant.

6.4.2 Numerical results

Figure 6.9 displays the temporal evolution of the H^1, L^2 and L^∞ norms of the velocity field during the simulation. We observe that we effectively reach a statistically stable equilibrium already at half of simulation. In Figure 6.10, we consider the temporal evolution

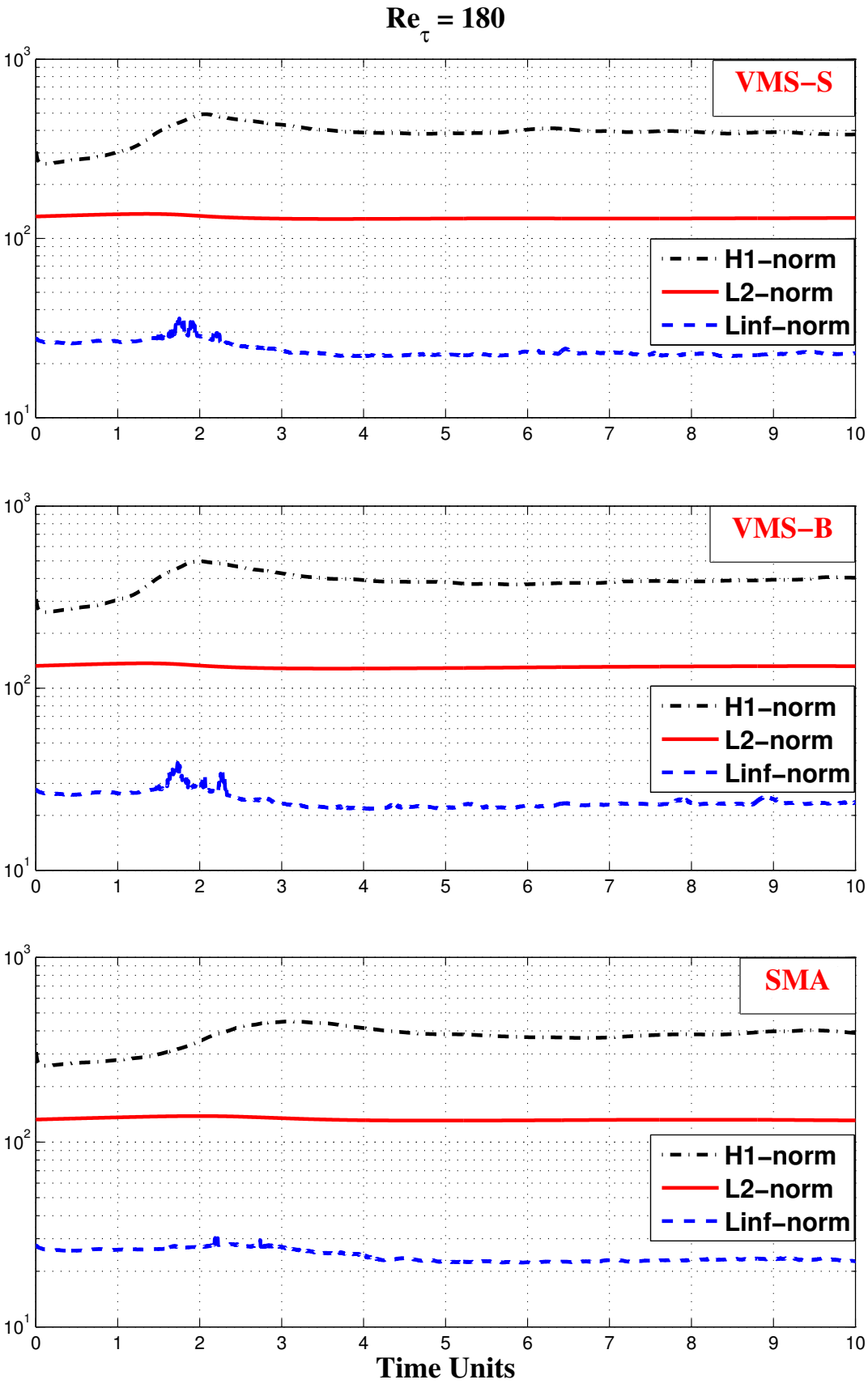

Figure 6.9:
Time evolution of the H^1, L^2 and L^∞ norms of the velocity field.

of the normalized mean wall-shear stress:

$$\langle \tau^* \rangle(t) = \frac{\langle \tau \rangle(t)}{\nu} = \frac{\partial \langle u_1 \rangle}{\partial y}(\pm 1; t),$$

where $\langle \cdot \rangle$ indicates in this case averaging over the homogeneous directions. We note that the curves are almost symmetric with respect to the centerline of the channel. Moreover, when a (quasi-)steady state is reached (at half of simulation), the mean quantities oscillates (in modulus) around 180, as indicated by the temporal averaged (from $t = 5$ to $t = 10$) values shown in Figure 6.10. These values have been used to compute for all methods the actual value of u_τ, subject to:

$$u_\tau = \left[\frac{\nu}{2} \frac{1}{N/2} \sum_{n=N/2}^{N-1} \left(\frac{\partial \langle u_1 \rangle}{\partial y}(-1; t_n) - \frac{\partial \langle u_1 \rangle}{\partial y}(+1; t_n) \right) \right]^{1/2}, \quad N = \#\text{ time steps} = 1\,250.$$

The simulated friction velocity u_τ (computed as the average of the computed friction velocities at both walls) is reported in Table 6.3, together with the corresponding computed Re_τ for all methods. We note that the friction velocity u_τ is within 0.2%-4.1% of the nominal value $u_\tau = 1$, and, as a result, so is the actual Re_τ.

Hereafter, we denote by $\langle \cdot \rangle$ the mean values and by $\widetilde{\cdot}$ the respective fluctuations, where mean values are obtained averaging over all time steps of the statistical period as well as over the homogeneous directions. In Figure 6.11, we show the mean stream-wise velocity profile $\langle u_1 \rangle$ (first-order statistic), normalized by the computed u_τ, in wall coordinates y^+. As usual, only half of the channel width is illustrated (i.e., the upper half-width here, ranging from $y = 0$ to $y = 1$). According to the definition of the wall coordinate y^+, the upper wall is located at $y^+ = 0$ and the channel center at $y^+ = u_\tau/\nu \approx 180$.

In particular, the displayed mean stream-wise velocity profiles are obtained by using both no-slip boundary conditions (for all methods) and wall-law boundary conditions (for VMS-S method), and a comparison is performed with DNS data [70] and the numerical results of Akkerman [1]. Note that the DNS data so as the RB-VMS results of Akkerman are obtained by the standard approach that uses no-slip boundary conditions at the walls. Actually, the grid resolution seems to be too coarse to reproduce exactly the DNS profile, so that in any case we have an over-estimation of the DNS data. Anyway, the results show an acceptable agreement with the fine DNS, even with the very coarse basic discretization at hand (8 times coarser than the DNS one). The profile obtained with the wall-law boundary conditions starting from $y^+ = 11.5$ is simply extended linearly up to the wall located at $y^+ = 0$. We are entitled to do so, because in this case the leading component of the velocity is the stream-wise velocity, so that we can "identify" the friction non-dimensional velocity u^+, defined in (4.7), by $\langle u_1 \rangle / u_\tau$. We display in Table 6.4 (first column) the deviation $e_0^{\langle u_1 \rangle}$ for the mean stream-wise velocity profile from the respective

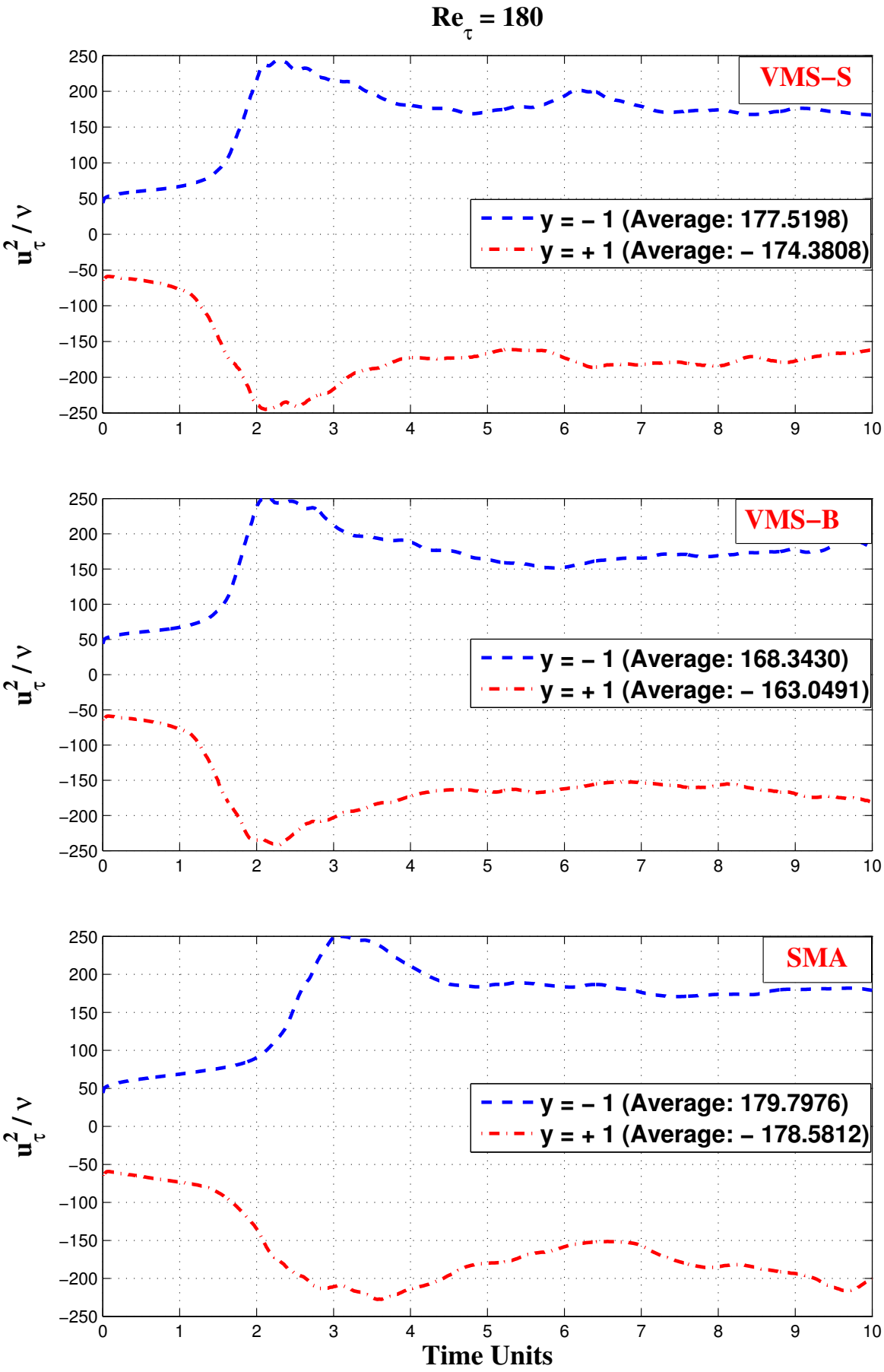

Figure 6.10:
Time evolution of the normalized mean wall-shear stress.

DNS data in a normalized discrete L^2-norm subject to:

$$e_0^{\langle u_1 \rangle} = \left[\frac{\int_{y^+=0}^{y^+=180} |\langle u_1 \rangle_h^+ - \langle u_1 \rangle_{DNS}^+|^2 \, dy^+}{\int_{y^+=0}^{y^+=180} |\langle u_1 \rangle_{DNS}^+|^2 \, dy^+} \right]^{1/2} . \tag{6.4}$$

We can observe as all methods gives similar errors levels between 10% and 20%.

	Nominal $Re_\tau = 180$	
Methods	Computed u_τ	Computed Re_τ
VMS-S	0.9887	177.966
VMS-B	0.9594	172.692
SMA	0.9977	179.586

Table 6.3:
Computed u_τ and Re_τ.

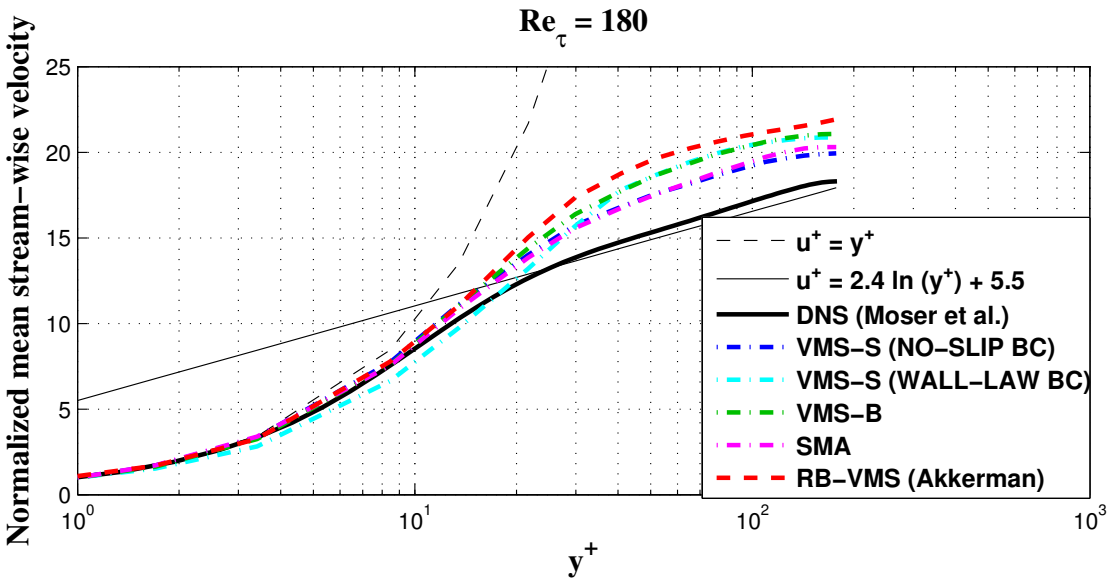

Figure 6.11:
Normalized mean stream-wise velocity profiles in wall coordinates y^+.

To investigate more in detail statistical properties of this wall-bounded turbulence test, we plot second-order statistics as measure of turbulence intensities, by using either no-slip (for all methods) and wall-law (for VMS-S method) boundary conditions. Figure 6.12 displays the normalized (by the computed u_τ) r.m.s. values of velocity fluctuations $\sqrt{\langle \tilde{u}_i^2 \rangle}$ $(i = 1, 2, 3)$ in wall coordinates y^+ at the upper half-width of the channel. If we compare

Methods	$e_0^{\langle u_1 \rangle}$ ($y^+ \in [0, 180]$)	$e_0^{\sqrt{\langle \tilde{u}_1^2 \rangle}}$ ($y^+ \in [30, 180]$, inertial layer)
VMS-S (NO-SLIP BC)	0.1141	0.2320
VMS-S (WALL-LAW BC)	0.1734	0.2094
VMS-B (NO-SLIP BC)	0.1786	0.3341
SMA (NO-SLIP BC)	0.1260	0.3123
RB-VMS (Akkerman)	0.2221	0.6104

Table 6.4:
L^2-norm of the deviation from the DNS profiles for the stream-wise velocity.

with DNS data the various methods tested with no-slip boundary conditions, we can see slight differences for the curves associated to wall-normal and span-wise velocities, while the curve related to stream-wise velocity shows a noticeable over-prediction. We can also observe as for the r.m.s. values, the results obtained by the application of wall laws are only meaningful for the stream-wise component of the velocity, that is the leading one. Note that in this case the related curve starts at $y^+ = 11.5$, since the computational domain starts at $y^+ = 11.5$, and no extension is possible, as for the mean stream-wise velocity. However, a comparison with the other curves is possible starting from $y^+ = 30$, i.e. in the so-called *inertial layer*, as we could physically expect. Indeed, the inertial layer is where the logarithmic approximation of the friction-velocity u^+ is more accurate (see Figure 6.11). Actually, the best approximation of the r.m.s. stream-wise velocity fluctuation in the inertial layer is effectively given by the use of wall-laws, as shown quantitatively in Table 6.4 (second column), where the normalized discrete L^2-norm of the deviation from the DNS profile is computed, analogously to formula (6.4). Nevertheless, the results for the other "minor" velocity components are not acceptable compared with the DNS data at hand. In particular, this is true for the wall-normal component of the velocity, as in this case the model itself contemplates the imposition of a null wall-normal velocity at the fictitious boundary of the resulting "reduced" computational domain (see the boundary condition $\mathbf{u} \cdot \mathbf{n} = 0$ on Γ_n in 4.2), that is not expected by the use of standard no-slip boundary conditions.

This consideration obviously influences also the behavior of the Reynolds shear stress $R_{x,y} = \langle \tilde{u}_1 \tilde{u}_2 \rangle$, where the wall-normal velocity trivially interferes. The Reynolds shear stress is plotted in Figure 6.13 in global coordinates y, and normalized by the computed friction velocity squared u_τ^2. Anyway, qualitatively we can observe that for all methods the Reynolds shear stress is antisymmetric, almost vanishes at the center of the channel ($y = 0$), and presents a linear trend. This also indicates that a statistically steady state is already reached (*cf.* [63]). If we compare with the DNS results of Moser et al. [70], the curves related to the use of no-slip boundary conditions at the walls are quite close.

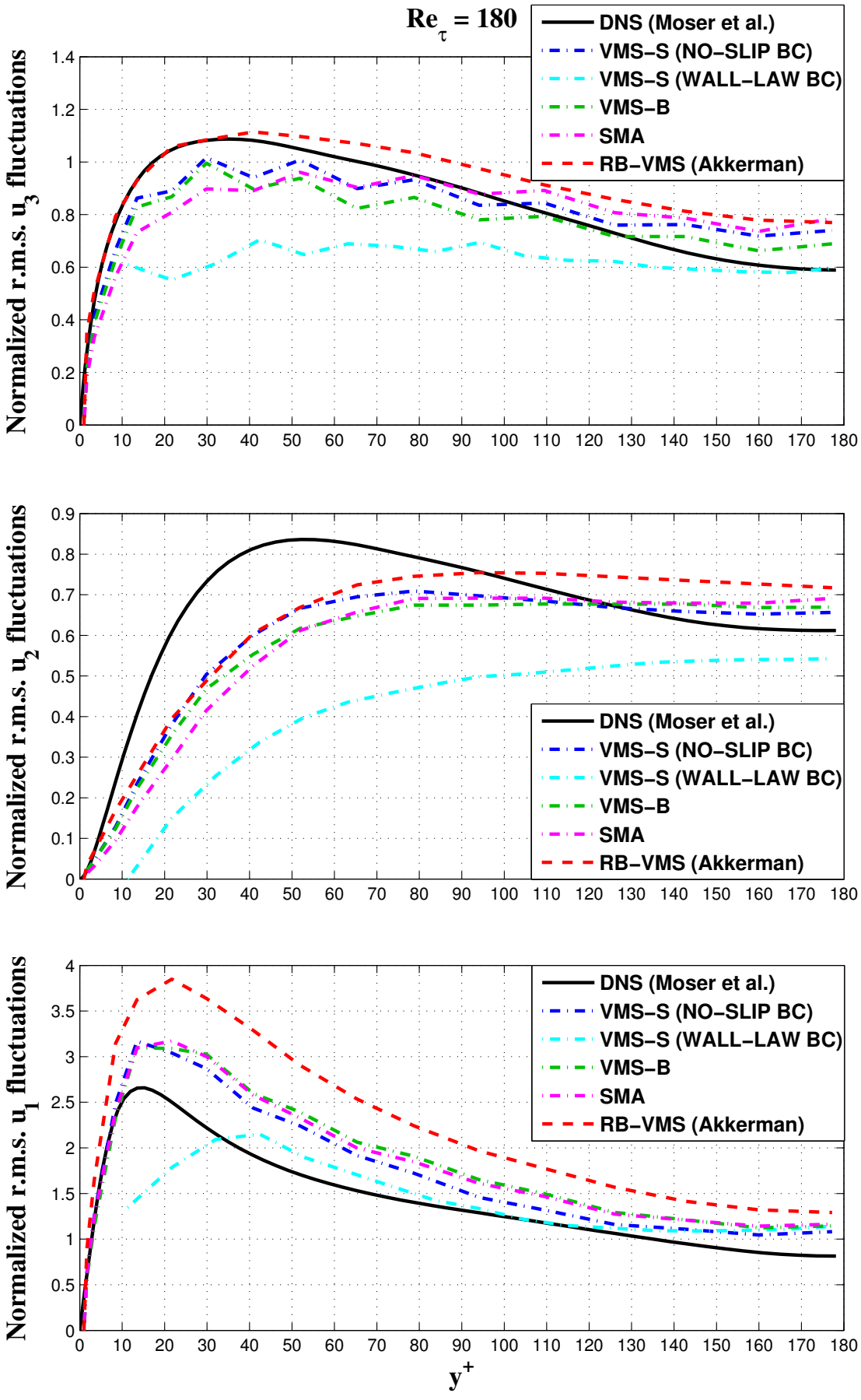

Figure 6.12:
Normalized r.m.s. velocity fluctuations profiles in wall coordinates y^+.

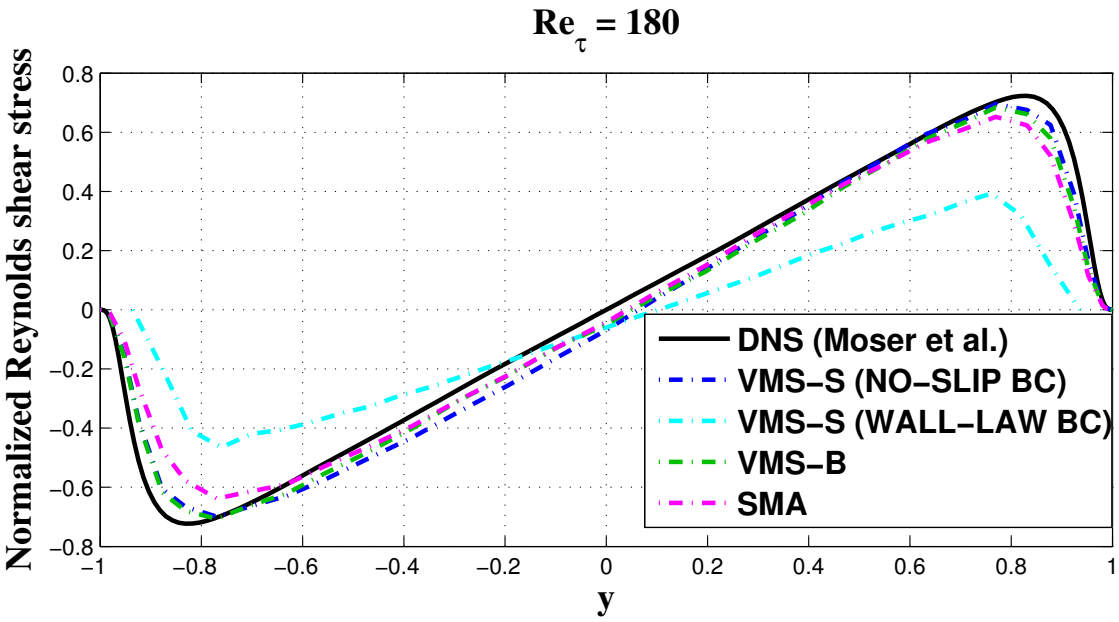

Figure 6.13:
Normalized Reynolds shear stress in global coordinates y.

Table 6.5 provides a quantitative picture for errors levels related to second-order statistics when the standard no-slip boundary conditions at the physical walls are incorporated in the various methods. Again, the VMS-S method is in general more in agreement with the DNS data.

Methods	$e_0^{\sqrt{\langle \tilde{u}_1^2 \rangle}}$	$e_0^{\sqrt{\langle \tilde{u}_2^2 \rangle}}$	$e_0^{\sqrt{\langle \tilde{u}_3^2 \rangle}}$	$e_0^{\langle \tilde{u}_1 \tilde{u}_2 \rangle}$
VMS-S (NO-SLIP BC)	0.2252	0.1652	0.1108	0.1249
VMS-B (NO-SLIP BC)	0.3002	0.2018	0.1246	0.1162
SMA (NO-SLIP BC)	0.2881	0.2236	0.1597	0.1706
RB-VMS (Akkerman)	0.5694	0.1753	0.1331	-

Table 6.5:
L^2-norm of the deviation from the DNS profiles for the second-order statistics.

We highlight also some considerations on the computational cost corresponding to the various methods. The computing times related to the statistical period from $t = 5$ to $t = 10$ time units (1 250 time steps) for all methods are given in Table 6.6. These are referred to the sequential execution of the numerical code on a MacPro with a Quad-Core Intel Xeon processor of 2.8 GHz and 10 GB of RAM. It can be seen that effectively the use of wall laws provides a significant reduction of the computing time, of about 34%, while the CPU time of both VMS approaches is comparable with the one of the standard

Smagorinsky approach, that saves at most a 4% of computing time.

Methods	CPU time
VMS-S (NO-SLIP BC)	398 207 (134)
VMS-S (WALL-LAW BC)	297 524 (100)
VMS-B (NO-SLIP BC)	401 128 (135)
SMA (NO-SLIP BC)	389 260 (131)

Table 6.6:
Computing times (in seconds); in parentheses: percentage to computing time with VMS-S (WALL-LAW BC).

6.4.3 Conclusions

Summarizing, on one hand we can state that the application of wall-law boundary conditions in this test could provide (at least for the leading stream-wise component of the velocity) similar results to those obtained by the standard approach based on the use of no-slip boundary conditions, a refined mesh towards the walls and the Van Driest damping improvement, with a noticeable reduced computational cost. On another hand, this preliminary study permits to assert that the VMS-S method gives for this test quite good results for both first and second-order statistics, in the worst condition of a very coarse basic discretization.

The results obtained in this section are quite promising as starting point for further improvements. Especially, the comparison with the numerical results of Akkerman [1] shows that the VMS-S method presents errors similar, or even smaller, than those of a RB-based method. The use of finer discretizations and the investigation of higher Reynolds numbers for this test need to be analyzed in order to draw more definitive conclusions. These issues are subject of a forthcoming paper [23], aimed at obtaining a more relevant benchmark for future works on the 3D turbulent channel flow.

In my opinion, the strength of the VMS-S method relies on the fact that it is not a simply projection-based VMS method, but a combination of (high-order term-by-term) stabilization and (projection) VMS-LES modeling. Similarly, the RB-VMS method of Akkerman [1] is a combination of (unusual) stabilization and (residual-based) VMS-LES modeling. The additional advantage introduced by the RB-VMS method is to keep all inertial (also convective) interactions between large and small scales, and to automatically insert also a stabilization of the divergence. In the VMS-S method, the stabilization of the divergence is not present. Actually, as we are applying a term-by-term stabilization, it could be considered by simply adding the corresponding (high-order) term. However, the divergence of the velocity is monitored and remains less than 10^{-12} throughout the simulation, thus the fulfillment of the continuity equation is approximately achieved in

the discrete case in a stable way. So that, it seems that the most relevant interactions between large and small scales are taken into account in the VMS-S method by the classical Galerkin term and the sub-grid eddy diffusion term, as well as the stabilization terms for the convection and the pressure gradient, which could lead to the higher instabilities, are already considered. This fact probably explains the achievement of similar error levels, that are not reachable without the aid of the stabilization procedure.

Nevertheless, Akkerman [1] shows that a $Q2$ FE discretization gives a marked improvement over the $Q1$ FE discretization. Also, increasing the continuity of the basis functions (e.g., C^1 quadratic NURBS) results in a further improvement of the results, as found in Bazilevs et al. [2] too. Effectively, a step in which we are working on is the efficient parallelization of the numerical code, by domain decomposition techniques and GMRES-like parallel iterative solvers. The aim is to reduce the computational cost when using the code on a double-refined mesh in each direction, at least. This should be sufficient to hopefully approach in reasonable CPU times the results pointed out in [1], [2] for at least second-order discretizations. Admittedly, these results are really impressive, as they reproduce with an excellent accuracy first and second-order statistics.

We have also to remark that the structure of RB-VMS methods is quite complex (*cf.* [1], [2]), and requires a large programming effort. Instead, projection-based VMS methods are highly simpler to work out, so that the proposed VMS-S method seems to provide a good compromise between accuracy and computational complexity, which is an important feature in the context of its practical performances, especially in view of its use in engineering and other applications.

Bibliography Part I

[1] Bennis, A. C., Chacón-Rebollo, T., Gómez-Mármol, M., and Lewandowski, R.: Stability of some turbulent vertical models for the ocean mixing boundary layer, *Appl. Math. Lett.* **21** (2008), 128–133.

[2] Bennis, A. C., Chacón-Rebollo, T., Gómez-Mármol, M., and Lewandowski, R.: Numerical modelling of algebraic closure models of oceanic turbulent mixing layers, *ESAIM-Math. Model. Num.* **44** (2010), 1255–1277.

[3] Blanke, B. and Delecluse, P.: Variability of the tropical atlantic ocean simulated by a general circulation model with two different mixed-layer physics, *J. Phys. Oceanogr.* **23** (1993), 1363–1388.

[4] Boyer Montégut, C., Madec, G., Fischer, A. S., Lazar, A., and Iudicone, D.: Mixed layer depth over the global ocean: An examination of profile data and a profile-based climatology, *J. Geophys. Res.* **109** (2004), C12003.

[5] Bramble, J. H., Pasciak, J. E., and Steinbach, O.: On the stability of the L^2 projection in $H^1(\Omega)$, *Math. Comput.* **71** (2001), 147–156.

[6] Brezis, H.: *Analyse fonctionelle: Théorie et applications*, Masson, 1983.

[7] Burchard, H. and Deleersnijder, E.: Stability of algebraic non-equilibrium second-order closure models, *Ocean Model.* **3** (2001), 33–50.

[8] Burchard, H., Bolding, K., Villarreal, M. R., Rippeth, T. P., Fisher, N., and Stips, A.: The GOTM modelling system, in: Baumert, H. Z., Simpson, J. H., and Sündermann, J. (eds.), *Marine Turbulence: Theories, Observations and Models*, Cambridge University Press (2005), 213–224.

[9] Cavalieri, D., Parkinson, C., Gloersen, P., and Zwally, H. J.: *Sea ice concentrations from Nimbus-7 SMMR and DMSP SSM/I passive microwave data, January 1979-June 2006*, National Snow and Ice Data Center, 2006.

[10] Chacón-Rebollo, T., Gómez-Mármol, M., and Rubino, S.: Numerical investigation of algebraic oceanic turbulent mixing-layer models, *Nonlin. Processes Geophys.* **20** (2013), 945–954.

[11] Chacón-Rebollo, T., Gómez-Mármol, M., and Rubino, S.: On the existence and asymptotic stability of solutions for unsteady mixing-layer models, *Discrete Cont. Dyn. S.-A* **34** (2014), 421–436.

[12] Chacón-Rebollo, T., Gómez-Mármol, M., and Rubino, S.: Analysis of numerical stability of algebraic oceanic turbulent mixing layer models, *Appl. Math. Model.* (2014), available online, doi: http://dx.doi.org/10.1016/j.apm.2014.04.050.

[13] Chacón-Rebollo, T. and Guillén-González, F.: An intrinsic analysis of existence of solutions for the hydrostatic approximation of Navier-Stokes equations, *C. R. Acad. Sci. Paris, Série I*, **330** (2000), 841–846.

[14] Chow, S. N. and Hale, J. K.: *Methods of bifurcation theory*, Springer-Verlag, 1982.

[15] Daru, V. and Tenaud C.: High order one-step monotonicity-preserving schemes for unsteady compressible flow calculations, *J. Comput. Phys.* **193** (2004), 563–594.

[16] Defant, A.: Schichtung und zirkulation des atlantischen ozeans, *Wiss. Ergebn.: Deutsch. Atlant. Exp. Forsch.* **6** (1936), 289–411.

[17] Deleersnijder, E., Hanert, E., Burchard, H., and Dijkstra, H. A.: On the mathematical stability of stratified flow models with local turbulence closure schemes, *Ocean Dynam.* **58** (2008), 237–246.

[18] Delecluse, P. and Madec, G.: Oceanic modelling and the role of the ocean in the climate system, In *Modeling the Earth's Climate and its Variability, Les Houches, Session LXVII 1997, W. R. Holland, S. Joussaume and F. David eds., Elsevier Science* (1999), 237–313.

[19] Fer, I.: Weak vertical diffusion allows maintenance of cold halocline in the central Arctic, *Atmos. Oceanic Sci. Lett.* **2** (2009), 148–152.

[20] Folland, G. B.: *Real analysis: Modern techniques and their applications*, John Wiley & Sons, 1999.

[21] Gaspar, P., Gregoris, Y., and Lefevre, J.-M.: A simple eddy kinetic energy model for simulation of the oceanic vertical mixing: Tests at Station Papa and long-term upper ocean study site, *J. Geophys. Res.* **16** (1990), 179–193.

[22] Gent, P. R.: The heat budget of the TOGA-COARE domain in an ocean model, *J. Geophys. Res.* **96** (1991), 3323–3330.

[23] Gill, A.-E.: *Atmosphere-Ocean dynamics*, Academic Press, 1982.

[24] Giusti, E.: *Minimal surfaces and functions of bounded variation*, Birkhäuser, 1984.

[25] Goosse, H., Deleersnijder, E., Fichefet, F., and England, M. H.: Sensitivity of a global coupled ocean-sea ice model to the parameterization of vertical mixing, *J. Geophys. Res.* **104** (1999), 13681–13695.

[26] Griffies, S. M. et al.: Coordinated Ocean-ice Reference Experiments (COREs), *Ocean Model.* **26** (2009), 1–46.

[27] Hecht, F.: New development in freefem++, *J. Numer. Math.* **20** (2012), 251–265.

[28] Jackett, D. R. and McDougall, T. J.: Minimal adjustment of hydrographic profiles to achieve static stability, *J. Atmos. Ocean. Tech.* **12** (1995), 381–389.

[29] Jones, J. H.: Vertical mixing in the equatorial undercurrent, *J. Phys. Oceanogr.* **3** (1973), 286–296.

[30] Kowalik, Z. and Murty, T. S.: *Numerical modeling of ocean dynamics*, World Scientific, 1993.

[31] Ladyženskaya, O. A., Solonnikov, V. A., and Ural'ceva, N. N.: *Linear and quasilinear equations of parabolic type*, AMS, 1968.

[32] Large, W. G., McWilliams, J. C., and Doney, S. C.: Oceanic vertical mixing: A review and a model with a nonlocal boundary layer parameterization, *Rev. Geophys.* **32** (1994), 363–403.

[33] Lemke, P.: A coupled one-dimensional sea ice-ocean model, *J. Geophys. Res.* **92** (1987), 13164–13172.

[34] Lewandowski, R.: *Analyse mathématique et océanographie*, Masson, 1997.

[35] Lilly, D. K.: The representation of small-scale turbulence in numerical simulation experiments, In *Proc. of the IBM Scientific Computing Symposium on Environmental Sciences* (1967), 195–210.

[36] Losch, M., Herlufsen, S., and Timmermann, R.: Effect of heterogeneous surface boundary conditions on parameterized oceanic deep convection, *Ocean Model.* **13** (2006), 156–165.

[37] Macdonald, A. and Wunsch, C.: An estimate of global ocean circulation and heat fluxes, *Nature* **382** (1996), 436–439.

[38] Madec, G., Delecluse, P., Imbard, M., and Levy, C.: *OPA version 8.0, Ocean General Circulation Model Reference Manual*, LODYC, Int. Rep. 97/04, 1997.

[39] Marshall, J. and Schott, F.: Open-ocean convection: observations, theory, and models, *Rev. Geophys.* **37** (1999), 1–64.

[40] Marshall, J., Adcroft, A., Hill, C., Perelman, L., and Heisey, C.: A finite-volume, incompressible Navier Stokes model for studies of the ocean on parallel computers, *J. Geophys. Res.* **102** (1997), 5753–5766.

[41] McDougall, T. J., Jackett, D. R., Wright, D. G., and Feistel, R.: Accurate and computationally efficient algorithms for potential temperature and density of seawater, *J. Atmos. Ocean. Tech.* **20** (2003), 730–741.

[42] McPhaden, M.: The tropical atmosphere ocean (tao) array is completed, *B. Am. Meteorol. Soc.* **76** (1995), 739–741.

[43] Meier, W., Fetterer, F., Knowles, K., Savoie, M., and Brodzik, M. J.: *Sea ice concentrations from Nimbus-7 SMMR and DMSP SSM/I passive microwave data, July-December 2006*, National Snow and Ice Data Center, 2006.

[44] Mellor, G. and Yamada, T.: Development of a turbulence closure model for geophysical fluid problems, *Rev. Geophys.* **20** (1982), 851–875.

[45] MITgcm Group: *MITgcm Release 1 Manual. (Online documentation), MIT/EAPS*, 2002. Available from: http://mitgcm.org/sealion/online_documents/manual.html

[46] Monin, A. S. and Obukhov, A. M.: Basics laws of turbulent mixing in the surface layer of the atmosphere, *Tr. Geofiz. Inst. Akad. Nauk. SSSR* **24** (1954), 163–187.

[47] Oltmanns, M., Straneo, F., Moore, G. W. K., and Mernild, S. H.: Strong downslope wind events in Ammassalik, Southeast Greenland, *J. Climate* **27** (2014), 977–993.

[48] Osborn, T. R. and Cox, C. S.: Oceanic fine structure, *Geophys. Fluid Dyn.* **3** (1972), 321–345.

[49] Pacanowski, R. C. and Philander, S. G. H.: Parameterization of vertical mixing in numerical models of tropical oceans, *J. Phys. Oceanogr.* **11** (1981), 1443–1451.

[50] Pedlosky, J.: *Geophysical fluid dynamics, 2nd Edn.*, Springer-Verlag, 1987.

[51] Peters, H., Gregg, M. C., and Toole, J. M.: On the parameterization of equatorial turbulence, *J. Geophys. Res.* **93** (1988), 1199–1211.

[52] Rahmstorf, S.: Thermohaline ocean circulation, In: *Encyclopedia of Quaternary Sciences*, Elsevier, 2006.

[53] Robinson, A. R.: An investigation into the wind as the cause of the equatorial undercurrent, *J. Mar. Res.* **24** (1966), 179–204.

[54] Rubino, S.: Numerical modeling of oceanic turbulent mixing layers considering pressure gradient effects, In *Mascot10 Proc.: IMACS Series in Comp. and Appl. Math.* **16** (2011), 229–238.

[55] Rudels, B., Jones, E., Schauer, U., and Eriksson, P.: Atlantic sources of the Arctic Ocean surface and halocline waters, *Polar Res.* **23** (2004), 181–208.

[56] Smagorinsky, J.: General circulation experiment with the Primitive Equations. I. The basic experiment, *Mon. Weather Rev.* **91** (1963), 99–164.

[57] Thomson, R. E. and Fine, I. V.: Estimating mixing layer depth from oceanic profile data, *J. Atmos. Ocean. Techn.* **20** (2003), 319–329.

[58] Timmermann, R. and Beckmann, A.: Parameterization of vertical mixing in the Weddell Sea, *Ocean Model.* **6** (2004), 83–100.

[59] Timmermann, R., Danilov, S., Schröter, J., Böning, C., Sidorenko, D., and Rollenhagen, K.: Ocean circulation and sea ice distribution in a finite element global sea ice-ocean model, *Ocean Model.* **27** (2009), 114–129.

[60] Verfürth, R.: A posteriori error estimates for nonlinear problems. Finite element discretizations of elliptic equations, *Math. Comput.* **62** (1994), 445–475.

[61] Veronis, G.: On properties of sea water defined by temperature, salinity and pressure, *J. Mar. Res.* **30** (1972), 227–255.

[62] Vialard, J. and Delecluse, P.: An ogcm study for the TOGA decade. Part I: Role of salinity in the physics of the western Pacific fresh pool, *J. Phys. Oceanogr.* **28** (1998), 1071–1088.

[63] Wang, Q., Danilov, S., and Schröter, J.: Finite element ocean circulation model based on triangular prismatic elements, with application in studying the effect of topography representation, *J. Geophys. Res.* **113** (2008), 1–21.

Bibliography Part II

[1] Akkerman, I.: *Adaptative variational multiscale formulations using the discrete Germano approach*, PhD thesis, Delft University of Technology, 2009.

[2] Bazilevs, Y., Calo, V. M., Cottrell, J. A., Hughes, T. J. R., Reali, A., and Scovazzi, G.: Variational multiscale residual-based turbulence modeling for large eddy simulation of incompressible flows, *Comput. Methods Appl. Mech. Engrg.* **197** (2007), 173–201.

[3] Bazilevs, Y., Michler, C., Calo, V. M., and Hughes, T. J. R.: Weak Dirichlet boundary conditions for wall-bounded turbulent flows, *Comput. Methods Appl. Mech. Engrg.* **196** (2007), 4853–4862.

[4] Bazilevs, Y., Michler, C., Calo, V. M., and Hughes, T. J. R.: Isogeometric variational multiscale modeling of wall-bounded turbulent flows with weakly enforced boundary conditions on unstretched meshes, *Comput. Methods Appl. Mech. Engrg.* **199** (2010), 780–790.

[5] Bernard, J. M.: Density results in Sobolev spaces whose elements vanish on a part of the boundary, *Chin. Ann. Math. Ser. B* **32** (2011), 823–846.

[6] Bernardi, C., Maday, Y., and Rapetti, F.: *Discrétisations variationnelles de problèmes aux limites elliptiques. Mathématiques & Applications* **45**, Springer-Verlag, (2004).

[7] Berselli, L. C., Iliescu, T., and Layton, W. J.: *Mathematics of large eddy simulation of turbulent flows*, Springer-Verlag, 2006.

[8] Brezis, H.: *Analyse fonctionelle: Théorie et applications*, Masson, 1983.

[9] Brezzi, F. and Fortin, M.: *Mixed and hybrid finite element methods*, Springer-Verlag, 1991.

[10] Brezzi, F., Rappaz, J., Raviart, P. A.: Finite dimensional approximation of nonlinear problems, Part I: branches of nonsingular solutions, *Numer. Math.* **36** (1980), 1–25.

[11] Brezzi, F., Rappaz, J., Raviart, P. A.:, Finite dimensional approximation of nonlinear problems, Part II: limits points, *Numer, Math.* **37** (1981), 1–28.

[12] Brezzi, F., Rappaz, J., Raviart, P. A.:, Finite dimensional approximation of nonlinear problems, Part III: simple bifurcation points, *Numer. Math.* **37** (1981), 1–30.

[13] Braack, M. and Burman, E.: Local projection stabilization for the Oseen problem and its interpretation as a variational multiscale method, *SIAM J. Numer. Anal.* **43** (2000), 2544–2566.

[14] Brooks, A. N. and Hughes, T. J. R.: Streamline Upwind/Petrov-Galerkin formulations for convection dominated flows with particular emphasis on the incompressible Navier-Stokes equations, *Comput. Methods Appl. Mech. Engrg.* **32** (1982), 199–259.

[15] Burman, E.: Interior penalty variational multiscale method for the incompressible Navier-Stokes equations: Monitoring artificial dissipation, *Comput. Methods Appl. Mech. Engrg.* **196** (2007), 4045–4058.

[16] Chacón-Rebollo, T.: A term-by-term stabilization algorithm for finite element solution of incompressible flow problem, *Numer. Math.* **79** (1998), 283–319.

[17] Chacón-Rebollo, T.: An analysis technique for stabilized finite element solution of incompressible flows, *M2AN Math. Model. Numer. Anal.* **35** (2001), 57–89.

[18] Chacón-Rebollo, T. and Domínguez-Delgado, A.: A unified analysis of mixed and stabilized finite element solutions of Navier-Stokes equations, *Comput. Methods Appl. Mech. Engrg.* **182** (2000), 301–331.

[19] Chacón-Rebollo, T., Gómez-Marmol, M., Girault, V., and Sánchez-Muñoz, I.: A high order term-by-term stabilization solver for incompressible flow problems, *IMA J. Numer. Anal.* **33** (2013), 974–1007.

[20] Chacón-Rebollo, T., Gómez-Mármol, M., and Restelli, M.: Numerical analysis of penalty stabilized finite element discretizations of evolution Navier-Stokes equation, Submitted, 2013.

[21] Chacón-Rebollo, T., Gómez-Mármol, M., and Rubino, S.: Derivation of the Smagorinsky model from a Galerkin discretization, In *Mascot11 Proc.: IMACS Series in Comp. and Appl. Math.* **17** (2013), 61–70.

[22] Chacón-Rebollo, T., Hecht, F., Gómez-Mármol, M., Orzetti, G., and Rubino, S.: Numerical approximation of the Smagorinsky turbulence model applied to the primitive equations of the ocean, *MATCOM J. Math. Comput. Simulat.* **99** (2014), 54–70.

[23] Chacón-Rebollo, T., Gómez-Mármol, M., and Rubino, S.: Numerical analysis of a finite element projection-based VMS turbulence model with wall laws, In preparation, (2014).

[24] Chacón-Rebollo, T., Gómez-Mármol, M., and Rubino, S.: *TurboMathS: a FreeFem++ numerical code for VMS turbulence models*, Research Group "Modelado Matemático y Simulación de Sistemas Medioambientales", University of Seville, 2014. (Published in [26])

[25] Chacón-Rebollo, T. and Lewandowski, R.: A variational finite element model for large eddy simulations of turbulent flows, *Chin. Ann. Math. Ser. B* **34** (2013), 667–682.

[26] Chacón-Rebollo, T. and Lewandowski, R.: *Mathematical and numerical foundations of turbulence models and applications*, In press, Birkhäuser, 2014.

[27] Choi, H. and Moin, P.: Effects of the computational time step on numerical solutions of turbulent flow, *J. Comput. Phys.* **113** (1994), 1–4.

[28] Clark, R. A., Ferziger, J. H., and Reynolds, W. C.: Evaluation of subgrid-scale models using an accurately simulated turbulent flow, *J. Fluid Mech.* **91** (1979), 1–16.

[29] Codina, R.: Comparison of some finite element methods for solving the diffusion-convection-reaction equation, *Comput. Methods Appl. Mech. Engrg.* **156** (1998), 185–210.

[30] Codina, R.: Stabilization of incompressibility and convection through orthogonal sub-scales in finite element methods, *Comput. Methods Appl. Mech. Engrg.* **190** (2000), 1579–1599.

[31] Codina, R.: A stabilized finite element method for generalized stationary incompressible flows, *Comput. Methods Appl. Mech. Engrg.* **190** (2001), 2681–2706.

[32] Codina, R., Principe, J. and Badia, S.: Dissipative structure and long term behavior of a finite element approximation of incompressible flows with numerical subgrid scale modeling, *Lect. Notes Appl. Comput. Mech.* Springer **55** (2011), 75–93.

[33] Collis, S. S.: Monitoring unresolved scales in multiscale turbulence modeling, *Phys. Fluids* **13** (2001), 1800–1806.

[34] Deardorff, J. W.: A numerical study of three-dimensional turbulent channel flow at large Reynolds numbers, *J. Fluid Mech.* **41** (1970), 453–465.

[35] Dubois, T., Jauberteau, F., and Temam, R.: *Dynamic multilevel methods and the numerical simulation of turbulence*, Cambridge University Press, 1999.

[36] Ekeland, I. and Temema, R.: *Convex analysis and variational problems*, North-Holland, 1976.

[37] Fortin, M.: Finite element solution of the Navier-Stokes equations, *Acta Numerica* **2** (1993), 239–284.

[38] Franca, L.P. and Farhat, C.: Bubble functions prompt unusual stabilized finite element methods, *Comput. Methods Appl. Mech. Engrg.* **123** (1995), 299–308.

[39] Galdi, G. P. and Layton, W. J.: Approximation of the larger eddies in fluid motion II: A model for space-filtered flow, *M3AS Math. Mod. Meth. Appl. Sciences* **10** (2000), 343–350.

[40] Germano, M., Piomelli, U., Moin, P., and Cabot, W. H.: A dynamic subgrid-scale eddy viscosity model, Phys. Fluids **3** (1991), 1760–1765.

[41] Ghia, U., Ghia, K. N., and Shin, C. T.: High-Re solutions for incompressible flow using the Navier-Stokes equations and a multigrid method, *J. Comput. Phys.* **48** (1982), 387–411.

[42] Girault, V. and Raviart, P. A.: *Finite element methods for Navier-Stokes equations: Theory and algorithms*, Springer-Verlag, 1986.

[43] Gravemeier, V.: *The variational multiscale method for laminar and turbulent incompressible flow*, PhD thesis, University of Stuttgart, 2003.

[44] Gravemeier, V.: Scale-separating operators for variational multiscale large eddy simulation of turbulent flows, *J. Comput. Phys.* **212** (2006), 400–435.

[45] Gravemeier, V.: The variational multiscale method for laminar and turbulent flow, *Arch. Comput. Meth. Engrg.* **13** (2006), 249–324.

[46] Gresho, P. M. and Sani, R. L.: *Incompressible flow and the finite element method*, John Wiley & Sons, 1998.

[47] Guermond, J. L., Minev, P., Shen, J.: An overview of projection methods for incompressible flows, *Comput. Methods Appl. Mech. Engrg.* **195** (2006), 6011–6045.

[48] Hecht, F.: New development in freefem++, *J. Numer. Math.* **20** (2012), 251–265.

[49] Hinze, J. O.: *Turbulence: An introduction to its mechanism and theory*, McGraw-Hill, 1959.

[50] Horgan, C. O.: Korn's inequalities and their applications in continuum mechanics, *SIAM Rev.* **37** (1995), 491–511.

[51] Hughes, T. J. R., Feijóo, G. R., Mazzei, L., and Quincy, J.-B.: The variational multiscale method-a paradigm for computational mechanics, *Comput. Methods Appl. Mech. Enrgrg.* **166** (1998), 3–24.

[52] Hughes, T. J. R., Franca, L. P., and Hulbert, G. M.: A new finite element formulation for CFD: VIII. The Galerkin/least-Squares method for advective-diffusive equations, *Comput. Methods Appl. Mech. Engrg.* **73** (1989), 173–189.

[53] Hughes, T. J. R., Oberai, A. A., and Mazzei, L.: Large eddy simulation of turbulent channel flows by the variational multiscale method, *Phys. Fluids* **13** (2001), 1784–1799.

[54] Hughes, T. J. R., Mazzei, L., and Jansen, K. E.: Large eddy simulation and the variational multiscale method, *Comput. Vis. Sci.* **3** (2000), 47–59.

[55] Hughes, T. J. R., Mazzei, L., Oberai, A., and Wray, A.: The multiscale formulation of large eddy simulation: Decay of homogeneous isotropic turbulence, *Phys. Fluids* **13** (2001), 505–512.

[56] Iliescu, T. and Fischer, P. F.: Large eddy simulation of turbulent channel flows by the rational large eddy simulation model, *Phys. Fluids* **15** (2003), 3036–3047.

[57] Iliescu, J., John, V., Layton, W. J., Matthies, G., and Tobiska, L.: A numerical study of a class of LES models, *Int. J. Comput. Fluid Dyn.* **17** (2003), 75–85.

[58] John, V.: On large eddy simulation and variational multiscale methods in the numerical simulation of turbulent incompressible flows, *Appl. Math.* **51** (2006), 321–353.

[59] John, V. and Kaya, S.: A finite element variational multiscale method for the Navier-Stokes equations, *SIAM J. Sci. Comput.* **26** (2005), 1485-1503.

[60] John, V. and Kaya, S.: Finite element error analysis of a variational multiscale method for the Navier-Stokes equations, *Adv. Comput. Math.* **28** (2008), 43–61.

[61] John, V., Kaya, S., and Kindl, A.: Finite element error analysis for a projection-based variational multiscale method with nonlinear eddy viscosity, *J. Math. Anal. Appl.* **344** (2008), 627–641.

[62] John, V. and Kindl, A.: Numerical studies of finite element variational multiscale methods for turbulent flow simulations, *Comput. Methods Appl. Mech. Engrg.* **199** (2010), 841–852.

[63] Kim, J., Moin, P., and Moser, R.: Turbulence statistics in fully developed channel flow at low Reynolds number, *J. Fluid Mech.* **177** (1987), 133–166.

[64] Kolmogorov, A. N.: The local structure of turbulence in incompressible viscous fluid for very large Reynolds numbers, *Proc. R. Soc. Lon.-A* **434** (1991), 9–13.

[65] Lilly, D. K.: A proposed modification of the Germano subgrid-scale closure method, *Phys. Fluids* **4** (1992), 633–635.

[66] Lions, J. L.: *Quelques méthodes de résolution des problèmes aux limites non linéaires*, Dunod, 2002.

[67] Jones, W. P. and Wille, M.: Large eddy simulation of a jet in a cross-flow, In *10th Symposium on Turbulent Shear Flows* **4** (1995), 1–6.

[68] Moin, P.: Advances in large eddy simulation methodology for complex flows, *Int. J. Heat Fluid Flow* **23** (2002), 710–720.

[69] Moin, P. and Kim, J.: Numerical investigation of turbulent channel flow, *J. Fluid Mech.* **118** (1982), 341–377.

[70] Moser, R., Kim, J., and Mansour, N. N.: Direct numerical simulation of turbulent channel flow up to $Re_\tau = 590$, *Phys. Fluids* **11** (1999), 943–945.

[71] Parés, C.: Existence, uniqueness and regularity of solution of the equations of a turbulence model for incompressible fluids, *Appl. Anal.* **43** (1992), 245–296.

[72] Parés, C.: Approximation de la solution des équations d'un modèle de turbulence par une méthode de Lagrange-Galerkin, *Rev. Mat. Apl.* **15** (1994), 63–124.

[73] Prandtl, L.: Über die ausgebildeten Turbulenz, *Zeitschrift für angewandte Mathematik und Mechanik* **5** (1925), 136–139.

[74] Prasad, A. K. and Koseff, J. R.: Reynolds number and end-wall effects on a lid-driven cavity flow, *Phys. Fluids* **1** (1989), 208–218.

[75] Richardson, L. F.: *Weather prediction by numerical process*, Cambridge University Press, 1922.

[76] Saad, Y. and Schultz, M. H.: GMRES - A generalized minimal residual algorithm for solving nonsymmetric linear systems, *SIAM J. Sci. Stat. Comp.* **7** (1986), 856–869.

[77] Sagaut, P.: *Large Eddy Simulation for Incompressible Flows, 2nd edition*, Springer, 2002.

[78] Schlichting, H. and Gersten, K.: *Boundary-layer theory, 8th edition*, Springer, 2000.

[79] Scott, R. and Zhang, S.: Finite element interpolation of non-smooth functions satisfying boundary conditions, *Math. Comput.* **54** (1990), 483–493.

[80] Smagorinsky, J.: General circulation experiment with the Primitive Equations. I. The basic experiment, *Mon. Weather Rev.* **91** (1963), 99–164.

[81] Spalding, D. B.: A single formula for the "law of the wall", *J. Appl. Mech.* **28** (1961), 455–458.

[82] Temam, R.: *Navier-Stokes Equations - Theory and Numerical Analysis*, AMS, 2001.

[83] Van Driest, E. R.: On turbulent flow near a wall, *J. Aerosp. Sci.* **23** (1956), 1007–1011.

[84] Verfürth, R.: Analysis of some finite element solutions for the Stokes problem, *RAIRO-Modél. Math. Anal. Numér.* **18** (1984), 175–182.

[85] Verfürth, R.: Finite element approximation of steady Navier-Stokes equations with mixed boundary conditions, *RAIRO Modél. Math. Anal. Numér.* **19** (1985), 461–475.

[86] Verfürth, R.: Finite element approximation of incompressible Navier-Stokes equations with slip boundary condition, *Numer. Math.* **50** (1987), 697–721.

[87] Von Kármán, T.: Mechanische Ähnlichkeit und Turbulenz, *Nachr. Ges. Wiss. Gottingen, Math. Phys. Klasse* **58** (1930).

[88] Wilcox, D. C.: *Turbulence modeling for CFD, 2nd edition*, DCW Industries, 1998.

[89] Zang, Y., Street, R. L., and Koseff, J. R.: A dynamic mixed subgrid-scale model and its application to turbulent recirculating flows, *Phys. Fluids* **5** (1993), 3186–3196.